PFC/RR-82-29

DOE/ET-51013-58
UC20

Electron Cyclotron Heating in the Constance 2 Mirror Experiment*

by

Michael E. Mauel

September 1982
Plasma Fusion Center
Research Laboratory of Electronics
Massachusetts Institute of Technology
Cambridge, MA 02139

*This report was originally submitted as a Doctoral Thesis to the Department of Electrical Engineering at the Massachusetts Institute of Technology on September 21, 1982.

This work was supported by DOE Contract No. DE-AC02-78ET-51013

Electron Cyclotron Heating in the Constance 2 Mirror Experiment

by

Michael E. Mauel

Submitted to the Department of Electrical Engineering and Computer Science
on September 21, 1982 in partial fulfillment of the requirements
for the Degree of Doctor of Science.

Abstract

Electron cyclotron heating of a highly-ionized plasma in mirror geometry is investigated. Of primary interest is the experimental diagnosis of the electron energy distribution and the comparison of the results of this diagnosis with a two dimensional, time-dependent Fokker-Planck simulation. These two goals are accomplished in four steps. (1) First, the power balance of the heated and unheated Constance 2 plasma is analyzed experimentally. It is concluded that the heated electrons escape the mirror at a rate dominated by a combination of the influx of "cool" electrons from outside the mirror and the increased loss rate of the ions. This analysis is used later to help construct the simulation. (2) The microwave parameters at the resonance zones are then calculated by cold-plasma ray tracing. High $N_{\|}$ waves are launched, and, for these waves, strong first-pass absorption is predicted. The absorption strength is qualitatively checked in the experiment by surrounding the plasma with non-reflecting liners. (3) A simplified quasilinear theory including the effect of $N_{\|}$ is developed to model the electrons. An analytic expression is derived for the RF-induced "pump-out" of the magnetically-confined "warm" electrons ($T_e \gtrsim 100 ev$). Results of the Fokker-Planck simulations show the development of the electron energy distribution for several plasma conditions and verify the scaling of the analytic expression for RF-induced diffusion into the loss cone. (4) Sample x-ray and endloss data are presented, and the overall comparison between the simulation and experiment is discussed. The x-ray signals indicate that, for greater RF power, the hot electron density increases more rapidly than its temperature. The time history of the endloss data, illustrating RF-enhancement, suggests the predicted scaling for warm-electron "pump-out". Finally, a comparison between the measured and predicted energy distribution shows that, over the range of parameters investigated ($2 \times 10^{11} cm^{-3} < n_e < 1 \times 10^{12} cm^{-3}$ and $\langle n_e T_e \rangle \lesssim 200 ev \cdot cm^{-3}$) and within the accuracy with which the plasma parameters can be determined, the "bulk", "warm", and "hot" components of the heated Constance 2 electrons are indeed reproduced by the simulation.

Thesis Supervisor: Louis D. Smullin
Professor of Electrical Engineering

Acknowledgment

I would like to sincerely acknowledge the guidance, support, and advice of my thesis advisor, Professor Louis Smullin. His technical insights and quick grasp of the fundamentals of this thesis have greatly helped to clarify the interpretation of these results. In particular, his insistence on my careful analysis of the electron "pump-out" resulted in one of the more important measurements of this thesis. His confidence in my ability to learn—throughout both my undergraduate and graduate work at M.I.T.—has been a continuous source of encouragement and motivation without which this thesis could not have been completed. Also, Professor Smullin's personal example of sincere concern for his students at M.I.T. and his community and world leadership has been inspiring. Throughout my work with him, Professor Smullin has been a teacher, colleague, and friend whose lasting contribution to my professional and personal growth receives my full appreciation and gratitude.

I would also like to thank the other members of the Constance 2 experiment, particularly Dr. Bob Klinkowstein, whose work helped motivate the Constance 2 experimental program. Bob was largely responsible for the design of the vacuum system and was a partner in the design of the magnet system. More importantly, Bob offered me his personal advice and instruction in all aspects of experimental mirror physics. The experiment technicians, Ken Retman, Bob Daveo and Mel Alpert, assembled most of the experiment and its electronics. Ken was also the mechanical designer of the LN$_2$-cooled Ioffe Bars and the cathode structure for the LaB$_6$ plasma gun. Dr. Jim Irby, Dr. Pete Kenyon, Rich Garner, Amin Ezzidine, Pat Rymer, Steve Voldman, and over a dozen undergraduate students all contributed much to this thesis, performing numerous necessary tasks from constructing diagnostic or control circuits to helping to determine confinement time scaling with density. Special thanks are due Jim for making the axial density measurements and to Rich for doing most of the work involved with the development of the ray-tracing code.

I gratefully acknowledge the courteous assistance of the staff of the Research Laboratory of Electronics. A special thanks should be given to Mr. George Leach, who helped considerably in the fabrication of vacuum parts, waveguide, and the prototype diverter coil.

Also, I received substantial help from Dr. John Kulp, Chuck Linton, George Charette, David Plummer, and the staff of the Macsyma Consortium Computer during the design and construction of the data acquisition system. George also assisted with the programming performed for the numerical part of this thesis. The thesis manuscript was prepared on The Macsyma Consortium Computer. The program "EFFI" and the CDC7600 at MFE-LLL was used to obtain the magnetic field information.

The thesis readers, Professor Ronald Parker and Dr. Richard Post, provided thoughtful feedback on the presentation and direction of this thesis, for which I would like to extend my sincere appreciation.

Finally, I would like to acknowledge the support and encouragement which I have received from my wife, Allison Moore.

The work of this thesis was supported by D.O.E. Contract No. DE-AC-78ET-51013.

Contents

Chapter 1

Introduction

1.1. Brief Statement of the Problem

With the invention of the thermal barrier, electron cyclotron heating has played a new and vital role in the design of tandem mirror experiments and the development of alternative tandem mirror concepts. According to current plans (Damm, 1980, Baldwin, *et al.*, 1980), the plug electrons will be heated to several times the energy of the central cell electrons, and thermal barriers (Baldwin and Logan, 1980) will slow the heat exchange between the two electron populations. ECRH might also be involved with negative tandem operation (Nexsen and Grubb, 1981) and the creation of hot, potential-modifying electrons which insure ion microstability (Kanaev, 1979). For all of these applications, ECRH is used to "shape" the electron energy distribution—producing, for example, the specific barrier and plug temperatures and densities which optimize the plug's confining potential. In TMX-U, ECRH must be *controlled* to prevent hot-tail runaway (Stallard, 1980), and the heating process must be *understood* in order to predict its effect on particle balance and potential modification (Baldwin *et al.*, 1981). A realistic procedure is required which can be used to evaluate ECRH in the various mirror applications. The WKB/quasilinear theory of RF heating provides this procedure. However, until now, the predictions of the full WKB/quasilinear model have not been compared to experimental measurements of ECRH in mirror geometry. ***This thesis makes this comparison by measuring the electron energy distribution from the Constance 2 experiment and calculating the "predicted" distribution with a Fokker-Planck simulation based on a bounce-averaged quasilinear model (Mauel, 1981).***

In order to correctly model the plasma and provide a practical means to compare the code and experiment, the four-step procedure described below was followed:

(i) The plasma's behavior and power balance were analyzed with and without heating. The data show that the plasma acts as a long column extending along the magnetic field between the two end-walls. The ion loss rate is proportional to the thermal speed. When ECRH is applied, only a slight increase in potential is observed which is consistent with the high density at the mirror peak. In addition, significant heating at the edge of the plasma is observed. (Chapter 2.)

(ii) The index of refraction, $N_{||}$, polarization, and absorption strength were calculated using geometric optics. The absorption strength was checked qualitatively in the experiment by measuring the heating efficiency with and without non-reflecting liners surrounding the plasma. (Chapter 3.)

(iii) The Fokker-Planck computer program was developed to model the electrons diagnosed in step (i) interacting with the wave described by step (ii). An analytic check of one of the results was derived—that of the RF-induced "pump-out" of the warm magnetically-confined electrons. The results of the simulations are summarized. (Chapter 4.)

(iv) Measurements of the hot-electron temperature using a target x-ray detector and the time history of the warm-electron endloss using a gridded endloss analyzer were compared to the "equivalent measurements" made during the simulations. (Chapter 5.)

Note that a separate chapter is devoted to each of the four steps outlined above.

1.2. Previous Work in ECRH of Mirror-Confined Plasma

Electron cyclotron heating of mirrors began in the 1960's with the successful experiments of Becker, Dandle, and others at Oak Ridge Laboratories (Becker, *et al.*, 1962, Dandle *et al.*, 1964), Ikegami at Nagoya (Ikegami, 1967), and Fessenden and Smullin at MIT (Fessenden, 1966). (See also the review Dandle, *et al.*, 1979.) These experiments were ECRH discharges which produced superthermal electron tails ($T_{hot} \sim 1 Mev$), well separated in energy from the cooler ($T_e \sim 10 ev$) and denser bulk electrons. The experiments usually operated at steady state (or continuously at high duty), and were fueled and stabilized by the ionization of the surrounding gas. It was felt that the hot electrons absorbed most of the microwave power and that the dominant loss mechanisms were pitch-angle scattering off the denser bulk electrons and ions and Rutherford scattering off the neutrals. Since the experiments were long-lasting, diagnostics were relatively simple, consisting of diamagnetic data and pulse-height analysis of the copious hard x-ray signals.

These early experiments preceded most of the theoretical work concerning ECRH in mirror geometry which was performed later, in the first half of the 1970's. Probably the most significant work was that of Lichtenberg, Lieberman, and Jaeger (Jaeger, *et. al.*, 1972, Lieberman, *et al.*, 1972). They realized that the overlap of the electron bounce-resonances due to the finite RF field strength leads to velocity-space diffusion—even for a mono-chromatic wave! Earlier, others (*eg.* Grawe, 1969) had shown that for a single pass through a cyclotron resonance, the particle receives a "kick" in energy (an increase in $v_\perp$ unless $N_\| \neq 0$). The energy "kick" is given by

$$\Delta E \approx B_{res}\Delta\mu \approx \frac{q}{m}|E|_{rf}\tau_{eff}v_{\perp,res}\sin\phi + \frac{1}{2}\frac{q^2}{m^2}|E|^2_{rf}\tau^2_{eff} \tag{1}$$

where E and μ are the particle energy and magnetic moment per unit mass, $|E|_{rf}$ is the electric field strength, and τ_{eff} is the effective resonance time.[1] Notice that the interaction is made up of a gyro-phase dependent term (where ϕ is the gyro-phase) and a non-linear, positive-definite term. The second term is smaller than the first term by roughly $\Delta v_\perp / v_\perp$. Grawe stated that *if ϕ was random for each pass through resonance*, then Equation 1 could be used with a Fokker-Planck equation to predict the heating rates of ECR heated plasma. Why or how ϕ became random was not known until the work of Lieberman and Lichtenberg. They realized that since ϕ, during successive resonance crossings, was non-linearly coupled with a particle's orbit (and, therefore, also coupled with the fluctuating E and μ), ϕ and $\Delta\mu$ become "naturally" random provided $\Delta v_\perp / v_\perp > \omega_B/\omega$, where ω_B is the bounce frequency. On the other hand, when the field-strength is small, ϕ is no longer random and no heating occurs.[2] For the Constance 2 experiment, the field strength is typically between 1 and $20v/cm$, and the RF-induced motion in velocity space can be either quasilinear or non-linear. The interaction is never superadiabatic. This is illustrated in Figure 1.

The only previous experimental comparison of measured heating rates with those predicted from a diffusive model was reported by Ikegami, *et al.*, 1973. He conducted his experiments before Lieberman's and Lichtenberg's study, and mistakenly believed that wave-particle interactions became random through a large spread in $N_\|$. Nevertheless, the form of his model equations was obtained from a general analysis by Sturrock, 1966 and is exactly the same as what would have been obtained from Equation 1. The model Fokker-Planck equation in $v_\perp$-space is written as

$$\left.\frac{\partial F}{\partial t}\right|_{rf} = -\frac{\partial}{\partial v_\perp}\left\langle\frac{\Delta v_\perp}{\Delta t}\right\rangle F + \frac{1}{2}\frac{\partial^2}{\partial {v_\perp}^2}\left\langle\frac{\Delta v_\perp \Delta v_\perp}{\Delta t}\right\rangle F \tag{2}$$

where the average, $\langle\ldots\rangle$, is the average over successive resonance passes. This means $1/\Delta t \sim \omega_B = v_\perp / L_B$, and, from Equation 1,

---

[1] In fact, it is not hard to show that Equation 1 is valid for *any* wave-particle resonance in an inhomogeneous magnetic field. However, for Landau damping at lower frequencies, τ_{eff} may be longer than the correlation time. In this case, the quasilinear diffusion coefficient is lowered by the factor τ_{cor}/τ_{eff}. (See Chapter 4,)

[2] This is called superadiabaticity (Aamodt, 1971 and Rosenbluth, 1972).

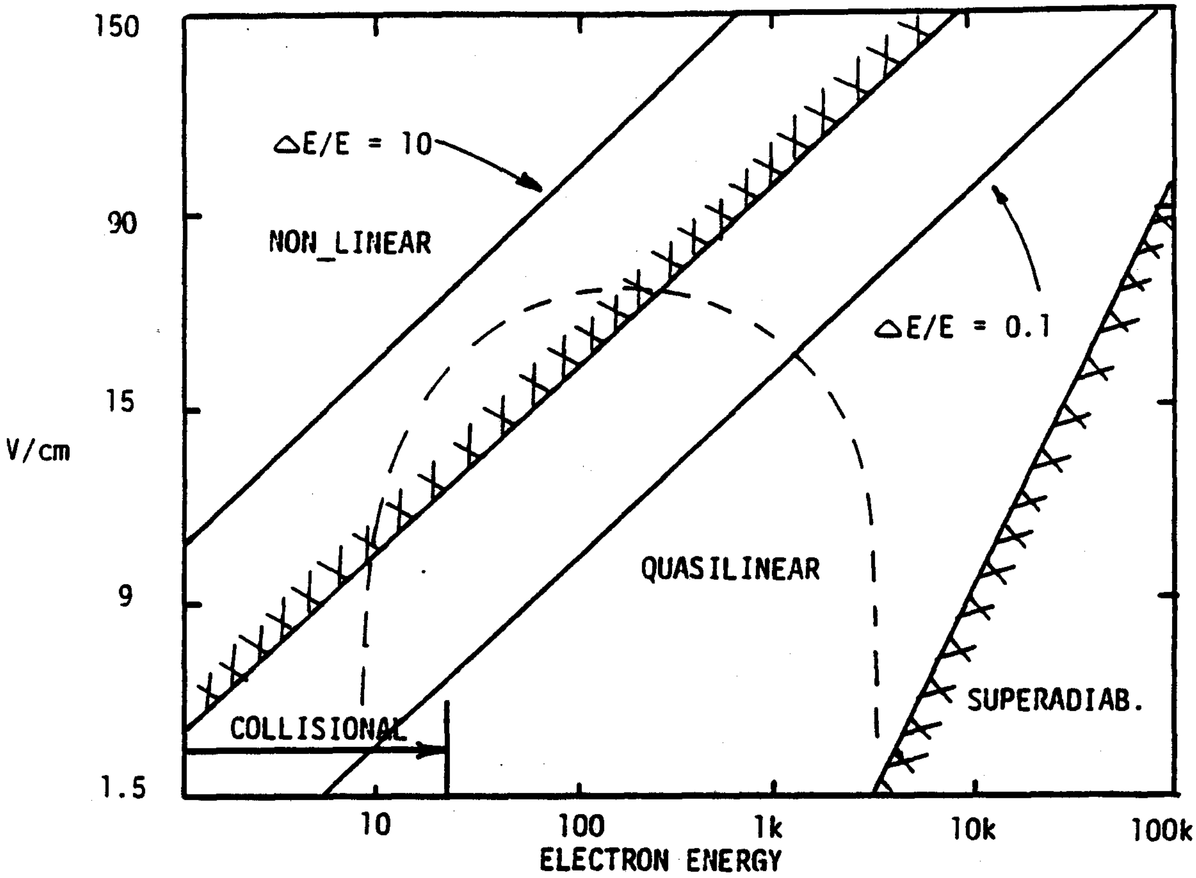

Figure 1. A diagram illustrating the three regions of RF heating in the Constance 2 experiment. The superadiabatic region occurs for low RF fields and high energy—when $\Delta v_\perp / v_\perp \lesssim \omega_{ll}/\omega$. The non-linear region occurs at high RF fields and low energy—when $\Delta v_\perp / v_\perp \gtrsim 1$. The quasilinear region is between. That portion outlined with the dotted-line is the approximate operating region for the experiment.

$$\left\langle \frac{\Delta v_\perp}{\Delta t} \right\rangle \sim \frac{1}{2v_\perp} \left\langle \frac{\Delta v_\perp \Delta v_\perp}{\Delta t} \right\rangle = \frac{1}{2L_B} \frac{q^2}{m^2} |E|^2_{rf} \, \tau^2_{eff} \equiv R \tag{3}$$

with the "RF acceleration", R, approximately independent of $v_\perp$. Combining Equations 2 and 3 gives Ikagami's one-dimensional diffusion equation

$$\left. \frac{\partial F}{\partial t} \right|_{rf} = R \frac{\partial}{\partial v_\perp} v_\perp \frac{\partial F}{\partial v_\perp} \tag{4}$$

The form of Equation 4 is equivalent to a one-dimensional version of the quasilinear equation used in this thesis. It could be considered valid for ECRH resonant at the midplane of a mirror "without a loss-cone".

Ikagami's key result was that he was able to match the time development of the hard x-ray signals ($T_{hot} > 30kev$) to an analytic solution of Equation 4 with a velocity-independent particle "sink" and a zero-energy particle "source". The procedure was actually a single-parameter fit since the measured loss-time (when the RF is turned off) determined the particle "sink" and the hot-electron density rise determined the particle "source". Ikegami was then free to choose an R which fit the data! It is interesting that the best fit corresponded to less than 10% of the input power being absorbed by the hot electrons.

Although Ikegami showed that a simplified diffusive model can in fact represent the hot electron development during ECRH, the model he used fails to provide the predictive power required for the new tandem mirror experiments. Presently, we expect the details of collisional and RF-induced pitch-angle scattering and the RF wave parameters (*eg.* $N_{||}$) to influence the development of the energy distribution (*i.e.* the R), the trapping of passing particles and heating of cold electrons (*i.e.* the "source"), and the loss rate mirror-confined electrons (*i.e.* the "sink"). In practice, a design procedure is needed which, when given a density, an initial temperature, a microwave launch geometry, and an injected power, computes the full 2-dimensional response of the plasma to the RF. This procedure is the self-consistent, WKB/quasilinear theory of wave and particle interactions used in this thesis.

The quasilinear theory in a magnetic mirror was first derived by Berk, 1978. His derivation was limited to the WKB solution of the Drift-Cyclotron-Loss-Cone instability and the self-consistent interaction of the wave with ions. He used this formalism to show that the instability is mono-chromatic and saturates at relatively low intensities due to wave-induced diffusion of ions into the loss-cone (*i.e.* ion "pump-out"). The extension of this work to electro-magnetic waves was performed by Bernstein and Baxter, 1981, and, in a form more suitable to numerical simulation, by Mauel, 1981. Using these theories, the "design procedure" mentioned above becomes a two-step process. First, geometric optics determines the wave characteristics: $N_{||}$, polarization, and resonant field-strength per input power flux. Next, the bounce-averaged quasilinear equation is used with the well-known Fokker-Planck equation[3] (for electron-electron and electron-ion collisions) to determine the development of the electron velocity-distribution.

The first example of this technique was prepared by Stallard, *et al.* 1981. He analyzed the single-frequency heating at the fundamental and harmonic resonances in the TMX-U experiment. Ray-tracing was used to determine that $N_{||} \lesssim 1$ and that the waves would be absorbed on the first pass through the plasma. Then, using techniques similar to those used in this thesis, the steady-state velocity-space distribution was calculated for $N_{||} = 0$ by solving the 2-dimensional partial differential equation given by $\partial F/\partial t = 0$. The simulation indicated the very important result that hot-tail runaway should *not* be expected in TMX-U provided that the RF-field strength is limited spatially along the mirror axis. (However, whether or not the runaway would in fact be a problem when the fields are *not* limited was not determined.)

---

[3] See, for example Killeen and Marx, 1972.

The experimental investigation of this result is presently underway as part of the TMX-U experiment.

Finally, it should be emphasized that theoretically (if not practically) the WKB/quasilinear techniques mentioned above and used in this thesis are valid during strong absorption of the incoming waves with $N_{\|} \neq 0$. However, in this case, the cyclotron resonances are Doppler-shifted so that particles of different parallel velocity interact with fields of different intensity. The particles with the largest $v_{\|}$ interact with the most intense fields. Those turning at resonance ($v_{\|} = 0$) interact with the weakest fields. Thus the quasilinear diffusion coefficient is a function of not only the interaction times, τ_{eff}, but also the damping length—which may change with time during heating. This "hot-particle shielding" may enhance hot-electron tail heating and is discussed further in Chapters 3 and 4.

1.3. General Approach

This thesis addresses two major goals: (1) the experimental measurement of the heated electrons using a diamagnetic loop, a Langmuir probe, a gridded endloss analyzer, and a target x-ray detector, and (2) the theoretical prediction of what these diagnostics "should" see based on a Fokker-Planck simulation.

As a first step towards accomplishing these goals, the power/particle balance of the heated and unheated plasma were diagnosed. This is reported in Chapter 2. The most important experimental technique was to observe the scaling of the particle and energy confinement times as density and temperature were varied. For instance, the endloss analyzer and diamagnetic loop indicate that the ions are cool, and the scaling of the particle confinement time with line-density is proportional to the square-root of the ratio of the diamagnetism to the line density—*i.e.* the ion thermal speed. Probe and endloss data are consistent with this conclusion. For the heated electrons, the initial energy loss rate (*i.e.* just after the turn-off of the ECRH) scales as $\sqrt{T_e}$. The losses are dominated by the "bulk" electrons ($T_e < 50ev$) which escape the mirror at a rate determined by a combination of the influx of cool electrons external to the mirror and the increased ion loss rate. The influx of cool electrons prevents a large rise of potential and allows the heated electrons to reach a quasi-equilibrium. This is analogous to the "passing" electron population of a tandem mirror (Cohen, *et al.*, 1980). Also, in Chapter 2, the observation that the radius of the heated plasma increases during ECRH is summarized.

In Chapter 3, examples of ray tracing calculations are presented for two of the three launch geometries analyzed during the experiment. The analysis uses the cold-plasma dielectric tensor in a geometry approximating the Constance 2 plasma. The procedure follows closely that used by Porkolab, *et al.* 1980. The ray-tracing determines the index of refraction and propagation angle at resonance. This information is then used with a "warm" plasma theory—which includes the bouncing-motion of the electrons (Mauel, 1982b)—to determine the wave polarization and single-pass absorption. For the two launchers at high magnetic field (*i.e.* $\omega < \omega_{ce}$), $N_{\|} > 3.0$ and single-pass absorption is expected. A check of the absorption strength was made by surrounding the plasma with a non-reflective liner and measuring the high ($\sim$ 30%), single-pass heating efficiency with the diamagnetic loop.

In Chapter 4, the large electron "passing" density inferred from the data in Chapter 2 and the high $N_{\|}$ calculated in Chapter 3 are used to construct the Fokker-Planck simulation. The experimental evidence that the plasma potential changes only slightly during ECRH and that the density at the mirror peak is high simplifies the Fokker-Plank analysis. Since the particle orbits depend upon the potential, a constant potential means that the quasilinear diffusion coefficient does not change during the simulation. The passing particles are modeled as a Maxwellian distribution at the mirror peak which enter the mirror region at a transit rate. Inclusion of $N_{\|}$ effects is also straightforward. The bounce-averaged theory evaluates the diffusion paths at the resonance point for each particle—even when that resonance is Doppler-shifted. However, the diffusion paths depend upon $N_{\|}$ in exactly the "right" way to cancel the change due to the Doppler-shift (Mauel, 1982a).[4] The important effects of finite $N_{\|}$ are (1) the modification of the effective interaction time, τ_{eff} (for example, a particle turning at resonance will interact much less strongly for large $N_{\|}$ than for small $N_{\|}$), (2) the increased number of particles which resonate with the wave (*i.e.* those turning before the $\omega = \omega_{ce}$ surface), and (3) the spatial dependence of the electric field strength due to damping along the field lines. A brief analysis of these effects is included. In addition, an approximate analytic expression for the relative ECRH-induced "pump-out" of the warm, magnetically-confined electrons is derived and checked against the simulations.

The main emphasis of Chapter 4, however, is not the theory on which the simulation is based, but rather the simulation's results. The Fokker-Planck code calculates the energy distribution, the target x-ray signals, and the endloss distribution as functions of the density at the mirror peak, the electric field strength, the ion density, and the magnetic field. In addition, the scaling of the hot-electron parameters with electric field strength and the time history of the warm electron endloss are examined.

In Chapter 5, target x-ray and endloss data during and after ECRH are compared with the predictions and scaling of the simulation. The scaling of the hot

---

[4] Busnardo-Neto, *et al.*, 1976 has called the (well known) $N_{\|}$-dependence of the diffusion paths "longitudinal cooling". This dependence reflects the fact that, for finite $N_{\|}$, a particle passing through resonance receives both a "kick" in $v_{\perp}$ and a "kick" in $v_{\|}$. However, the electron motion is described by the *bounce-averaged* diffusion paths (*i.e.* the "normal" diffusion paths evaluated at the Doppler-shifted resonance) which are independent of $N_{\|}$.

electron temperature and density with increasing RF power and the measurements of the time history of the warm electron endloss which suggest ECRH enhancement are emphasized. The intensity of the x-ray signal increases with RF-power while the ratio of signals from detectors with different filters (which indicate temperature) changes more slowly. The warm endloss was measured with a gridded analyzer with one of the grids biased to repel the ions and the other biased to detect only those electrons heated to energies greater than 100ev (*i.e.* magnetically-confined). In this way, the current detected at the analyzer is proportional to the total rate of velocity-space diffusion into the loss cone. A measure of the RF-diffusion relative to the collisional diffusion is made by observing the rapid decrease in measured current when the microwaves are turned off. The data collected suggest that the observed decrease is due to the end of ECRH diffusion of warm electrons into the loss cone. The scaling of this data with density is consistent with that predicted in Chapter 4. The uncertainty in this interpretation results from the possibility of electron heating from electron plasma waves excited from parametric instabilities (Porkolab and Chen, 1977). Thus, although the endloss data clearly shows RF-enhancement, the enhancement may not be due to ECRH diffusion. This possibility was discovered accidently when non-*cyclotron*-resonant, parallel electron heating was observed with the endloss analyzer. To make certain that the "non-resonant" heating did not result from the cyclotron resonance between the endloss analyzer and the mirror peak, a metallic screen was used to eliminate any external RF interaction. The non-resonant, parallel heating was still present, demonstrating that the interaction occurred within the mirror region. Nevertheless, at low RF power, the time histories of the non-resonant and resonant heating can often be distinguished, and it is these data which are compared with the simulation.

The final chapter summarizes the parameters measured during the experiment and compares these measurements with the Fokker-Planck code. In principle, the comparison is straightforward since the simulation calculates the "numerical equivalent" of the measured data. However, due in part to the complicated geometry of the experiment (which limits the accuracy with which the diamagnetism and line-densities can determine the average energy *sampled* by the diagnostics) and in part to the limitations of the target x-ray analysis, the comparison is often qualitative. Nevertheless, the Langmuir probe measurement of the "bulk" electron temperature, the endloss measurement of the "warm electrons", and the target x-ray measurement of the "hot" electron tail are all consistent with equally energetic "simulated" measurements.

Chapter 2

The Constance 2 Experiment

In the first half of this chapter, the Constance 2 mirror experiment and its diagnostics are briefly described. The second half presents analysis of the power balance of the unheated and heated plasma and parameterizes the electron distribution during heating. The data with direct bearing on the goals of this thesis are emphasized. Further details can be found in Klinkowstein, *et al.*, 1981 and Mauel, *et al.*, 1980.

2.1. Description

The Constance 2 vacuum chamber and geometry were modeled after the Constance 1 and PR-6 experiments. (See Kanaev, 1979 and Klinkowstein, 1978.) As with these machines, the plasma is produced from a gun located at the far end of a long (3 meters for Constance 2) solenoidal guide field. During injection, the plasma produced by the gun travels down the guide-field, filling the machine with a long column of plasma. At the end of injection, the plasma-gun discharge is crowbarred, and the plasma decays within $100\mu sec$. At the beginning of the decay, a fast-rising diverter coil is energized to separate the long guide-field plasma from the mirror-region. A schematic of the vacuum vessel and magnet set is shown in Figure 1.

The following description of the experiment is organized into three subsections. The first deals with the magnetic geometry, the second with typical machine operation, and the third with a brief description of the ECRH system.

2.1.1. Magnetic Geometry . For Constance 2 (and mirror-machines in general), magnetic geometry significantly influences the operation and diagnosis of the experiment. The magnetic geometry determines ECRH resonant zone location, influences ion-confinement, determines the plasma density at the wall, and, for this experiment, modifies the plasma injection and neutral gas evolution.

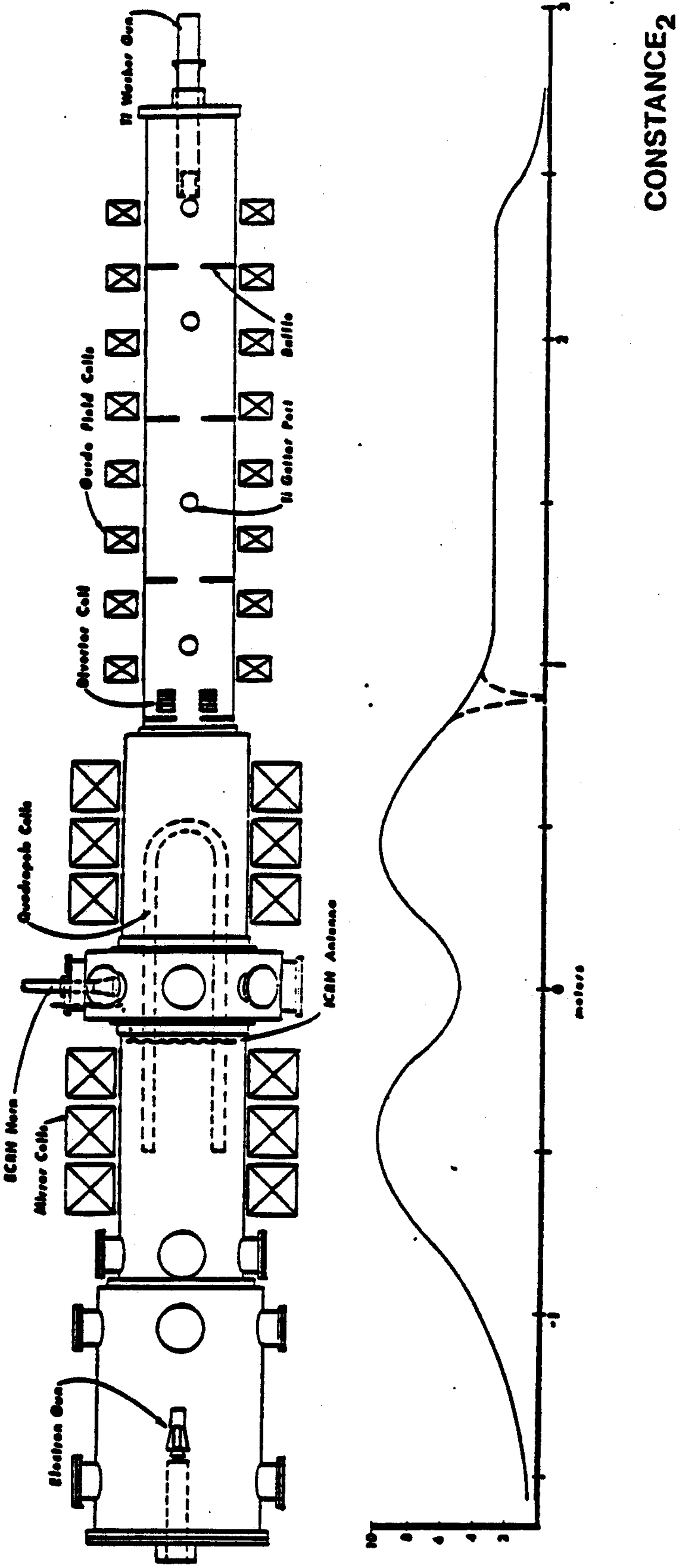

Figure 2. A schematic of the Constance 2 vacuum vessel and magnetic coils. (The guide field is actually one meter longer than shown.)

To calculate the field geometry, the computer code *EFFI*[1] was used. EFFI generates plots of the mod-B surfaces and of the field lines. The surfaces of constant field strength determine the resonant zone location, the mirror ratio and the field strength at the walls. The axial field was measured with a Hall-effect probe and found to agree with the code's output. The code determined both the mapping of the flux from the plasma gun through the mirror and the mapping of the trapped plasma through the mirror peaks during the plasma decay. In addition, the flux tubes which pass through the diamagnetic loop and to the endloss analyzer were calculated. Finally, the code also computes the integral, $\int dl/B$, which was used to determined line-average MHD stability.

Figure 3 shows a plot of the magnetic geometry for the typical ratio of Ioffe bar current to main magnetic current. This typical ratio was low and gave a neutral or slightly negative radial well depth at the midplane. However, the configuration was still found to be line-averaged minimum-B stable. The primary reason for operating with the low Ioffe currents was to reduce the amount of injection current which bombards the chamber walls near the mirror peaks. This wall bombardment contributed most to the neutral density rise. Also in Figure 3 is a sketch of the shape of the plasma during injection and after re-circularization. For the typical Ioffe current, the ellipticity, ϵ, of the mirror-trapped plasma is about 7:1. A circular plasma, 5cm diameter at the midplane, maps into an ellipse 10cm long and 1.2cm wide at the mirror peaks. Note that the Larmor diameter for a 100ev ion at 6kgauss is 0.3cm so that the fan is four 100ev ion diameters wide. For the injection stream, the ellipticity at the midplane is 7:1, but then increases to $\sim$ 50:1 at the mirror peak due to the rapid fanning as the field lines approach the bars. The 2cm diameter plasma gun maps into an ellipse 10cm long by 0.2 cm wide—less than one 100ev ion Larmor diameter.

Two observations related to the field geometry (these will be presented later in Section 2.4) are the influence of the external plasma on the energy confinement of the heated plasma and the density rise during ECRH due to the ionization of gas at the walls. The first effect is largely due to the cool ions created by the gun (Section 2.1.2). The remaining part of the first effect and the second effect stem from the high magnetic field strength at the walls. The value of B at a wall determines the density of cold wall plasma (*i.e.* secondaries and ionized gas) and the mirror-ratio at the wall, inhibiting flow into the mirror. When the field is low, the density is also low ($n \sim 1/B$), reducing the collision frequency and the "access" cone (in velocity-space) for particle flux into the mirror. When the field is high, the wall plasma is dense, collisional, and more able to flow into the mirror. Unless the mirror-plasma is highly mirror-confined (so that the external density is much

---

[1] This code was made available to users of the MFE-LLL computer system. EFFI was written by S. Sackett and can be referenced in LLL report no. UCRL-52402.

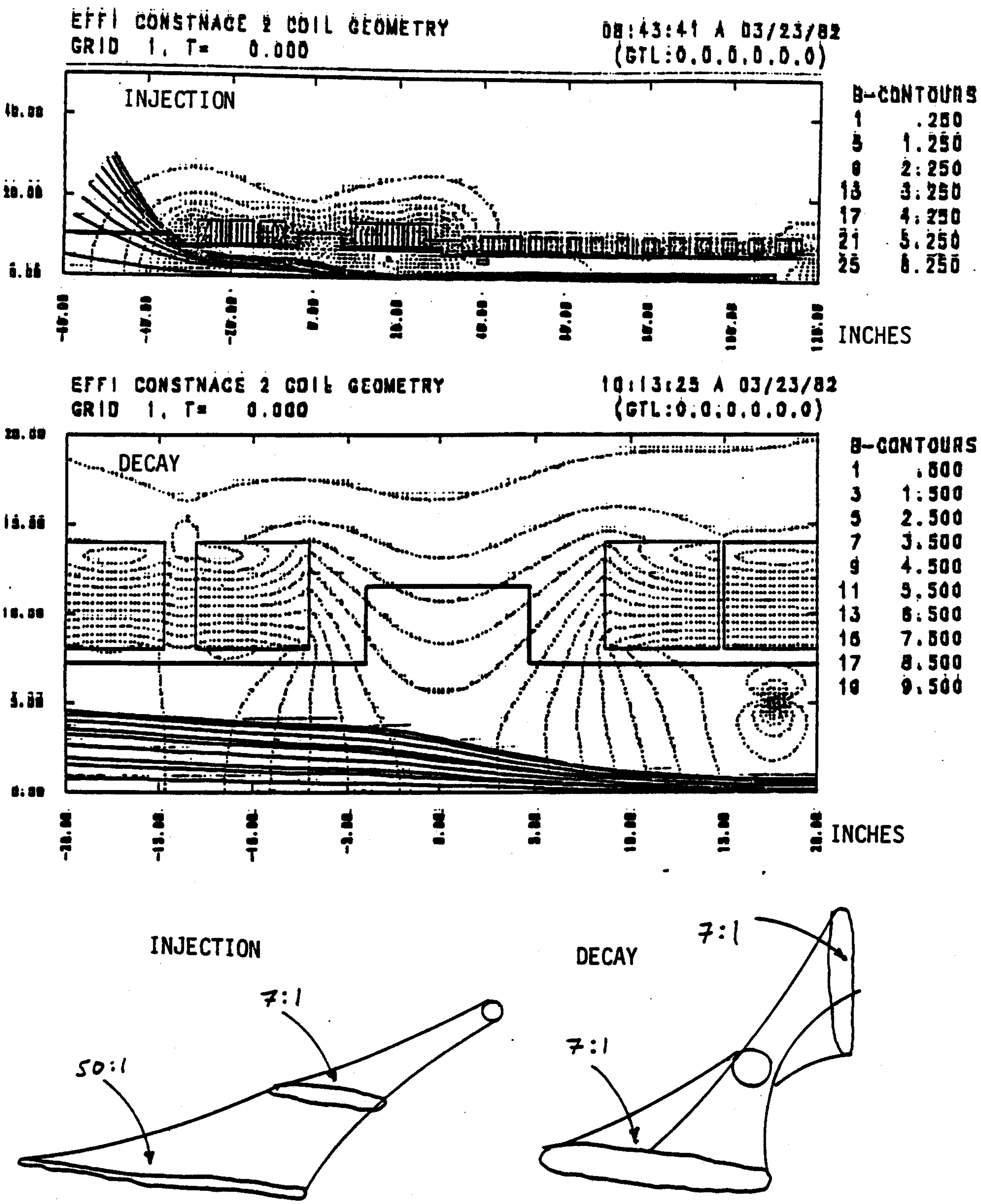

Figure 3. Typical magnetic geometry during and after injection. The circular flux tube at the plasma gun becomes an 7:1 ellipse at the midplane and a 50:1 ellipse at the second mirror peak. The enhanced ellipticity results from the close proximity of the Ioffe bars to the axis. After injection, for a circular plasma at the bottom of the trap, the ellipticity of the end fans is about 7:1.

smaller than the mirror-density), the high-field, wall contact in Constance 2 suggests the possibility of the wall interactions discussed in Section 2.4.

Finally, the magnetic surface(s) corresponding to cyclotron resonance usually extend across the cross-section of the mirror chamber. (The surfaces are actually quite complicated because of the presence of the Ioffe bars in the chamber.) The Mod-B surfaces, shown in Figure 3, are also the cyclotron heating zones. Note that, as the midplane field is reduced, the resonance zones move axially towards the mirror peak. As it is raised, the resonance zones move toward the midplane, and, raised further, move radially to the walls.

2.1.2. Operation

The behavior of the plasma is largely determined by the properties of the plasma source. Three basic types of plasma guns were used in these experiments, the titanium washer stack gun, the pulsed-gas, molybdenum washer gun, and the LaB_6, hot-cathode gun. The various gun designs were continuously modified and tested to try to increase the trapped diamagnetism. Although no reproducible improvement was achieved, superior ion temperatures at highest densities were occasionally observed with the hot cathode gun. The reasons for the wide variation of parameters are not known, although the parameters which "optimize" the diamagnetism produced from each gun have been determined. Most of the data of this thesis were taken with the hot-cathode gun.

The endloss analyzer (Section 2.2.3) provides much of the quantitative information about the injection stream. Figure 4 shows endloss data which give the ion and electron energies during and after injection. Data for both on axis and slightly off axis are shown. The initial, low density ion energy is about 150ev, falling to about 40ev as the line-density increases beyond 10^{12}cm^{-2}. The electron energy also decreases from about 70 ev to about 30 ev during injection and drops rapidly afterwards.

Charge exchange and Langmuir probe measurements are consistent with these endloss measurements. Initially, some hot ions ($T_i \sim 150ev$) are trapped in the mirror.[2] The charge-exchange analyzer—which only measures trapped ions—begins to observe a decrease in intensity at $\sim 1 \times 10^{12} cm^{-2}$, roughly corresponding to the decrease in ion endloss energy. A swept Langmuir probe at the edge of the plasma shows a $40ev$ initial electron energy which drops to 5 to $10ev$ within $7\mu sec$ after the crowbar of the discharge current. These data are presented in Figure 5.

Except when a specific density was required, the length of the injection usually corresponded to the maximum diamagnetism that could be obtained for the

---

[2] The trapping process is a combination of collisions and fluctuations occurring in the mirror midplane. In fact, ion cyclotron fluctuations at the midplane have been measured during injection; however, it is not known whether the fluctuations result from the streaming hot ions or whether the hot ions are a result of the fluctuations.

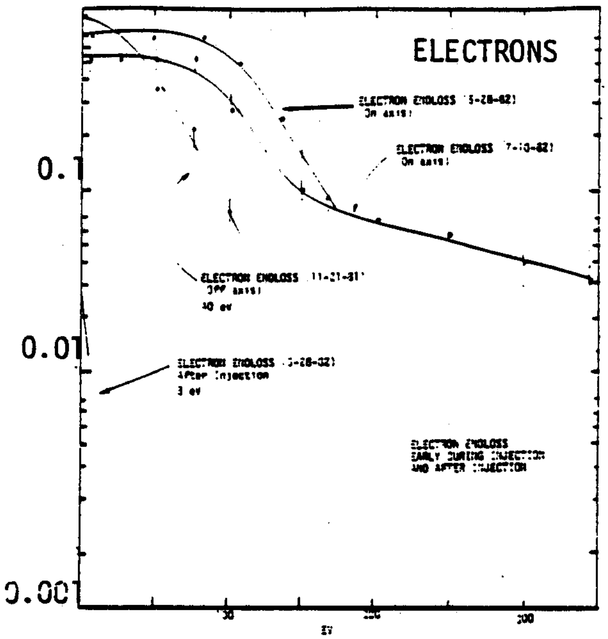

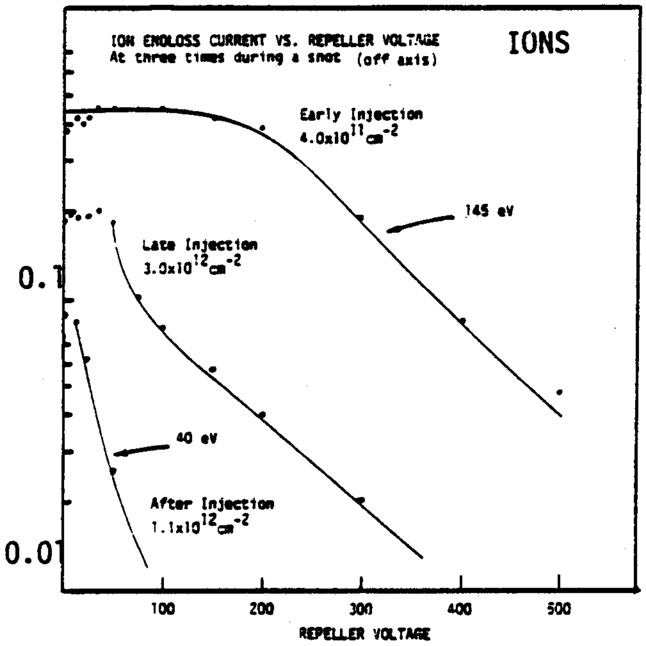

Figure 4. Endloss data showing the ion and electron stream currents as functions of particle energy. The data were taken both on and off axis, therefore, intercepting either the stream, or the plasma which has drifted off axis. The slope of the distribution is related to the mean energy and the "knee" determines the minimum energy of the species which results when the particles originate at a region of definite potential. For both the electrons and the ions, the average energy drops during the shot.

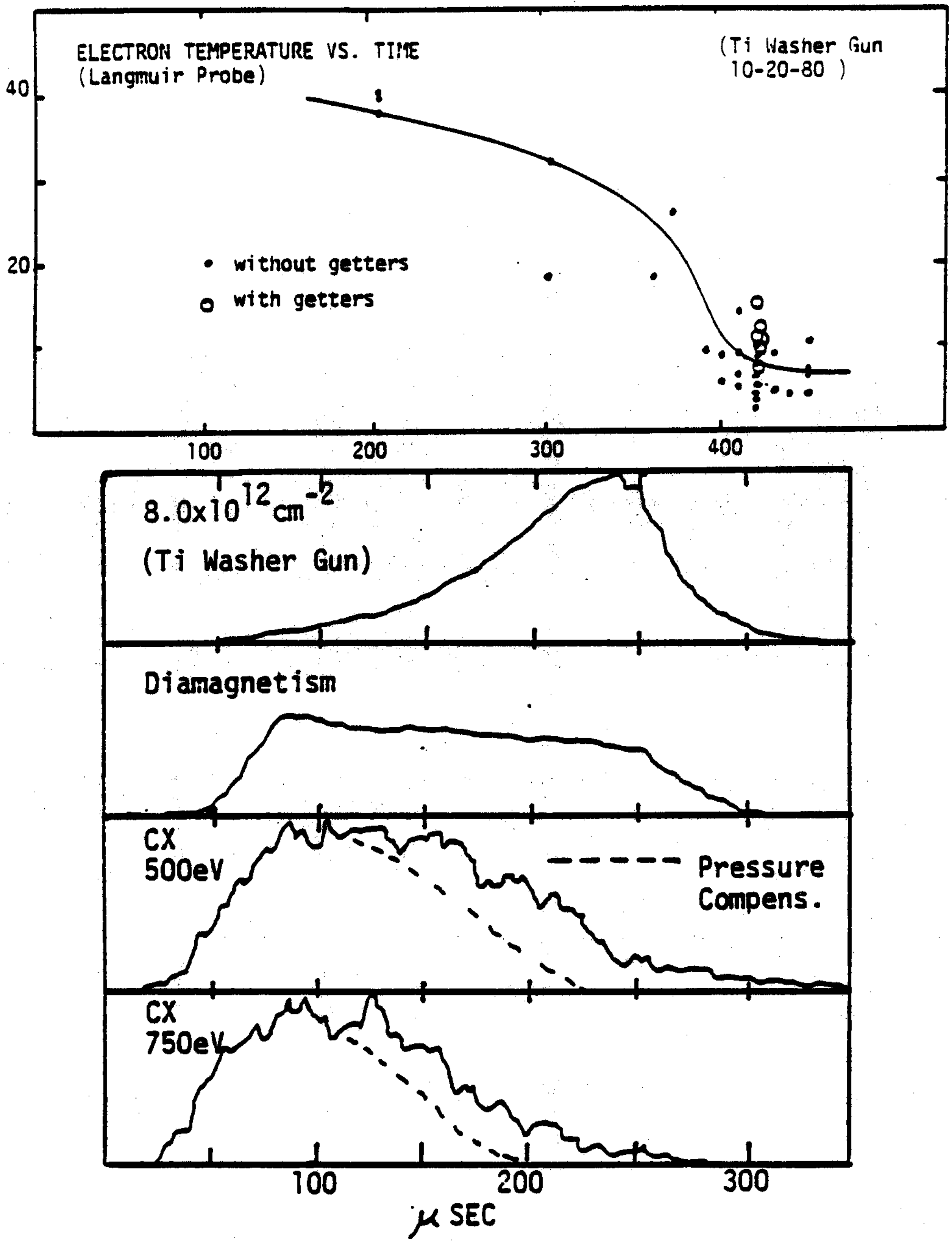

Figure 5. (Top) The electron temperature during and after injection measured with a Langmuir probe at the edge of the plasma. (Bottom) An example of the charge exchange signal along with diamagnetism and line-density.

"optimum" gun parameters. This usually gave a filling time roughly equal to or longer than the decay time.

Near the end of the injection, the diverter coil is used to "valve off" the plasma in the guide-field. This occurs either simultaneously with the crowbar of the plasma gun discharge or 50μsec beforehand. (The diverter coil current rises in 50μsec and decays with an L/R time of 600μsec.) If the diverter coil is left off, then the plasma density usually continues to rise after crowbar, indicating that the plasma is denser

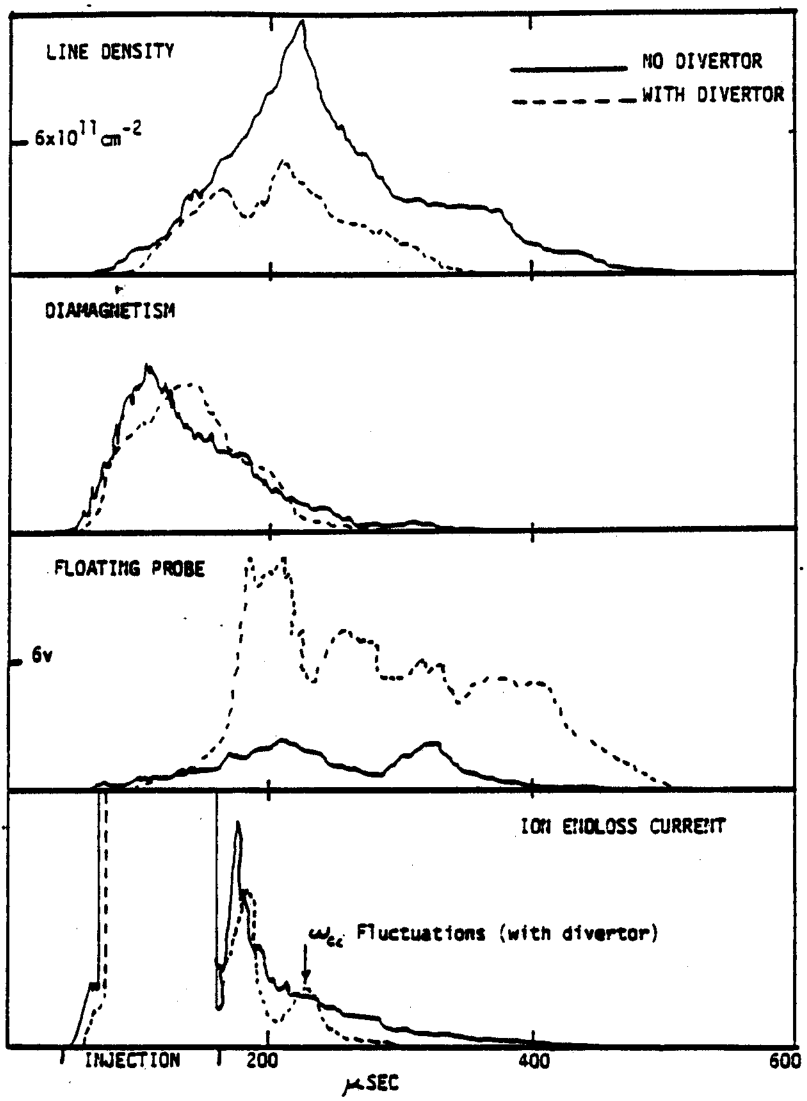

Figure 6. An example of the effect of the diverter coil on the plasma parameters. The solid line is the data without energizing the diverter coil. and the dotted line is typical of the data with the diverter coil.

"upstream" in the guide-field. As the diverter coil is energized, slow (~ 50μsec) density oscillations are observed by the interferometer and a Langmuir probe. It is likely that these are due to the re-circularization of the elliptical cross-section of the injected plasma. Figure 6 shows an example of the effect of the diverter on plasma line-density, ion endloss, floating potential, and diamagnetism.

During the decay of the plasma, the ECRH pulse is applied. Usually the pulse is delayed 50 to 100μsec to allow some of the plasma to re-circularize. The characteristic particle decay-time of the plasma is between 50 and 120μsec.

2.1.3. ECRH System . The ECRH system consists of the magnetron and modulator, the waveguide and power monitors, and the three launching antennae. The Varian SFD-303 X-band magnetron donated for the Constance 1 experiments generated the microwaves. The tube is powered by a spark-gap modulator which can deliver up to 5 joules of energy in pulses up to 40μsec. The forward and reflected power is monitored with calibrated detectors. The waveguide is inserted into the vacuum chamber in one of three different orientations. Each orientation launches the waves at different propagation angles with respect to the magnetic field. (See Figure 29 in Chapter 3.) For two of the orientations, the waveguides are located at the high-field side of resonance (*i.e.* at launch $\omega_{ce} > \omega$) and launch waves having propagation angles with respect to the magnetic field of either 10° or 30°. These two waveguides are pressurized past the cyclotron surface so that all of the evacuated guide has $\omega_{ce} > \omega$. The other orientation launches from low fields, (*i.e.* $\omega > \omega_c$ at the mirror midplane) and is limited to about 25kWatt due to RF breakdown.

Finally, the spark-gap/magnetron system produces a short ($\sim 0.7\mu sec$, $P_{burst} \approx 45kWatt$) "burst" of RF power at the beginning of every RF pulse. This increases the initial rate of rise of diamagnetism and influences the interpretation of the endloss results. (See Section 5.2.) This effect must be considered even though the reason for the "burst" is unknown.

2.2. Diagnostics

Figure 7 shows an exploded view of the diagnostics used in this thesis. They are arranged approximately as they are used in Constance 2. (The Thompson scattering and VUV diagnostics shown were either not operating or not used during this thesis.) The principal diagnostics were the interferometer, the diamagnetic loop, a charge-exchange analyzer, an endloss analyzer, the x-ray detectors, and several movable probes. In addition, a twenty-channel data-acquisition system recorded and processed the data.

2.2.1. Interferometer. A 60GHz microwave interferometer was used to obtain the line-averaged density. The microwaves were launched with ordinary polarization, normal to the injection fan. Thus, the measured phase-shift is proportional to the average density and the "width" of the fan, $2w$. The formula below was used:

$$\langle 2wn_e \rangle = 2.2 \times 10^{13} cm^{-2} \frac{\Delta\phi}{2\pi} \tag{5}$$

$\Delta\phi$ is the measured phase-shift, and ω_p is assumed to be much less than the freqency of the interferometer.

To make the most use of this diagnostic, the plasma thickness must be estimated. This was done with a Langmuir probe (Section 2.2.6). The probe was biased to measure the ion-saturation current and was moved radially to obtain the density profile. For the unheated plasma, after injection, the plasma radius was $\sim 3cm$. However, the radii during and after injection appear different because of the (partial or complete) re-circularization of the plasma during the plasma decay. The effects

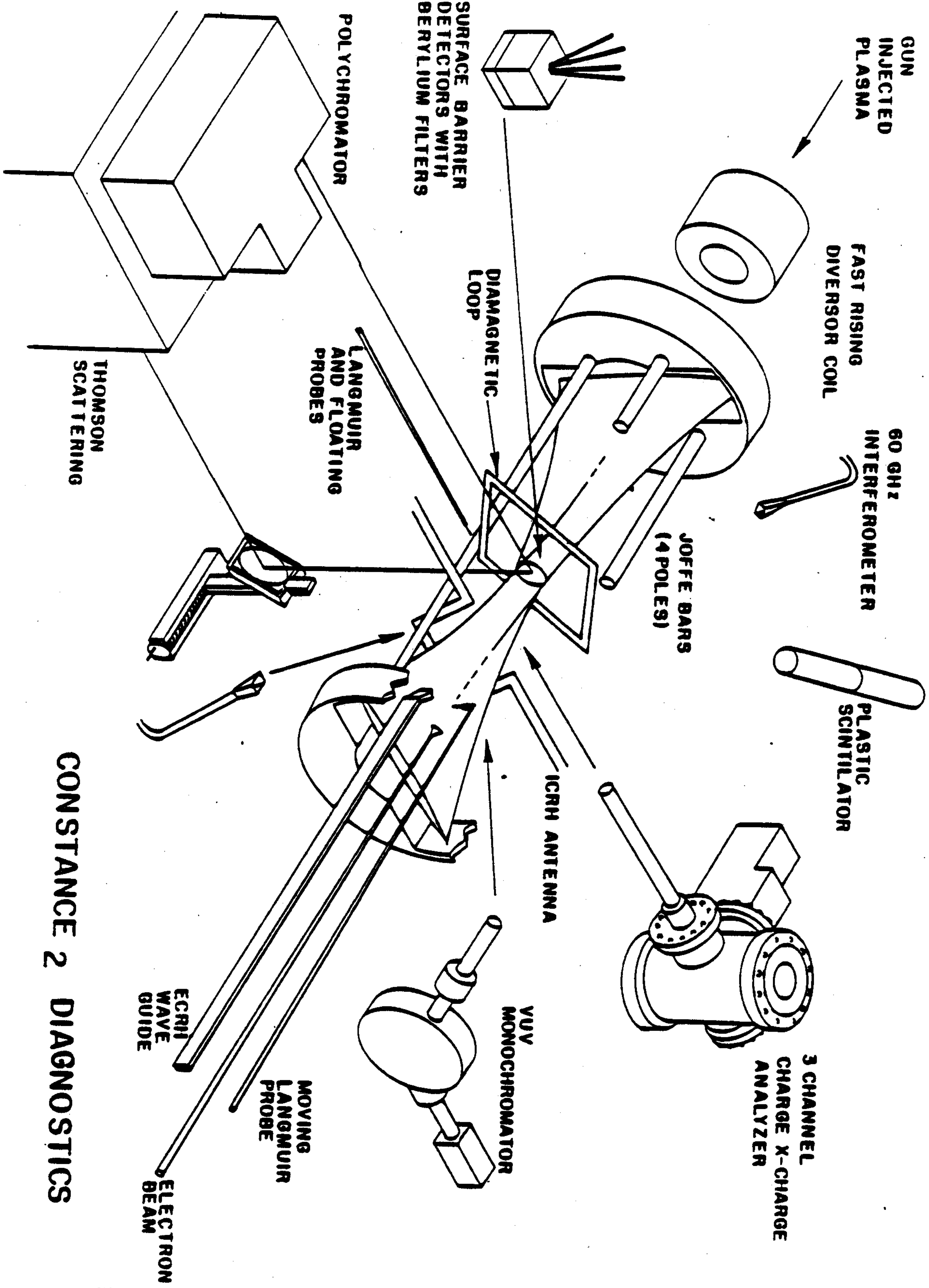

Figure 7. A schematic of the Constance 2 diagnostics.

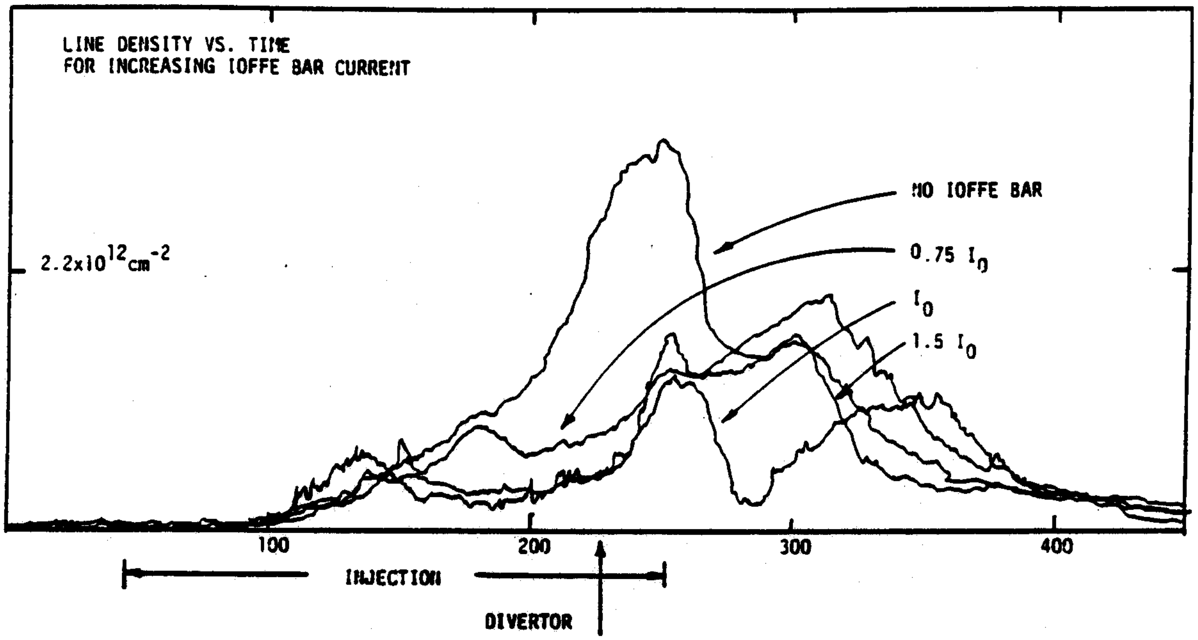

Figure 8. Variation of the plasma line density with increasing Ioffe bars illustrating the changing ellipticity, and presenting evidence for re-circularization.

of the re-circularization appear in the interferometer signal through the variation of the ellipticity, ϵ. In fact, as the Ioffe current is increased, the expected $1/\sqrt{\epsilon}$ decrease in the line-density can be observed. After injection, the plasma re-circularizes, and the line-densities with and without Ioffe bars remain slightly different since the plasma radius after re-circularization with Ioffe bars is larger than the plasma radius without Ioffe bars. Figure 8 illustrates this effect.

2.2.2. Charge Exchange Analyzer. A three-channel charge exchange analyzer was built by modifying the single-channel analyzer used in the Constance 1 experiment. The energy resolution of each channel was calibrated with an ion source. Since the analyzer is collimated, only neutrals which result from charge exchange with trapped, hot ions are measured. For typical parameters, the current in each channel can be related to the ion energy distribution, hot-ion density, and neutral pressure by the following formula

$$\Gamma_{cx}(E) \approx V_{det} R_{det}(E, E_i) \Omega_{det} (\sigma v) n_o n_p S(E) \tag{6}$$

In this formula, $V_{det} R_{det}(E, E_i) \Omega_{det}$ is the product of the volume of plasma observed by the detector, the energy resolution per channel, and the solid angle. $(\sigma v) n_o n_p S(E)$ is the product of the charge exchange reaction rate, neutral and plasma density, and stripping efficiency. The equation is valid when the plasma is transparent to neutrals (the usual case). The charge exchange analyzer was mostly used during the initial evaluation and comparison of the plasma guns. These studies showed that the hot-ion density increased with line-density until the line-density exceeded

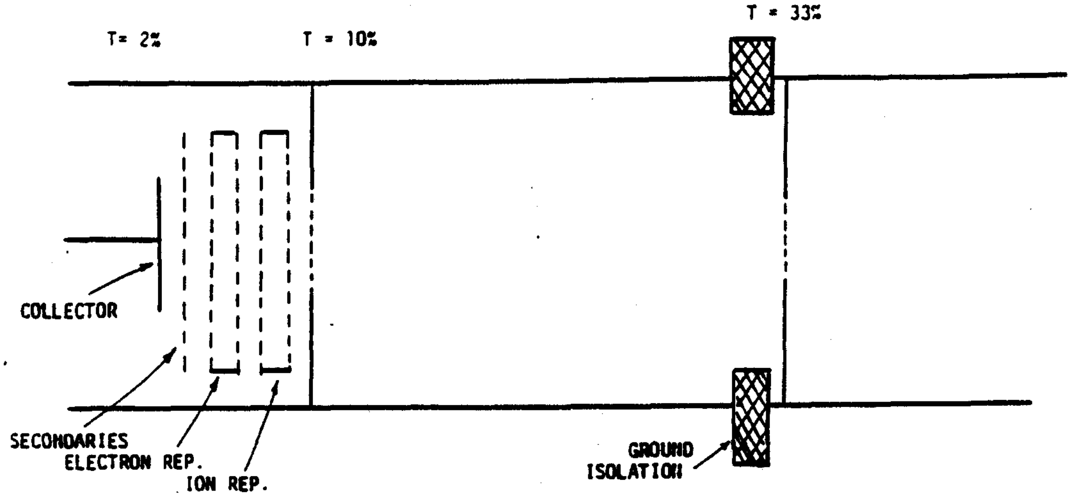

Figure 9. A schematic of the gridded endloss analyzer. Ions are analyzed by repelling electrons by placing -1000 volts on the first (electron) analyzer grid. Electrons are analyzed by putting +500 volts on the second (ion) analyzer grid. The first two grounded grids attenuate the plasma density and current. The analyzer grid spacings were determined by the requirement that the expected current density not exceed the space-charge limit. The double analyzer grids improved the energy resolution of Molvik's analyzers and was, therefore, also used here.

$\sim 1-2 \times 10^{12} cm^{-3}$. Thereafter, the hot-ions were cooled (and out-numbered) by the denser cool ions flowing from the gun. Further discussion of these results can be found in the two references listed at the start of this chapter.

2.2.3. *Endloss Analyzer*. One of the most useful diagnostics on Constance 2 was the gridded, electrostatic endloss analyzer. The analyzer was placed in line with the streaming endloss plasma on the dump-tank's vacuum wall. It was slightly off the machine's axis, but it still intercepted the elliptical end fan. Small motion perpendicular to the fan was possible, $\pm 2.5cm$ (which maps to $\pm 0.6cm$ at the midplane), so that the analyzer could be positioned either to examine the thin injection stream (as well as the decaying plasma after injection) or to examine only the plasma outside the gun-mapping. Typically, the analyzer mapped to a thin, elliptical "slice" at the midplane, 1.8cm off axis, 0.5mm wide by 3.5mm long and aligned to intercept the injection stream. The design of the analyzer followed the prescription given by Molvik, 1981. The endloss analyzer monitored electron and ion stream parameters during injection and monitored plasma loss rates and energy distributions during the decay and heating of the plasma. In addition, plasma potentials could be estimated from minimum ion or electron energies. Figure 9 shows a schematic of the endloss analyzer.

The analyzer current is given by the formula

$$I_{el} = A_{el}T_{el}J_{mid}\frac{B_{wall}}{B_{mid}} \approx 0.001\,J_{mid} \tag{7}$$

where $A_{el}T_{el}$ is the product of the grid transmission and detector area averaged over the angles of the incoming particles and J_{mid} is the effective endloss current density in amps/cm^2 at the mirror midplane. The grid transmission has an angular width of $\pm 20^\circ$. The absolute transmission of the analyzer was checked by using an electron beam.

The endloss analyzer is useful because it can measure both the endloss energy distribution and the current. The product of these gives the plasma power to the end wall. The following formulae are useful:

$$I_{end} = 0.8\text{amps}\ V_{det}[mv](R_p/3)^2 \tag{8}$$

$$P_{end} = I_{end}E_{end}[volt]\ \text{Watts}(R_p/3)^2 \tag{9}$$

where V_{det} is the detected current into 50Ω and E_{end} is the endloss energy. Notice the dependence on R_p^2 which results from the assumption that the endloss *sampled* by the analyzer is representative of the total endloss, leaving the mirror with a cross-section of πR_p^2.

In addition to wall current and power, careful analysis may also give information about the plasma lifetime and potential. For a trapped, isolated plasma, J_{mid} is related to the loss rate by $J_{mid} = qn_pL_p/\tau_{loss}$. In addition, if a minimum ion energy is measured this would correspond to the positive, mirror potential, or if a minimum electron energy is measured, this would indicate a negative, mirror potential. However, if the mirror is not isolated, all of the endloss current will not originate at the midplane. For example, the plasma can not be isolated for at least an ion-transit time after crowbar, ($\sim L/v_{thi}$), since during injection the density external to the mirror must be at least as great as the density in the mirror.[3] In this case, the endloss analyzer will measure both the decaying mirror plasma and the streaming external plasma. Also, any ionization occurring in the external plasma will eventually be detected at the wall whether or not the ionization occurred outside or inside the mirror region. Thus, if the lifetime of the mirror-plasma is much longer than the ion-transit time and if the volume-averaged, external ionization rate is small compared to that in the mirror, then the endloss current scales inversely with the trapped-plasma loss rate, and the minimum ion energy will reflect the mirror potential. Unfortunately, this type of endloss behavior has only been observed at very low densities. (See in particular Appendix 3.) For typical operation (Section 2.3), the ions are not well mirror-confined, the endloss current does not represent the trapped-plasma loss time, and potential measurements of the mirror are complicated by the ions external to the mirror region.

---

[3] Notice that a 30ev ion requires about 40μsec to reach the end wall from the midplane!

2.2.4. Diamagnetic Loop . A diamagnetic loop encircled the plasma and monitored the change of the magnetic field induced by the plasma. The loop is double shielded and integrated passively using the inductance of the coil and a terminated, 50Ω cable. The time constant was $\tau_{l/r} \sim 40\mu sec$, which acted to reduce the low-frequency field fluctuations of the Ioffe bars and the decaying main field. The data were numerically integrated in the computer after compensating for the average linear offset due to the low-frequency signals.

The diamagnetic loop gives a voltage proportional to the flux linked by the loop and is therefore very sensitive to the geometry of the plasma. The formula used in this analysis is

$$\pi R_p^2\left\langle nT_\perp\right\rangle = K_g \frac{B}{n\mu_0}\left(\tau_{L/r}V_{loop}(t) + \int_0^t dt' V_{loop}(t')\right) \qquad (10)$$

with the factor, $K_g \sim 2.2$, representing the effect of the wall eddy currents and the return flux due to the axial gradient of the diamagnetism. R_p is the effective radius of the plasma. In conjunction with the measurements of the radial density profile (with Langmuir probes) or the magnetic profile (with a magnetic probe), Equation 10 gives the product of the density and perpendicular temperature averaged over the plasma cross section. The total, perpendicular plasma energy is given by the product of the diamagnetic signal and the plasma length, $\pi R_p^2 L_p K_g \left\langle nT_\perp\right\rangle$ (where $K_g L_p$ are estimated). The energy confinement time was obtained from the decay of the diamagnetism.

The loop was calibrated by using a small circular coil, 30 cm long and with a 3.0cm radius. The response of the loop to the known flux was used to determine $\tau_{L/R}$ and estimate K_g.

2.2.5. X-ray Detectors . Four silicon surface barrier detectors (SBD) and a plastic scintillator were used to measure target x-rays emitted from the plasma. Beryllium filters of various thicknesses were placed in front of the detectors. Ratios of the detected currents indicate temperature, and the changing intensities determine changing hot electron density. Each detector was collimated to look at the target—the SBDs with stainless steel, and the scintillator with lead. The array of four SBDs was placed inside the vacuum chamber to allow detection of soft (~100ev) x-rays. The scintillator was outside the chamber and was sensitive to x-rays $\gtrsim 4kev$.

As an x-ray photon penetrates the depletion layer of a surface barrier detector, electron-hole pairs are created and collected in the biased depletion layer. The current detected is equal to the total absorbed photon energy divided by $3.6volt$. The SBD current is amplified with a low noise transimpedance amplifier built from an FET. The amplifier-detector system gave about 1 to 2namps of noise current at 200kHz bandwidth. The noise and bandwidth were limited by the large (~150pf) capacitance of the detectors. The response curves of the filtered SBDs are shown

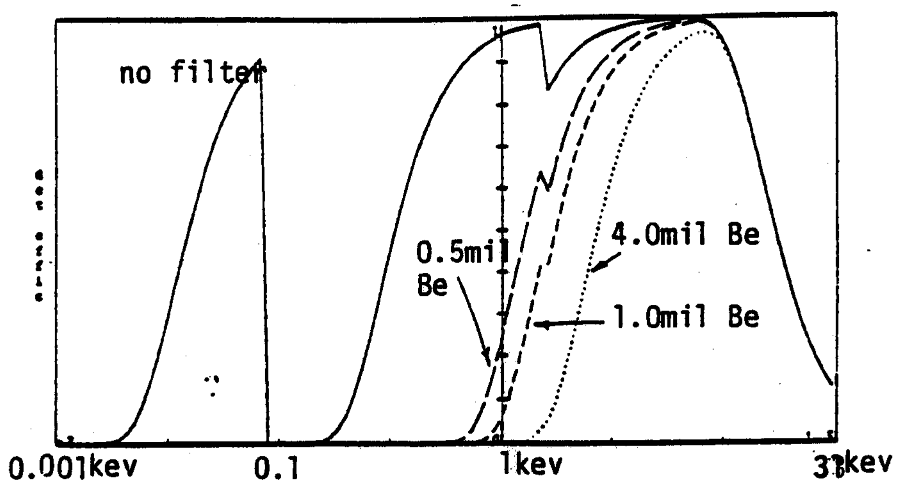

Figure 10. Absorption curves for surface barrier detectors without a filter and with 0.5, 1, and 4mil Be filters. The low energy limit is due to the deposited, thin aluminum anode through which the x-rays must pass. The high energy limit is due to the thickness of the detector.

in Figure 10. The scintillator emits light proportional to the incident x-ray intensity and the light is monitored with a photomultiplier.

The surface barrier detectors were calibrated in three steps. First, each detector and amplifier was bench tested with a radioactive Fe^{55} calibration source. Since the signal level was low, a box car integrator was used to improve the signal to noise ratio. Secondly, within the vacuum chamber, an electron beam at 3.6kev and 2.8kev was fired at the target, and the detected signals were compared with those expected from the target x-ray analysis presented in the next paragraphs. This is shown in Figure 11. Finally, the relative solid angle of the detectors was measured by placing windows of equal thickness over each detector and then comparing the received signals as a function of target's radial position. This final calibration determined the hottest measurable temperature to be $\sim 2kev$ due to the uncertainty of these solid-angle correction factors.

Target x-ray analysis was used throughout this thesis, since it allowed examination of the short-lived and low-density hot-electrons. To illustrate this, a comparison was made between the bremsstrahlung and target x-ray intensities. For bremsstrahlung (Griem, 1965),

$$\frac{dP_{Br}}{dE} = 3.28 \times 10^{-27}\left(\frac{\chi_H}{T}\right)^{1/2} Z^2 n_e n_{Z+1}\left(g_{ff} + \sum_{E>\chi_{Hn}} \frac{2\chi_H Z^2}{E}\frac{g_{fn}}{n^3}e^{\chi_{Hn}/T}\right)e^{-E/T} \tag{11}$$

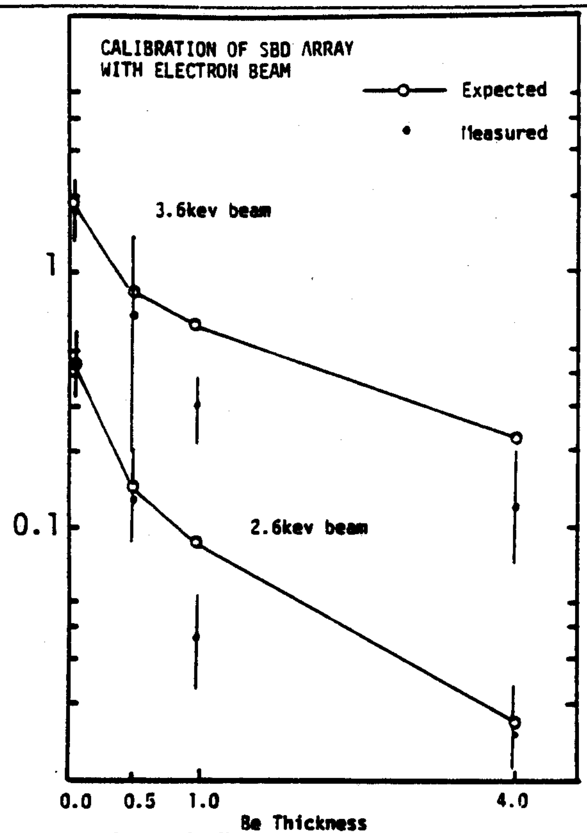

Figure 11. A calibration of the SBD detectors with an electron beam. The relative signals are not expected to be equivalent due to the unknown x-ray radiation pattern. However, the ratios of the signals are well represented by the target x-ray analysis used in this thesis.

which gives the radiated power per ev in units of (erg/sec·ev) per steradian·cm^3. $\chi_H = 13.6$ev, and χ_{Hn} is the ionization energy from the nth shell. The Gaunt factor, $g_{ff} = 1.2$. Integrating over E, the total radiated bremsstrahlung power per cm^3 is

$$4\pi P_{Br} = 4\pi\, 3.28 \times 10^{-27}\left(\frac{\chi_H}{T}\right)^{1/2} Z^2 n_e n_{Z+1} T\left(g_{ff} + \frac{2.2\chi_H Z^2}{T}\right) \tag{12}$$

$$= 0.18\mu\mathrm{Watt}\,\frac{n_e}{10^{12}\mathrm{cm}^3}\,\frac{Z^2 n_i}{10^{12}\mathrm{cm}^3}\sqrt{T} \tag{13}$$

where $\sum_{n>1} g_{fn}/n^3 \approx 1.2$, and T is in units of ev. Notice that free-free bremsstrahlung dominates for $T_e \gg 2.2\chi_H Z^2/g_{ff} \sim 25ev\ Z^2$.

The emissions for target x-rays were obtained from the formula (Evans, 1955, Bengtson, *et al.*, 1974)

$$\frac{dI_{tg}}{dE} = 10^2 Z_{tg}(E_0 - E) \tag{14}$$

where E is now in ergs, and the units of the equation is erg/(erg·steradian) per incident electron of energy E_0. To obtain dI_{tg}/dE for a target immersed in the

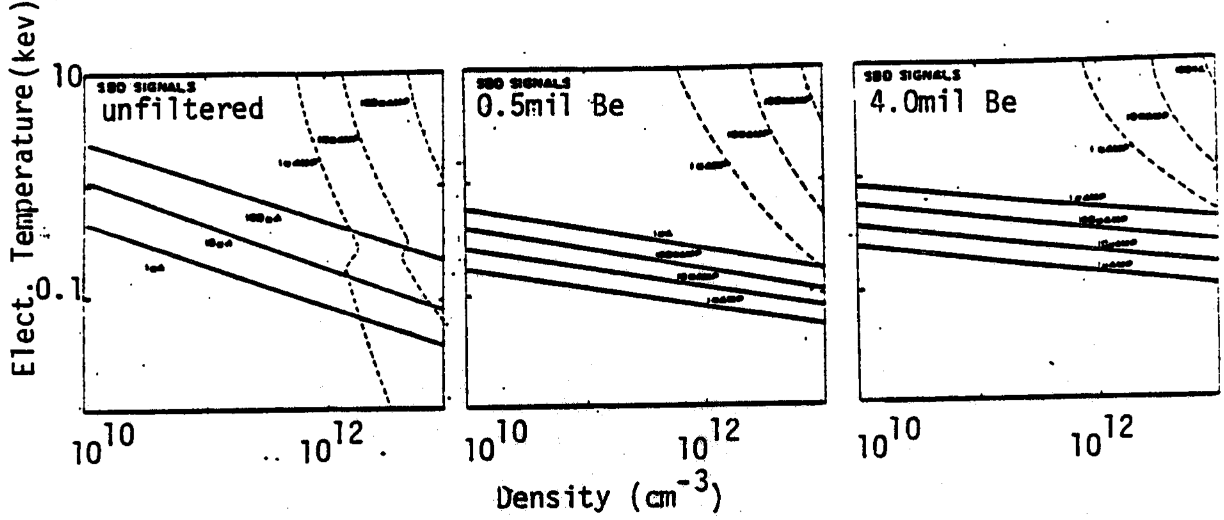

Figure 12. Diagrams of the target and bremsstrahlung currents as measured by the surface barrier detectors for typical plasma parameters. Three plots are shown for three thicknesses of beryllium filters. (Left: Unfiltered, Middle: 0.5mil Be, Right: 4mil Be.)

plasma, Equation 14 is integrated over an incident flux of electrons. For a Maxwellian plasma incident at the thermal speed, integration of Equation 14 gives

$$\frac{dI_{tg}}{dE} = 4.5 \times 10^{15} Z_{tg} n_e T^{3/2} (2 + \frac{E}{T}) e^{-E/T} \tag{15}$$

with the units, erg/(erg·streradian·sec) per cm^2 of target surface. For target x-rays, the total radiated power is therefore

$$4\pi I_{tg} = 0.54 \times 10^{-12} Z_{tg} n_e T^{5/2} \tag{16}$$

$$= 0.054 \mu\text{Watt} \cdot \text{cm}^{-2} \, \frac{Z_{tg} n_e}{10^{12}\text{cm}^3} \, T^{5/2} \tag{17}$$

where, now, T is in ev. Comparing target and bremsstrahlung x-ray intensities for a typical case of $T = 500$ev, $n_e = 10^{11}$, $n_i = 10^{12}$, $Z_{eff} \approx 1$, $Z_{tg} = 25$ (for stainless steel), a target area of 1.2cm^2, and a viewing volume of 140cm^3 gives

$$4\pi P_{Br} = 56 \mu\text{Watt} \tag{18}$$

$$4\pi I_{tg} = 0.95 \text{Watt} \tag{19}$$

The target intensity is more than four orders of magnitude higher! Figure 12 shows calculations of target and bremsstrahlung signals received by the SBDs for three Be filter thicknesses. For this reason, only target x-rays were analyzed in this thesis. The target analysis has the advantage of spatial localization and eliminates the need for a viewing dump. The target has the obvious disadvantage of perturbing the plasma.

In fact, because the target (or anything else inserted into the plasma) effectively eliminates all incident hot electrons, the hot electron density at the target should be lower than the hot electron density on other magnetic flux surfaces. A crude estimate of the density reduction can be made by re-calculating the hot electron flux based either on the drift-speed into the flux tube containing the target or on cross-field collisional transport. In the former, when the target diameter is wider than $R_p(\omega_D/\omega_B)$ (*i.e.* the plasma radius times the ratio of the drift and the bounce frequencies), the density should be lowered by the factor $(V_D/v_{th})(L_P/R_{tg})$, where V_D is the drift speed. In the latter, the density is lowered by an amount $(r_l/\Delta r)(r_l/\tau_{ee})(L_P/R_{tg})$, where r_l is the hot electron Larmor radius, Δr is the scale length of the perpendicular temperature gradient, and τ_{ee} is the collision frequency. For both of these limits, the density is reduced by less than a factor of 10^2 for the $\lesssim 4kev$ hot-electron temperatures measured. Notice that since the velocity dependence of the hot-electron flux is small compared to the *exponential* dependence on the hot-electron distribution, the ratio of the SBD signals will faithfully represent the temperature (if not the density) of the electrons near the target.

The problem remains, however, to relate the measured temperature (with the target) to what the temperature *would have been if the target had not been in the plasma.* Stated in another way, for an accurate measurement, the probe should not effect the power balance of the heated electrons. This was roughly tested by monitoring the diamagnetism as the target was inserted into the plasma. Usually, the target was inserted up to the point where the effect on the energy confinement time was first noticeable. This was 3-4cm. Nevertheless, it is likely that the temperature of the hot electrons on the *measured* flux surface was still limited in some way. For instance, electrons with energies greater than 500ev will probably drift completely around the plasma—and hit the target—before being pitch-angle scattered out of the mirror! In other words, the target x-ray signal represents only those electrons heated during one drift period. This creates an additional limitation to the hot electron temperature imposed by the target. The target loss-rate scales as the magnetic drift speed, or $\sim T_{hot}$, independent of density.

2.2.6. Probes . Several movable probes were used to measure the radial and axial density profiles, the radial diamagnetic profile, the floating potential, and the bulk electron temperature.

The radial and axial profiles of the plasma were measured with Langmuir probes. The tungsten-tipped probes were biased to measure the ion-saturation current (either 45 or 90 volts). The bias was DC for low densities and pulsed for high densities in order to avoid breakdowns.

The bulk electron temperature was obtained from the slope of the electron current as the probe's bias was swept up to 500volts in 7μsec. The probe capacitance was nulled by using a differential current measurement between the probe inserted into the plasma and an identical "bucking" probe not in the plasma.

To obtain the magnetic profile, a small, 100-turn magnetic probe was inserted near the plasma midplane. It gives a voltage proportional to the rate of change of the *local* magnetic field. An external RC-integrator with the same time constant as the diamagnetic loop was used to passively integrate the signal. The radial variation of the field helps to determine the radial distribution of the diamagnetic current.

Finally, a floating potential probe was used to obtain qualitative information of the radial potential variation, to measure the presence of hot electrons by observing the rapid reduction of the floating probe signal during heating, and to monitor the ion cyclotron fluctuations related to microstability work discussed in the Appendix 3.

2.2.7. Data Acquisition System. Almost all of the Constance 2 data were digitized, recorded and processed with a CAMAC-based data acquisition system. The system consists of a CAMAC crate, with its interface and digitizers, connected to the Plasma Physics TV display system and the Macsyma Consortium Computer.

Two, eight-channel 400kHz digitizers are used for the slowly varying signals. Four fast 20MHz digitizers allow processing of fast-sweeping Langmuir and endloss signals, fast rising diamagnetic data, and 10MHz fast-Fourier analysis of probe data. Automatic processing of standard diagnostics, interactive recording of experimental parameters, self-documentation, and ease of programming special-purpose data processing functions made the system very easy to operate. The system was most commonly used to record several nearly identical shots, and then average and plot the data and the standard deviation.

2.2.8. Miscellaneous Diagnostics. A nude vacuum gauge was calibrated in the magnetic field and used to monitor the pressure in the chamber. The guage was located near the wall at the midplane. A photo-diode mounted at the back of a long collimator monitored the plasma light.

2.3. The Unheated Plasma

Figure 13 shows an example of raw data describing the Constance 2 plasma without ECRH. The peak line density is $4.6 \times 10^{12} cm^{-2}$, and the peak diamagnetism is $40 \times 10^{12} ev \cdot cm^{-3} K_g(\pi \epsilon w^2/\pi 9)$.[4] The ratio of the two gives the average energy, $\left\langle E_\perp \right\rangle = 52 ev\ K_g(3/\epsilon w)$, where these measurements depend upon the plasma geometry (through the factors ϵ, w, and K_g). If the peak signals corresponded to a circular plasma with $R_p = 3cm$ (estimated from probe analysis), then the average energy was $115 ev$ and $\langle n_e \rangle = 0.78 \times 10^{12} cm^{-3}$. More likely, for the peak parameters, the plasma was elliptical (Sections 2.1 and 2.2.1). Assuming $\epsilon \sim 4$, gives $\left\langle E_\perp \right\rangle = 57 ev$ and $\langle n_e \rangle = 1.5 \times 10^{12} cm^{-3}$. $\sim 50 \mu sec$ after crowbar, the

---

[4] Throughout this thesis. formulae will contain parameters—such as $K_g(\pi \epsilon w^2/\pi 9)$—which represent the unknown or approximate parameters which were assumed in order to obtain the numerical value.

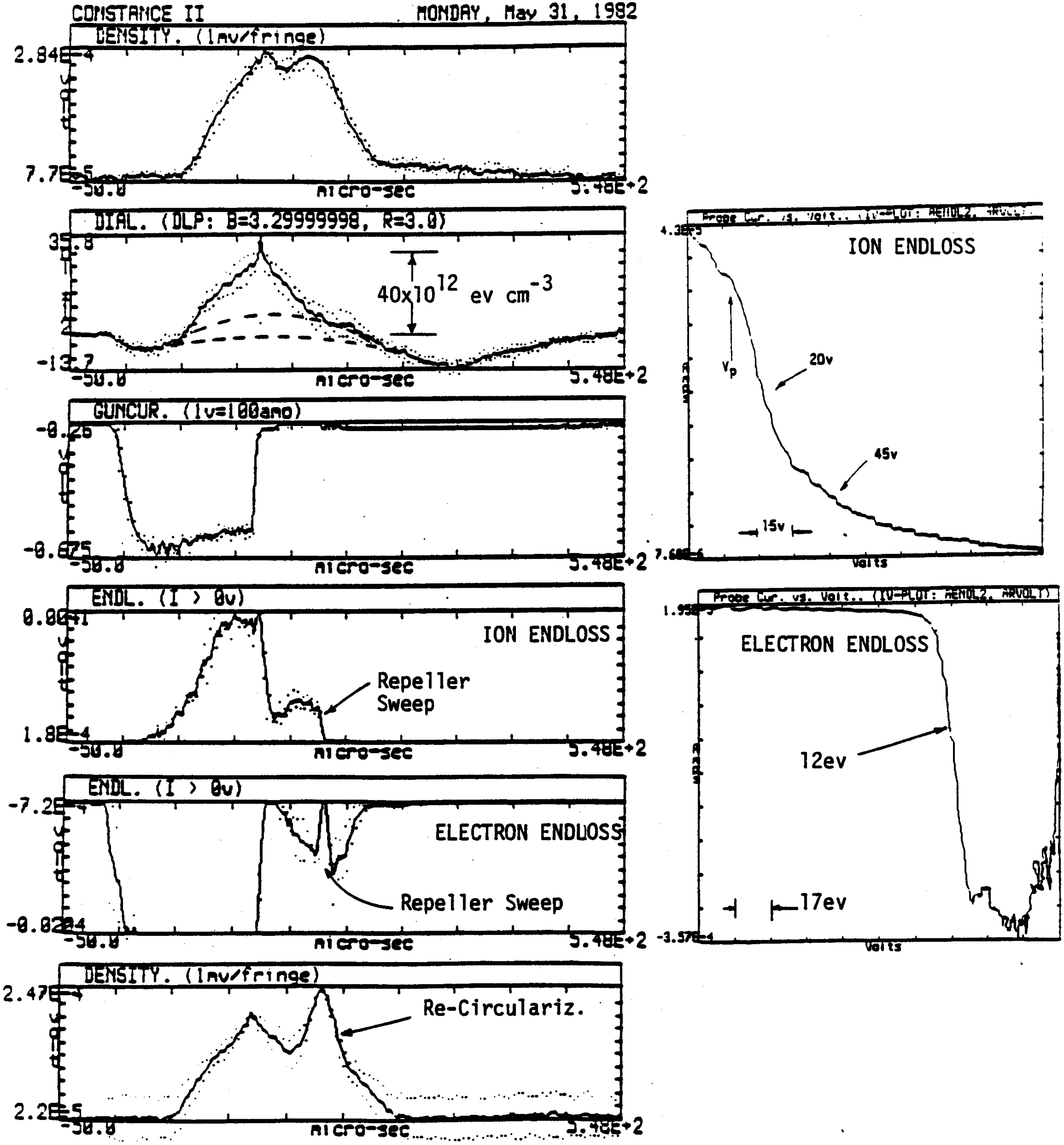

Figure 13. Example of a discharge without RF heating. Shown are the line density, $\langle 2wn_e\rangle_{peak} \sim 4.6 \times 10^{12} cm^{-2}$, the diamagnetism, $\langle n(T_{i,\perp} + T_{e,\perp})\pi \epsilon w^2\rangle_{peak} \sim 40 \times 10^{12}(\pi 9cm^2) ev \cdot cm^{-3}$, gun current, ion endloss and energy distribution, and electron endloss and energy distribution.

plasma should have re-circularized, and, therefore, the average energy is $39ev$ and $\langle n_e \rangle = 0.78 \times 10^{12} cm^{-3}$ with $R_p = 3cm$.

The endloss analyzer measures the loss power to the end-wall, and the decay of the diamagnetism measures the power loss from the mirror region. When these are compared, the endloss data must be multiplied by the *plasma area* and the diamagnetic signal by the *plasma length.* At $50\mu sec$ after crowbar, the electron current for the example is $I_e = 8amps(R_p/3)^2$ and the ion current is smaller by a factor of 1.5. (Some of this unbalance probably represents secondary electron emission.) Using the measured endloss energies, the wall power is $250watts(R_p/3)^2$, 75% of which is due to the ions and the remaining due to the electrons. Notice that R_p determines the plasma area and was estimated to be $\sim 3cm$ from Langmuir probe data. The peak power loss measured by the diamagnetic loop is roughly $P_{dia}^{peak} \approx 600watts(L_P/100)$, and, $50\mu sec$ after crowbar, the power is lowered by the decrease in diamagnetism to be about $P_{dia}^{+50\mu sec} \approx 200watts(L_P/100)$—in reasonable agreement with the endloss measurements. Notice that L_p was *assumed* to be 100cm. This is equal to the distance between mirror peaks. This equivalence of the diamagnetic and endloss powers with $L_p \gtrsim 100cm$ implies that even $50\mu sec$ after crowbar the plasma density is uniform throughout the mirror. In fact, this can also be considered as the first piece of evidence that the density external to the mirror region is high since the external density is related to the density at the mirror-peak by the ratio of the magnetic field outside the mirror to the magnetic field at the mirror peak.

Actually, the presence of plasma external to the mirror is characteristic of cool, gun produced plasmas. In the PR-6 experiment (Kanaev, 1979), the cool ion density ($T_i \lesssim 20ev$) was roughly equal to the density of hotter ions ($T_i \sim 100$ to $200ev$). By waiting a cool ion transit time, $\sim 50\mu sec$, the cool ions external to the mirror decayed while the hotter ions, trapped by the mirror, remained mirror-confined for up to four times longer. An important goal of the Constance 2 program was to determine whether or not Constance 2 operates in a similar fashion.

This determination was made by examining the scaling of the particle confinement time as the line-desnity was varied by changing the gun-injection time. When enough hot ions are produced, the confinement will be dominated by the ion-ion collisions of these hot ions. In this case, the particle (and energy) confinement-time scales as $T_i^{3/2} n^{-1}$. On the other hand, if the ions are cool (and dense) enough so that the ions in the loss cone scatter into and out of the loss cone during a bounce period (*i.e.* $\omega_B \tau_{ii} \sim 1$), then the ions will "flow" out of the mirror—only weakly dependent on the magnetic mirror—at the ion thermal speed.[5]

---

[5] Some very elegant work has been done by Wong and others Ferron, *et al.*, 1981 at UCLA's LAMEX experiment which investigate the scaling of this confinement with mirror ratio. They find the confinement time to scale as $\tau_{flow} \sim R\,L/v_{thi}$, where R is the mirror ratio, L the distance between mirror peaks, and v_{thi} is the ion thermal speed.

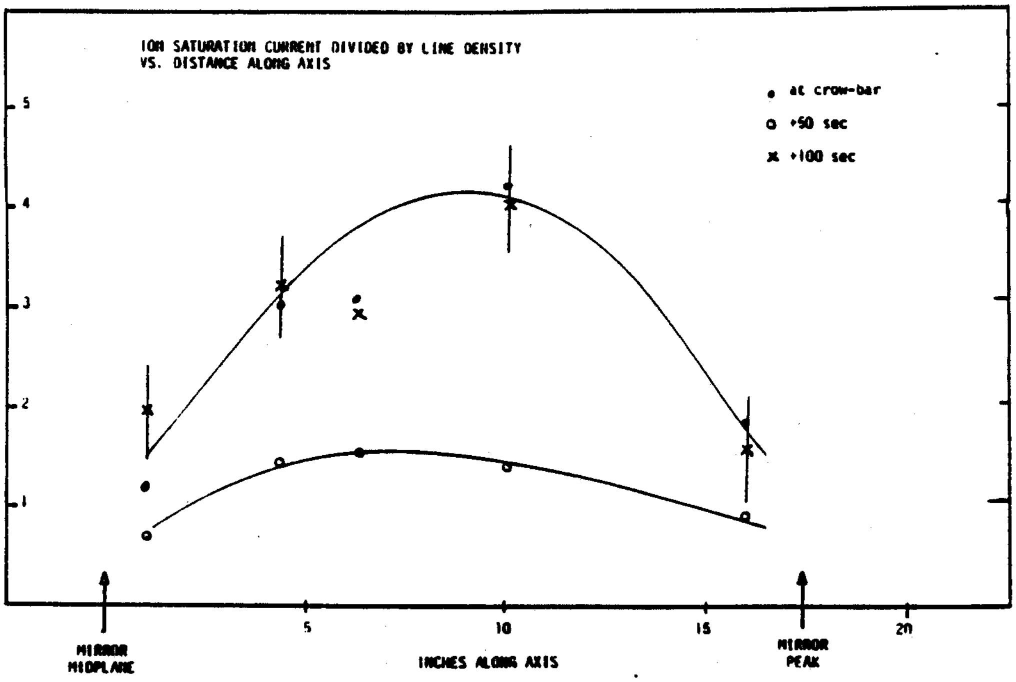

Figure 15. The ratio of the ion saturation current to the line density for several axial positions and for three times during the decay of the plasma.

In this case, the particle (and energy) confinement times will scale as $T_i^{-1/2}$ and will be independent of the density.

Figure 14 (top) illustrates the observed scaling of the particle confinement time as the line density is increased. The behavior of the confinement times can be separated into two regions of operation. On the left-hand side of the figure, "low-density" operation is roughly described by $1/n$-scaling. At these densities, the ions are hottest and can bounce several times (as much as 40 times for $T_i = 100ev$ and $n \sim 10^{11}cm^{-3}$) before scattering into the loss cone. On the right-hand side, as the density increases, the ions cool and the confinement time actually increases! At the higher densities, the ions "flow" out of the mirror at their thermal speed.

To further illustrate this phenomenon, the square-root of the ratio of the diamagnetism to the line-density (*i.e.* the average energy) is plotted against line-density for the same data. After normalizing the data, the fit of this ratio (bottom) to the confinement time (top) is quite good.

Referring back to the description of the experiment operation in Section 2.1.2, it is not surprising that the plasma is described by mirror-confinement at low densities and "collisional" confinement at higher densities. As the gun produces plasma, the low density ions are initially hot (bottom of Figure 5) and rapidly cool as the density builds up. The injection process can be pictured as the gradual formation of a long column extending from gun to the end wall. If the injection lasts for a long time, the line-density in the trap reaches a steady value of $\sim 10 - 20 \times 10^{12}cm^{-2}$, and the

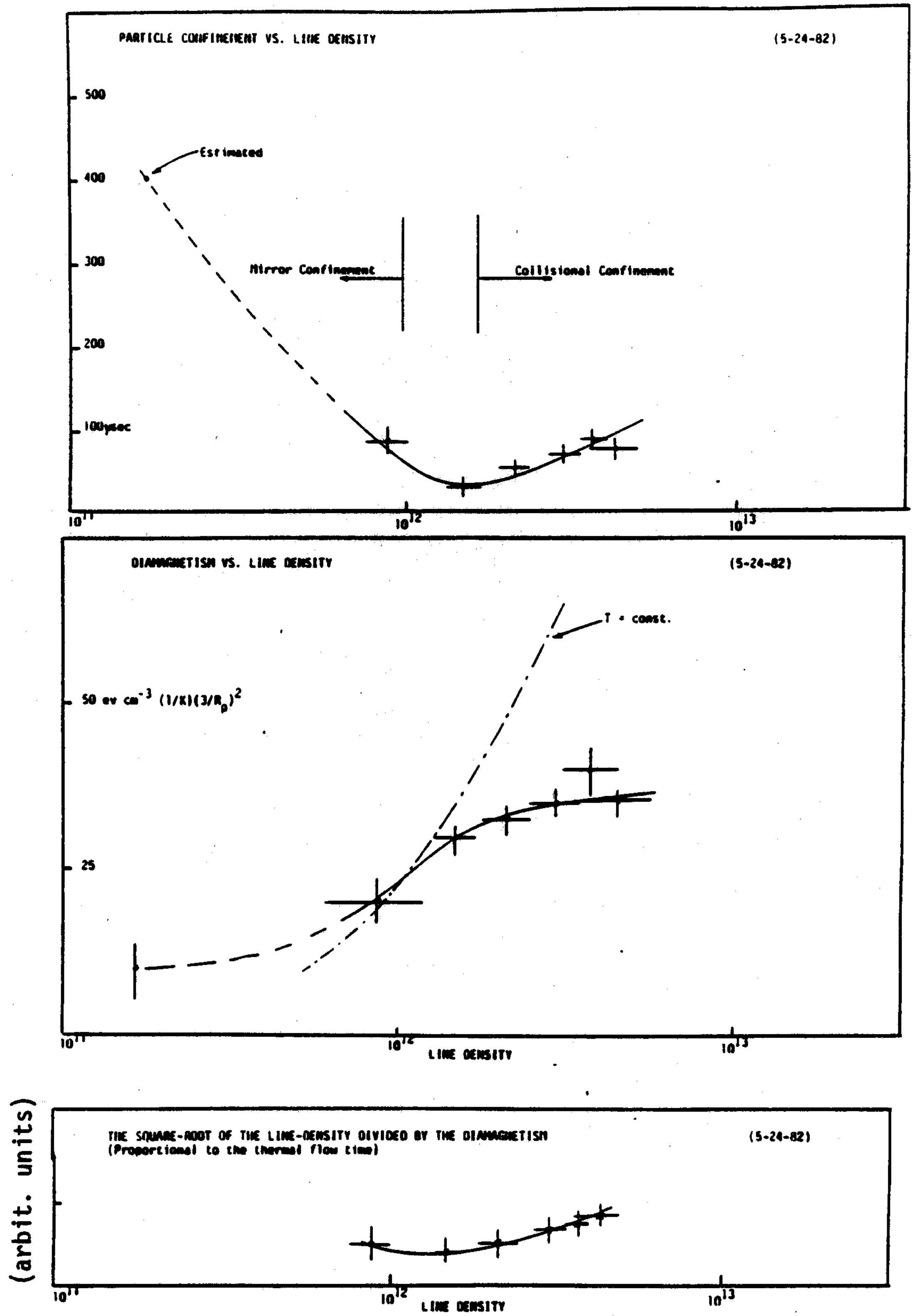

Figure 14. The scaling of the particle confinement time (top), the increase of the diamagnetism (middle), and the square-root of the ratio of the peak diamagnetism to the peak line-density with increasing line-density. The data indicate "mirror-confinement" at low densities and "collisional confinement"—dependent upon the ion thermal speed—at high densities.

column's density is (likely to be) uniform. Usually, the gun is crowbarred to limit the density so that the density towards the plasma gun is higher than the density toward the dump tank (Figure 6).

By limiting the injection to very short times, the ion temperature is maximized, and low density minimizes the collisionality. Also, since the gas rise in the chamber is due to plasma bombarding the chamber walls, the short injection time also reduces the neutral pressure. Occasionally, under these conditions, ion-cyclotron fluctuations, characteristic of mirror-confined ions, have been observed. However, for the conditions typical during most of the experiments reported here, even for short injection times, unstable plasmas were not produced. Further discussion of experiments with ion-cyclotron instabilities is found in Appendix 3.

Another important experiment[6] was to measure the axial length of the plasma in the mirror chamber during the decay of the plasma. The results of this experiment are shown in Figure 15. The ratio of the ion-saturation current measured by an axially movable probe to the line-density was plotted for three times during the decay of the plasma. The data indicate that even $100\mu sec$ after crow-bar, the plasma profile has not significantly changed from the profile at the end of injection.

Figure 16 summarizes the typical unheated plasma parameters described in this section.

2.4. The ECR Heated plasma

2.4.1. Analysis of Power Balance. When the ECRH pulse is applied to the plasma several changes occur: (1) a large increase of the diamagnetism is observed, (2) the Langmuir probe shows an increase of the bulk electron temperature, (3) target x-ray signals are observed, (4) a (small) positive increase in the potential is observed with the endloss analyzer, and (5) the plasma light and neutral pressure increase. This section explains how the diagnostics are used to examine of the heated electrons and describes the analysis used to determine the dominant power loss mechanisms.

Examples of some of these measurements are shown in Figures 17 to 19. For Figure 17, the input power was $15kWatt$[7], and the resonance zones were approximately $11cm$ to either side of the midplane. The measured diamagnetism was $275 \times 10^{12} ev \cdot cm^{-3} K_g(3/R_p)^2$, and the line-density was $3.8 \times 10^{12} cm^{-2}$. Following the arguments in Section 2.3, the average density is $\sim 0.5 \times 10^{12} cm^{-3}$, giving $\left\langle \omega_{pe}^2/\omega^2 \right\rangle \sim 0.5$. The average energy is $475 ev\, K_g(3/R_p)$.

By examining the rate of rise and decay of the diamagnetism, the heating efficiency is estimated to be $\eta_{init} \approx 64\%(L_p/30)$ initially, and $\eta_{final} \approx 60\%(L_p/30)$ at the end of the heating pulse.

---

[6] This was performed by J. Irby.

[7] Except for the $0.7\mu sec$ "burst" at the start of the pulse (Section 2.1.3).

Typical Constance 2 Parameters without ECRH

Line density	$4.0 \times 10^{12} cm^{-2}$
Diamagnetism (R_p = 3cm)	$100 \times 10^{12} ev \cdot cm^{-3}$
Plasma radius (re-circularized)	$3cm$
Axial length	$\gtrsim 60cm$
Average density	$0.7 \times 10^{12} cm^{-3}$
Ion temperature (bulk)	$20 - 45ev$
Hot ion temperature (low density)	$100 - 150ev$
Electron temperature (unheated, decay)	$7 - 12ev$
Injection time	$200\mu sec$
Observed containment time	$50\mu sec$
$\omega_B \tau_{ii}/2\pi$ (typical densities)	< 4
Neutral density	$\lesssim 3 \times 10^{11} cm^{-3}$
Ellipticity (ϵ, injection)	7
End power—ions (R_p = 3cm)	$\lesssim 200watts$
End power—electrons	$\lesssim 70watts$

Figure 16. Summary of typical parameters for the Constance 2 plasma without ECRH. Notice that for the parameters shown $\omega_b \tau_{ii} \sim 1$ and the plasma is "collisionally confined".

Presumably, the loss power measured by the diamagnetic loop is lost to the end-walls. The diamagnetic loop gives $3.1kWatt\, K_g(L_p/30)$ at the end of the heating pulse and $0.73kWatt\, K_g(L_p/30)$ $10\mu sec$ later. (Notice that $L_p \sim 30cm$ was used to compute the loss power instead of $\sim 100cm$ used in the previous section. This distance is an assumption since no measurement of the length of the *heated* electrons was made. However, if the length were longer, the absorbed power measured with the diamagnetic loop would exceed the input power. Since L_p is about 1/3 the distance between the mirror peaks, this assumption corresponds to mirror-confined electrons.) To check the power balance, this loss power is compared with that measured by the endloss analyzer. As before, this requires a measurement of the radius of the heated plasma. By *assuming* the same radius used in Section 2.3, the data in Figure 18 gives a total endwall power which is only ~12% of the diamagnetic loss power. The electron endloss power is $0.53kWatt(R_p/3)^2$ at the end of the pulse and only $0.08kWatt(R_p/3)^2$ $10\mu sec$ later. During heating 90% of the electron power to the wall is from the "bulk" electrons and 10% is from the "warm" electrons. $10\mu sec$ later, the bulk and warm electrons contribute equally to the measured wall power. The ion power also increases (due partly to the increased total current and

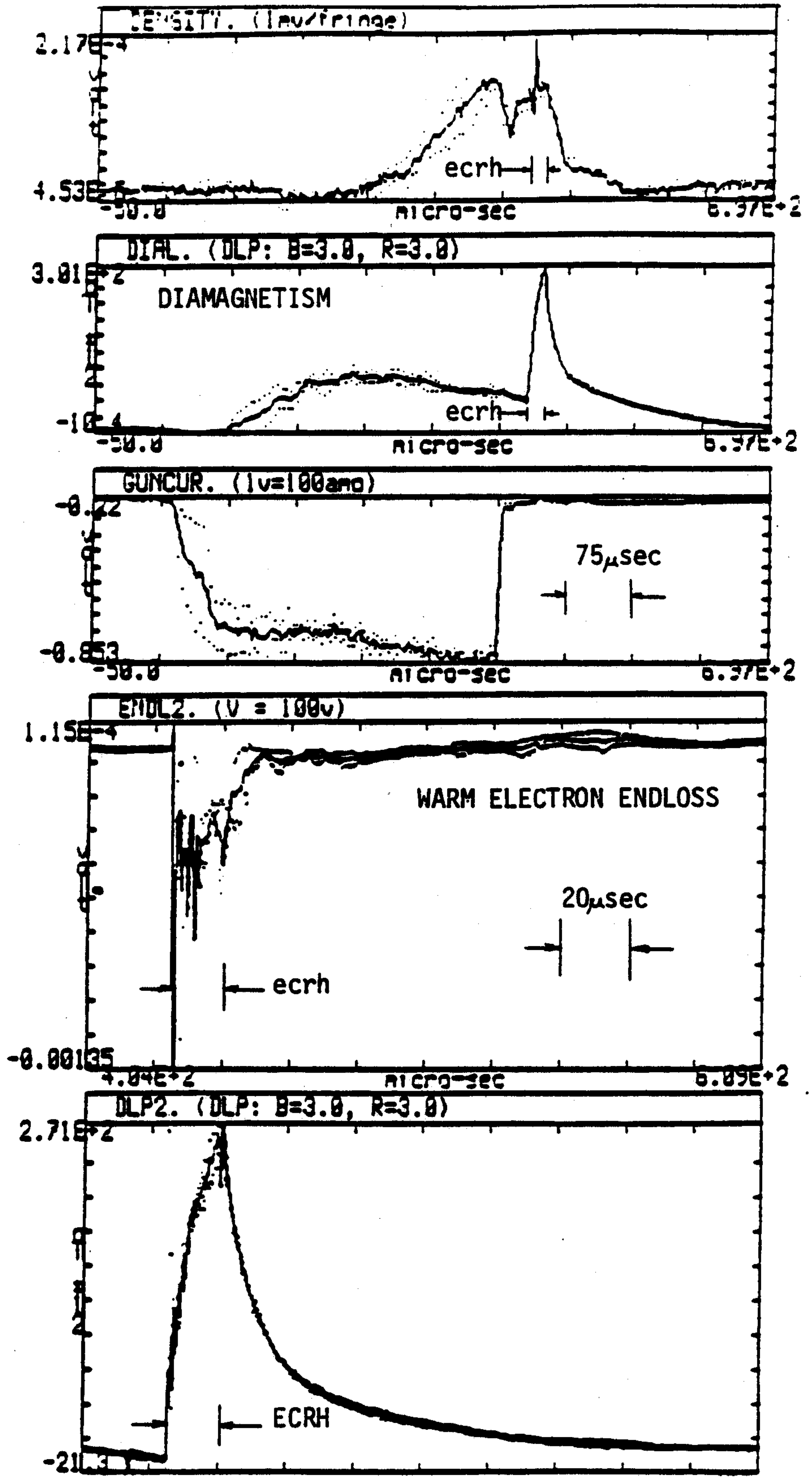

Figure 17. An example of the line-density, diamagnetism, and warm, endloss signals during ECRH.

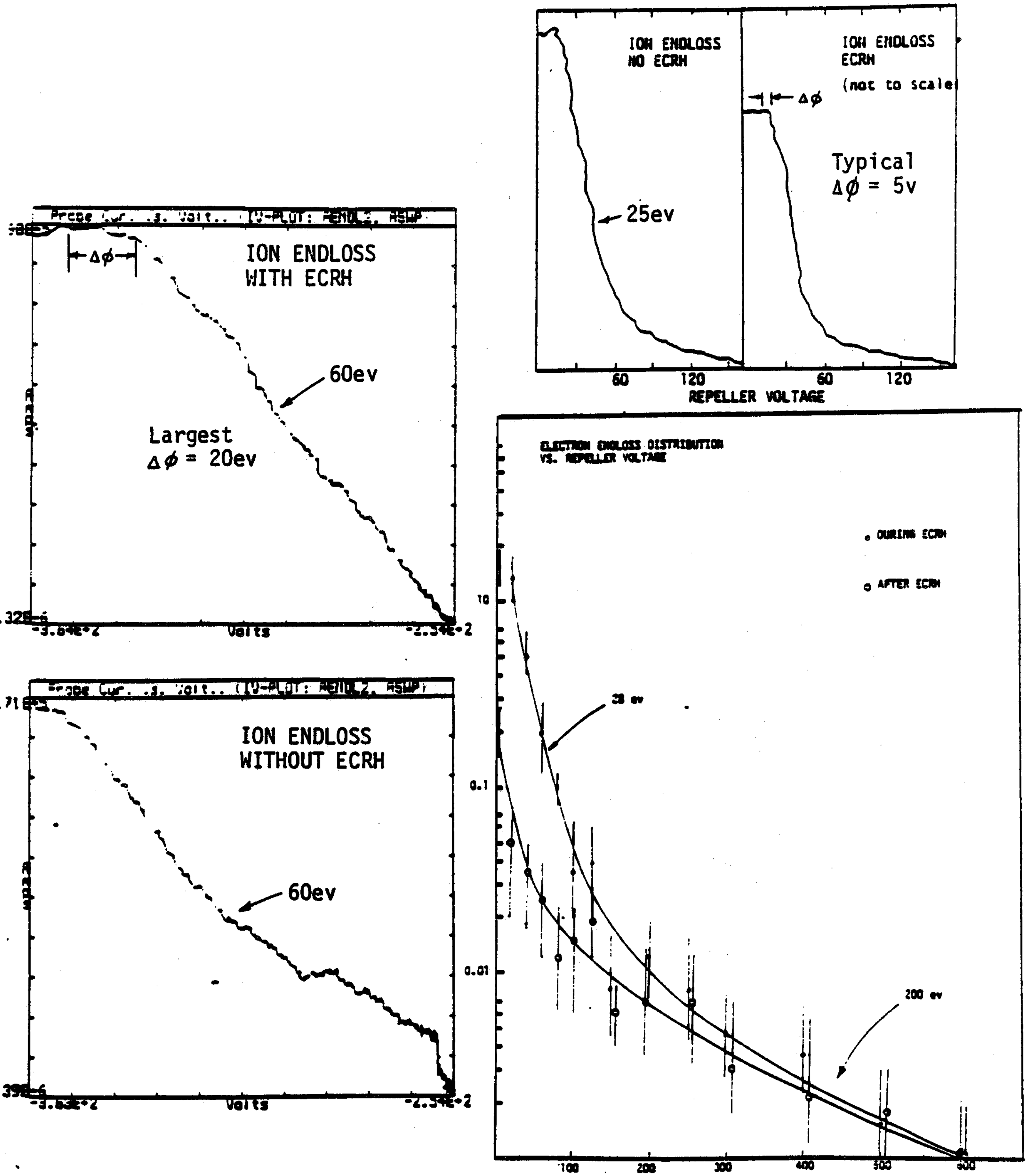

Figure 18. Example of the electron and ion endloss distribution for shots similar to that shown in the previous figure. The ion distribution was found by averaging the endloss current over 10 shots while the repeller grid was swept in 7μsec. The electron distribution was found by averaging over three shots at each of the repeller voltages shown.

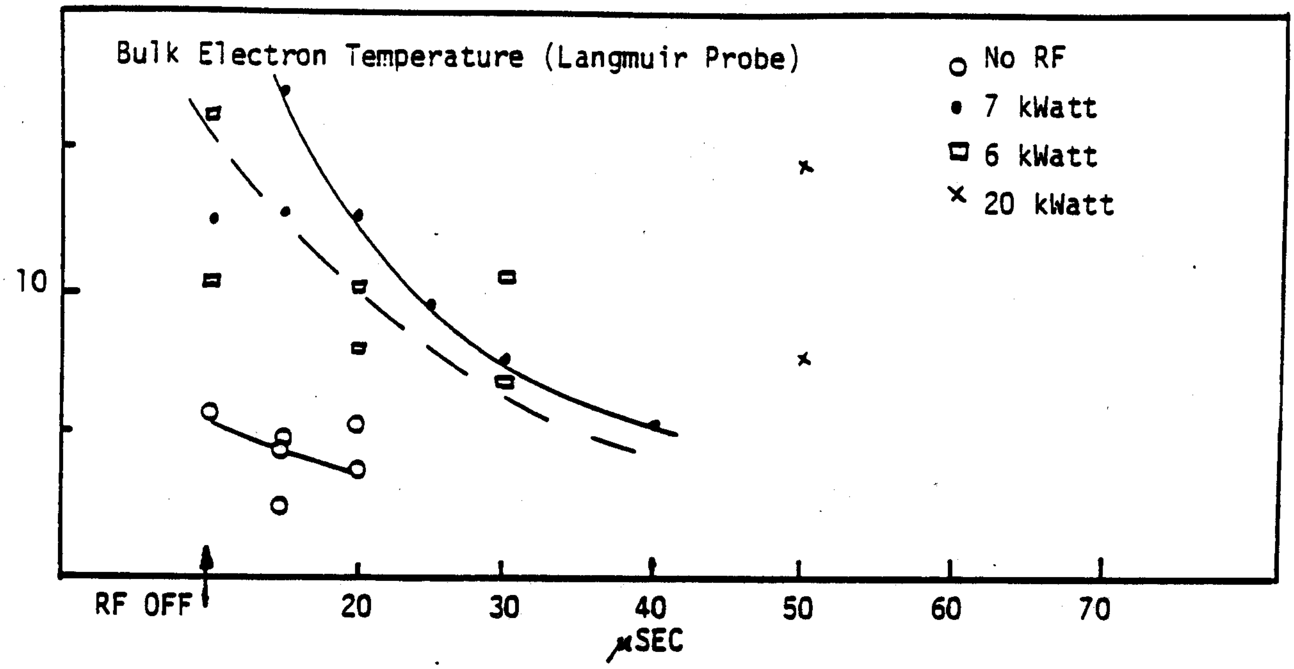

Figure 19. The "bulk" electron temperature measured with a Langmuir probe inserted placed at the plasma's edge.

partly to the increased potential), giving a peak wall power of $0.48kWatt\,(R_p/3)^2$, but this increase is insufficient to account for the difference between the endloss and diamagnetic signals.

Notice that, *by assuming* that the wall power flows uniformly through a (circular) cross section of $R_p = 3cm$, the measured wall power is nearly a factor of 10 lower than that measured by the diamagnetic loop! This discrepancy was resolved by examining the *increase of the radius of the heated plasma.* In other words, equal (or greater) power flux bombards the walls at larger radii during ECRH than without heating.[8]

To diagnose the increasing radius, floating, Langmuir and magnetic probes were moved in radially at the midplane. In this way, the density, floating potential, and diamagnetic profiles were monitored with and without ECRH. Figure 20 shows both the radial increase of the density profile and the depression of the floating potential (indicative of fast electron production) extending out at least 12cm from the axis. Figure 21 gives examples of the magnetic probe signals at increasing distances from the axis and also shows the magnetic profile with and without ECRH.

---

[8] Actually, the increased radial power loss was only qualitatively measured by examining the power loss with the Ioffe bars turned off. In this case, the endloss analyzer maps to a point at the midplane ~ $5cm$ off axis. Here, hot electrons were measured during ECRH even though no signal could be measured without ECRH. For the most part, however, the conclusion that the radius of the *power flow* increases is inferred from the profile measurements described in the following paragraphs.

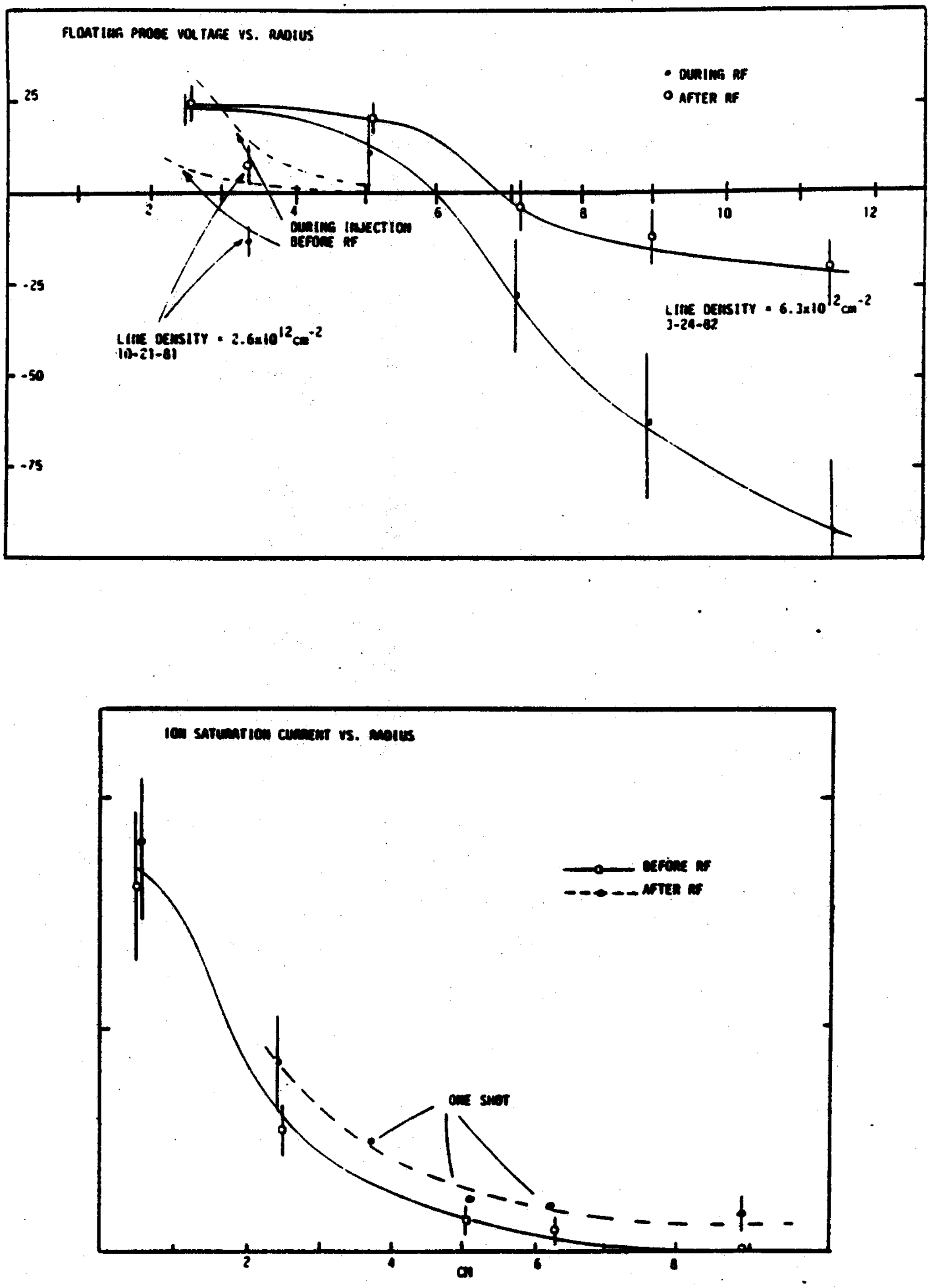

Figure 20. Floating probe measurements (top) with and without ECRH showing the large negative depression drop of the potential indicative of fast electron production. Also, Langmuir probe measurements (bottom) of the radial profile of the ion saturation current with and without ECRH.

The point of neutral magnetic flux is a measure of the "edge" of the energy density. This clearly increases in radius during ECRH.[9] Notice also that without the Ioffe bars, the heated radius extends even further outward than when the quadrapole is energized. Since 6cm (with Ioffe bars) and 8cm (without Ioffe bars) correspond to the flux tube which hits the diamagnetic loop, the diamagnetic loop may be limiting radial expansion of the energy. However, in addition to the field-lines which hit the diamagnetic loop, with the Ioffe bars energized, the outer field lines also map to the chamber walls at high field (see Figure 3). Also, the difference between the density *profile* and the "edge" of the energy density suggests that the outer electrons are hotter than the inner, denser electrons. In other words, if both the inner and outer plasma absorb equal power flux, the outer, low density plasma will be hotter than the inner plasma. Note that the endloss analyzer measures the "inner" plasma and the target x-ray detector measures the "outer" plasma.

The rapid density rise during ECRH implies an increased ionization rate.[10] To account for this density, the pressure must rise by at least a factor of 5. However, the pressure, monitored by a nude vacuum gauge and shown in Figure 22, increases by only a factor of two. Nevertheless, the actual increase at the walls, *where the gas evolves* is probably much greater than indicated by nude gauge. Most of the gas increase probably occurs well within $50\mu sec$ of the ECRH pulse since this is the length of time within which the energy of the plasma increases and decays. In this time, the gas cannot reach the gauge, and the pressure at the end-walls (*i.e.* where the gas is generated) is likely to be more than sufficient to account for the observed density increase.

To help model the electron heating with the Fokker-Planck simulation, the dominant loss mechanisms were analyzed. A simple model illustrating the particle/power balance is expressed in the following two equations

$$\frac{n_i}{\tau_i} = \frac{n_{bulk}}{\tau_p} + \frac{n_{hot}}{\tau_{hot}} - J_{ext} - \langle ionz \rangle \tag{20}$$

describing the particle balance, and

$$P_{loss} = \frac{n_i T_i}{\tau_i} + \frac{n_{bulk} T_{bulk}}{\tau_p} + \frac{n_{hot} T_{hot}}{\tau_{hot}} + 13.6 \langle ionz \rangle \tag{21}$$

representing the total loss power. In these equations, τ_p is the modified Pastukhov confinement time (Cohen, *et al.*, 1980), τ_{hot} is the hot electron confinement time, τ_i is the ion confinement time, J_{ext} is the net inward flux of cool electrons from the

---

[9] It should be mentioned that the magnetic probe was outside the turning point resonance during these measurements. As the resonance zones moved past the probe position the signal was always "paramagnetic," suggesting that the presence of the probe does not allow the "build-up" of energetic electrons at the probe's position.

[10] An increase of the plasma light was observed during heating, as expected during an increase of the electron temperature and neutral density.

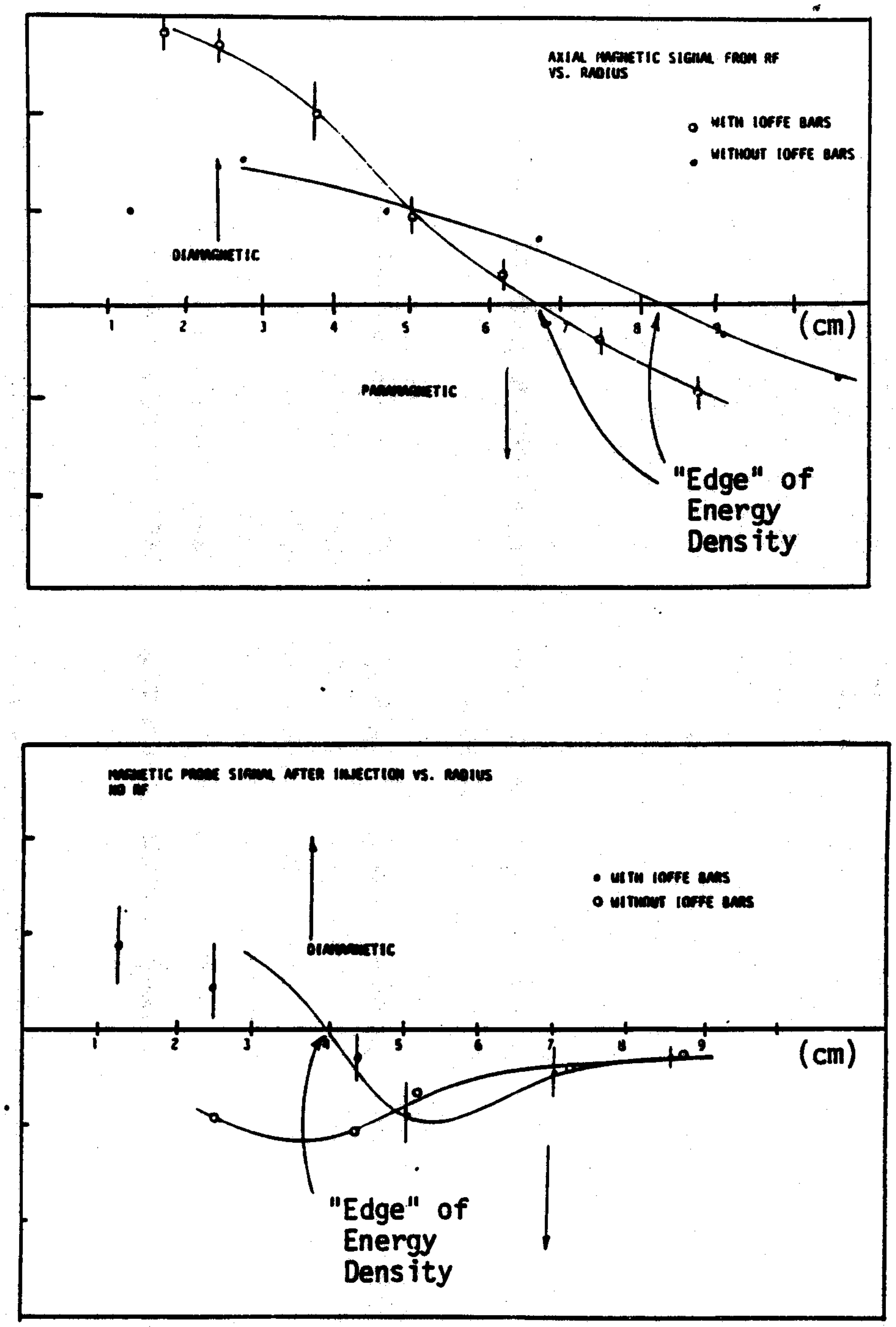

Figure 21. Samples of magnetic probe data during ECRH and examples of the magnetic profile with and without ECRH are shown. The radial limitation to the energy-density profile might be related to the diamagnetic coil acting as a "limiter".

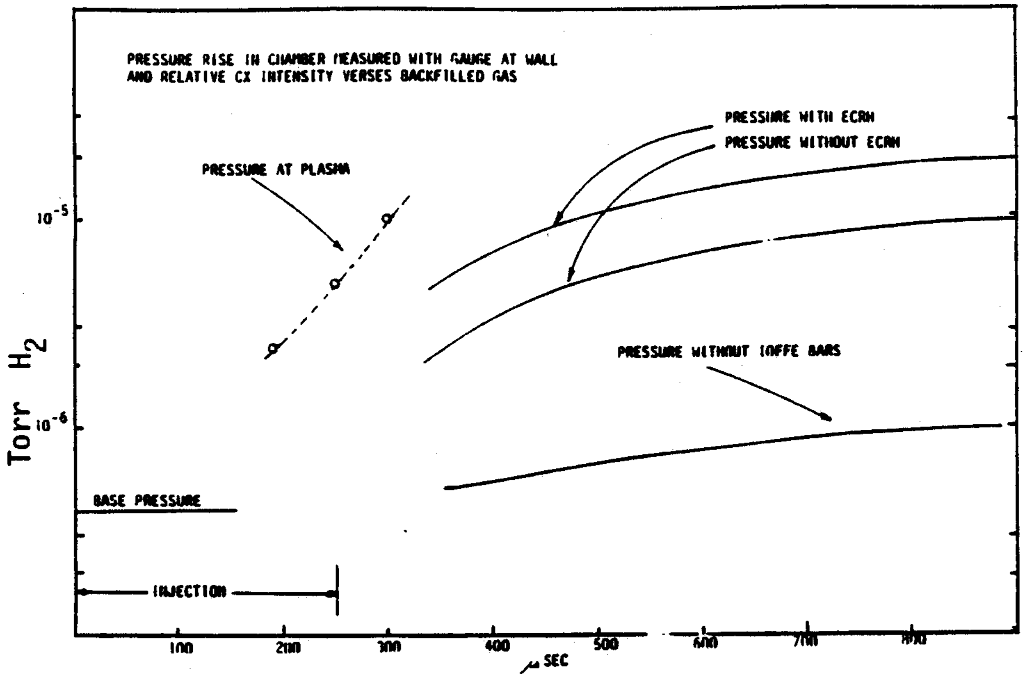

Figure 22. Sample data showing the pressure rise at the chamber wall at the midplane, with and without ECRH. The curve labeled "pressure at plasma" was measured with the charge exchange analyzer (Section 2.2.2).

mirror peaks, and $\langle ionz \rangle$ is the particle creation rate due to ionization. Calculation of the total power loss, P_{loss}, first requires solution of Equation 20 which insures particle balance and determines the potential, Φ. Physically, the potential is a "free parameter" which adjusts itself to equate total electron and ion loss rates. Once Φ is known, the loss rates for each species and, consequently, P_{loss} are determined. Note that magnetically-confined, hot electrons ($E_{hot} \gg \Phi$) initially depress the potential by roughly $\delta\Phi \sim T_{bulk}(n_{hot}/n_{bulk})$. As explained by Ioffe, *et al.*, 1974, after the depression has formed, it is reduced by electrostatically-confined, cool ions. Furthermore, negative potentials would form whenever the ions are *more* collisional than the ions, or $T_e > (m_i/m_e)^{1/3}T_i \sim 12T_i$. For 20ev ions, the potential becomes negative whenever T_e exceeds ~240ev.

The simple model expressed by Equations 20 and 21 predicts several possible "scaling laws" which can be checked against the observed scaling of the experiment (as in Section 2.3). Two limits are considered. First, when $J_{ext} \rightarrow 0$, $\tau_p = \tau_i(n_{bulk}/n_i)[1-(n_{hot}/n_i)(\tau_i/\tau_{hot})]^{-1}$, and the potential must adjust itself so that the bulk electron loss rate equals the ion loss rate modified slightly by the hot electrons. This is the usual picture of mirror confinement, implying that the bulk electron losses will scale as the ion confinement time. For hot ions, $\tau_i \sim T_i^{3/2}/n$. For cool ions, $\tau_i \sim T_i^{-1/2}$, and, when T_e or Φ exceeds T_i, τ_i scales as $T_e^{-1/2}$—the ion-sound speed. Notice also that, for this case, *the particle and energy confinement* *times will be equal.* In addition, until the electron temperature is of the order of $12T_i$, Φ will increase with T_e. The second case is when J_{ext} is larger than the ion loss rate. This is expected in plasma with high densities at the mirror throat. In this case, the potential is nearly constant along the entire length of the plasma column (Boltzman's law gives $\Phi(s) \approx T_{bulk} \ln(n_{bulk}(s)/n_0)$), and a large density of nearly Maxwellian "passing" electrons bounce electrostatically between the wall sheaths. (Secondaries and ionization reduce the potential and cool the external plasma.) The net rate of electrons entering the mirror when the mean-free-path of the passing electrons is much longer than the distance between mirrors has been calculated by Cohen, *et al.*, 1981. In this case, the characteristic time of the entering electrons scales as $(n/n_{ext})(T_{ext}/T_{bulk})^{1/2}\tau_{ee}$. However, as the incoming electron temperature decreases ($T_{ext} < 20ev$), Cohen's formula is no longer valid, and $J_{ext} \sim n_{ext}v_{th,ext}$. Essentially all of the electrons entering the mirror contribute to the particle balance. For this case, the characteristic time of the power loss will scale as $(n/n_{ext})T_{ext}^{-1/2}$, independent of the density. Notice that when the external current dominates the power balance, then *the potential will not increase with T_{bulk} and the particle and energy confinement times will differ.*

By changing the RF power for fixed plasma injection time, the scaling of the initial energy loss-time was observed to scale inversely with the square-root of the ratio of the diamagnetism to the line density and to be roughly independent of density and magnetic field. This is shown in Figure 23. Endloss power measurements agree with this scaling (Figure 24). In addition, since the loss power scales as $P_{loss}/V \sim \sqrt{nT}(nT)$, an equilibration is expected with $(nT)_{eq} \sim P_{rf}^{2/3}$. An example of the observed "ECRH equilibrium" is shown in Figure 26. The $\sqrt{T_e}$-scaling indicate that the dominant loss process is either the sound-speed dependence of the ion confinement or the increasing external flux of cool electrons proportional to the heated diamagnetism. Both of these are independent of density and have characteristic times which scale as $1/\sqrt{T}$. However, as mentioned previously, the potential does not significantly rise with T_e. This fact implies the presence of a high external electron flux. For instance, with $T_{ext} \sim 16ev$, the ratio of the mirror-peak density to the midplane density need only be ~0.25 to account for the observed power loss. Nevertheless, as shown by the examples in Figure 26, the particle loss time is also decreased as a result of heating! In fact, the increased endloss flux is consistent with this observation. This suggests that a *combination* of both the increased ion loss rate (as the ion sound-speed) and the flow of external electrons into the mirror (high density at the mirror peak) are needed to adequately describe the heated electron power balance.

The relative amounts of energy which are lost either because of the influx of external electrons or from the changing ion-confinement time have not been determined. However, the following data suggest that the energy processes differ at

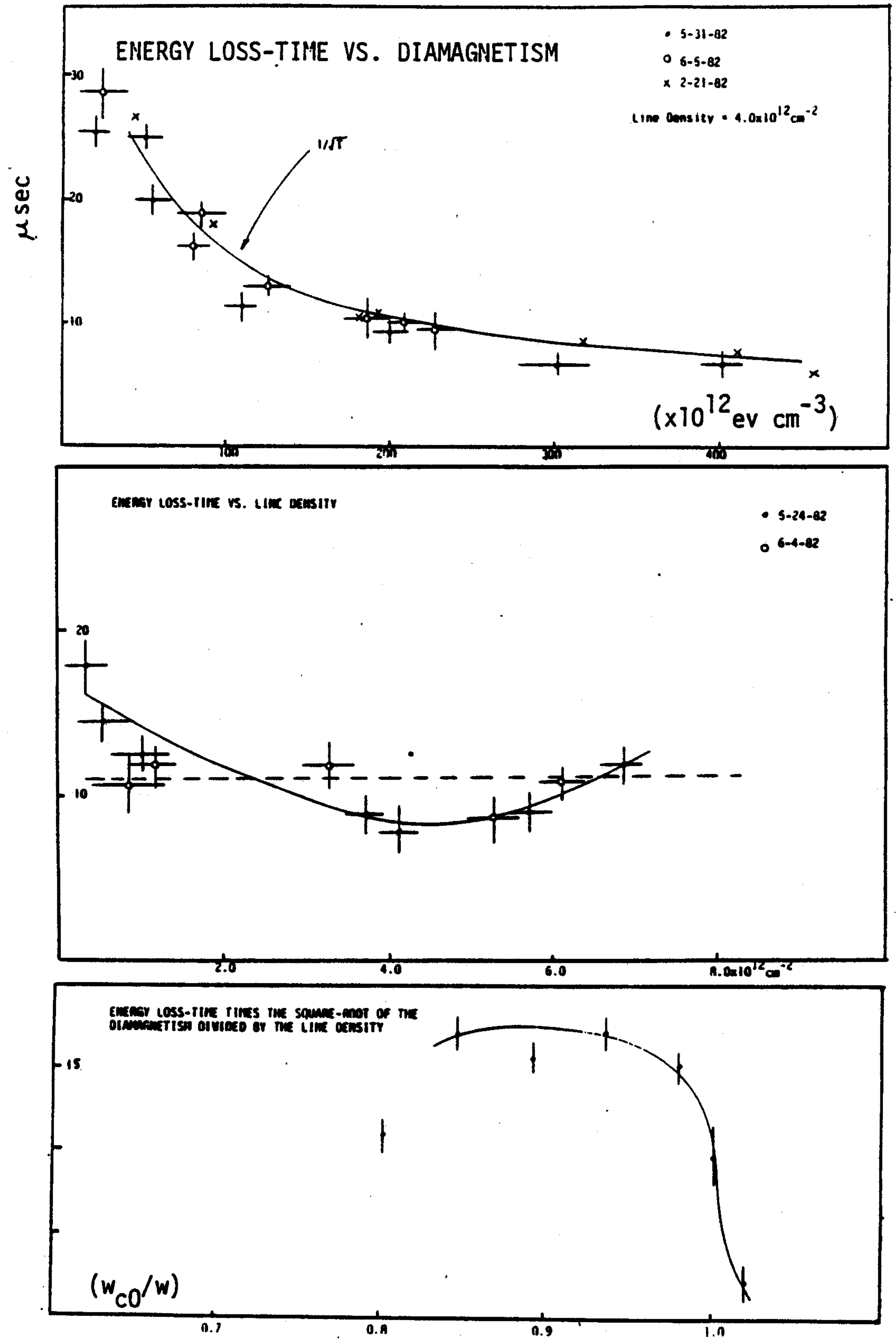

Figure 23. The scaling of the initial energy loss-time with average temperature, line density and magnetic field. The data indicate that the dominant loss process is either the decreasing confinement of the ions (due to their dependence on the sound-speed) or increasing external flux of cool electrons proportional to the heated diamagnetism.

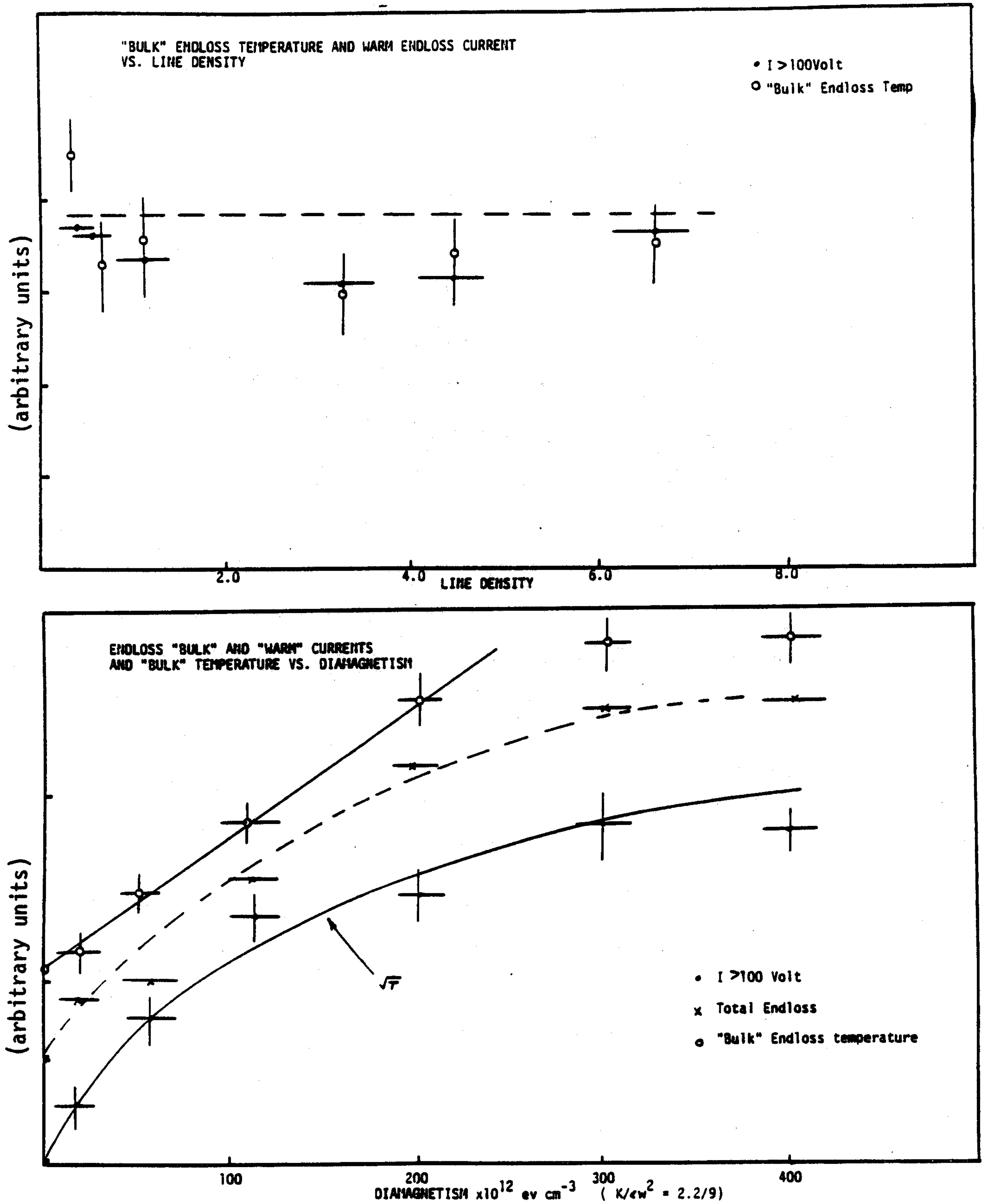

Figure 24. The scaling of the endloss parameters with density (top) and diamagnetism (bottom).

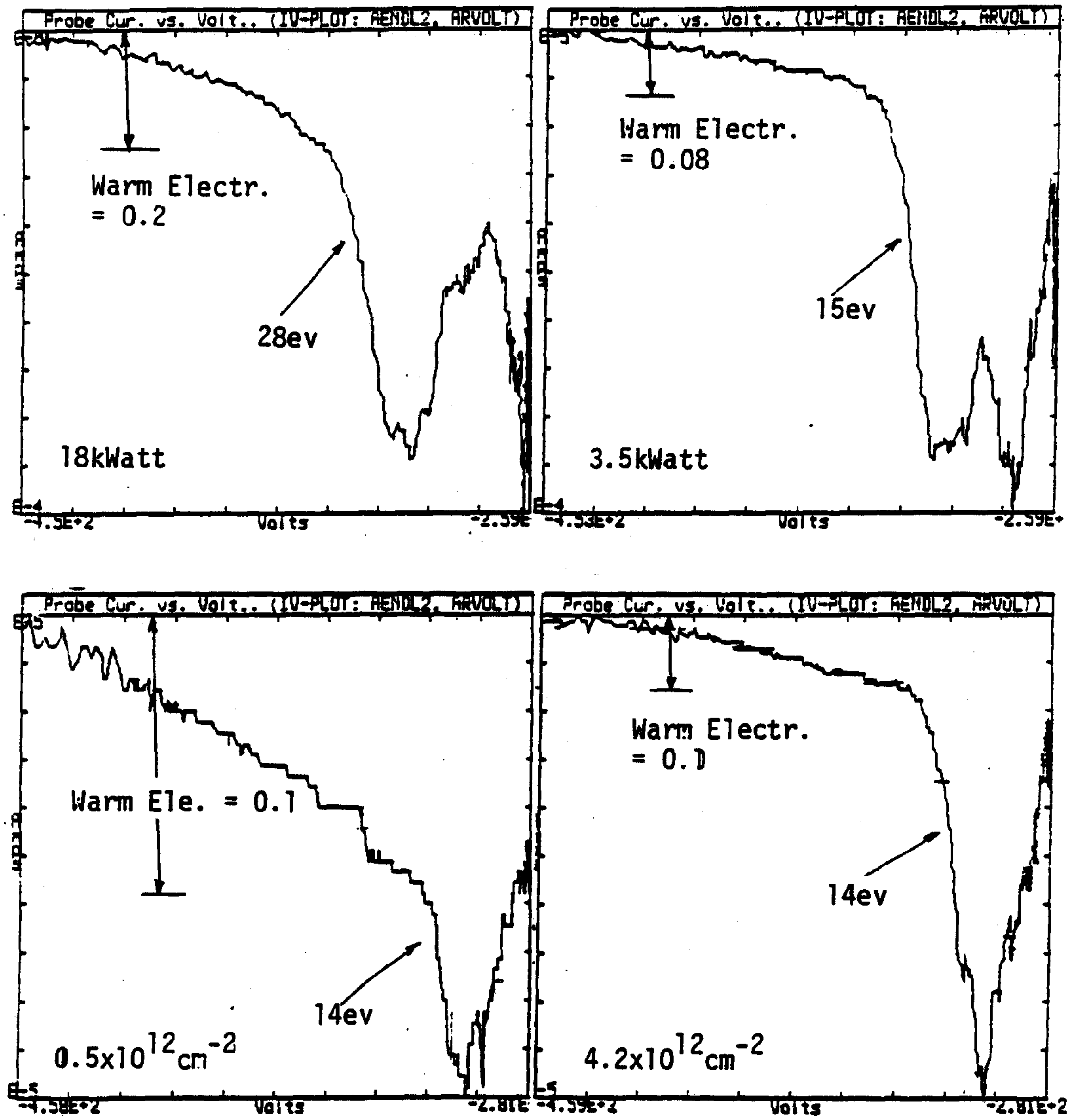

Figure 25. Examples of the endloss distribution as measured by sweeping the electron repeller grid. Shown are four cases: (top) variation of RF power with fixed plasma density, (bottom) variation of density with fixed RF power.

different radii. Also in Figure 26, an example of the interferometer signal for a long RF pulse ($35\mu sec$) is shown. The density remains constant during ECRH (although it initially increases). If the increase in ion loss rate dominated, then the density would begin to decrease immediately. This difference between the confinement times just before and just after the ECRH is turned-off must result either from cold-ion electrostatic trapping, or from a steady source of ions created at the walls which maintains the density. Either explanation is possible. Since the RF power appears to be as strongly absorbed at the edge of the plasma as at the center, the edge electrons should be hotter than those at the center. These low-density, energetic electrons bombard the walls, ionizing absorbed gas. Then, *in order for the edge density to increase*, these newly ionized cold ions must enter the mirror region. This flow will occur whenever there is a density gradient and will be further increased if the edge potential is *negative* with respect the wall potential.[11] In the event of a negative edge potential, the cold ions would be electrostatically-confined as long as the electron temperature was maintained. The equilibrium potential would depend on the influx of cold ions from the walls and the temperature of the (probably slightly hotter) ions confined at the edge. However, even if the potential was not negative, if the cold-ion generation rate remained constant throughout ECRH, the edge density should still be maintained. It is interesting to further speculate whether trapping might also occur at the center of the plasma with the denser (and probably hotter) ions; however, no evidence was found which supported this conclusion. On the contrary, by lowering the Ioffe current the density increase observed with the interferometer was found to decrease—presumably due to the reduced contact with the walls.

The picture which finally emerges is complicated, but the following conclusion seems consistent with the data presented in this and the preceding sections. At the start of the RF pulse, the plasma is a long column of plasma relatively uniform along the axis. The microwave power is absorbed at the edges as well as in the middle of the plasma, enlarging the area of power flow to the walls. The line-density of the plasma increases, presumably from ionization of gas at the walls. This wall plasma flows into the mirror region and is perhaps confined at the edge electrostatically. Since the density at the mirror peak is comparable to the density at the midplane, there is a large influx of "passing" electrons from outside the trap. This keeps the potential low and allows the heated "bulk" electrons to leave at the rate which keeps the net electron loss rate equal to the ion loss rate. In a sense, an external electron enters the mirror and leaves a moment later, warmed up. This provides a mechanism for the observed saturation of the heated diamagnetism. When the ECRH is turned off, the ions escape the mirror at a rate proportional to the sound-speed, and the

---

[11] Although no evidence of a negative potential was ever observed, Figure 20 shows that the floating potential measured at the edge is negative.

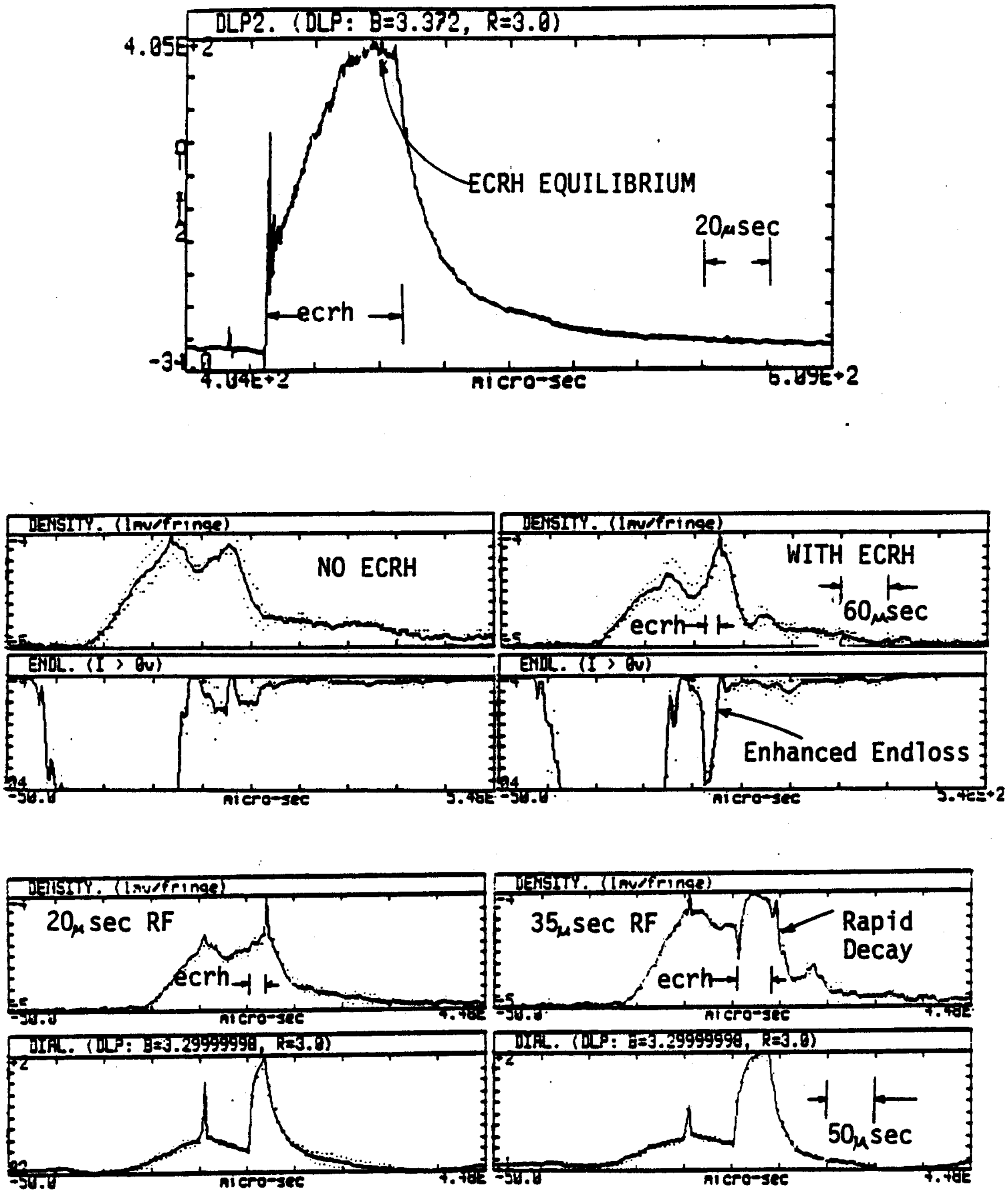

Figure 26. (Top) Example of ECRH equilibrium expected due to the $\sqrt{T}$ dependence of the electron loss rate. (Bottom) Examples of the increased loss rate of the line density and the time history of the endloss. The line density shows both the *increase* in density during ECRH and the rapid *decrease* after the heating pulse ends.

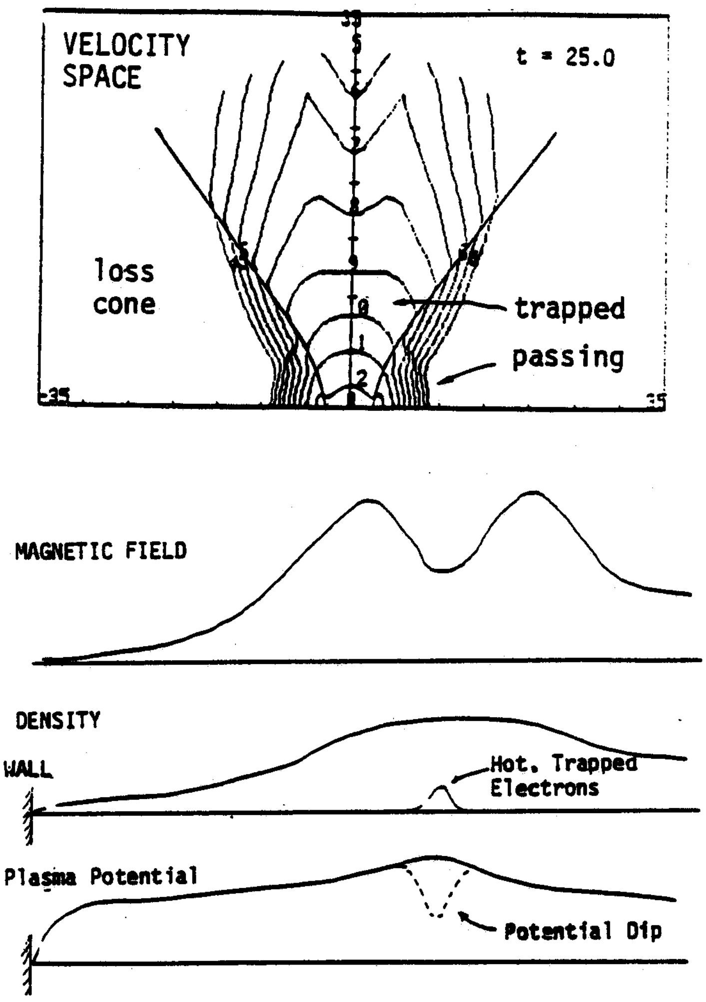

Figure 27. A sketch of the plasma configuration showing the magnetic field, plasma density, and the potential. Two electron populations are shown: the trapped warm and hot electrons, and the external, or "pasing" distribution. The "bulk" electrons can be considered to be a combination of the "passing" and coldest part of the trapped distribution.

bulk electrons cool rapidly due to the continual influx of electrons from the external plasma. A diagram illustrating these ideas is shown in Figure 27. In addition, the velocity-space distribution (from a simulation run) corresponding to the drawing is shown, identifying the "trapped" and "passing" electron distributions. As will be explained in Chapter 4, by using the cool electron flux as the dominant loss mechanism the potential can be *fixed* during a simulation, greatly simplifying the Fokker-Planck code.

2.4.2. A Summary of the Electron Parameters During ECRH . Figure 28 summarizes this section by presenting the typical plasma parameters as a result of heating. These parameters are based on the following diagnostics: (1) the ratio of the diamagnetism to the line density which determines the average energy, (2) Langmuir probe and endloss measurements which determine the "bulk" electron population, (3) a tail, observed with the endloss analyzer, which determines a "warm" electron population, (4) finally, (discussed in Chapter 5) surface barrier detectors which determine the hot electron temperature. Estimations of the relative densities of these populations are more difficult. The main difficulty results from the inability to calculate the density of the hot electrons from the target x-ray intensities (Section 2.2.5). However, from the endloss analyzer, an estimate of the fraction of "warm" electrons can be made by using the measured "warm" endloss current along with the pitch-angle scattering time corresponding to the measured energy and density. This gives $(n_{warm}/n) \sim I_{loss,warm}\tau_{loss,warm}/n^2$. Using the parameters from the example discussed previously, $T_{warm} = 200ev$, $I_{warm} = 0.24amps$, giving $(n_{warm}/n) \approx 0.15/n^2 \sim 60\%$. For this example, the average energy was between 150ev and 250ev, indicating that at least half of the observed energy rise consisted of the "warm" component.[12] Furthermore, as the power is lowered or density raised, this fraction decreases (Figure 24). As shown in Chapter 4, the Fokker-Planck simulation reproduces this conclusion.

---

[12] This was also the conclusion reached in the Constance 1 ECRH experiments. Notice too that this is indeed a sizable fraction of "warm" electrons which may locally, depress the potential. This is an important issue related to the stabilization of the DCLC instability. (See Appendix 3.)

Typical Constance 2 Parameters with ECRH

Input power	$< 20kWatt$
Heating efficiency	$> 60\%$
Heating pulse length	$< 40\mu sec$
ω_{pe}^2/ω^2	< 1.0
Diamagnetism ($R_p = 6cm$)	$\sim 200 \times 10^{12} ev \cdot cm^{-3}$
Average energy	$50 - 200ev$
Bulk electron temperature	$\sim 30ev$
Warm electron temperature	$100 - 500ev$
Hot electron temperature	$> 2kev$
Warm electron fraction	$10 - 60\%$
Radius of energy density	$6cm$
Energy loss time	$\sim 15\mu sec$
Particle loss time (after ECRH)	$15 - 30\mu sec$
Passing density	~ 0.5

Figure 28. Summary of typical parameters for the Constance 2 plasma during ECRH.

Chapter 3

Accessibility and Absorption

This chapter: (1) presents sample results of cold-plasma calculations of the flow of RF power through the plasma, (2) estimates the absorption of the wave energy by the plasma, and (3) shows experimental data which indicate the predicted strong absorption of the plasma. The important conclusions used in the following chapters are that the parallel index of refraction at resonance is large ($N_{\parallel} > 3$) and that the plasma is strongly absorbent. A separate section is devoted to each point. The first two sections highlight the theoretical steps used to analyze the WKB propagation and absorption of the RF in Constance 2. More detailed descriptions of the methods can be found in Appendix 1 and in the cited references.

3.1. Geometric Optics

Because of the complicated plasma and magnetic geometry found in Constance 2, an approximate, WKB technique is used to estimate the RF power flow through the plasma and the wave parameters at resonance (Bernstein, 1975). (See also Appendix 1, Section 7.) This approximation can be considered as an expansion of the *non-local* dispersion relation

$$\int d^3r' \mathsf{D}^{ij}(\mathbf{r}' - \mathbf{r}, (\mathbf{r}' + \mathbf{r})/2)\overline{E}^j(\mathbf{r}')e^{-i\lambda(\mathbf{r}'-\mathbf{r})} = 0 \tag{22}$$

in the small variation over a wavelength of the quantities: D^{ij}, the local dispersion tensor, $\mathbf{k}(\mathbf{r}) \equiv \nabla\lambda(\mathbf{r})$, the wave vector, and $\overline{E}^j$, the electric field strength. To first order in the expansion, Equation 22 becomes

$$\begin{aligned}&[\mathsf{D}_R^{ij}(\mathbf{k}(\mathbf{r}), \mathbf{r}) + i\mathsf{D}_I^{ij}(\mathbf{k}(\mathbf{r}), \mathbf{r})]|\overline{E}^i\overline{E}^j|_k + \\ &\qquad i\nabla\cdot\left(-\frac{\partial \mathsf{D}_R^{ij}}{\partial \mathbf{k}}\frac{1}{2}|\overline{E}^i\overline{E}^j|_k\right) + i\frac{\partial}{\partial t}\left(\frac{\partial \mathsf{D}_R^{ij}}{\partial \omega}\frac{1}{2}|\overline{E}^i\overline{E}^j|_k\right) + \ldots = 0\end{aligned} \tag{23}$$

where $\mathsf{D}^{ij} = \mathsf{D}_R^{ij} + i\mathsf{D}_I^{ij}$, the Hermetian and anti-Hermetian parts.

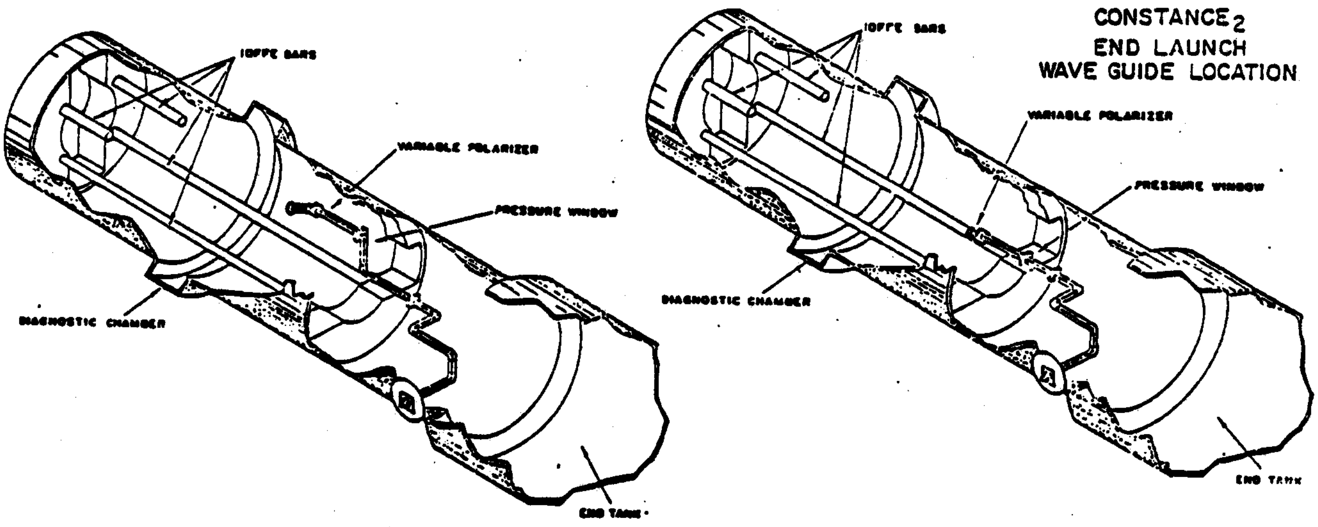

Figure 29. Drawings illustrating the waveguide orientations evaluated with geometric optics.

The WKB approximation used in this thesis consists of satisfying Equation 23 by separately satisfying each of the two equations

$$D^{ij}_R(\mathbf{k}(\mathbf{r}),\mathbf{r})|E^iE^j|_k = 0 \tag{24}$$

$$\nabla\cdot(\mathbf{v}^i_g W^i_k) + \frac{\partial W^i_k}{\partial t} + 2\mathbf{k}_I\cdot\mathbf{v}^i_g W^i_k = 0 \tag{25}$$

Solution of the first equation is called "geometric optics", and the solution of the second is called "physical optics". The symbols, $\mathbf{v}_g$, W_k, and k_I, are respectively the group velocity, wave energy density, and spatial damping rate. They are given by the formulae:

$$\mathbf{v}^i_g \equiv -\frac{\partial D^i_R}{\partial \mathbf{k}}\left(\frac{\partial D^i_R}{\partial \omega}\right)^{-1} \tag{26}$$

$$W^i_k \equiv \frac{1}{8\pi}|E^i|^2\frac{\partial D^i_R}{\partial \omega} \tag{27}$$

$$\mathbf{k}_I \equiv -D^i_I\left(\frac{\partial D^i_R}{\partial \mathbf{k}}\right)^{-1} \tag{28}$$

where D^i_R is an eigenvalue of D^{ij}_R. The eigenvectors define each mode's polarization. "Geometric optics" demands that the local dispersion relation be satisfied throughout space, and "physical optics" relates the divergence of the power flow to the spatial damping rate.

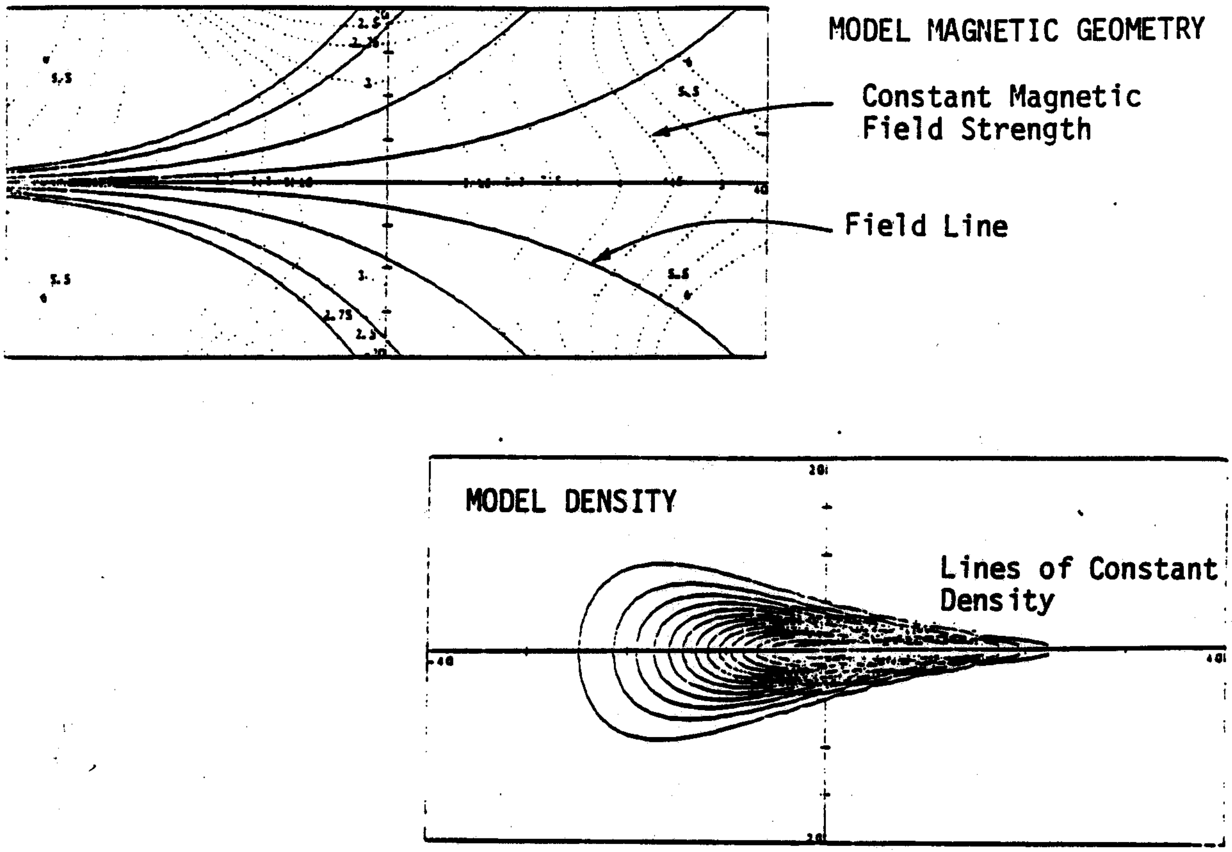

Figure 30. The model magnetic and density profiles used to calculate the ECRH ray paths.

The first step of the solution consists of calculating the power flow (both in coordinate space and in k-space!) as a mode is launched from the antenna through the plasma. A computer code was programmed for this purpose.[1] Drawings of the two wave-guide orientations studied are shown in Figure 29. The magnetic field and plasma density were modeled by using an equation which reproduced the overall characteristics of the experiment.[2] Figure 30 illustrates the model geometry. Using this model, the rate of change of the wave-vector,

$$\mathbf{v}_k^i = \frac{\partial D_R^i}{\partial \mathbf{r}}\left(\frac{\partial D_R^i}{\partial \omega}\right)^{-1}$$

is advanced along the ray path parametrically with the group velocity, $\mathbf{v}_g^i$. The code simply increments the phase-space position $(\mathbf{r}, \mathbf{k})$ according to the velocity $(\mathbf{v}_g, \mathbf{v}_k)$, calculated from central differences.

---

[1] Most of the work involved with the development of the cold-plasma ray-tracing code was performed by R. Garner. His results have been summarized in Garner, *et al.*, 1981.

[2] This was similar to the model used in Porkolab. *et al.*. 1981. The major modification was the inclusion of the negative radial well-depth at low Ioffe currents.

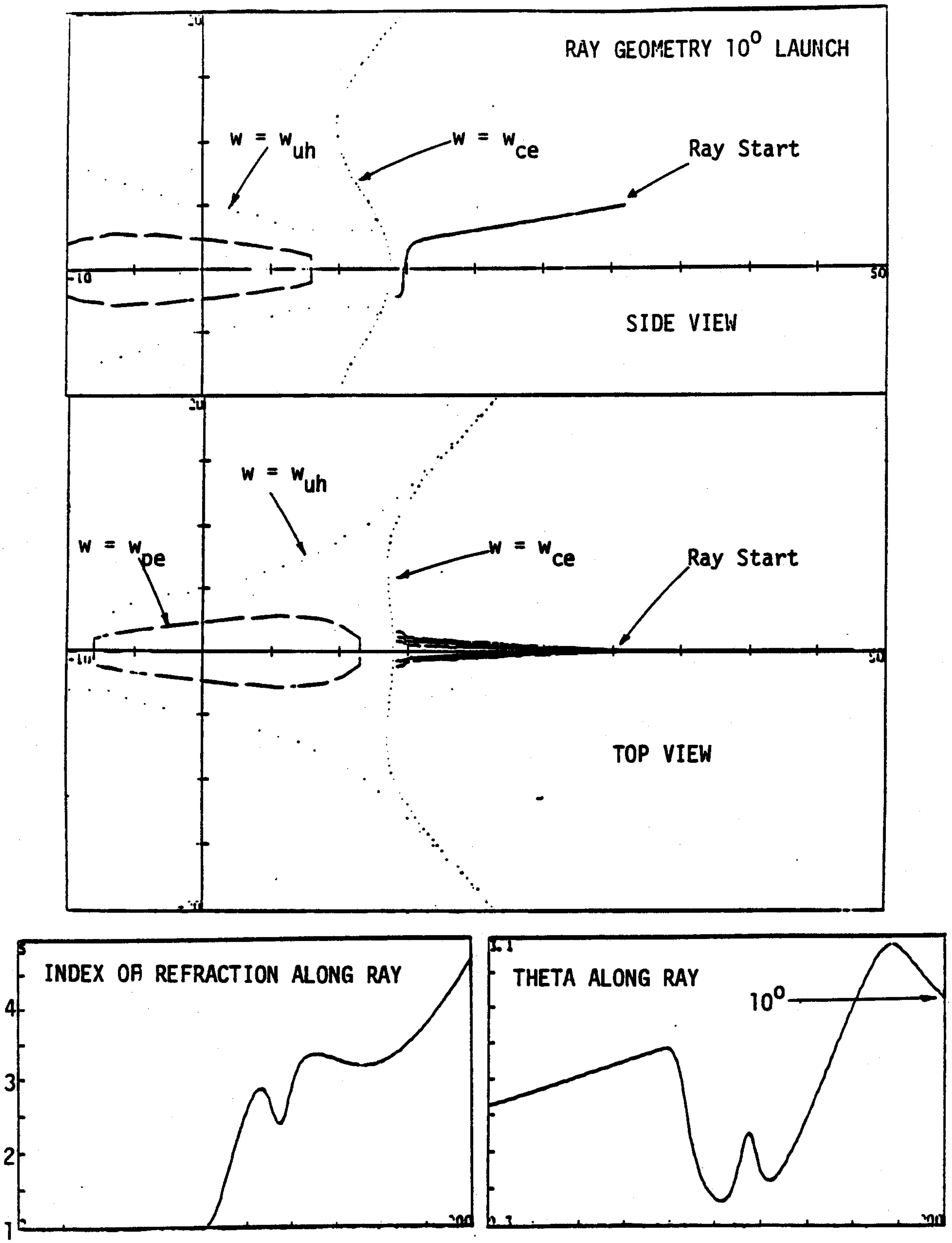

Figure 31. A sample of ray-tracing results for the 10°, axial launcher. $N_{\parallel} = 4.5$ and $\theta = 10^{\circ}$. The dashed line is the $\omega_p = \omega$ surface, the close-dotted line is the cyclotron resonance, and the loosely-dotted line is the upper-hybrid resonance.

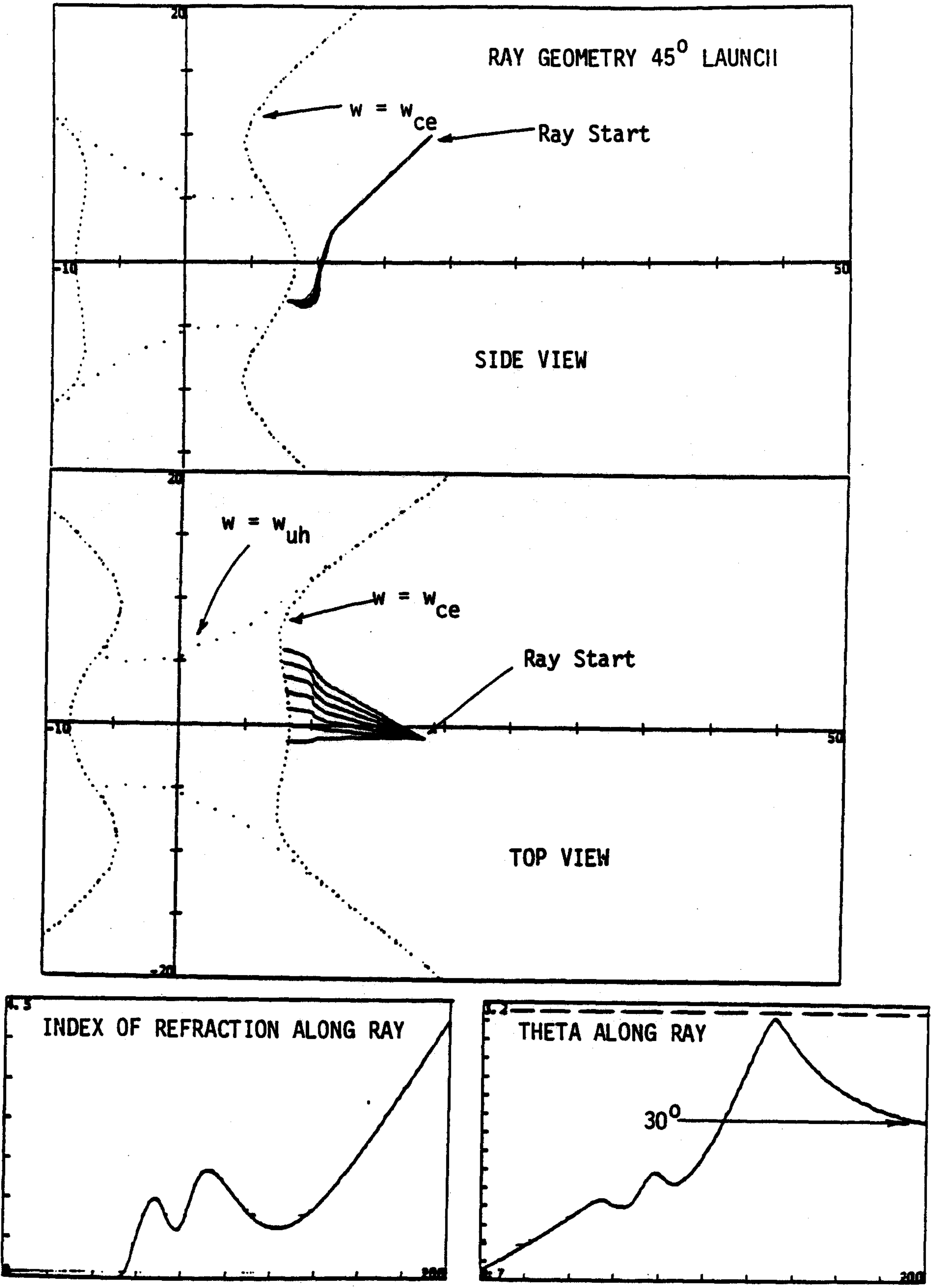

Figure 32. A sample of ray-tracing for the 45° launcher. $N_{\parallel} = 3.6$ and $\theta = 30°$.

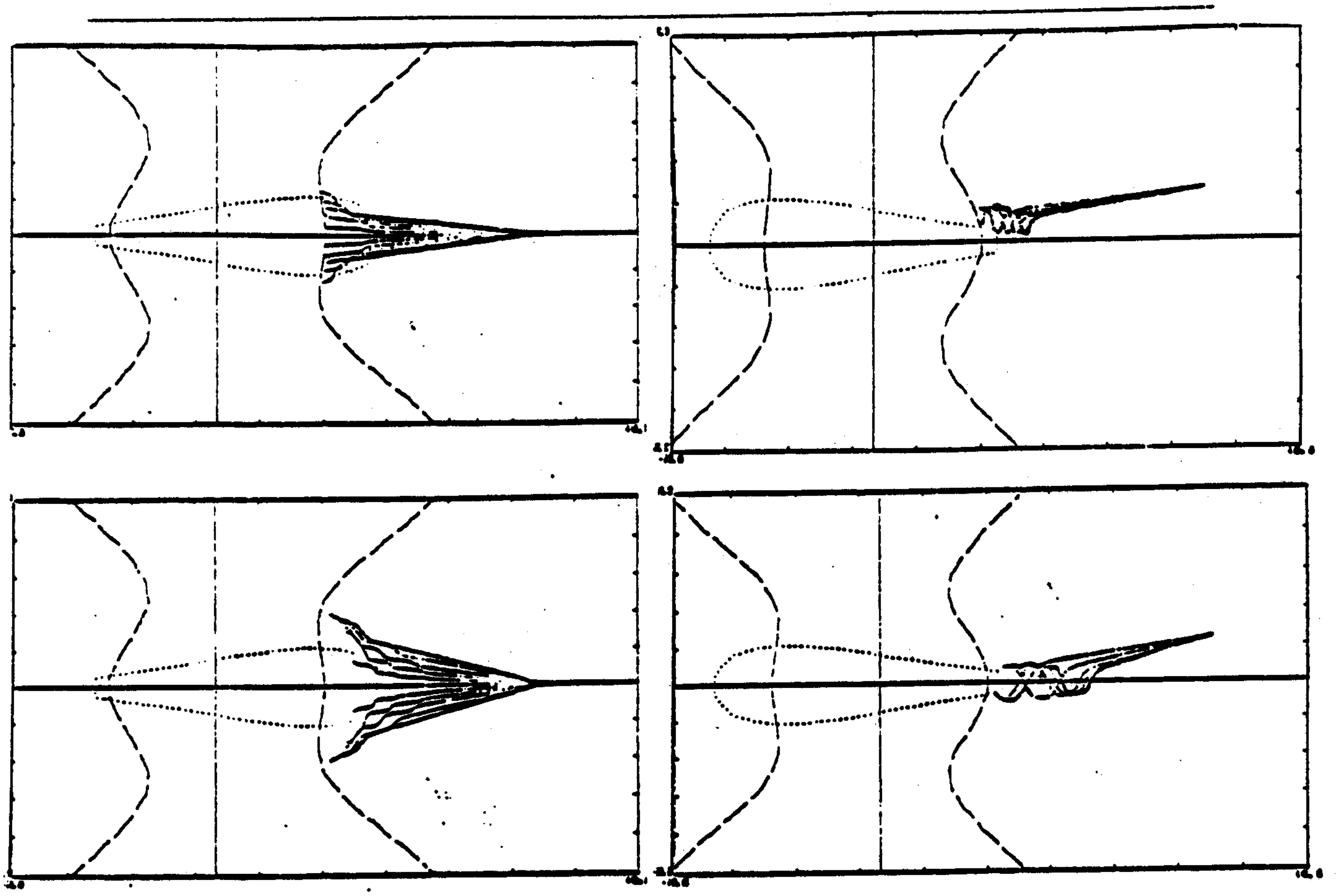

Figure 33. Examples of ray paths in an overdense plasma. Notice the refraction of the waves to the sides of the plasma where they are absorbed.

Sample results from the code are shown in Figures 31 and 32. The rays turn toward the regions of high index of refraction (*i.e.* near cyclotron resonance) and away from the regions of low index of refraction (*i.e.* near $\omega = \omega_p$). When the plasma density increases, as in Figure 33, refraction of the rays around the overdense plasma and their subsequent absorption at the edges of the plasma is seen. It should be mentioned that even though the whistler mode $\theta = 0$ propagates in an overdense plasma, the mode is not accessible from the Constance launch geometries since the rays bend (*i.e.* $\theta \neq 0$) before reaching the $\omega = \omega_{pe}$ surface. Other examples are shown in Garner, *et al.*, 1981. For the purposes of this thesis, the important results obtained from the ray-tracing calculation are the value of the propagation angle and the index of refraction at resonance.

3.2. Physical Optics

To determine the absorption strength of the plasma, "physical optics" is used. In the manner used here, this amounts to evaluation of the inner-product of the anti-Hermetian part of the dielectric tensor with the electric field vector and to calculation of the group velocity. Furthermore, since $N_\perp \beta \ll 1$, where $\beta = v/c$, only the right-handed, diagonal element of D_I^{ij} is non-zero. Thus, *all of the energy transferred between the particles and the wave can be expressed in terms of the strength of the right-handed polarization at resonance.* To emphasize the importance of the right-handed field, E^r, and to simplify the following formula, the right-handed, resonant field energy per input power flux is defined (Mauel, 1982b). This is

$$\mathcal{E}_{res} \equiv - \frac{|\overline{E}^r|^2}{|\overline{E}^i\overline{E}^j|_k|\frac{\partial \mathsf{D}_R^{ij}}{\partial \mathbf{k}}|} \tag{29}$$

$\mathcal{E}_{res}$ has units of $speed^{-1}$, and for a right-handed wave in vacuum, $\mathcal{E} = 1/2c$.

To show the utility of the new expression, the local spatial damping rate becomes simply

$$k_I = D_I^{rr}\mathcal{E}_{res} \tag{30}$$

and the heating rate per input power flux is

$$\frac{1}{(v_g W_k)_{res}} \frac{\partial(nE)}{\partial t} = 2\sum_{res} \overline{\mathsf{D}}_I^{rr}\mathcal{E}_{res} \tag{31}$$

where the "bar" over D_I^{rr} refers to the use of the bounce-averaged resonance function (Appendix 1) when calculating the average over the thermal electrons. In this form it's easy to recognize that k_I is equal to the local rate of energy transfer between the particles and the wave, $D_I^{rr}|\overline{E}_r|^2$, per input power flux. The heating rate is just the sum over resonances of the averaged energy exchange between particles and wave.

As expected, the total first-pass absorption coefficient, $\langle 2k_I L_{res}\rangle$ is proportional to the heating rate (Equation 31) and is equal to the integral of $\mathbf{k}_I \cdot \mathbf{v}_g$ along the ray path. Since the most rapidly changing part of the integral is D_I^{rr}, the other more slowly varying quantities can be approximated by their values at resonance. The remaining integral of D_I^{rr} can be related to the bounce-averaged resonance function (described in the next chapter) by first transforming the integral along the ray trajectory to an integral along the field lines, as in

$$\langle 2k_I L_{res}\rangle \approx 2\frac{\cos\phi}{\cos(\phi - \xi)} \oint \hat{b} \cdot \mathbf{k}_I ds \tag{32}$$

where $\cos\phi \sim \nabla|\mathbf{B}| \cdot \mathbf{B} \sim 1$ and $\cos\xi \sim \mathbf{v}_g \cdot \mathbf{B}$ define the geometry of the transformation.[3] Now, by performing the integral along the field line *before* the integral over the electron's velocity distribution, Equation 32 can be written as

---

[3] This approximation was motivated by a similar transformation made by Frieland and Porkolab, 1981.

$$\langle 2k_I L_{res}\rangle \approx \left\langle v_{\parallel}\tau_B\right\rangle \frac{\cos\phi}{\cos(\phi-\xi)}\frac{1}{(v_g W_k)_{res}}\frac{\partial(nE)}{\partial t} \tag{33}$$

$$\approx 8\pi^2 L_B\omega(X\mathcal{E}_{res})\frac{\cos\phi}{\cos(\phi-\xi)} \tag{34}$$

which is the desired statement of energy conservation. (See Section 9 of Appendix 1.) The expression $\left\langle v_{\parallel}\tau_B\right\rangle$ is approximately $2\pi(\nabla\ln B)^{-1}$ provided $(\nabla\ln B)^{-1}$ is not too small. (See Equation 45 in Section 4.2.)

Notice that the outcome of the WKB framework is a complete description of the total energy transfer between waves. Only three items are required: (1) the ray geometry, (2) the resonant field energy per input power flux, and (3) the integral of the bounce-averaged resonance function over the particle distribution. The ray geometry (shown in Section 3.1) gives $N_{\parallel}$, ϕ, and ξ. The second point, $\mathcal{E}_{res}$, is discussed in the next paragraph. The third item, the rate of wave-particle energy transfer per resonant field energy, $\overline{D_I^{rr}}$, is found to be well approximated by $2\pi\omega_{pe}^2\left\langle\omega_B\tau_{eff}^2\right\rangle$ (Mauel, 1982b).

To calculate $\mathcal{E}_{res}$, further numerical analysis was performed, finding the real roots, polarization, and group velocity for a "warm plasma". The results of the calculation are shown in Figure 34 for a $50ev$ Maxwellian plasma and for several values of the propagation angle, $\theta=\cos^{-1}(\hat{k}\cdot\hat{b})$. The two limiting cases of parallel and perpendicular propagation are the well-known whistler and extra-ordinary modes. (See for example Akhiezer, et al., 1975, Fidone, et al., 1978.) For parallel propagation, nearly all of the field energy is right-hand polarized and $\mathcal{E}_{res}$ is almost independent of $X\equiv\omega_{pe}^2/\omega^2$. On the other hand, for perpendicular propagation, the electrons "short-out" the resonant field. In this case, $\mathcal{E}_{res}\sim(\Delta\omega/X)^2$ with $\Delta\omega$ representing a combination of Doppler broadening (proportional to $\omega N_{\parallel}\beta$), "geometric" or transit-time broadening (proportional to τ_{eff}^{-1}), and relativistic broadening (proportional to $\omega\beta^2$) (Mauel, 1982b). For $T_e\lesssim 30kev$, relativistic broadening is not important since as $N_{\parallel}\rightarrow 0$, the transit term dominates.

The bottom half of Figure 34 shows the product of the density and the resonant field, $X\mathcal{E}_{res}$. This is proportional to the both the heating rate and the first-pass absorption. A horizontal line has been drawn which roughly separates the strongly and weakly absorbent parameters (for $T_e=50ev$). Notice that for propagation angles less than $\sim 30^\circ$ or for low densities the plasma is strongly absorbent; whereas, for high densities ($X\gtrsim 0.7$) or perpendicular propagation, the plasma is weakly absorbent. For the cases examined with the ray-tracing code, $\langle 2k_I L_{res}\rangle$ was always greater than one. For most cases, $\langle 2k_I L_{res}\rangle\gtrsim 10$ due to the small propagation angle at resonance.

When the waves are strongly damped, the WKB/bounce-averaged description of the total energy transfer, *assuming constant resonant electric field for all particles,*

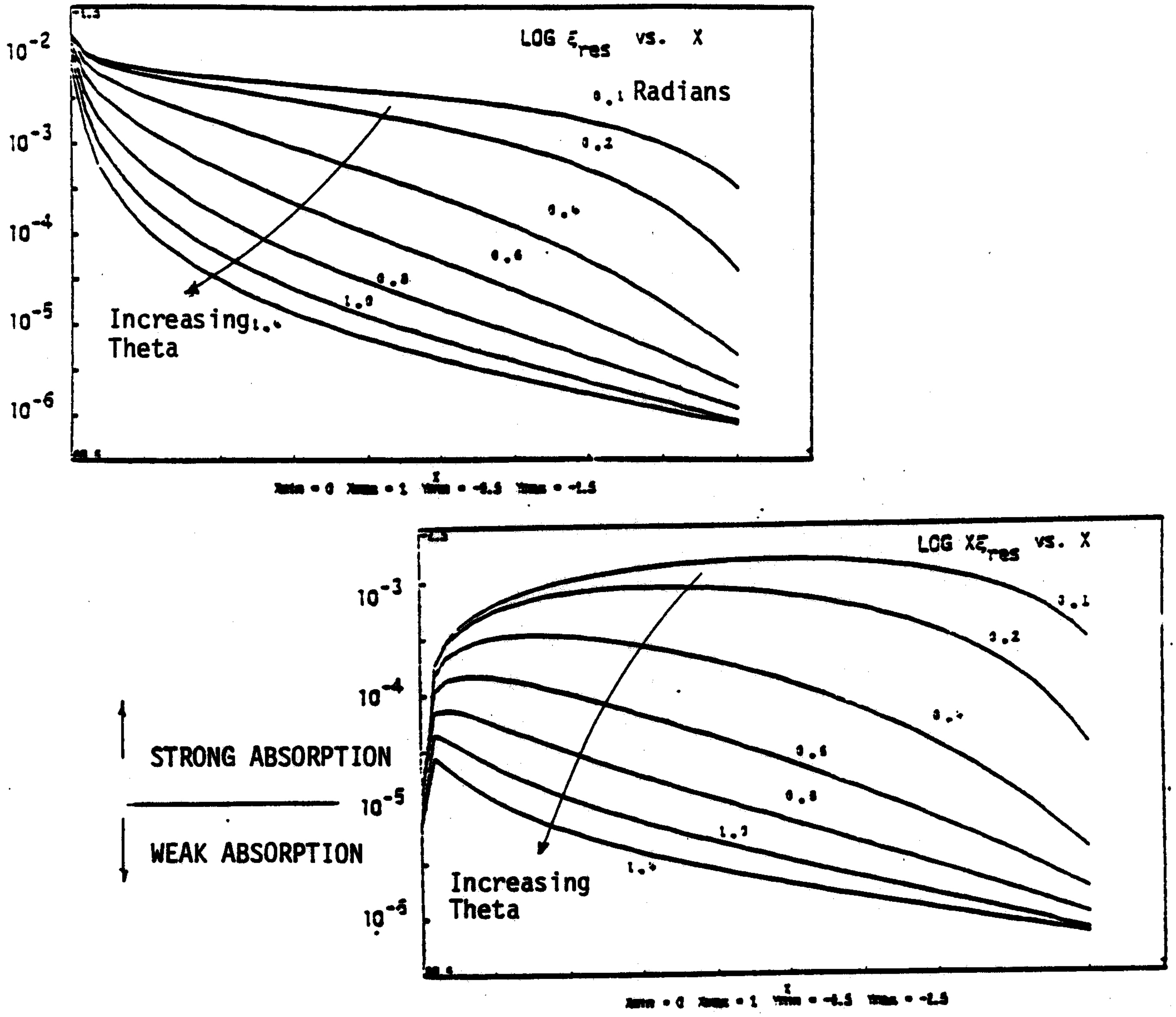

Figure 34. Top: The resonant, electric field energy per input power flux, $\mathcal{E}_{res}$ versus density, $X = \omega_{pe}^2/\omega^2$. The units are *nsec/cm*. Bottom: $X\mathcal{E}_{res}$ versus density for the same cases as above. $X\mathcal{E}_{res}$ scales as the first-pass absorption and the heating rate. The horizontal line roughly indicates the threshold between strong and weak absorption.

is no longer valid. In this case, the field strength decays rapidly and particles turning before or at the resonance zone interact with weaker fields than those turning at higher magnetic fields. This is illustrated in Figure 35. For example, consider the heating at the sides of the mirror with $L_B^{-1} = \nabla \ln(B) \approx 1/40cm$. Then, for $N_{\|} = 4.0$, $\theta = 10 - 15°$, $\beta_{\|} \sim 0.01$ (for 100ev electrons), the Doppler shifted resonance is 1.2cm from the point where $\omega_c = \omega$, and the first-pass absorption coefficient is about 10^2! In fact, since the absorption is proportional to density, even if there was a small, ~10%, population of 100ev electrons, the electric field

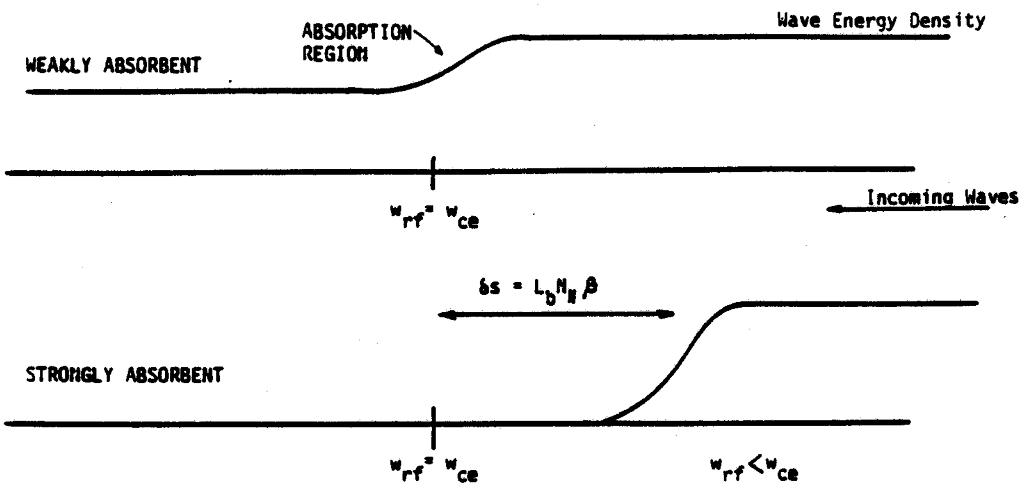

Figure 35. An illustration of the variation of the RF field strength for a weakly and strongly absorbent plasma.

strength may still decay rapidly enough so that those electrons turning at resonance interact with weaker fields as indicated in Figure 35. The implication of this is that particles with different orbits interact with different field strengths and the quasilinear diffusion coefficient must be modified. This will be briefly examined in Section 4.3.

The other important use of Figure 34 for $\mathcal{E}_{res}$ is to estimate the electric field strength from the power flux. In the units of the figure, $E^r[V/cm] = 30\sqrt{\mathcal{E}_{res}\Gamma_{rf}[Watt/cm^2]}$. For the open-ended waveguide used as launchers in Constance 2, the far-field antenna pattern is roughly elliptical, $\epsilon \sim 2$, with the half-power angles given by ±25° and ±45°. Ignoring the self-focusing of the whistler-waves, the power flux is then roughly $\Gamma_{rf} \sim P_{rf}/\epsilon\pi w^2$, where $w^2 \sim (d/2)^2$, and $d \sim 20cm$ is the distance from the waveguide to the plasma. For $\mathcal{E} = 10^{-3}$, $E^r[V/cm] \sim 3.8(P_{rf}/10kWatt)^{1/2}$. Notice, however, a slight inconsistency with the expression for the heating rate and the scaling of $\mathcal{E}_{res}$ with density—for strongly absorbing plasma. As the density increases, $X\mathcal{E}_{res}$ must be constant to maintain the same power absorbed. However, when θ is small, $X\mathcal{E}_{res}$ actually increases with n—implying an increasing heating rate—even though the power flux is constant. This points to the same breakdown of the WKB theory as mentioned in the previous paragraph. In other words, the RF field strength calculated above for $\mathcal{E}_{res}$ represents the field strength at resonance assuming weak damping. For strong damping, the field strength decays toward the resonant zone and particles with different turning-points interact with different RF field strengths.

3.3. Evidence of a Strongly Absorbent Plasma

An experimental check of one of the predictions of the WKB theory was made by surrounding most of the plasma with a non-reflecting liner. The goal of the test was to measure the heating efficiency with the diamagnetic loop when the reflected waves are absorbed by the liners. The result of the test indicated first-pass absorption, since the observed heating efficiency with the liners was ~30%.

The absorbing liners were quarter-wave resonant, polyurethane sheets purchased from Emerson-Cuming. The absorbers were bench tested with and without a magnetic field and were found to reflect only 1 to 3% of the incident power. The liners were then placed around most of the mirror-chamber walls. The two uncovered areas were the dump-tank baffle at the mirror-peak and the 8-inch long diagnostic chamber at the mirror midplane. Note that the 90° waveguide is located within the diagnostic chamber so that most of the reflected power directed into the diagnostic chamber will be reflected back at the plasma. (See Figure 1.) The effect of this reflection is not known and leads to the uncertainty of the final results. A small loop monitored the power at different locations in the chamber with and without the absorbers. For the 10° and 45° launchers, the chamber power was found to be lowered by at least a factor of 20 except when the probe was near an antenna output. For the 90° launcher, the reflected power appears greater, presumably because of the reflections from the uncovered diagnostic chamber. Figure 36 summarizes the measurements.

Next, the heating efficiencies were measured using the diamagnetic loop as in Section 2.4. Several values of the midplane magnetic field were tested while keeping the plasma density relatively constant. Figure 37 show the results of these measurements with and without the absorbing liners. The data indicates 30% first-pass absorption when the resonant zones are near the midplane ($\omega_{c0}/\omega \sim 1.0$) and decreasing absorption as the resonant zone moves out past 3 inches ($\omega_{c0}/\omega \sim 0.95$) for the 45° and 90° launchers and past 5 inches ($\omega_{c0}/\omega \sim 0.85$) for the 10° launcher. These distances roughly correspond to the launch positions for each antenna geometry.

The "expected" absorption for the 10° and 45° launchers is equal to roughly one half of the percentage of RF intercepting the plasma. The factor of one half results from the linear polarization of the waveguide mode coupling to the right-handed polarization of the resonant wave.[4] An estimate for the antenna pattern comes from

---

[4] A possible way to measure the coupling of the antenna would be to launch polarized waves. For example, the heating observed from a left-handed wave results from chamber reflections and the coupling to the right-handed wave due to non-zero density and field gradients. On the other hand, for right-handed waves, the difference between the measured heating efficiency and 100% represents that power which misses the plasma or which couples to the left-handed mode due to plasma gradients. In fact, a variable polarizer was designed and built in square-waveguide; however, an evaluation of the polarizer could not be performed.

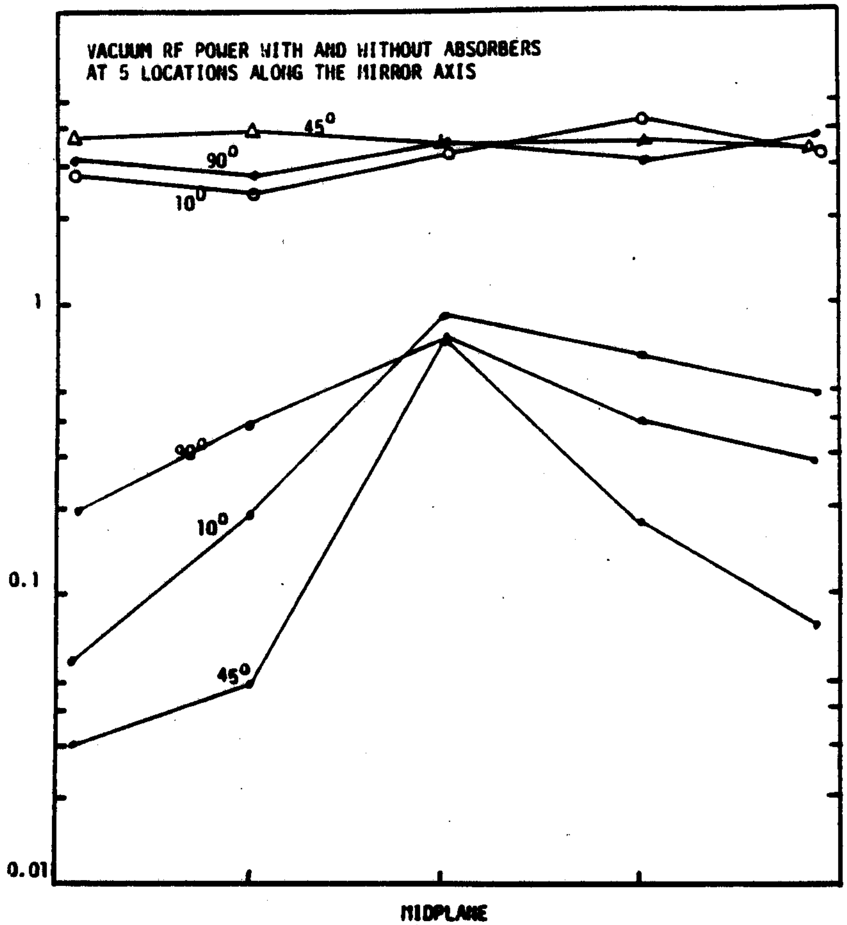

Figure 36. Relative measurements of the chamber power sampled by a small loop in the mirror chamber. Except when the probe is near the waveguide output (*i.e.* the midplane), the measured power is lowered by roughly a factor of 20.

the far field of a radiating slot which gives an elliptical pattern ($\epsilon \sim 2$) expanding in the long direction twice as fast as it moves out. (The half-power points are ±45° and ±25°.) For each launch angle, the distance from the plasma to the launch waveguide was approximately 20cm (6 wavelengths) which means that at most half of the injected power is incident on the plasma. From these (rough) estimates, the "expected" power absorbed should be about 25%. The measured 30% absorbtion, therefore, suggests strong absorption.

An estimation of the "expected" absorption for the 90° launcher is more difficult. In this case, the heating zones are not linearly accessible to the RF since the microwaves are launched from low magnetic fields (*i.e.* $\omega_c < \omega$). In this case, the right-hand cutoff occurs between the launcher and resonant surface and only that power which tunnels through this cutoff can heat the plasma. The remaining power is reflected back to the launcher and diagnostic chamber. Calculations of the fraction

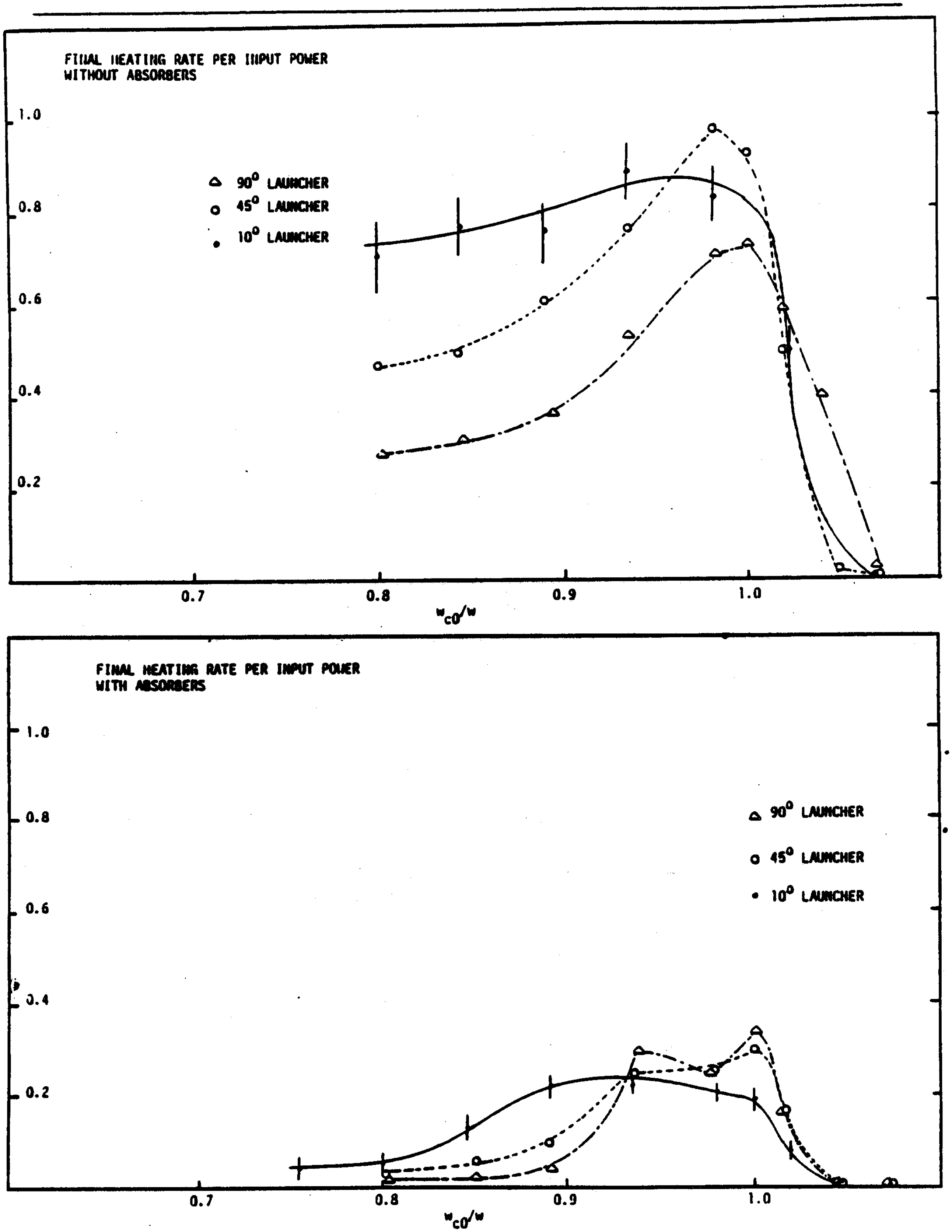

Figure 37. The heating efficiency of ECRH versus midplane magnetic field without absorbing liners (top) and with liners (bottom). The heating efficiency was measured with the diamagnetic loop as in Section 2.4

of power which tunnels through this barrier[5] and which is subsequently absorbed have been recently performed by Batchelor, 1981. For Constance 2 parameters, his calculations indicate absorption greater than 20% for low densities, $X < 0.3$. This is only a factor 1.5 smaller than that observed. However, larger reflection coefficients are calculated for higher densities even though no experimentally observed density variation of the heating efficiency has ever been observed. (In fact, no variation of the heating efficiency has ever been observed for any of the three launchers). It is likely that the high absorption for the 90° launcher is related to (an unknown amount of) "multiple-pass heating" since the diagnostic chamber is not lined with the absorbers.

---

[5] This is called Budden Tunneling after the original work contained in Budden, 1966.

Chapter 4

Fokker-Planck Simulation of ECRH

The quasilinear theory of RF heating calculates the velocity-space diffusion of particles in response to random interactions with specified electric and magnetic fields. In homogeneous geometry, if particles interact with many uncorrelated waves (with correlation time given by τ_{cor}), then the particles "diffuse" in velocity-space and are described by

$$\frac{\partial F}{\partial t} \sim \frac{\partial}{\partial v} \mathsf{D}_{cor} \frac{\partial F}{\partial v} \tag{35}$$

where

$$\mathsf{D}_{cor} = \left\langle \frac{\Delta \mathbf{v} \Delta \mathbf{v}}{\Delta t} \right\rangle \sim \frac{1}{2} \frac{q^2}{m^2} |E_k|^2 \tau_{cor} \tag{36}$$

since $|\Delta v| \sim (q/m) E_k \tau_{cor}$ and $\Delta t \sim \tau_{cor}$. As explained in the introduction (and further in Appendix 1), Lieberman and Lichtenberg showed that, in an inhomogeneous geometry, the successive interactions of particles with a *single wave* can still be random provided that the bounce resonances overlap. The condition for the overlap is $\Delta v / v > \omega_B / \omega$, where ω_B is the effective bounce frequency. For the inhomogeneous case, the quasilinear equation has the same form as above, but the diffusion coefficient is

$$\mathsf{D}_{eff} = \left\langle \frac{\Delta \mathbf{v} \Delta \mathbf{v}}{\Delta t} \right\rangle \sim \frac{1}{2} \frac{q^2}{m^2} |E_k|^2 \tau_{eff}^2 \omega_B \tag{37}$$

since $|\Delta v| \sim (q/m) E_k \tau_{eff}$ and $1/\Delta t \sim \omega_B$. In both cases, ***the usefulness of the quasilinear theory is its ability to predict the motion of the particles in velocity-space under the influence of fluctuating electric and magnetic fields.***

The first section in this chapter describes the principal features of the quasilinear theory of ECRH in mirror geometry. Here the bounce-averaged resonance function and the RF diffusion paths are defined. In the second section, quasilinear and "collisional" diffusion are analytically compared. This analysis yields an estimate of the RF-induced "pump-out" of the particles into a mirror's loss-cone and provides a good understanding of the RF diffusion process. The final section briefly describes the Fokker-Planck code (more details can be found in Appendix 2) and presents sample numerical results of the simulation for several plasma and wave parameters.

4.1. Quasilinear Theory

From Equation 32 in Appendix 1, the quasilinear equation in a mirror geometry can be written as

$$\frac{\partial F}{\partial t} = \frac{q^2}{m^2}\sum_{res}\sum_{n,k}\left\langle v^i \frac{\partial}{\partial \chi} v^m |E^i E^m|_k Re\{\Omega_n^{-1}\}\frac{\partial F}{\partial \chi}\right\rangle_{orbit} \tag{38}$$

It describes the evolution of the velocity distribution under the influence of *any* random interaction between the wave(s) and the particles. In this equation, E^i_k is the wave's electric field vector, and v^i is the particle velocity. The symbol, $\partial/\partial\chi$, is the gradient along the particle diffusion path (the particle trajectory) and is defined as

$$\frac{\partial}{\partial \chi} = (1 - N_{\|}\beta_{\|})\frac{1}{B}\frac{\partial}{\partial \mu} + \frac{\partial}{\partial E} \tag{39}$$

The symbol, Ω_n^{-1}, is the local resonance function (Appendix 1), which for a homogeneous plasma is the well-known expression, $\Omega_n^{-1} = J^2_{n'}(k_\perp \rho)\, i/(\omega - n\omega_c - k_{\|}v_{\|})$. The imaginary part of Ω_n^{-1} is related to the reactive power "sloshing" between the wave and particle and the real part is related to the power transferred between the wave and particle. The average, $\langle\ldots\rangle_{orbit}$, means that the entire expression must be averaged along the orbits of each of the particles. The dominant contribution to the integral comes from the highly peaked term, $Re\{\Omega_n^{-1}\}$, which is non-zero only near resonance (*i.e.* when $\nu_n \equiv \omega - n\omega_c - k_{\|}v_{\|} = 0$). The other slowly varying terms can be approximated by their values at resonance. In particular, the "bounce-averaged" diffusion paths are

$$\left.\frac{\partial}{\partial \chi}\right|_{res} = \begin{cases} \dfrac{1}{B_{res}}\dfrac{\partial}{\partial \mu} + \dfrac{\partial}{\partial E}, & \text{for } n \neq 0 \\[2ex] \dfrac{\partial}{\partial E}, & \text{for } n = 0 \end{cases} \tag{40}$$

where B_{res} is defined from $n\omega_{c,res} = \omega$, and $R_{res} = B_{res}/B_0$. The only orbit integral is contained in the real part of the bounce-averaged resonance function given by

$$Re\{\overline{\Omega}_n^{-1}\} = J^2_{n'}(k_\perp \rho)\int_{-\infty}^{0} dt' \exp[-i\int_0^{t'} dt'' \nu_n] \tag{41}$$

where n' must be determined with knowledge of the velocities, $v^i v^m$, in Equation 38. ("Raising" and "lowering" operators which do the proper book-keeping for the order of the bessel function are defined in Appendix 1.)

For electron cyclotron heating, only the right-handed polarization interacts with the electrons (provided $k_\perp \rho \ll 1$, see Section 3.2). Then, for $n = 1$, $n' = 0$, and the quasilinear equation becomes

$$\frac{\partial F}{\partial t} = \frac{1}{2}\frac{q^2}{m^2}\sum_{res}\frac{\partial}{\partial \chi_{res}} v^2_{\perp,res}|E^r|^2_{res} Re\{\overline{\Omega_1^{-1}}\}\frac{\partial F}{\partial \chi}_{res} \tag{42}$$

where the subscript "res" means "evaluate at resonance", $v_{\perp,res} = R^{1/2}_{res} v_{\perp,0}(1 - N_\parallel \beta_\parallel) \approx v_{\perp,res} = R^{1/2}_{res} v_{\perp,0}$, and where $v_{\perp,res}\partial(\ldots)/\chi = \partial(v_{\perp,res}\ldots)/\partial\chi$ has been used. For waves which Landau damp, $n = 0$, and $n' = 0$ for polarizations parallel to the magnetic field, giving

$$\left.\frac{\partial F}{\partial t}\right|_{Lan} = \frac{1}{2}\frac{q^2}{m^2}\sum_{res} v_{\parallel,res}\frac{\partial}{\partial \chi_{res}} v_{\parallel,res}|E_\parallel|^2_{res} Re\{\overline{\Omega_0^{-1}}\}\frac{\partial F}{\partial \chi}_{res} \tag{43}$$

the same form as in Equation 42.

Examination of Equations 42 and 43 reveal that all of the wave-particle dynamics are represented by the bounce-averaged resonance function. By comparing these to Equation 37, the approximate relationship results

$$Re\{\overline{\Omega_n^{-1}}\} \sim \tau^2_{eff}\omega_B \tag{44}$$

Physically, the bounce-averaged resonance function is the product of the square of the time a particle interacts with the wave, τ^2_{eff}, with the rate, ω_B, at which particles cross the resonant zone.[1] Performing the integrals in Equation 41 (See Appendix 1, Section 6),

$$Re\{\overline{\Omega_n^{-1}}\} = \begin{cases} \frac{1}{4}\omega_B \tau^2_{eff}, & \text{where } \tau^{-2}_{eff} = \nu'_n/2 \\ 2\pi\omega_B\tau^2_{eff} Ai^2(\nu_n \tau_{eff}), & \text{where } \tau^{-3}_{eff} = \nu''_n/2 \end{cases} \tag{45}$$

The first form in Equation 45 is valid provided $\nu'_n \neq 0$. When $\nu'_n \to 0$, the second form should be used. This means τ_{eff} increases as $(\nu'_n)^{-1/2}$ until it reaches a maximum given by the bottom of Equation 45. The first and second derivatives of ν_n *along a particle's orbit* and *evaluated at resonance* are denoted by ν'_n and ν''_n. They are given by

$$\nu_n = \omega - n\omega_c - k_\parallel v_\parallel \tag{46}$$

$$\nu'_n = -[nv_\parallel - k_\parallel \mu(B/\omega_c)](\hat{b}\cdot\nabla)\omega_c \tag{47}$$

$$\nu''_n = n(\omega_c/B)[n(\hat{b}\cdot\nabla B)^2 - (v^2_\parallel/\mu)\omega^2_B] + k_\parallel v_\parallel \omega^2_B \tag{48}$$

---

[1] Of course, the bounce frequency vanishes for particles near the loss cone and is undefined for passing particles. Nevertheless the same expressions used for the trapped particles can be used for the untrapped particles by defining the local bounce frequency: $\omega^2_B \equiv \mu(\hat{b}\cdot\nabla)^2_{res}B$. Physically, it is the *rate* at which the particles cross the resonance zone which determines the heating rate. In fact, this local evaluation of ω_B is good way to evaluate the particle exchange between the untrapped and trapped regions of veolicity-space. This is also necessary in order to equate the energy lost from the wave with the energy gained by the electrons—trapped and untrapped.

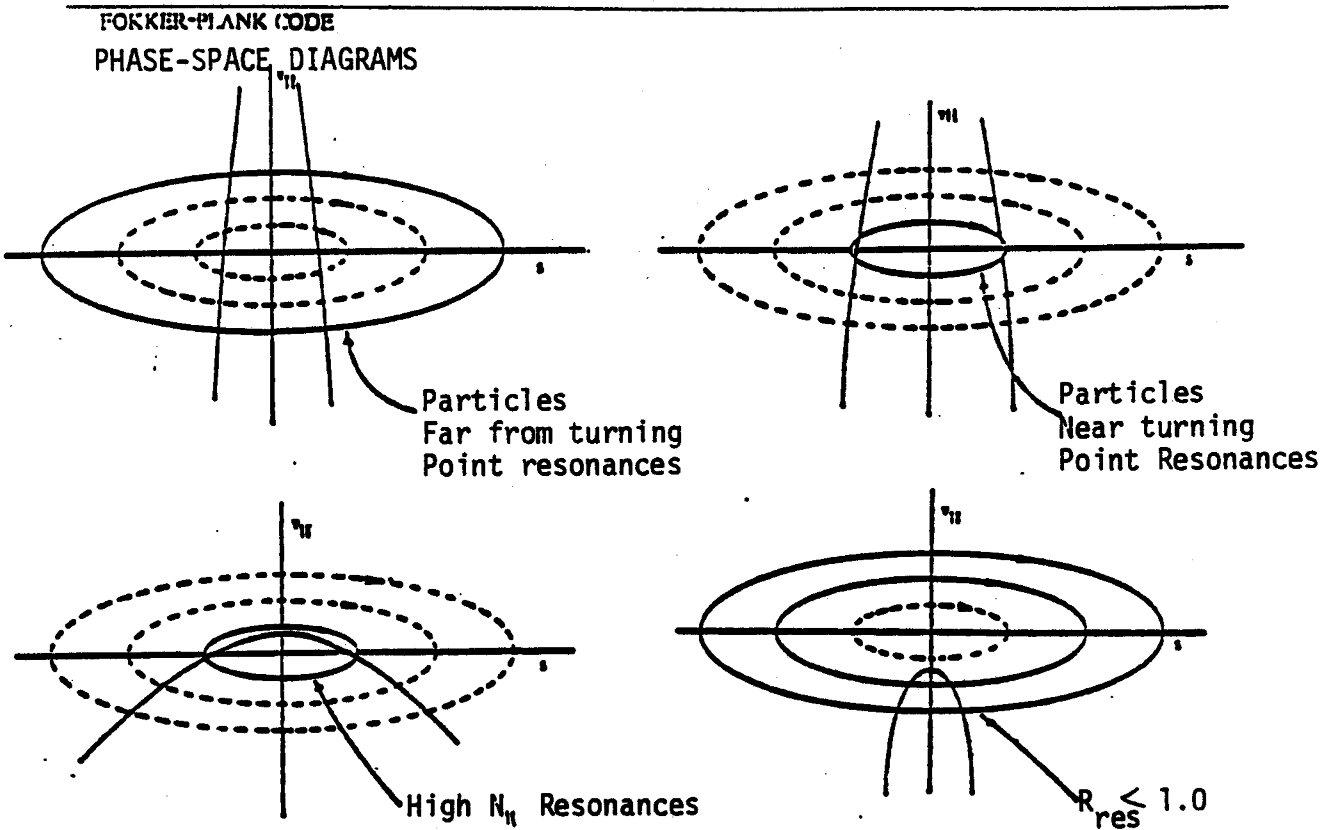

Figure 38. A schematic of four "classes" of wave-particle interactions described by phase-space diagrams. The difference between the four diagrams is in the resonant-zone location and in the size of $N_{\|}$.

where $\omega_B^2 \sim \mu(\hat{b} \cdot \nabla B)^2 B$ is the local bounce frequency.

The physics underlying the math of the previous analysis can be illustrated by the phase-space diagrams of the particles' orbits. shown in Figure 38. The particle orbits in $(v_{\|}, s)$-phase-space are shown along with the loci of resonance points. Since each velocity-space location (*eg.* E, μ) corresponds to a definite orbit in phase-space, τ_{eff} for every resonance crossing can be uniquely determined from the derivatives expressed above. The phase-plots also indicate the effect of changing resonant-zone location and $k_{\|}$. (Except for the plasma potential, these are the only "free" parameters which determine the diffusion coefficient.) As the resonant-zone location moves toward the midplane: (1) particles with higher pitch angles can interact with the wave, (2) the strong, turning-point resonance moves in velocity-space, and (3) the diffusion paths change due to the decreasing $B_{res}/B_0 = R_{res}$. As $k_{\|}$ increases, particles turning *before* B_{res} can resonate with the wave, and τ_{eff} is modified. It is interesting that with finite $k_{\|}$ the longest interaction times, τ_{eff}, always occur at resonances inside of the turning-point resonance, and those outside of R_{res} are shortened. Nevertheless, the integral of the interaction time over the particle velocities—which is proportional to the heating rate for constant E^r—does not change as $k_{\|}$ increases (Mauel, 1982b).

Finally, it is helpful to simplify the notation of Equations 42 and 43 by defining the characteristic RF-diffusion time

$$\frac{1}{\tau_{rf}} \equiv \frac{1}{2}\frac{q^2}{m^2}|E^r|^2\frac{1}{\omega v_{th}^2} = \frac{1}{55\mu sec}(\frac{|E^r[v/cm]|^2}{T_e[ev]})(\frac{9.3GHz}{f_{rf}}) \tag{49}$$

which allows the diffusion equation for ECRH to be written as

$$\frac{\partial F}{\partial t} = \frac{v_{th}^2}{\tau_{rf}}\frac{1}{v_{\perp,res}}\frac{\partial}{\partial v_{\perp,res}} v_{\perp,res}(\omega Re\{\overline{\Omega_1^{-1}}\})\frac{\partial F}{\partial v_{\perp,res}} \tag{50}$$

for the distribution mapped to the resonance location. Note that this equation is equivalent to Ikagami's equation found in Section 1.2, except Equation 50 is correctly expressed for cylindirical coordinates. For Landau heating,

$$\frac{\partial F}{\partial t} = \frac{v_{th}^2}{\tau_{rf}}\frac{\partial}{\partial v_{\|,res}}(\omega Re\{\overline{\Omega_0^{-1}}\})\frac{\partial F}{\partial v_{\|,res}} \tag{51}$$

Finally, the terms $(\omega Re\{\overline{\Omega_n^{-1}}\})$ can be shown to depend mainly on the geometry of the particle orbits and very weakly on the speed, $|\mathbf{v}|$. $(\omega Re\{\overline{\Omega_n^{-1}}\})$ does, however, depend strongly upon the pitch-angle, reaching a maximum value proportional to $(\omega/\omega_B)^{1/3}$ for particles turning at resonance for ECRH or resonating at the midplane for either type of wave.

4.2. RF-Induced Velocity-Space Currents: "Pump-Out"

4.2.1. General Comments about RF Currents . As for any diffusion process, the quasilinear equation can be written in terms of the divergence of an RF-induced velocity-space current. This is the requirement of particle conservation.[2] For ECRH, Equation 42 can be written as

$$\frac{\partial F}{\partial t} = \nabla_X \cdot \Gamma_{rf} \tag{52}$$

where Γ_{rf} is the velocity-space current density. In (μ, E)-space, $\Gamma_{rf}(\mu, E)$ has units of $[F] \cdot Energy \cdot sec^{-1}$ and is equal to

$$\bar{\Gamma}_{rf}(\mu, e) = |\Gamma_{rf}|(\hat{e} + \hat{\mu}/B_{res}) \tag{53}$$

where

$$|\Gamma_{rf}| = 2R_{res}\mu B_0\,\omega Re\{\overline{\Omega_n^{-1}}\}\,\frac{v_{th}^2}{\tau_{rf}}\frac{\partial F}{\partial \chi} \tag{54}$$

In the spherical coordinates used in the Fokker-Planck simulation (Section 4.3), $\Gamma_{rf}(v, \theta)$ has units of $[F] \cdot Velocity \cdot sec^{-1}$ and is given by

---

[2] In an actual bounce-averaged theory, the distribution at any particular location in the trap is not in general conserved. Instead the "bounce-averaged" distribution, $F(\mu, E)\oint(ds\omega_B/2\pi v_{\|})(B(s)/B_0)$ is conserved (Bernstein and Baxter, 1981). However, for the "square-well" approach used in this thesis, $\oint(ds\omega_B/2\pi v_{\|})(B(s)/B_0) = 1$ and is independent of (μ, E).

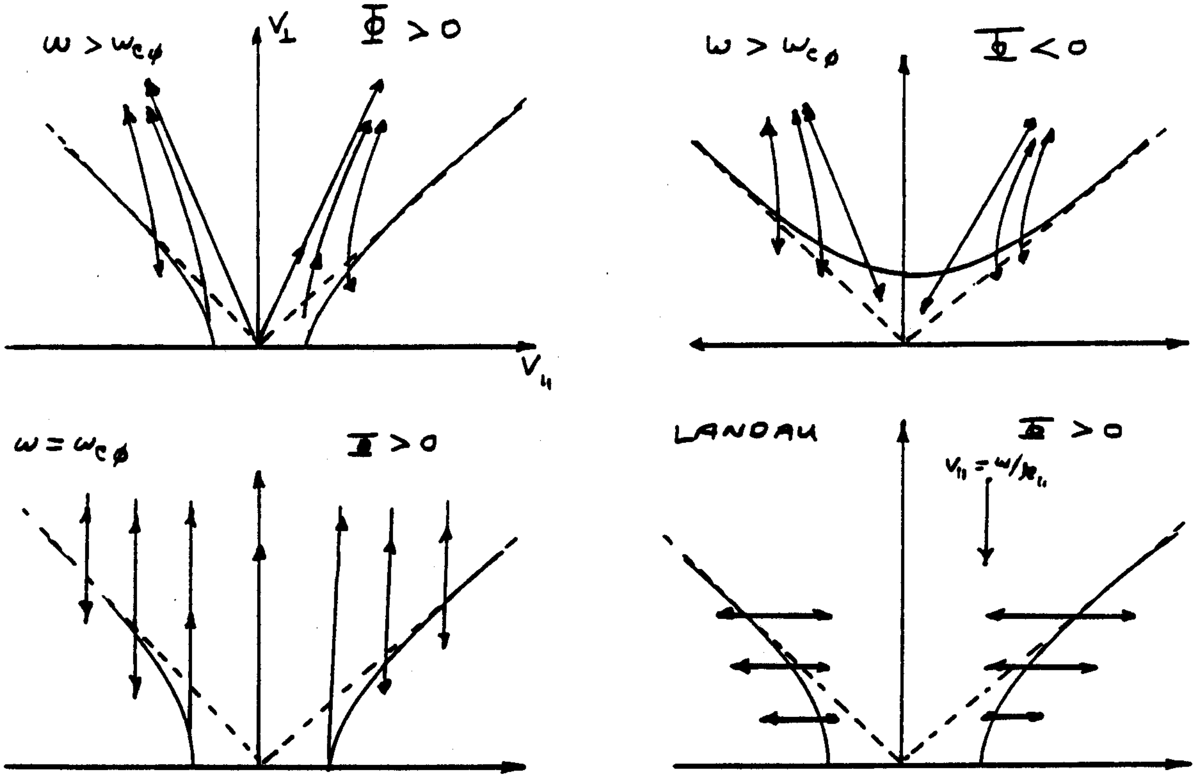

Figure 39. Four examples of the diffusion paths, or the trajectories of the particles under the influence of RF, for different ECRH parameters. Also shown is an example of Landau resonances.

$$\Gamma_{rf}(v,\theta) = |\Gamma_{rf}|(\hat{v}/v + \xi\hat{\theta}) \tag{55}$$

where $\xi \equiv (1/R_{res} - \sin^2\theta)/v^2 \sin\theta\cos\theta$. These currents simply represent the trajectories of the electrons as they move under the influence of the RF. For ECRH, the trajectories are defined from $B_{res}\Delta\mu = \Delta E$. For Landau heating, $\Delta E = v_{\|}\Delta v_{\|}$.

Figure 39 diagrams four examples of the RF-currents induced during ECRH for different parameters. The solid lines denote the electron trajectories and the arrows represent the *net* particle flow which always smooths velocity-space gradients. For the "typical" mirror operation, with a positive potential, the velocity-space regions with diffusion paths which enter the loss-cone contribute to the enhanced loss rate of the warm, mirror-confined electrons. In the same way, the "trapping" of the passing electrons is also enhanced. Those velocity-space regions either far from the loss-boundary (*i.e.* electron energies greater than a few times T_e) or with diffusion paths which do not intercept the loss-region contribute to the heating of the plasma according to the diffusion rate and the gradients along the diffusion paths. When the potential is negative, all of the confined region of velocity-space can diffuse into the loss-region. In this case, ECRH acts on the trapped electrons in exactly the same manner as the DCLC instability acts on an unstable ion distribution, described in

Berk, 1978.[3]

The benefit of expressing the quasilinear equation in terms of the velocity-space currents is the ability to use Gauss's Law to calculate particle loss rates and (to some degree) heating rates. A surface integral of the flux,

$$\left.\frac{\partial n}{\partial t}\right|_{\Sigma} = \int_{\Sigma} d\mathbf{A} \cdot \Gamma_{rf} \tag{56}$$

can yield, for example, the "pump-out" of the magnetically trapped particles or the "fueling" of a hot electron tail. A volume integral gives the heating rate

$$\frac{\partial(nE)}{\partial t} = \int_V d^3v \frac{1}{2} v^2 \nabla \cdot \Gamma_{rf} = \int_V d^3v \mathbf{v} \cdot \Gamma_{rf} \tag{57}$$

which is the same equation used in Section 3.2, since $\int d^3v \mathbf{v} \cdot \Gamma_{rf} = 2 \sum_{res} \overline{\mathsf{D}}_I^{\tau\tau} |E_k^{\tau}|^2$ is proportional to the bounce-average of the imagninary part of the dispersion tensor.

4.2.2. Estimation of RF-Enhanment of Warm Electron Endloss. An example of the use of this formula is in the calculation of the RF-enhancement of the warm-electron endloss (*i.e.* "pump-out"). In Chapter 5, measurements illustrating enhancement are presented. In what follows, the ratio of the RF to collisional currents into the loss cone is calculated.

The total endloss current (the "real", measurable current) is equal to the surface integral of the sum of the collisional, Γ_{col}, and RF-induced, Γ_{rf}, *velocity-space* current densities. If the repeller grid on the endloss analyzer is biased to measure electrons having energies greater than E^*, then the surface integral is written as

$$I_{endloss}(E > E^*) = \int_{E>E^*}^{\infty} d\mathbf{A} \cdot [\Gamma_{col} + \Gamma_{rf}] \tag{58}$$

The desired result requires the estimate of the integral defined above.

In spherical velocity-space coordinates, the RF flux is obtained from Equation 50, or

$$\Gamma_{rf} \approx 2\pi \frac{v_{th}^2}{\tau_{rf}} (\omega \omega_B \tau_{eff}^2) R_{res} v^2 \sin^2\theta \, \frac{\partial F}{\partial \chi} (\hat{v}/v + \xi \hat{\theta}) \tag{59}$$

where $(\omega\omega_B\tau_{eff}^2) \sim (\omega Re\{\overline{\Omega}_n^{-1}\})$ contains the details of the wave-particle interaction. The gradient of the distribution at the loss cone is approximately

$$v^2 \sin^2\theta \frac{\partial F}{\partial \chi} \approx \sin\theta_l \cos\theta_l \frac{\partial F}{\partial \theta} \tag{60}$$

---

[3] In fact, one of the important unanswered questions of negative potential operation is the microstability of the hot electrons. An example of hot-electron instability is described in Mauel, 1979, and similiar instabilities have been seen in Constance 2.

and, from Equation 47, $(\omega\omega_B\tau_{eff}^2) \approx (2/\sqrt{R_{res}})(v_\perp/v_\parallel)_{res}\,(1/L_B\nabla \ln B)$, assuming $N_\parallel = 0$. This is independent of velocity since the pitch-angle is constant over the loss-boundary. Using the parabolic magnetic profile $B(s) = B_0(1+(s/L_B)^2)$ and the indentity $(v_\perp/v_\parallel)_s = 1/\sqrt{R_s - 1}$, the interaction strength can be written in the simple form $(\omega\omega_B\tau_{eff}^2) \approx \sqrt{R_{res}}/[(R_{res}-1)(R_m/R_{res}-1)]^{1/2} \approx 1/\sqrt{R_{res}-1}$, where $R_m = 2$ is the mirror ratio. Note that as $R_{res} \to 1$, $\nu_n' \to 0$ since the particles are interacting with the wave at the midplane. (See comment at the end of Section 4.2.) In this case, Equation 48 must be used in place of Equation 47, and the maximum value of $(\omega\omega_B\tau_{eff}^2) \to \sqrt{2}\tan\theta_l(\omega/\omega_B)^{1/3} \sim 30$—proportional to $(\omega/\omega_B)^{1/3}$. Rewritting the integral, the RF component is

$$I_{RF,endloss}(E > E^*) = \left\{\int_{v^*}^{\infty} 2\pi dv v_{th}^2 \frac{\partial F}{\partial \theta}\right\} \frac{2\pi}{\tau_{rf}} (\omega\omega_B\tau_{eff}^2) \sin^2\theta_l \cos\theta_l \qquad (61)$$

To calculate the collisional endloss, an equivalent expression for the pitch-angle scattering of the warm electrons from the electons and ions is calculated. The collisional currents expressed in terms of the Rosenbluth potentials are used in the limit of $E^* > T_e$ (Appendix 2.) This means that the Rosenbluth potentials are assumed spherically symmetric and are expanded for the fast particles scattering off the denser bulk electrons and ions. In this limit,

$$\Gamma_{col} \approx \frac{v_{th}}{\tau_{col}} \left(\frac{v_{th}}{v}\right)^2 \frac{\partial F}{\partial \theta} \qquad (62)$$

where $\tau_{col} \approx 10^{-8} T_e^{3/2}/n[10^{12} cm^{-3}]$, including both the electron and ion contributions. Rewriting in a form similar to Equation 61, gives

$$I_{COL,endloss}(E > E^*) = \left\{\int_{v^*}^{\infty} 2\pi dv (v_{th}^3/v) \frac{\partial F}{\partial \theta}\right\} \frac{1}{\tau_{col}} \sin\theta_l \qquad (63)$$

showing the familiar $1/v$-dependance of pitch-angle scattering. The desired ratio is, therefore,

$$\frac{\text{RF-endloss}}{\text{COL-endloss}} \approx 2\pi \left(\frac{E^*}{T_e}\right)^{1/2} \frac{\tau_{col}}{\tau_{rf}} \sin\theta_l \cos\theta_l (\omega\omega_B\tau_{eff}^2) \qquad (64)$$

$$\approx 0.005(\omega\omega_B\tau_{eff}^2) \frac{|E[v/cm]|^2}{n[10^{12} cm^{-3}]} \qquad (65)$$

where, in Equation 65, $E^* = 100ev$. Note that the ratio is independent of T_e and proportional to $|E^r|^2/n_e$. The independance of T_e results from the fixed endloss analyzer energy and the assumption that $E^* > T_e$. Choosing for example, $R_{res} = 1.03$, then $(\omega\omega_B\tau_{eff}^2) \sim 6$, and, for $|E| \gtrsim 6v/cm$ and $n = 10^{12} cm^{-3}$, the RF-induced endloss is larger than that resulting from pitch-angle scattering. By re-examining Equations 56 and 57, the heating rate—or absorbed power—is seen to scale as the volume integral of $(\omega\omega_B\tau_{eff}^2)|E|^2\partial F/\partial\chi$. In other words, $P_{abs} \sim$

$n\,|E^{r}|^2$ and, fixed absorbed power, the relative RF-diffusion goes as $\sim P_{rf}/n^2$. Furthermore, the volume integral dependence implies that, for equally absorbed power, the observed RF "pump-out" will depend upon the ratio of the power absorbed near the loss-boundary to the power absorbed throughout velocity-space. Therefore, caution must be used when interpreting the scaling of Equation 65 with R_{res} since for a given absorbed power, the RF-enhancement should *decrease* as the resonant zone moves toward the midplane. This is due to the corresponding reduction in $|E^{r}|^2$ and the increase in resonant volume in velocity-space.

It is interesting to compare the enhanced endlosses induced by electron cyclotron heating to those induced by Landau damping. Besides the possible use of other types of heating for potential modification in tandem mirror endplugs, the examination of Landau damping stems from the suspected parametric instabilities responsible for the non-resonant heating in Constance 2. One product of a possible instability is an electron plasma wave which would Landau-damp on the electrons. To provide a basis for the comparision, the ratio of the induced current to the absorbed power is compared. Using Equations 56 and 57, the result is

$$\frac{\text{ECRH-current/power}}{\text{LAND-current/power}} \approx \frac{\int_{\Sigma} dA \cos\theta_l \,(\omega\omega_B\tau_{eff}^2)_{EC} \left.\frac{\partial F}{\partial\theta}\right|_{EC}}{\int_{\Sigma} dA \sin\theta_l \,(\omega\omega_B\tau_{eff}^2)_{LA} \left.\frac{\partial F}{\partial\theta}\right|_{LA}} \times \frac{\int_V d^3v \sin^2\theta \,(\omega\omega_B\tau_{eff}^2)_{LA} \left.\frac{\partial F}{\partial v_{\|}}\right|_{LA}}{\int_V d^3v \cos^2\theta \,(\omega\omega_B\tau_{eff}^2)_{EC} \left.\frac{\partial F}{\partial v_{\perp}}\right|_{EC}} \tag{66}$$

Note that even when $\tau_{cor} < \tau_{eff}$, Equation 66 is correct since the factors τ_{cor}/τ_{eff}, occuring equally in the volume and surface integrals, cancel.

The key observation from the preceding equation is that *in both cases* the amount of "pump-out" per absorbed power is equal to the fraction of power absorbed near the loss-boundary. Except for the geometry factors represented by the $\sin\theta$ and $\cos\theta$ terms, no fundamental difference exists between the currents induced from either cyclotron or Landau damping. However, two (more subtle, but very important) differences do exist. First, the resonance-condition which determines which particles absorb the power is (by definition) very different. For instance, the damping of an electron-plasma wave on the tail of the distribution ($T_{tail} \sim 100ev > q\Phi$, defined from the parallel phase velocity) deposits much more of the absorbed power near the loss boundary than either slower plasma waves or cyclotron heating. Second, the steady-state gradients of the velocity-space distribution will be different since cyclotron heating "smooths" the gradients in the $v_{\perp}$-direction and Landau heating "smooths" the parallel gradients.

4.3. Fokker-Planck Results

The Fokker-Planck simulation computes the solution of the time-dependent, two-dimensional partial differential equation which describes the evolution of the electron velocity-space distribution. Essentially, a rate equation for each point in velocity-space is solved numerically—the rate of change of density depending upon the both the inputs to the computer program and the neighboring velocity-space points. Except for the modification of the plasma potential and the ion loss rate, and the square-well approximation used to calculate collisions, the simulation includes all of the known effects which influence the electron energy and pitch-angle distribution. For each effect, the code has one or more inputs which can be effectively "turned-on" or "turned-off". In Figure 40, a table is provided which lists all of these terms and their controlling inputs.

Once the solution of the velocity distribution (*i.e.* $F(v,\theta,t)$) is known as a function of time, the average energy, endloss and energy distributions, and the target x-ray signals can be computed. The target x-rays are calculated according to Equation 14 with the assumption that the target does not influenece the distribution. The endloss distribution is calculated from the product of the loss-cone density and the transit-rate of these particles out of a parabolic well. Usually added to the calculated current is the current of the plasma at the mirror peak (an input to the program), which also contributes to the measured current at the analyzer.

The most serious limitation of the simulation is the fixed plasma potential. The main reason for holding the plasma potential constant was to avoid the re-calculation of the diffusion coefficient at every time step. If the potential changed, each particle's orbit at resonance would have to be re-evaluated. Fortunately, from experimental analysis (Section 2.4), the potential does not (appear to) significantly rise with temperature due to the large passing density. However, as a consequence of the assumed fixed potential, the code cannot satisfy electron-ion particle balance. Instead, a "hidden source" or "sink" is added which equates the two loss rates. This means that if the "normal" loss-rate of the electrons exceeds the trapping rate (by an amount greater than the assumed, ion loss-rate—an input to the program), then a "hidden source" is added to the distribution by simply multiplying the distribution by a constant to equate the ion and electron densities. In reality, the potential should rise, decreasing the electron loss rate. On the other hand, when the loss-rate is *less* than the trapping rate (which happens for instance at high RF fields), then the distribution is reduced (*i.e.* a "sink") to equate the ion and electron loss-rates. In this case, a "real" plasma would decrease its potential, throttling the influx of external electrons and increasing the trapped-electron loss-rate. Usually, the initial potential was adjusted so that the net loss-rate was comparable to the ion-loss rate, and the "hidden source/sink" was small. Another limitation is the grid-spacing. A unequally-spaced mesh, 45-points in the v-direction and 16-points in the θ-direction, Summary of Inputs to Fokker-Planck Simulation

Electron-Electron Collisions:	Fully non-linear collisional diffusion
T_{e0}	Initial electron temperature
n_{i0}	Initial ion density
Ion-Ion Collisions:	Scattering and Drag from Maxwellian Ions
T_i	Ion temperature
n_{i0}	Initial ion density
Quasilinear Diffusion:	Transit-averaged, as Section 4.1
n	Harmonic number, 1, 2, or both
E_r	Right-handed field at resonance (each n)
$N_\parallel, N_\perp$	Index of refraction
B_0, L_B	Midplane magnetic field and axial scale
$L_{decay}, T_{e,decay}$	Parameters defining wave decay near res.
ω	The RF frequency (rad/sec)
Φ	Plasma potential (fixed)
T_{on}, T_{off}	The start and stop times for ECRH
Ionization:	Particle and energy loss due to ionization
P_H	Pressure of H atoms
Transit-Time Loss:	Loss-rate of particles in loss cone
Φ	Plasma potential, positive or negative
L_B	Magnetic scale length
Transit-Time Source:	Influx of cool electrons from mirror-peak
Φ	Plasma potential, positive or negative
L_B	Magnetic scale length
$T_{e,ext}$	Temperature of external density
n_{ext}/n_0	Density at mirror-peak to midplane density
"Hidden" Source/Sink:	Fix for unequal ion/electron loss rates

Figure 40. A summary of all of the terms included in the Fokker-Planck simulation. For each effect, the controlling inputs are listed and described.

was used which gave good numerical stability for average temperatures greater than 20ev and less than 1.5kev.[4] Further details of the mechanics of the simulation and the collision operators can be found in Appendix 2.

Before discussing the Fokker-Plank results, it's helpful to first write the dominant terms of the equation symbolically and in dimensionaless form as

$$\begin{aligned}\frac{\partial F}{\partial t} = & -\frac{1}{\tau_{rf}}\nabla\cdot\Gamma_{rf} - \frac{1}{\tau_{col}}\nabla\cdot\Gamma_{col} \\ & + \frac{1}{\tau_{transit}}[(n_{ext}/n)(T_e/T_{ext})^{3/2} - (n_{loss}/n)(T_e/T_{loss})^{3/2}]\end{aligned} \qquad (67)$$

where, in the above, the ionization term has been left out since it is small. It is clear that the solution to the equation depends upon three rates, $1/\tau_{rf}$, $1/\tau_{col}$, and $1/\tau_{transit}$. The ratio $\tau_{col}/\tau_{rf} \approx 3 \times 10^{-4}|E[v/cm]|^2 T^{1/2}/n[10^{12}cm^{-3}]$ will determine the shape of the distribution far from the loss boundary. The density within the loss-region will depend upon a combination of all three rates. For steady-state, the loss and passing rates are equal, $(\partial F/\partial t) = 0$, and the final distribution is determined by the relative geometry of the collisional and RF currents (*i.e.* the resonant zone location) and τ_{col}/τ_{rf} (Stallard, *et al.*, 1981). For times so short that steady state is not reached, the development of the energy distribution will be determined by the RF-diffusion rate, $1/\tau_{rf}$, and will be roughly independent of density.

Samples of the code's output are shown in Figures 41 and 42. The initial density was $0.5 \times 10^{12} cm^{-3}$, the potential was $30v$, the initial electron temperature and the passing electron temperature were both $20ev$, and the passing density ratio at the mirror-peak was 0.8. The ECRH parameters were specified by $E = 5v/cm$, $N_{\|} = 2.0$, and $R_{res} = 1.04$. In Figure 41, the distribution function at eight times during the build-up and decay of the electron energy is plotted in $(v_{\perp}, v_{\|})$-space. Initially, the distribution is set to be a Maxwellian. As the ECRH is turned on $(t = 2\mu sec)$, the electrons diffuse to higher energies. A small (~0.1%) population of "sloshing" electrons forms at the turning point resonances. The warm electrons are more uniformly distributed throughout the trapped region of velocity-space. After the ECRH is turned off $(t = 12\mu sec)$, the plasma cools and the distribution becomes more uniform in pitch-angle. Figure 42 shows the corresponding electron energy and endloss distributions and the time development of the average energy, warm endloss and target x-ray signals. In addition, the warm-electron endloss current $(E^* > 100ev)$ shows an increasing signal proportional to the warm electron density and then, as the RF is turned-off, the rapid reduction of the endloss characteristic of the end of RF-induced "pump-out". Notice that for this example, the maximum average energy was 120ev, and was made up of a ~30ev "bulk" population (electrostatically

---

[4] The grid spacing was doubled and halved for a typical run, and the evolution of the energy distibution did not change.

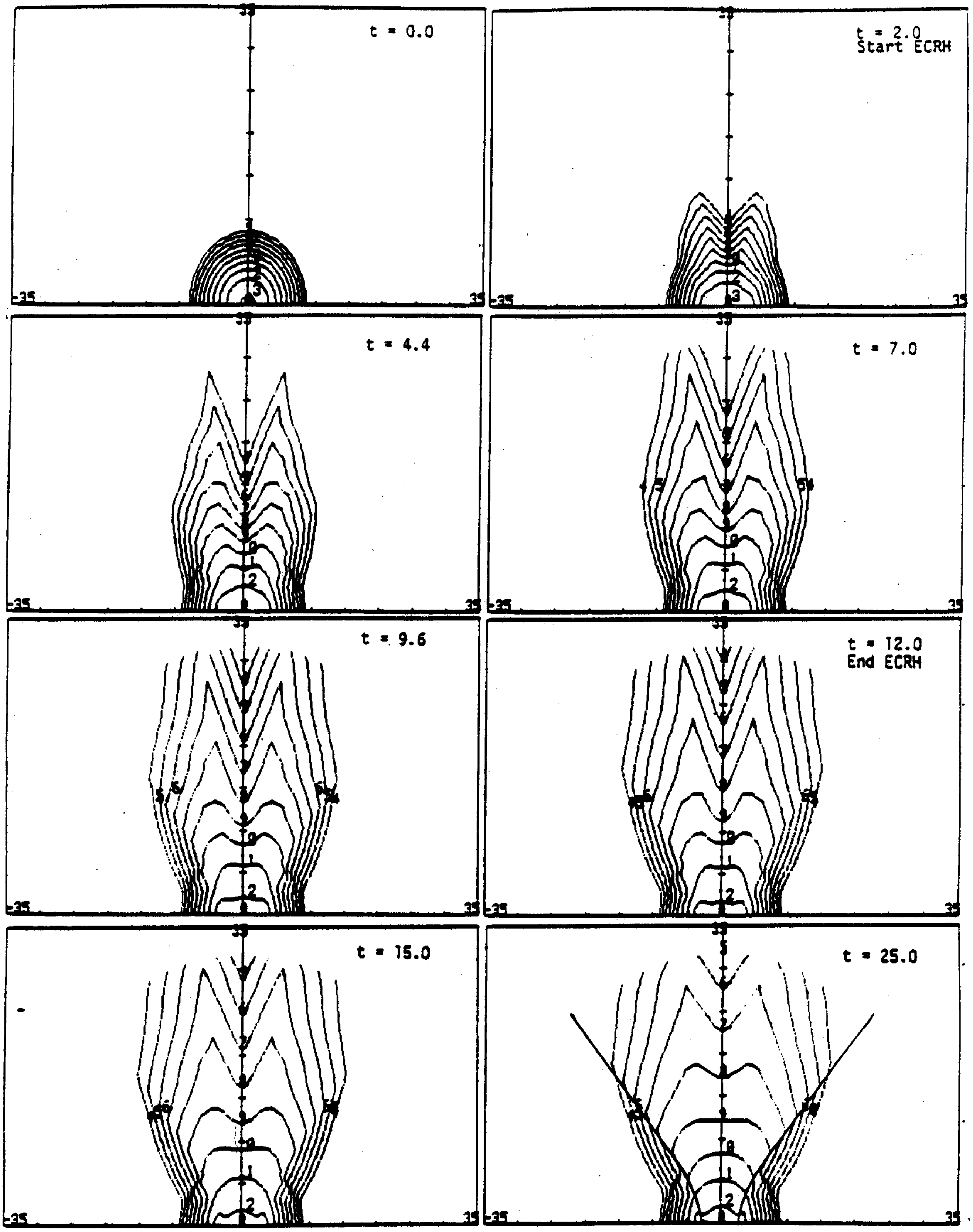

Figure 41. A sample of the code's output showing the development of the velocity distribution function. Each contour represents one order of magnitude. The time (in μsec) for each frame is shown in the upper right-hand corner.

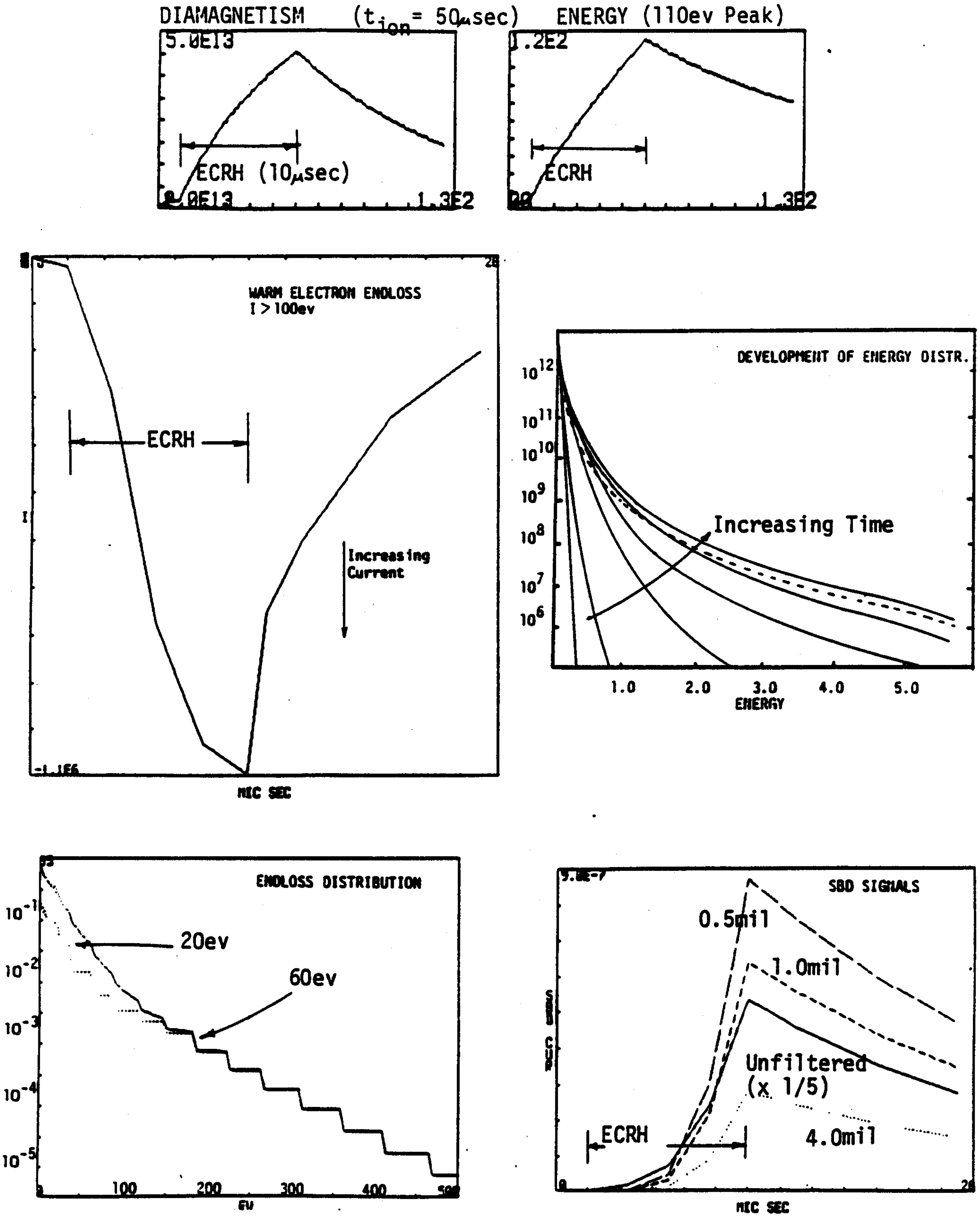

Figure 42. The overall energy, diamagnetism, warm electron endloss, energy distribution, endloss distribution, and target x-ray signals for the example shown in Figure 41.

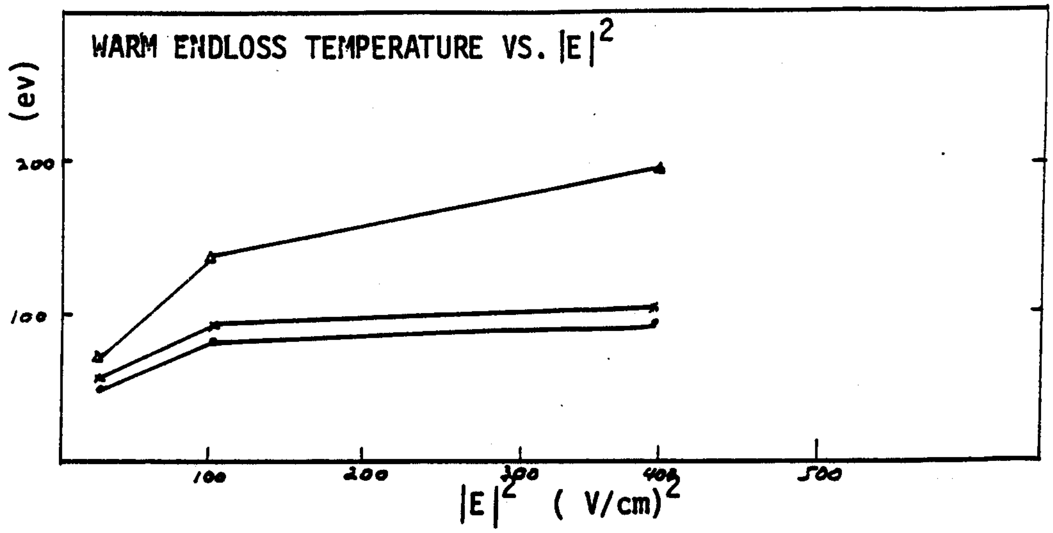

Figure 44. The change of the warm electron temperature as calculated from the endloss analyzer as the electric field strength and density is varied. These results correspond to those in Figure 43.

confined with a temperature partly constrained by the passing particles), a 100-200ev "warm" population (contributing most to the observed energy rise), and a small ($< 1\%$) population of "hot", 1kev electrons. The endloss (which must include the passing electrons) is made up of the "bulk" ($T \sim 20ev$) and "warm" ($T \sim 70ev$) components. The calculated x-ray signals largely represent the "hot" tail. The ratio of the unfiltered to 0.5mil-filtered signals gives $T_{hot} \sim 800ev$, and the ratio of the 0.5mil-filtered to the 4mil-filtered signals gives $T_{hot} \sim 1.1kev$. Notice that the example behaves qualitatively like the examples discussed in Section 2.4. ***This qualitative equivalence between the "three parts" of the measured and simulated distribution is a major result of this thesis.***

To examine further the predictions of the Fokker-Planck simulation, the electric field strength and density were varied, keeping the other parameters constant. The results are presented in Figures 43 and 44. At the top of Figure 43, the average energy of the distribution is plotted for $n_e = 0.2, 0.5$, and $1.0 \times 10^{12} cm^{-3}$ as the electric field strength is changed to $E^r = 5$, 10 and $20V/cm$. The energy increases for both increasing RF-power (*i.e.* $P_{rf} \sim |E^r|^2$) and for decreasing density. The middle graph shows the changing hot electron density, and the bottom graph the increasing hot electron temperature. It is interesting that the average energy

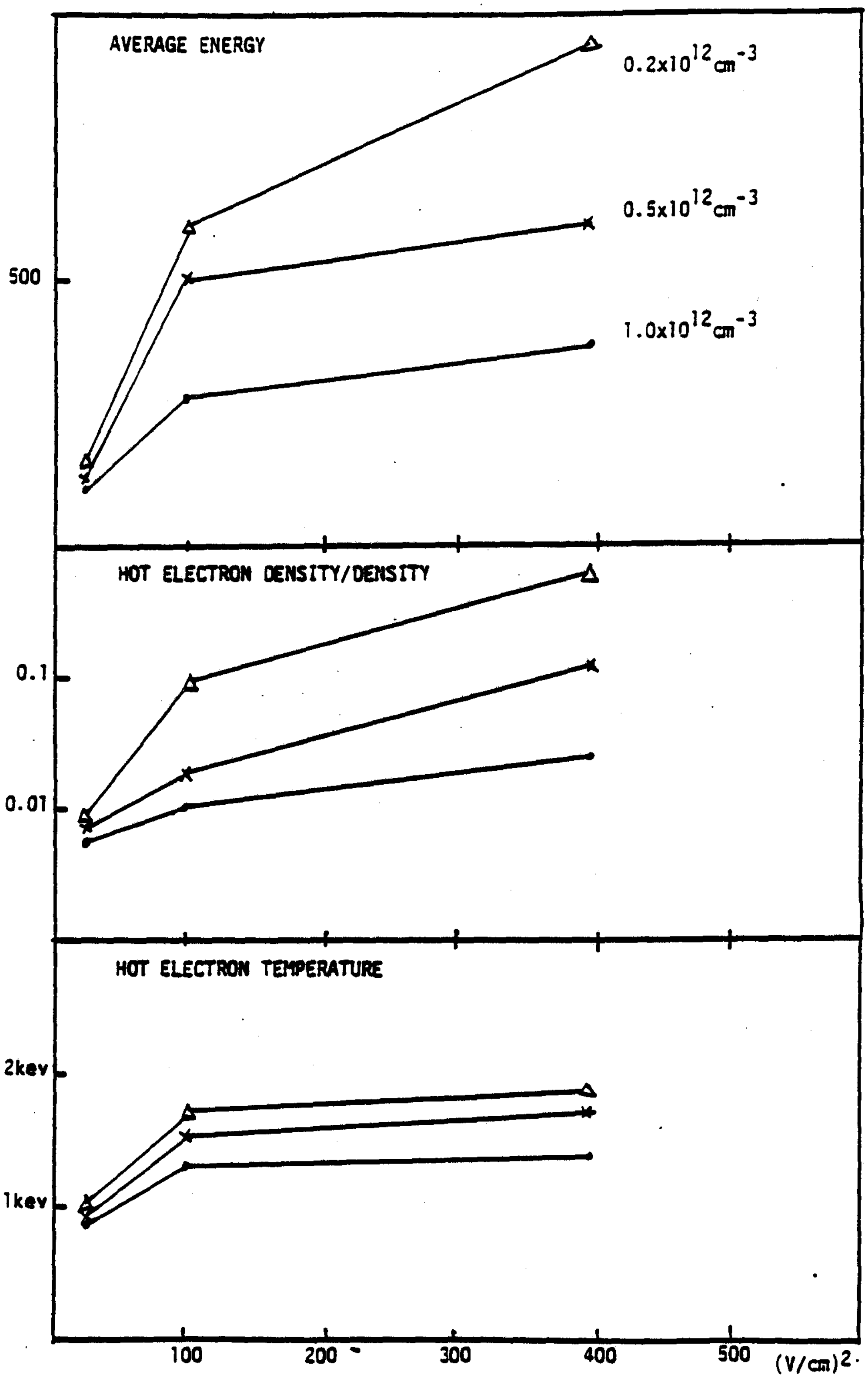

Figure 43. A summary of the average energy, hot-electron fraction, and hot-electron temperature as the electric-field strength and density are varied.

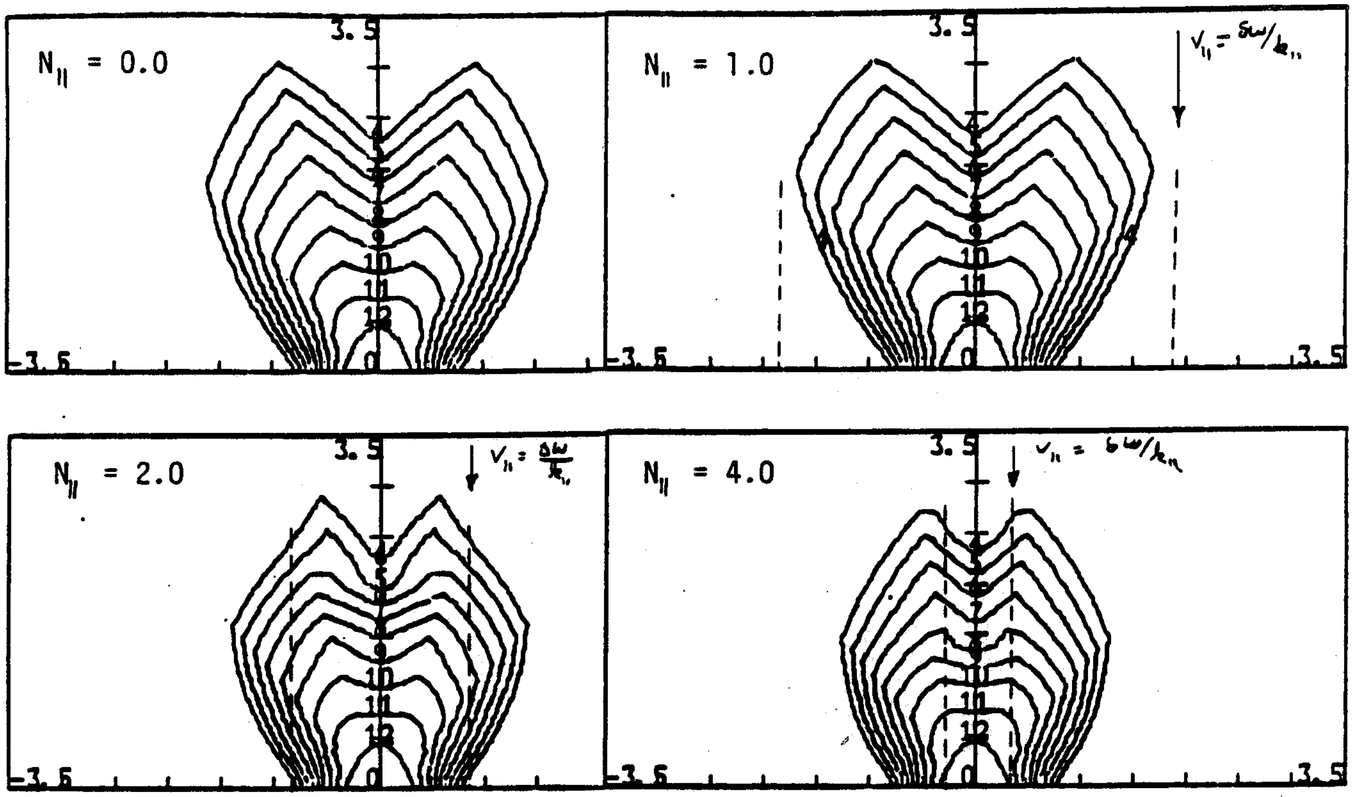

Figure 45. Four velocity-space distributions for $R_{res} = 1.06$ and $N_{\|} = 0, 1, 2$, and 4. Notice that as $N_{\|}$ increases the tail of the distribution begins to accumulate before the turning-point resonance. Also shown in the diagrams are (dotted) lines which indicate those particles which resonate at the midplane, $v_{\|,0} = \delta\omega_{c0}/k_{\|}$, where $\delta\omega_{c0} = (\omega - \omega_{c0})$.

increases more rapidly at low powers than at higher powers. This can be explained, in part, by the increased loss rate of the electrons which (for the fixed potential) are no longer potentially confined. The increase of the warm component of the endloss can be observed in Figure 44. However, another factor is the enhanced trapping of the passing electrons which was monitored by the reduction of the bulk endloss for constant influx of the external electrons. It is also interesting, that for fields $\gtrsim 10V/cm$, the energy reaches saturation and it is this saturation level which differs with density. When $E^{r} \lesssim 5V/cm$, saturation is not reached within the $10\mu sec$ heating time, and the average energy is approximately *independent* of density. This is expected when $1/\tau_{rf}$ dominates the other velocity-space rates in the simulation. Finally, over the range of energies reproduced by the simulation, the hot electron temperature does not increase beyond $\sim 2kev$. In fact, the *temperature* of the tail does not increase as much as the *density* of the hot electrons. This indicates that "fueling-rate" of the hot-tail from the warm electrons is larger than the corresponding heating rate of of the hot electrons.

The next variation that was examined was the effect of $N_{\|}$. Physically, changes in the index of refraction at resonance correspond to changes of the launch geometry

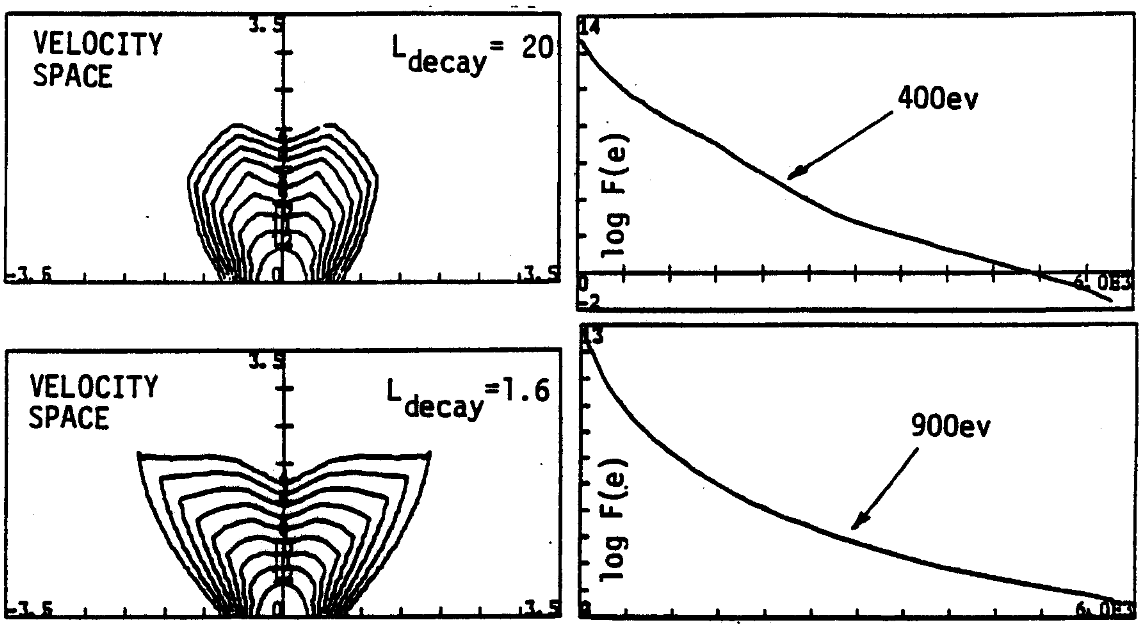

Figure 46. The velocity-space and energy distributions for $N_{\|} = 4$ with and without a spatially varying electric field. For both cases the average energy rise was equivalent (60ev), indicating equal transfer of power. The field decayed from the doppler shifted resonance of a $1kev$ electron (~6cm for $R_{res} = 1.06$) with a characteristic length of $L_{decay} = 1.6cm$.

and ray-path (Chapter 3). For the cases considered in the program, $R_{res} = 1.06$ and $N_{\|} = 0$, 1, 2, and 4. As $N_{\|}$ increased, the average energy ($\sim 100ev$) of the distribution was approximately constant (decreasing by only 5%) while the hot electron density ($n_{hot}/n \sim 0.5\%$) decreased by a factor of two. The most interesting effect was observed in the plots of the velocity-space distributions which are shown in Figure 45. Notice that as $N_{\|}$ increases the tail of the distribution begins to accumulate *before* the turning-point resonance. This is due to the decrease in τ_{eff} for those electrons turning at or after resonance and an increase of τ_{eff} for those which can now resonate with the wave with $\omega_c < \omega$.

However, as discussed in Chapter 3, increasing $N_{\|}$ leads to stronger absorption. In these cases, the field is expected to decay rapidly as the wave propagates from the high-field side of resonance. The effect of this will be to preferentially heat those electrons with resonances Doppler shifted in the direction of the incoming waves (*i.e.* $\omega_c > \omega$). To examine what happens in this case, the diffusion coefficient was weighted by the factor $\exp(-\delta s_{res}/L_{decay})$ where δs_{res} was calculated for each point in velocity-space and is equal to the distance from the Doppler shifted resonance of a 1kev electron (~6cm for $R_{res} = 1.06$) to the position of each of the resonances of the velocity-space point in question and $L_{decay} = 1.6cm$, the characteristic length of the (spatial) decay of the RF-intensity. With this factor, the quasilinear diffusion coefficient (in velocity-space) incorporates the *spatial* variation of the electric field due to the strong damping expected for high $N_{\|}$. Figure 46 gives the velocity-space and energy distributions for $N_{\|} = 4$ with and without a spatially varying electric field. For both cases the average energy rise was equivalent (60ev), indicating equal transfer of power; however, the hot electron temperature increased from 400ev to 900ev. This indicates that strong absorption may indeed enhance the hot tail temperature.

A final use of the simulation was in the estimation of the enhancement of the warm electron endloss due to ECRH diffusion. From Equation 65, the enhancement was predicted to scale as $|E^r|^2/n$. To check this, the density was changed for fixed RF-field and the RF-field was changed for fixed density. First, the density was changed with $E^r = 5V/cm$ and $R_{res} = 1.04$. This gave an energy rise of ~110ev. The warm endloss current at the end of the ECRH, I_{ecrh} was compared to that computed 1μsec later, I_{after}. This defines the enhancement factor, $(I_{ecrh} - I_{after})/I_{after}$—which is equivalent to the factor calculated in Section 4.2. An sample of the computer output, shown at the top of Figure 47, illustrates this factor. The results of the simulation (bottom of Figure 47) resemble the predicted $1/n$ scaling, although at low densities the enhancement "appears" higher due to the "normal" collisional decay of the warm electrons. Also shown in Figure 47 is the prediction of Equation 65 which is larger than calculated in the simulation by about a factor of 2. For the second step, the electric field strength was increased, for fixed $n = 0.5 \times 10^{12} cm^{-3}$. Figure 48 illustrates this scaling with RF-field. Here, the result differs slightly from the expected straight-line probably due to the relaxation of the pitch-angle distribution when the RF is turned off.

The simulation's prediction of the effect of changing magnetic field on the "pump-out" was also computed. Figure 49 shows both the changing velocity-space distribution and the ratio of the warm-electron endloss just before and just after the end of the ECRH. Most noticeable is the change of the pitch-angle distribution of the hot-electron tail due to the change of the resonance-zone location. Also calculated was the *reduction* of the RF-enhancement at higher magnetic fields. As mentioned in the analysis of Section 4.2, this can be understood in part by the fact that for equal absorbed powers, the endloss enhancement will be proportional to the fraction of the power absorbed near the loss-cone. As B increases, this fraction decreases. In addition, as the ECRH is turned-off, the pitch-angle distribution relaxes—reducing the density near the loss-cone when R_{res} is large and increasing the this density when the heating occurs near the midplane.

Finally, the electron parameters which have been characterized by the

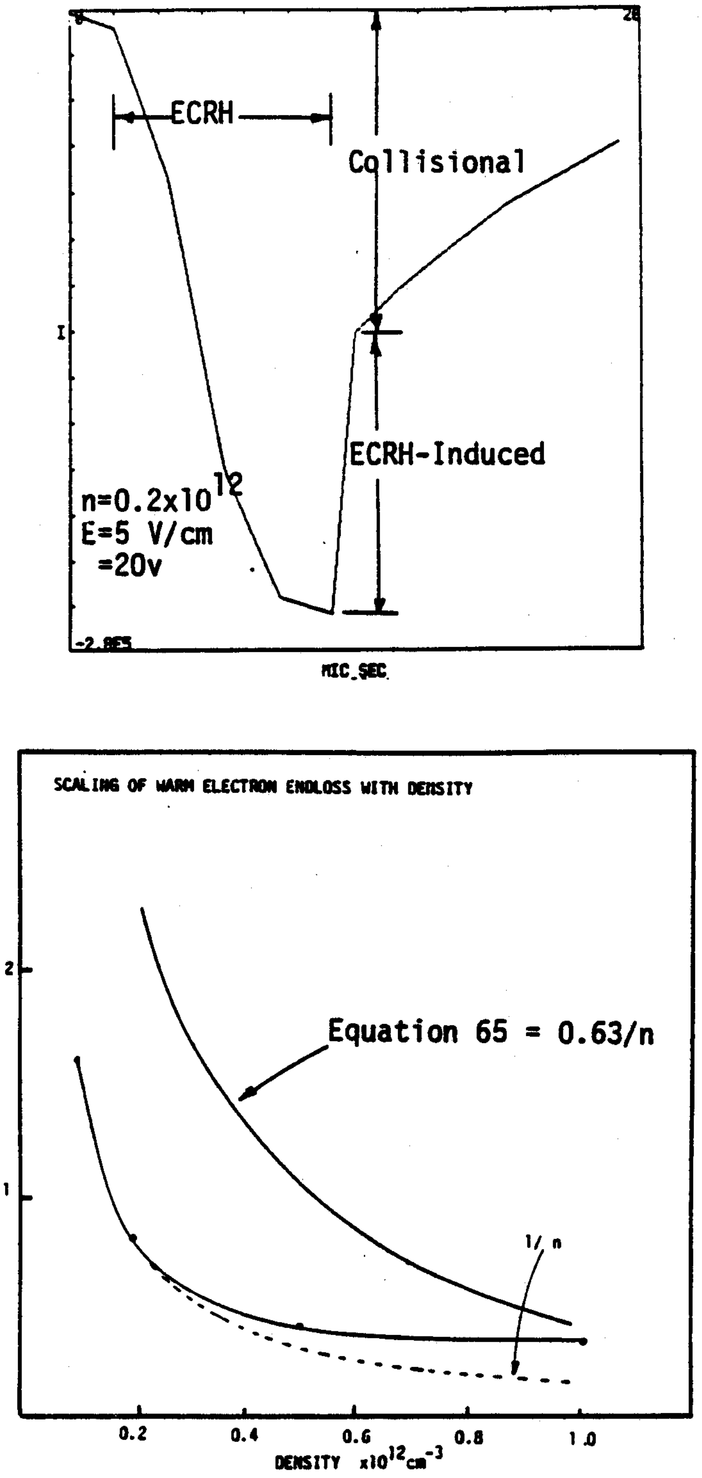

Figure 47. Top: A sample of the warm endloss signal as computed by the simulation. The ratio of the difference of the currents at the end of the ECRH pulse, I_{ecrh}, and 1μsec later, I_{after} to the current after gives the enhancement factor, $(I_{ecrh} - I_{after})/I_{after}$. Bottom: The scaling of the RF enhancement with density computed from the Fokker-Planck simulation with fixed $E^r = 5V/cm$ and $R_{res} = 1.04$. Also shown is the analytic prediction from Equation 65.

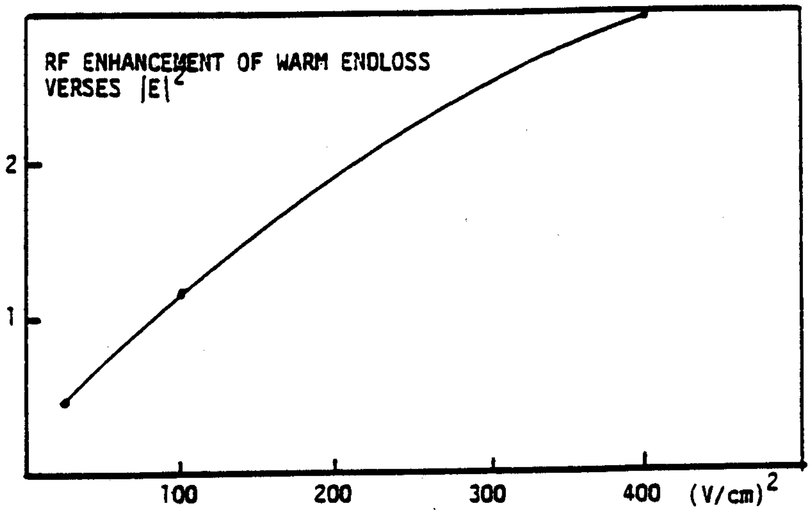

Figure 48. The variation of the RF-enhancement with RF-power (*i.e.* $|E^r|^2$) for fixed $n = 0.5 \times 10^{12} cm^{-3}$.

ECRH Fokker-Planck Parameters

Densities examined	0.2 to $1.0 \times 10^{12} cm^{-3}$
Average energies	$40ev$ to $1kev$
Bulk temperature	$\sim 20 - 40ev$
Warm temperature	$\sim 60 - 200ev$
Hot electron temperature	~ 0.7 to $2kev$
Warm endloss enhancement	scales as $\lvert E^r\rvert^2/n \sim P_{rf}/n^2$
Scaling of hot electrons with P_{rf}	Density rises faster than Temp.

Figure 50. A summary of the electron parameters computed with the Fokker-Planck simulation.

computations summarized in this chapter are tabulated in Figure 50.

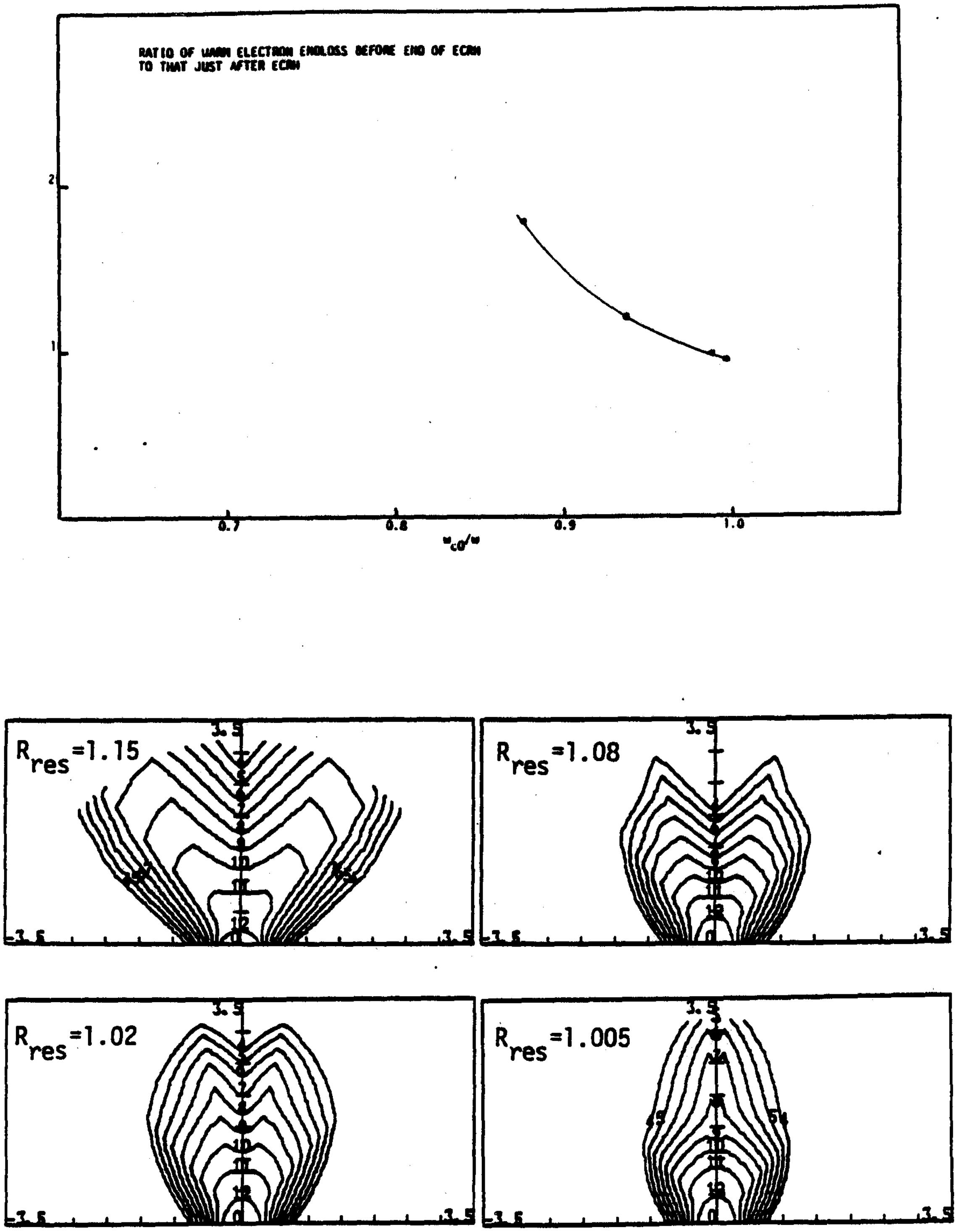

Figure 49. Top: Variation of warm electron "pump-out" versus midplane magnetic field. Bottom: Variation of the velocity-space distribution verse midplane field.

Chapter 5

X-Ray and Endloss Measurements

In this chapter, sample target x-ray measurements of the hot-electrons and measurements of the time histories of the warm electron endloss are presented. Within the limits of target x-ray analysis, the x-ray measurements indicate a slightly hotter tail temperature than that predicted by the simulation; however, measurements of the scaling of the density and temperature with RF power are similar to that found in Chapter 4. The time-histories of the endloss illustrate RF-enhancement and behave qualitatively according to the predictions of the simulation and the analytic model given in Chapter 4. However, it is not known whether or not the measured enhancement is due to ECRH diffusion, to parallel Landau damping (from parametrically excited waves), or to a combination of both types of heating.

5.1. Target X-ray Measurements of the Hot Electron Tail

Figure 50 gives a typical example of the target x-ray signals. The average energy increased by 60-100ev and the density was approximately $0.5 \times 10^{12} cm^{-3}$. The bottom four traces show the build-up and decay of the hot electrons. The ratio of the signals indicate the effective hot-electron temperature. The ratio of the signals from the unfiltered to the 0.5mil filtered detector gives 500ev, while the remaining detectors measure nearly the same current and can only be used to indicate a lower bound on the temperature of ~2kev. (As explained in Section 2.2, the uncertainty in the calibration of the relative solid angles determines the highest discernible temperature.) Notice that the presence of these hot electrons was expected from the Fokker-Planck simulation; however, the measured temperature appears hotter by at least a factor of 2 than that calculated in the previous chapter.

To obtain a better estimate of the temperature of the tail, three Be filters, 5mil, 10mil, and 15mil were used with the plastic scintillator. The filters look roughly at energies above 6.5, 6.7 and 6.9kev respectively, and their close-spacing limits their usefulness to hot electron temperatures below ~6kev. When these experiments were

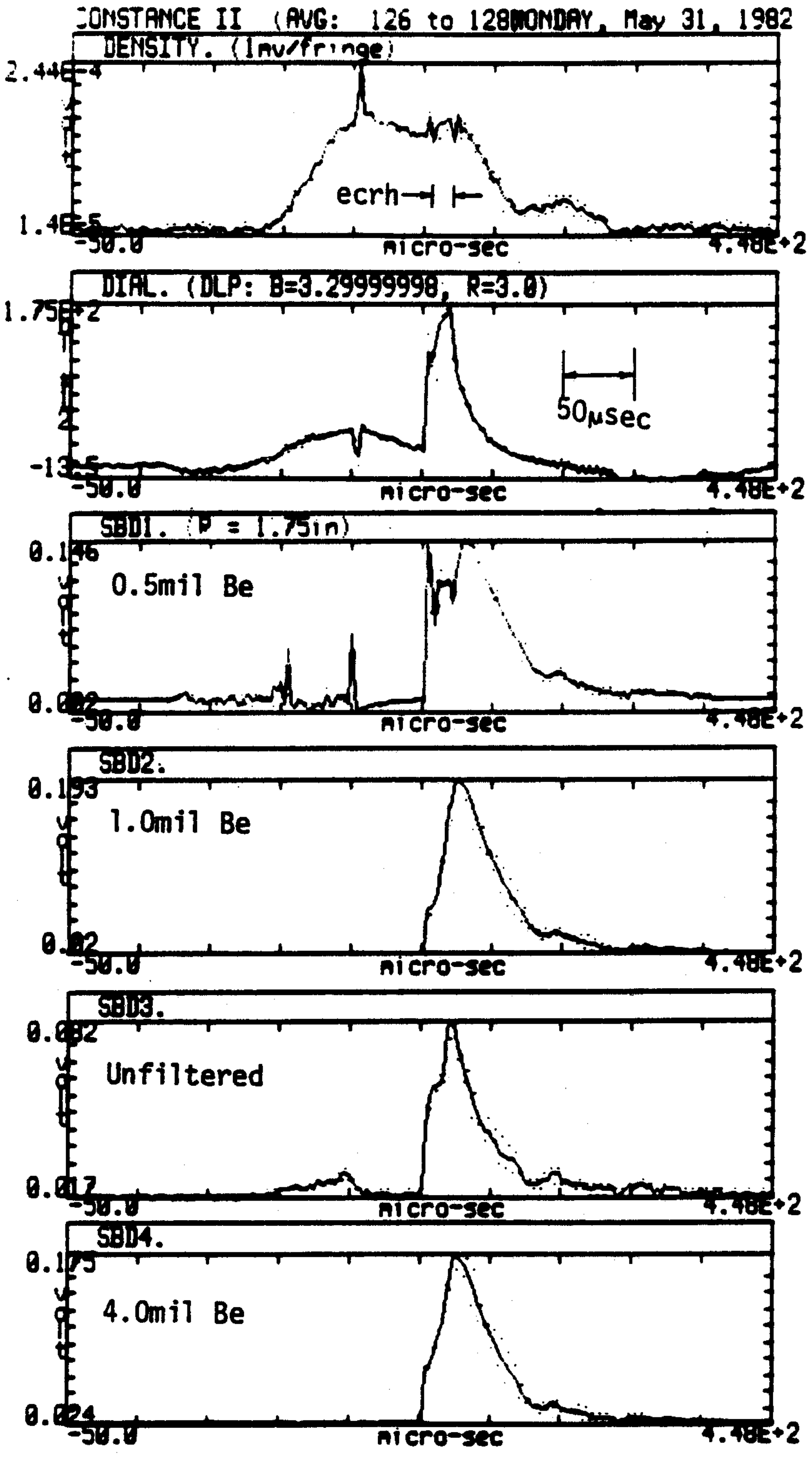

Figure 50. Example of the target x-ray signals. The ratio of the unfiltered to the 0.5mil filtered detector gives an effective temperature of 500ev. The ratios of the remaining filtered detectors are so close to 1 that they can only indicate a lower bound on the temperature of 2kev.

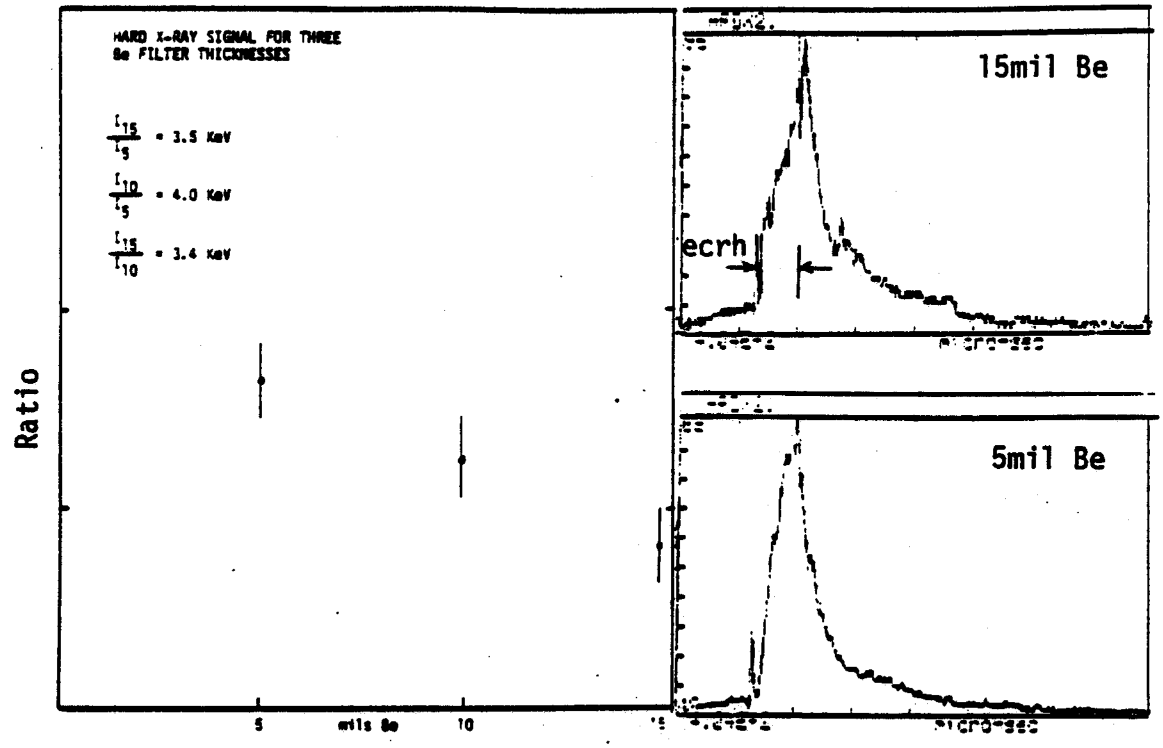

Figure 51. Examples of hard x-ray signals used to determine the hot electron temperature during a high-power ECRH pulse.

performed, the density was lower than in the previous example ($\sim 0.1 \times 10^{12} cm^{-3}$) and the average energy (measured with the diamagnetic loop and interferometer) was between 500ev and 800ev. The results are shown in Figure 51, and the ratio of the signals clearly indicate a hot-electron temperature of ~4.0kev.

Some parameterization of the surface-barrier detector signals was conducted and samples of these results are collected in Figure 52. The top graph shows the variation of the signals versus magnetic field, indicating that only when the resonance zone was located in the mirror were x-rays detected. The middle graph illustrates the variation of the signal with target radius. Since the ratios of the signals do not change significantly with radius while the intensities do change, the increasing signal toward the axis indicates rising hot electron density. The bottom figure shows the variation of the SBD signals with line density. Although at very low densities the x-ray intensity would increase, over the typical range of line-density, the measured signal was constant. This "constant" density scaling is unexplained and *not predicted* by the Fokker Planck simulation (Figure 43). However, the diamagnetism and warm endloss current also changed slowly (if at all) over this range of densities (see Figures 23 and 24 in Section 2.4).

One of the most revealing experiments was to observe the scaling of the hot electron temperature and density with increasing RF power. These experiments were made to compare this scaling with that predicted by Figure 43. As stated in Chapter 4, if the density increases faster than the temperature, hot electron "fueling" from the warm electrons instead of "heating" dominates the hot-tail formation. An example illustrating this is shown in Figure 53. The average density was $\lesssim 0.5 \times 10^{12} cm^{-3}$ and the average energy rose to $\sim 350 ev$ at peak power (25kWatt).[1] The data clearly indicate a weak (about a factor of 2 for the low energy ratio) increase in the hot electron temperature even though the power increased by a factor of 5. On the other hand, the intensity of the SBD signals indicates that the density of the hot electrons is more strongly effected by the increasing power.

Further investigation of the hot-electron formation was made by measuring the temperature and density of the hot electrons for longer heating times. An example of a $35 \mu sec$ heating time is shown in Figure 54, and the peak x-ray signals during ECRH and those $\sim 10 \mu sec$ after the RF-pulse measured for increasing heating times are shown in Figure 55. The average electron parameters were similar to those discussed in the previous paragraphs. For both cases, the hot electron signal increases during the first $\sim 10 \mu sec$ and then saturates.[2] Notice that the diamagnetism also equilibrates with the hot-electron intensity. This equilibration is not expected. As the hot electrons become more energetic, their losses are (normally) reduced, allowing them to increase their energy even if their fueling rate (from the warm electrons) was reduced. (This is called "hot-tail runaway".) However, as explained in Section 2.2.5, the losses due to the *target itself* actually *increase* with increasing electron energy due to the linear energy dependence of the magnetic drift speed. For this reason, it is unclear whether the measured saturation of the hot electron temperature occurs "naturally"—possibly due to a limitation of the fueling rate—or because of the presence of the target.

To summarize these x-ray measurements, the major result was *the observation that there is indeed a hot tail of electrons although with a temperature as much as a factor of 2 to 4 higher than that predicted by the simulation.* Also, (1) the density of the hot electrons appears to increase faster than their temperature as the RF

---

[1] The diamagnetism appears to scale roughly as $P_{rf}^{2/3}$—which is the expected scaling during saturation.

[2] The saturation of the x-ray signal with time was also observed with the simulation and occurred whenever the diamagnetism saturated.

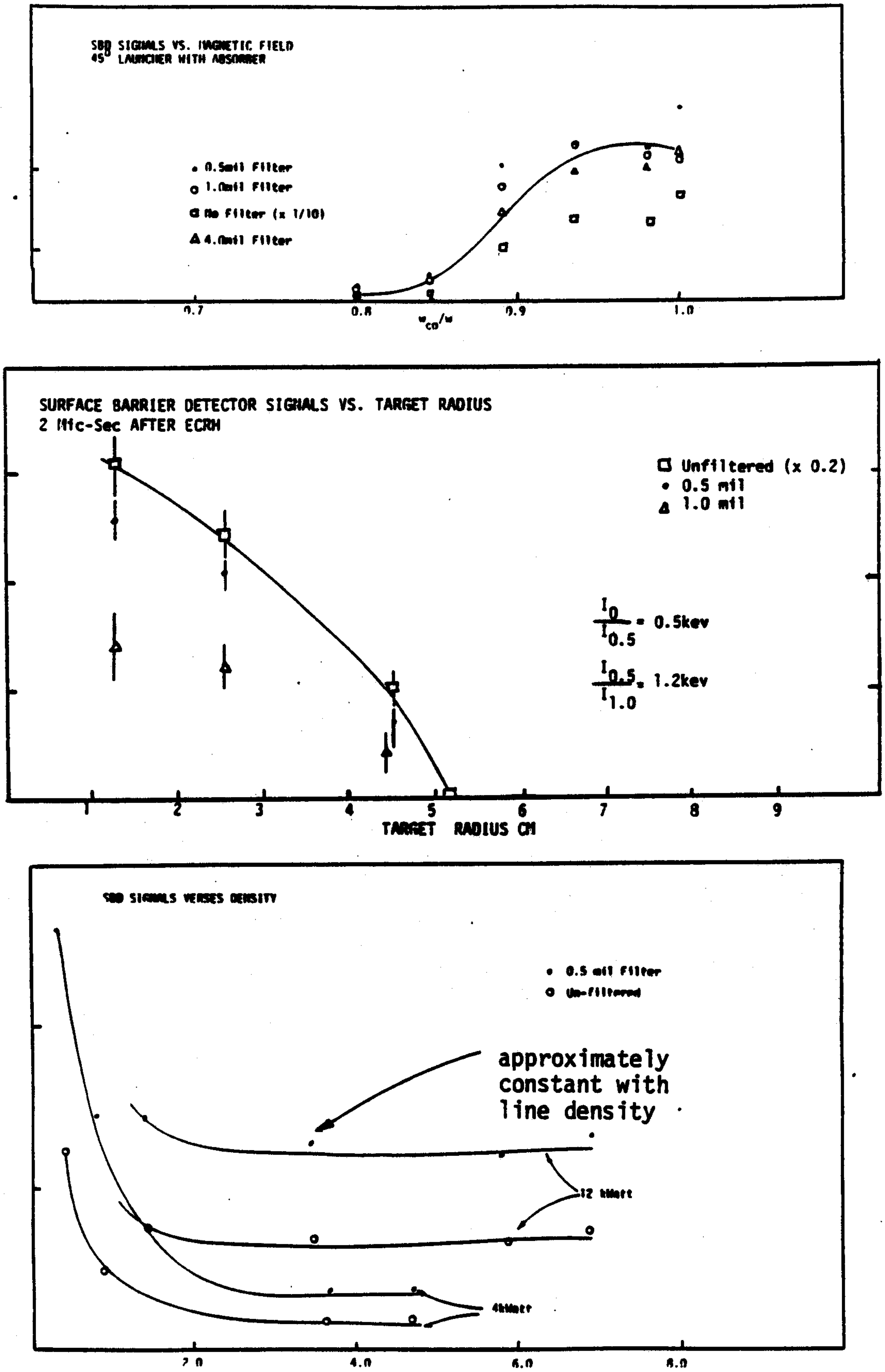

Figure 52. Some examples of the parameterization of the SBD x-ray signals as the magnetic field (top), target radius (middle), and line-density (bottom) were changed.

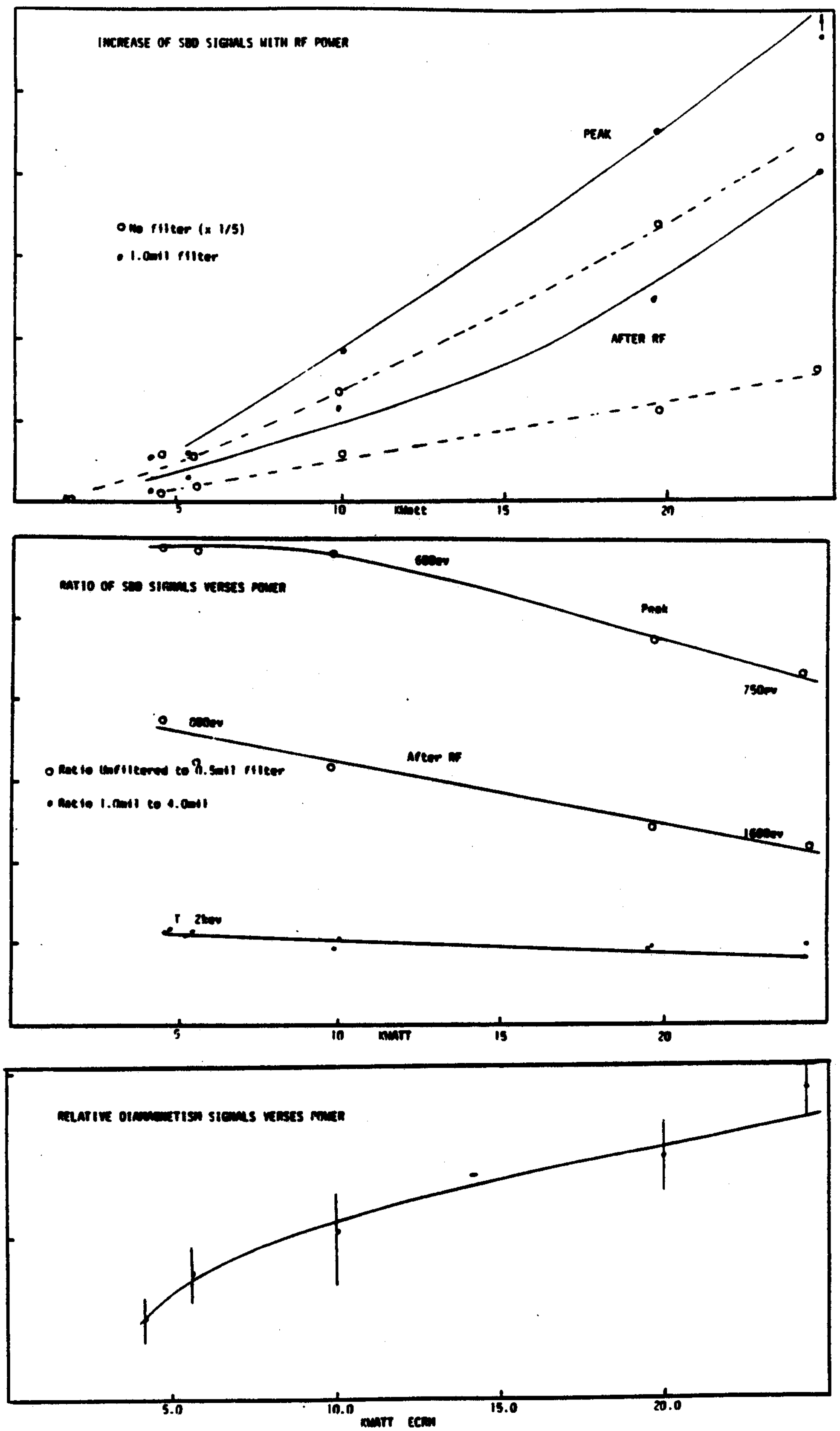

Figure 53. SBD intensity (top), ratio (middle), and diamagnetism (bottom) as the RF power is varied. The curves labeled "after" correspond to the intensity of the x-ray signal ~ $10\mu sec$ after the end of the RF-pulse.

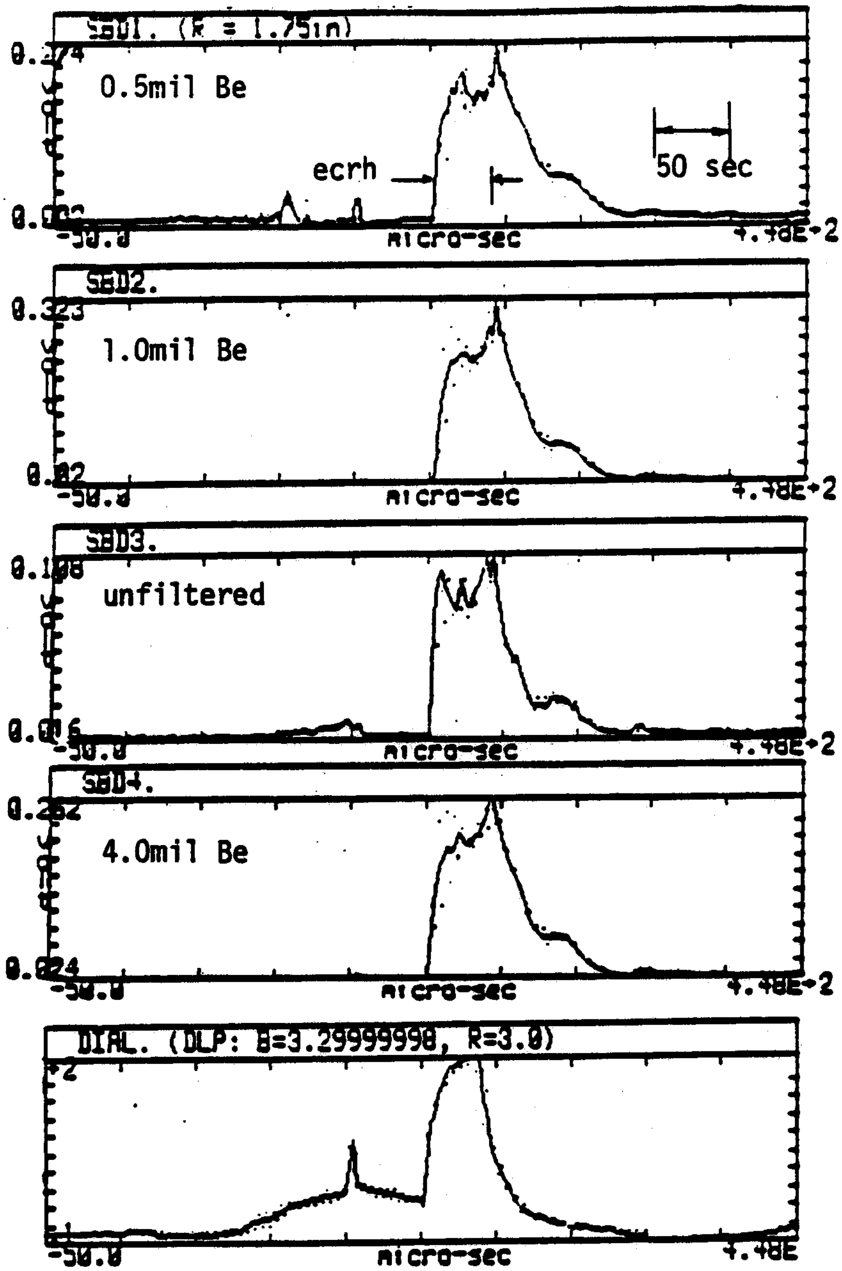

Figure 54. Example of the time-history of the SBD signals for a long, 35μsec, RF heating time. The bottom trace is the corresponding diamagnetism.

power increases, (2) only a weak density dependance on the hot electron density was observed, and (3) the hot-electron density and temperature appear to saturate for long RF heating times. Only the first of these was predicted by the simulation. The second contradicts the simulation's predictions. The third was not investigated. Whether or not this scaling would also be measured *without* the presence of a target is not known.

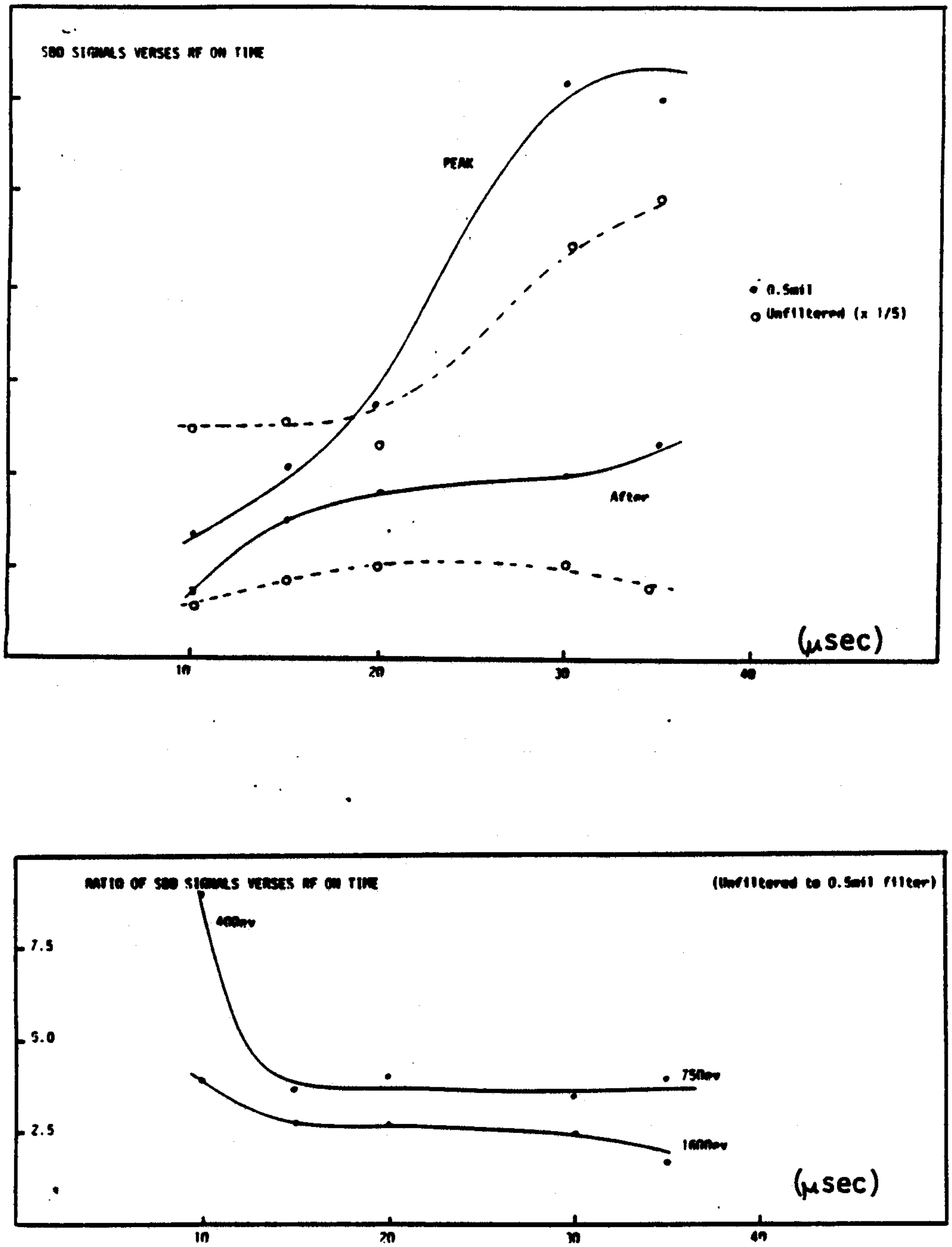

Figure 55. Example of the variation of the SBD intensity and ratio with RF heating time.

5.2. Endloss Measurements of RF-Induced "Pump-Out"

When the electron repeller grid is biased to examine warm electrons ($T_{warm} \gtrsim 100ev$), the endloss current is proportional to the warm electron density (near the loss-cone boundary) and the diffusion rate of these particles into the loss-cone. By measuring the decrease of the current immediately following the turn-off of

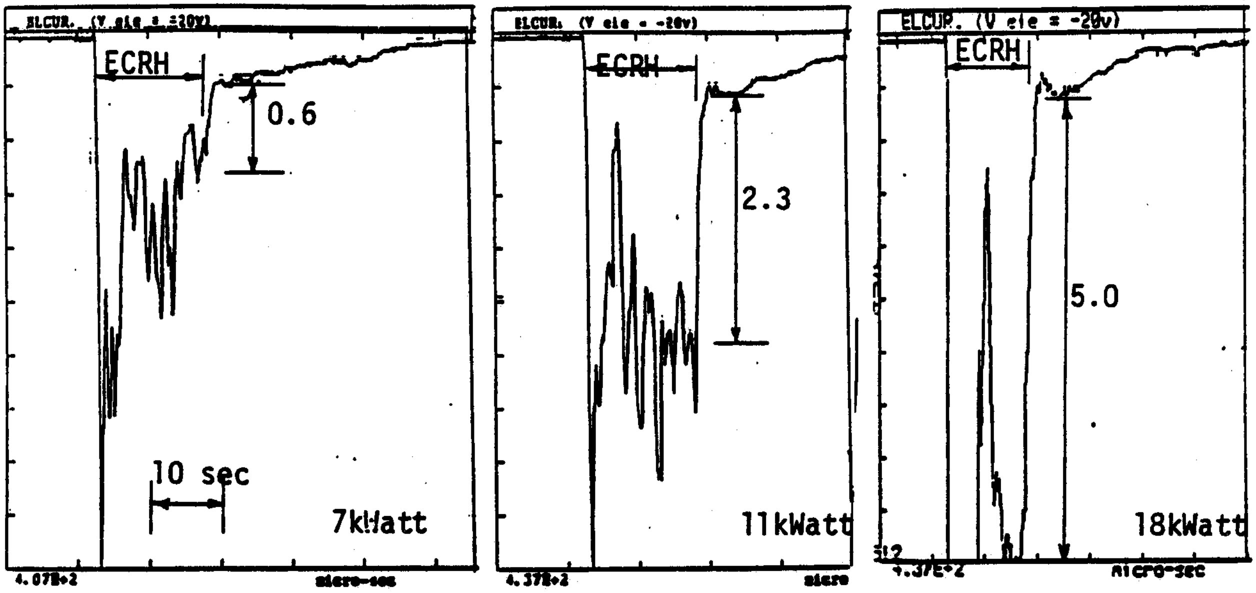

Figure 56. Examples of the enhancement of the electron endloss with increasing RF power. Notice the rapid decrease in the measured current as the ECRH is turned off.

the RF, that part of the total diffusion due to ECRH can be measured relative to the "ever-present" collisional diffusion (Section 4.2). This effect was observed and sample data are shown in Figure 56. In fact, the enhancement effect increased with RF power roughly as expected from Equation 65.

To verify that the observed increase in the warm electron loss rate was due to ECRH diffusion, two tests were performed. First, the midplane magnetic field was increased so that no cyclotron resonance existed in the mirror region. In this case, there cannot be any ECRH interaction. Nevertheless, substantial warm endloss current was monitored. This is illustrated in Figure 57. Since no rise in diamagnetism was observed during this experiment, the endloss signal must have been produced either from non-*cyclotron*-resonant, parallel heating or from cyclotron interaction at the resonance between the endloss analyzer and the mirror peak. This motivated the second test which consisted of lining the mirror chamber with the microwave absorbers and putting a stainless-steel screen at the mirror peak. The RF power in the end chamber was thus reduced by more than a factor of 10^3. It was observed that even under these conditions non-*cyclotron*-resonant heating occurred. The heating was characterized by increased endloss signals with undetectable rises of the diamagnetic loop and the x-ray detector. In fact, by measuring the ratio of the end-wall power for the non-resonant and resonant heating, the non-resonant heating efficiency was found to be roughly 1/4 to 1/3 that of the cyclotron heating—at the point sampled by the endloss analyzer.[3] Examples of the endloss distribution for non-resonant and resonant heating are shown in Figure 58.

A discussion of the relevant analysis of the parametric excitation of slower waves which would parallel heat (*i.e.* Landau damp) the electrons has been given in the review by Porkolab and Chen, 1978. For the Constance 2 geometry, a likely possibility is the decay of the right-handed (high $N_{||}$) high-frequency wave into an ion-acoustic and electron plasma wave. The threshold for this excitation is

$$\frac{|E^r|^2}{nT_e} > K\,\frac{\omega^2(\omega_c-\omega)^2}{\omega_p^4} \tag{67}$$

where K is a function of the energy density and damping rates of the decay modes. Two points are emphasized in the above equation. First, the threshold becomes very small near cyclotron resonance, and, second, it depends inversely on density. The higher the density, the *lower* the threshold. Another point made by Porkolab and Chen, 1978 is that these instabilities are convective. This implies that if the growth rate of the instability is not short compared to the scale-length of the inhomogeneities, then the three modes may de-tune before the slower waves (the decay modes) can grow to appreciable intensities.

For the Constance 2 experiment, the analysis of Porkolab and Chen implies two conclusions. First, for steep gradients of the magnetic field—when the resonance zones are at the side, the decay instabilities may be *less intense* due to the steeper gradients at the resonance zone. Secondly, as the density is lowered, the decay threshold increases, and the parametric-excited waves would again become *less intense*. Fortunately, this is *exactly the opposite* of the predicted scaling of the relative ECRH pump-out analyzed in Chapter 4. The relative enhancement should *increase* with deceasing density and *decrease* with increasing magnetic field.

While the screen and absorbers were installed in the vacuum chamber, the scaling of the enhancement with magnetic field and density was measured. Since the enhancement was observed to *increase* with *decreasing* density and magnetic field, it is more likely that the "pump-out" was due to ECRH diffusion instead of Landau heating from parametrically excited waves. Sample results are shown in Figures 59 to 62.[4] The data clearly indicate the rapid decrease in the endloss signal within $\sim 2\mu sec$ following the end of ECRH. Figure 59 illustrates how the warm-electron enhancement factor is computed from the time history of the endloss signal. It is interesting that a large "burst" of current is observed at the start of the ECRH pulse which corresponds to the "burst" of power (~45kWatt) mentioned in Section 2.1.3.

---

[3] The efficiency for parallel heating is compared to that for ECRH by comparing the relative end-wall powers and adding to the ECRH power the observed rate of rise of the diamagnetism. This does not include the radial increase of the heated electrons, but rather represents the relative efficiencies of the power present at the point sampled by the endloss analyzer.

[4] For these data, the computerized data acquisition system was not operating.

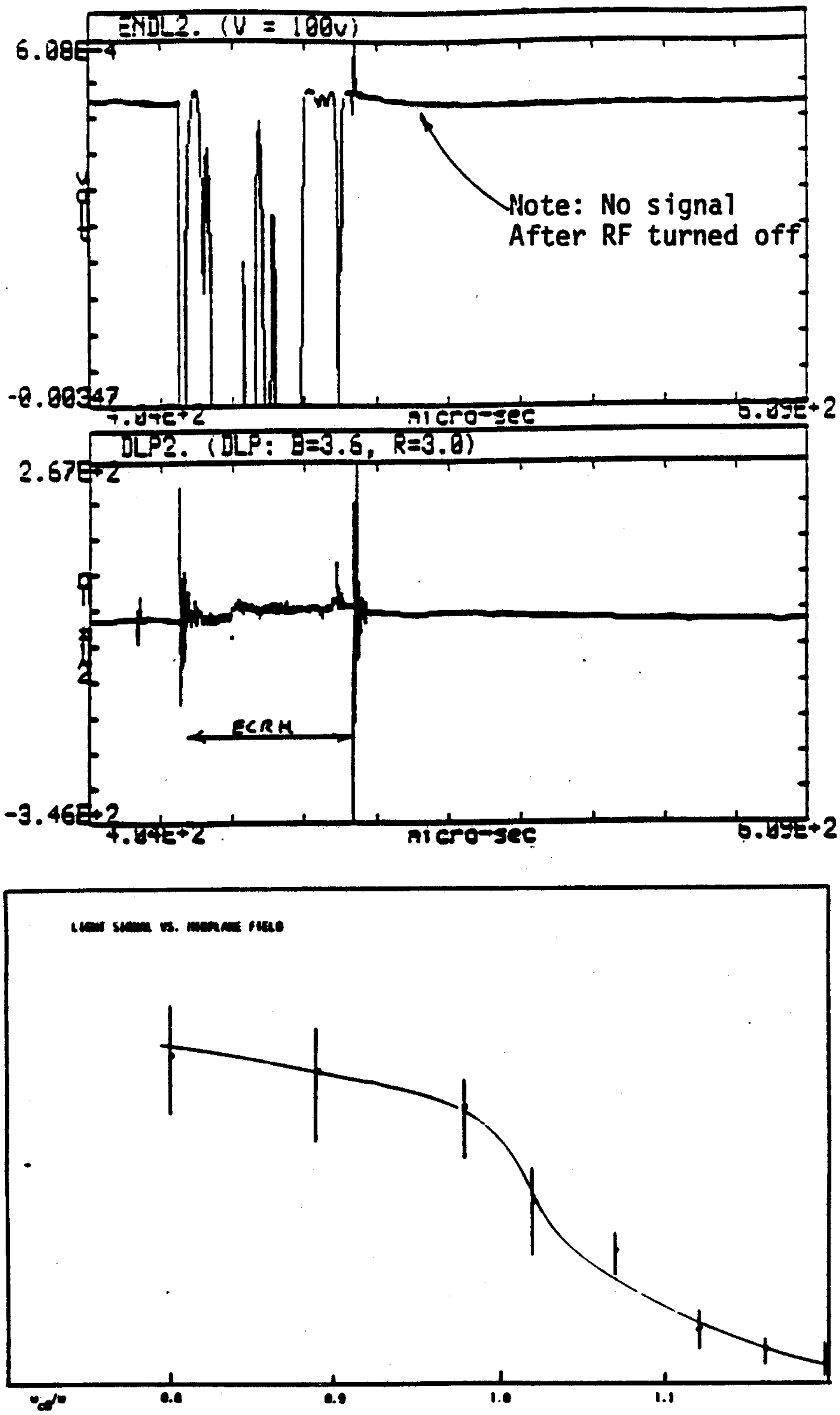

Figure 57. An illustration of the non-*cyclotron*-resonance heating observed as the midplane field is raised so that no resonance exists in the mirror. Large warm endloss signals are seen even though no increases in diamagnetism (or x-ray signals) are observed. Notice also that after the ECRH is turned-off, no endloss signal is observed, indicating an absence of trapped warm electrons which would collisionally scatter into the loss-cone. Besides the endloss signal, the plasma light signal also indicated electron heating when there is no resonance zone in the mirror. This is illustrated on the bottom graph which shows the increased plasma light due to the RF as the magnetic field is increased.

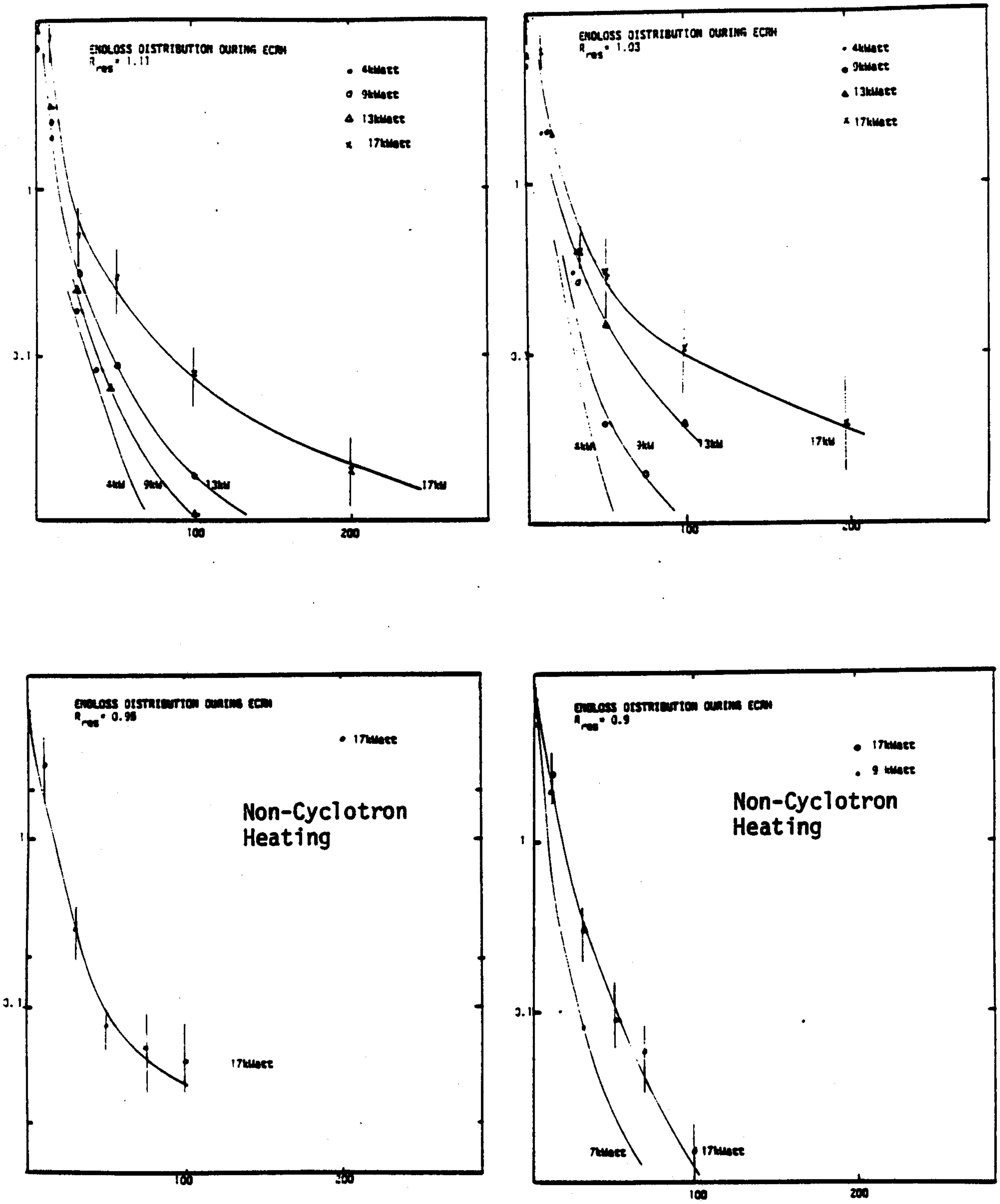

Figure 58. Examples of resonant (top) and non-*cyclotron*-resonant heating as measured by the endloss analyzer during the RF pulse. Each plot shows the endloss energy distribution for several RF powers.

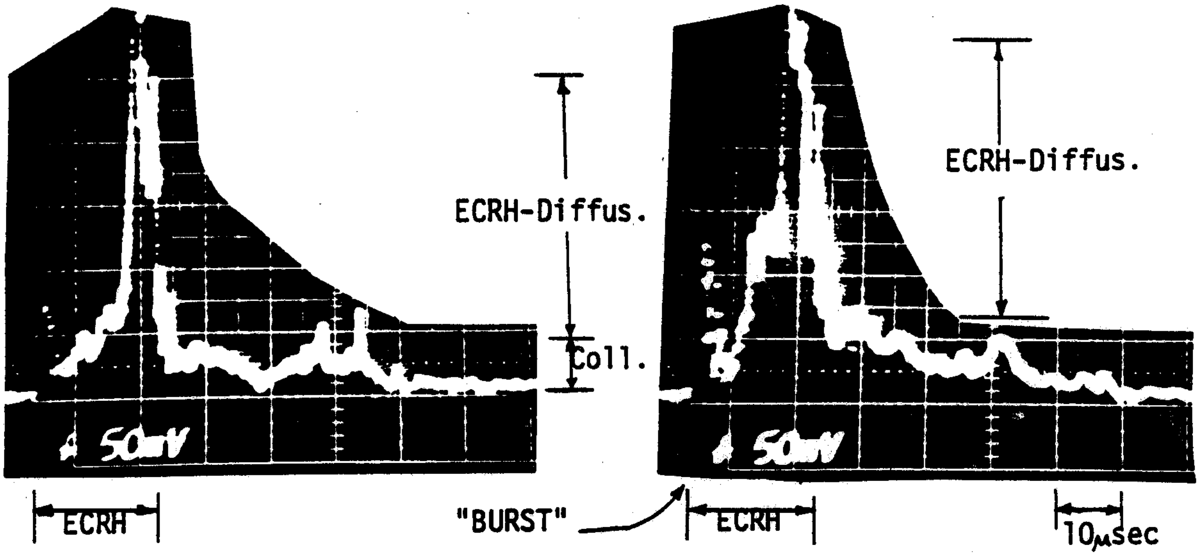

Figure 59. Sample data illustrating how the RF-induced enhancement factor is calculated from the time-history of the warm-endloss signal.

Figure 60 shows the time histories of the endloss for fixed RF power and density as the midplane field was raised. As the field was raised (*i.e.* the resonant zones move toward the midplane), the relative enhancement decreases. Nevertheless, when the resonant zone completely vanishes from the mirror region, sizable warm-electron currents are still occasionally seen. The largest non-resonant current detected is shown in Figure 60 along with the more "typical" examples. In Figure 61, sample data are shown which indicate the reduction of the RF-enhancement as the density increases. Three to five shots were recorded at each density and the averaged results are shown in Figure 62. The data show the decrease of the enhancement factor with increasing density and roughly indicate the expected $1/n^2$ scaling for ECRH diffusion,

Finally, it is interesting to note that the average energy of the electrons (as measured with the diamagnetic loop and interferometer) during the density-scaling experiment ranged from ~500ev for the low density shots to ~120ev for the high density shots. For equally energetic electrons, the simulation predicts enhancements of the endloss of the order of 2 to 3 (Figure 48), which is in rough agreement with the measured values.

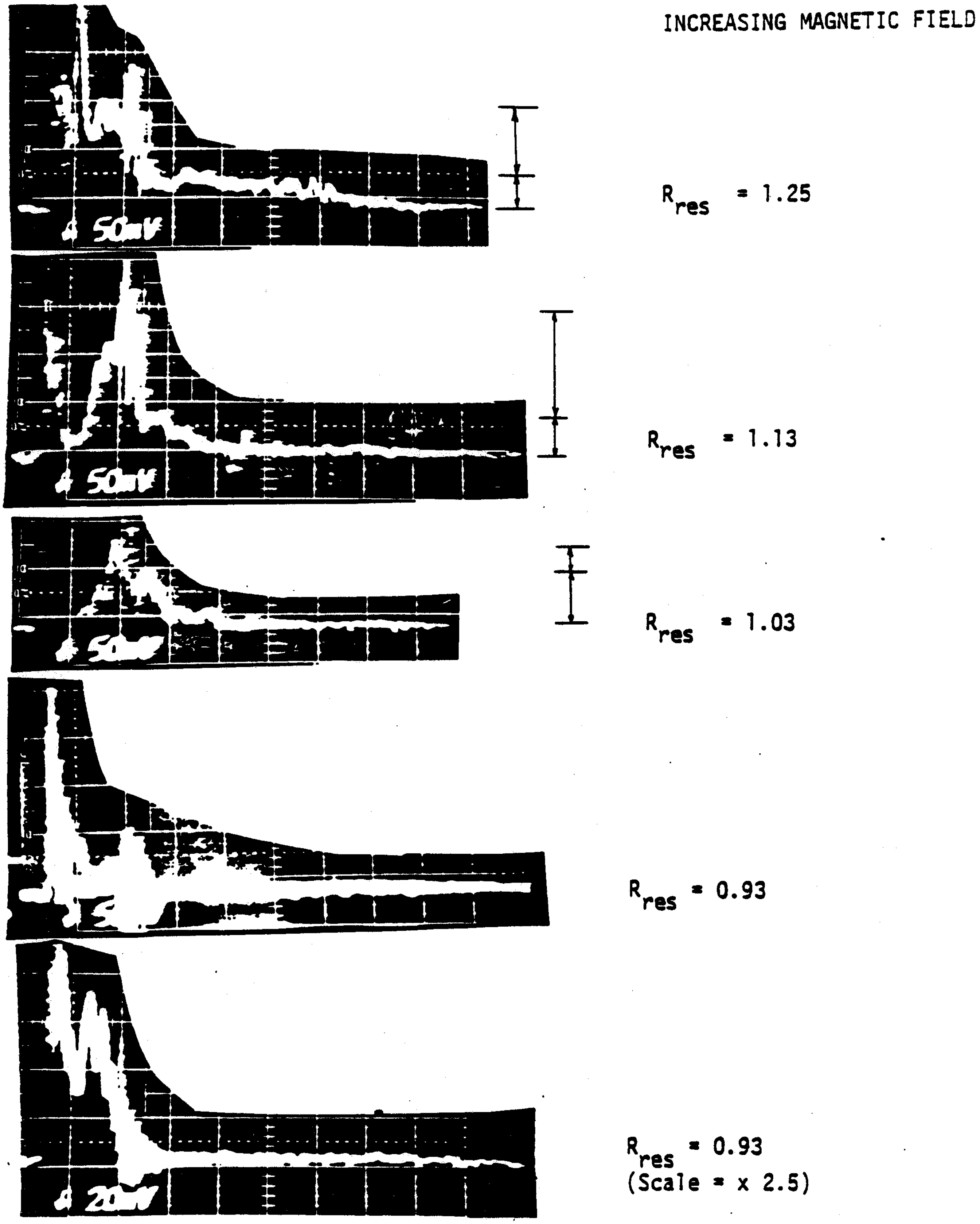

Figure 60. Sample data indicating the reduction of the RF-enhancement of the endloss current as the magnetic field increases.

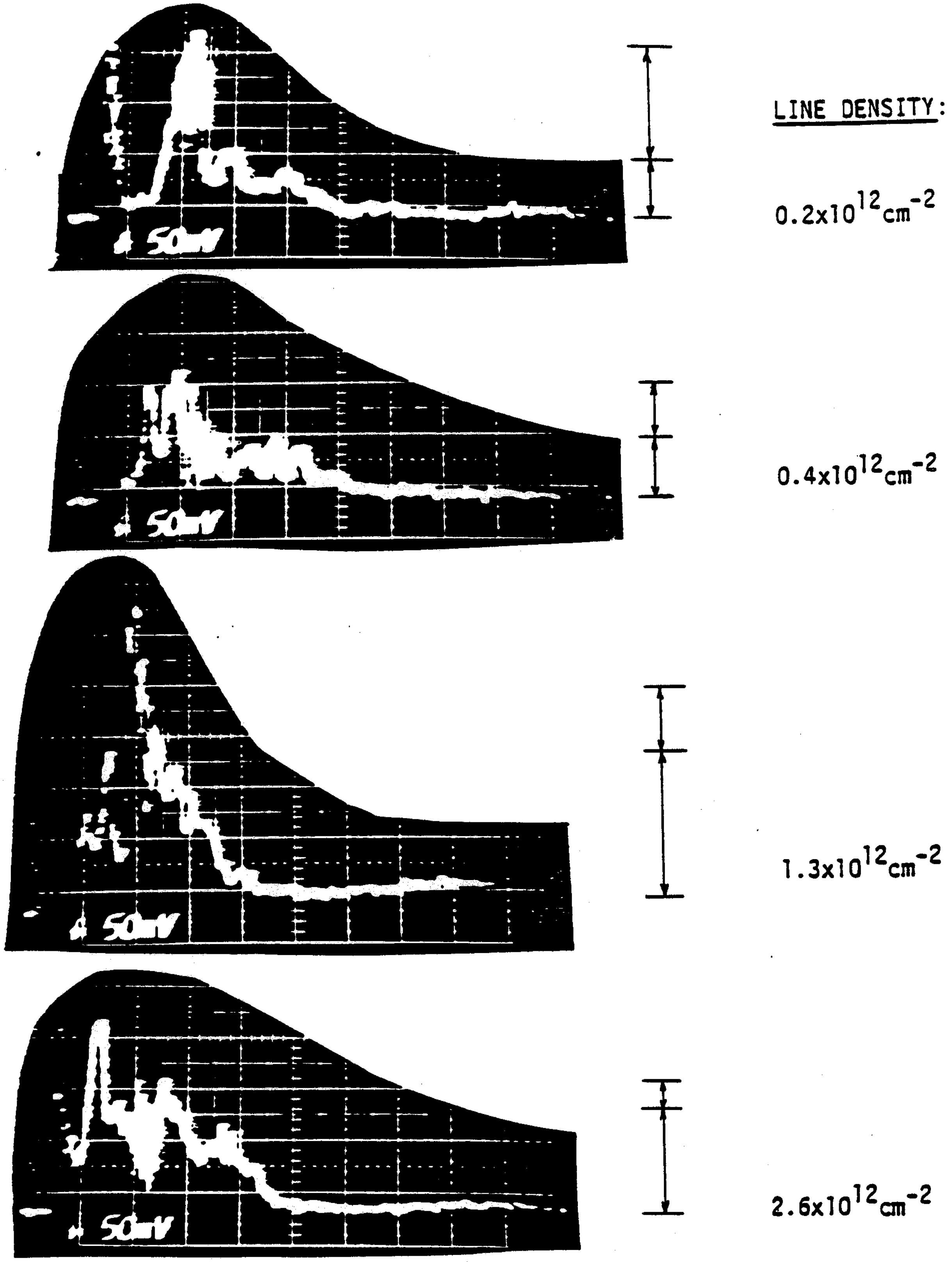

Figure 61. Sample data indicating the decrease in the RF-enhancement of the endloss as the density increases.

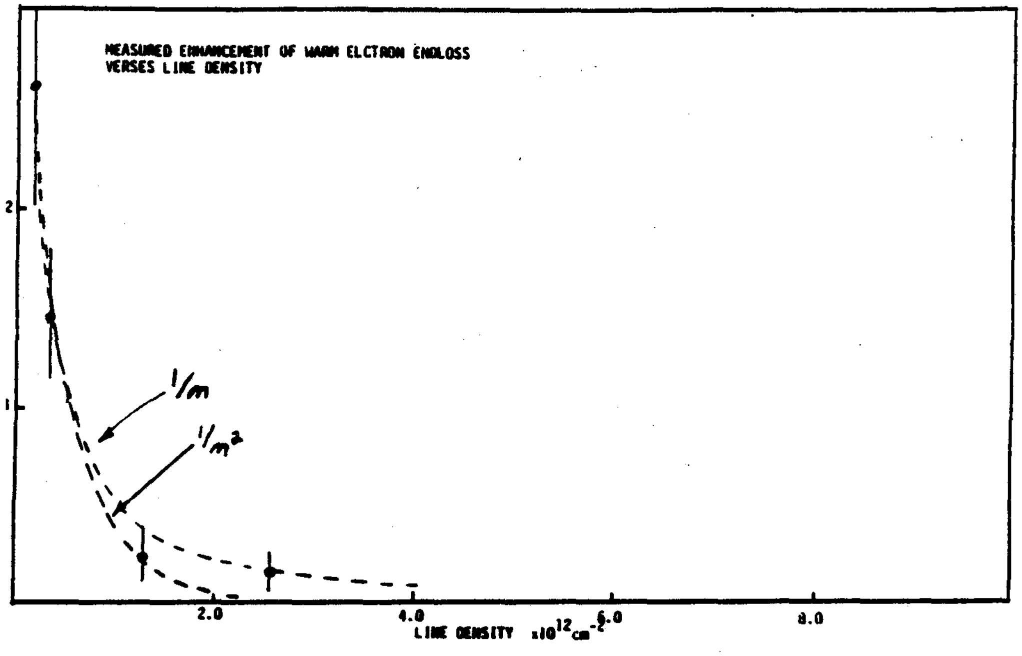

Figure 62. A summary of the enhancement of the warm electron endloss as the density increases. The two high density points represents the average of three shots and the two low density points represent the average of five shots.

Chapter 6

Conclusions

6.1. Measured and Predicted Electron Energy Distribution

The three-part energy distribution measured by the Langmuir probe, endloss analyzer, and target x-ray detector characterizes the electrons heated by ECRH in Constance 2. The "bulk" electrons are in thermal contact with the large "passing" density of electrons which flow into the mirror from the mirror peaks. The bulk temperature rises from $\sim 11ev$ to $\lesssim 30ev$ over the range of parameters investigated (Figures 18 and 19). The "warm" electrons are measured with the endloss analyzer (Figures 24 and 25) and are found to make up the largest fraction of the observed energy rise. The temperature of the warm electrons has been observed in the range of 60ev to 200ev—increasing with power. Target x-ray analysis confirms that there is a small population of hot electrons whose temperature was measured between 1.5kev and 4.0kev (Figures 50 and 53).

A Fokker-Planck simulation of ECRH was developed to represent the fundamental interactions of the electrons with a single, high-frequency wave. The program is based only on the orbit-averaged wave-particle interaction times and the premise that successive interactions are random. ***The major result of this thesis is that the computer simulation shows the same three-part energy distribution as measured on the Constance 2 experiment (Figures 42, 43, and 44).*** This is illustrated schematically in Figure 63. Within the accuracy with which the overall density and energy of the plasma can be determined, the "bulk" electron temperature, "warm" endloss temperature, and the hot electron temperature are reasonably well reproduced by equally energetic "simulated" electrons. In addition to the similarity between these general features of the experiment and the simulation, the increase in the warm endloss temperature and hot electron density with increasing power was common to both the simulation and the experiment.

Finally, the measurement of the time-history of the warm electron endloss

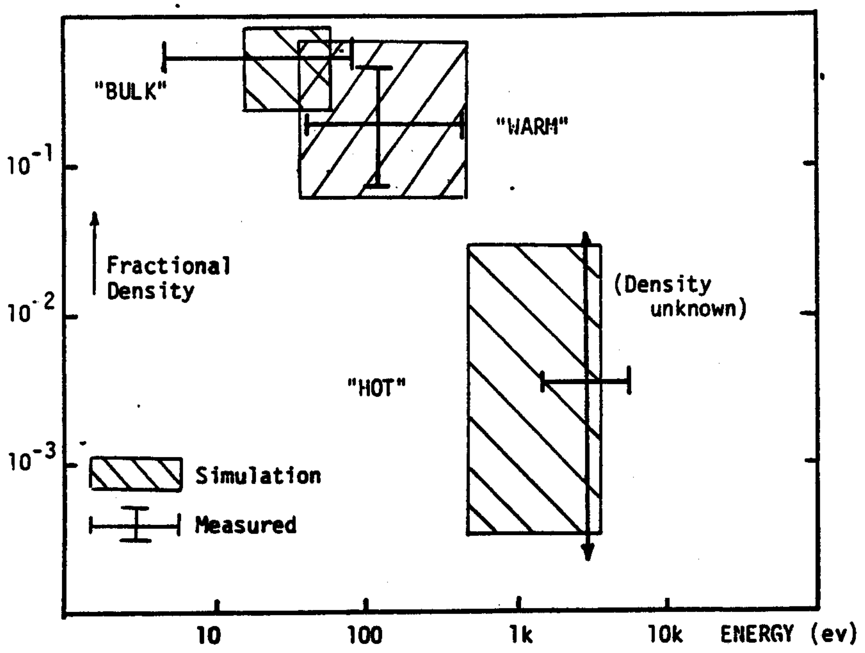

Figure 63. A schematic of the electron energy distribution pointing out the "bulk", "warm", and "hot tail" components. The shaped regions indicate the range of density and temperature calculated by the simulation, and the crossed-lines indicate the range of measured values.

suggests ECRH enhancement due to induced diffusion into the loss-cone. The magnitude of the enhancement and the approximate $1/n^2$ scaling with density was predicted analytically and confirmed by the Fokker-Planck calculations. There is some uncertainty in these measurements, however, due to the very interesting observation that non-resonant, parallel heating of the electrons was also observed which could also explain the observed "pump-out".

6.2. Suggestions for Future Work

The most exciting implication of this thesis is that the quasilinear theory of ECRH heating does indeed reproduce the electron energy distribution. A well-defined procedure has been developed with which a mirror ECRH system can be designed and evaluated. For instance, with modifications, the Fokker-Planck simulation developed for this thesis can help evaluate ECRH assisted, tandem-mirror start-up, the effect of finite $N_{\|}$ on ECRH runaway, and the conditions creating a population of hot electrons which may stabilize ion-cyclotron instabilities.

A serious theoretical limitation of the Fokker-Planck simulation is the inability to correctly model the development and modification of the plasma potential.

This problem can be remedied by either simplifying the diffusion coefficient or just running the program on a faster computer. This will enable the changing diffusion coefficient (due to the changing orbits) to be re-calculated as the potential changes. By correctly modeling the potential, the important use of ECRH for potential modification can be investigated. This will help determine the conditions for positive plug enhancement, barrier formation, and the creation and maintenance of negative potential mirrors.

Finally, a great experimental frustration was the inability to measure the x-ray spectrum without having to resort to target analysis. By repeating the comparison of the predicted and measured energy distribution on a long-lasting ECRH experiment, relatively simple pulse-height analysis of the free-free *bremsstrahlung* radiation can give an accurate description of the development of the energy distribution. Furthermore. by having a Thompson scattering diagnostic, the Langmuir probe—another source of uncertainty—can be eliminated. Both the Thompson scattering and x-ray diagnostics can determine radial profiles which would also allow better measurement of the increased radius of the energy density of the heated electrons. The new tandem mirror experiments, TMX-U and TARA, will provide ideal conditions to further verify the predictions of the quasilinear model.

Appendix 1

WKB/Quasilinear Theory of ECRH

[Most of this appendix originally appeared as a research report: "Theory of Electron Cyclotron Heating in the Constance 2 Experiment", PFC-RR-81/2, (1981).]

A1.1. Introduction

Current plans to test tandem-mirror reactors require electron cyclotron heating to maintain the temperature difference between the central-cell and plug electrons[3,4,5]. Bulk heating will be applied at the fundamental cyclotron resonance to raise the confining potential of each plug. Second harmonic heating will create a hot-electron thermal barrier which should insulate the plug from the central-cell electrons. In both cases, ECRH is used to control the development of the electron distribution function. To be efficient, the bulk heating must guard against tail heating, and the barrier heating must not permit "hot tail runaway"[3]. ECRH has never been used in mirrors for these applications, and, for this reason, Constance II is conducting experiments to study the development of the electron energy distribution with ECRH[6].

This report derives the ECRH theory that will be used to analyze the data. The theory consists of two parts: (1) the derivation of the correct expression for the resonant energy exchange between the waves and particles, and (2) the WKB theory for the propagation of the wave energy from the launching horns to the absorption layers. On the average, an electron gains energy from the waves only at a few local resonances along its orbit. For collisionless particles, low electric fields, and narrow RF bandwidths, the particle's gyro-phase with respect to the wave frequency is not random, and the electrons are purely reactive. As the electric field increases, the bounce resonances overlap resulting in stochastic energy diffusion[7]. Lieberman and Lichtenberg[8] were the first to derive the diffusion equation for a uniform, stationary electric field. Berk[1] was the first to derive a self-consistent bounce-averaged quasi-linear theory which also included the correct WKB theory for the propagation of electrostatic waves. Bernstein and Baxter[2] were the first to extend the theory to relativistic plasmas and to electromagnetic waves. Finally, Porkolab, *et al.*[9] first performed ray tracing calculations for ECRH in mirrors.

The contents of the report are organized into eight sections and an introduction. First, the geometry of the particle orbits are discussed. Then, an expression for the diffusion equation is intuitively derived for a specified electromagnetic wave.

The fourth section discusses the conditions for the validity of the linear, stochastic theory. And, in the fifth section, the bounced-averaged quasi-linear theory is derived for non-relativistic particles. The sixth section is devoted to the bounce-averaged resonance function used in the quasi-linear theory. Next, the WKB theory for wave propagation is derived from the requirement of energy conservation. This gives the geometric and physical optics solutions to the problem of estimating the field intensity and power absorption at the resonance zones. Finally, the last two sections describe the local resonance function used in the WKB theory and the bounce-averaged energy conservation equation.

A1.2. Geometry

For simplicity, the geometry of the plasma used in the kinetic theory is assumed to be locally cylindrical. Non-axisymmetric effects are ignored, and only trapped, bouncing particles are treated. The unperturbed orbits used to describe the trapped electrons, bouncing in the mirror, are

$$s = s_m \cos(\omega_B t + \psi) \tag{1}$$

$$y = Y(0) + \rho(s)\sin\left(\int_0^t \omega_c dt + \phi\right) + \int_0^t \mathbf{V}_D \cdot \hat{y}\, dt \tag{2}$$

$$x = X(0) + \rho(s)\cos\left(\int_0^t \omega_c dt + \phi\right) + \int_0^t \mathbf{V}_D \cdot \hat{x}\, dt \tag{3}$$

where $\rho^2(s) = 2B(s)\mu/\omega_c^2(s)$ and $\mathbf{V}_D$ is the sum of the $\nabla\mathbf{B}$ and curvature drifts. If the particles are deeply trapped, then $\omega_c(s) = \omega_{co}(1 + s^2/L_B^2)$, $\omega_B = V_{\perp,0}/L_B$, and $s_m = V_{\|,0}/\omega_B$. In general, $B(s)$ is not parabolic, so that ω_B is also a function of $v_\|$ and s. For combination electrostatic and magnetic wells, ω_B also depends upon $\Phi(s)$. A particle's phase-space is designated by the variables $(E, \mu, \psi, \phi, X, Y)$ or equivalently $(E, \mu, \phi, \mathbf{R})$, where (X, Y, s) represents the particle's guiding-center position on its drift surface, and $\mathbf{R} = X\hat{x} + Y\hat{y} + s\hat{s}$. ψ is the bounce angle and ϕ is the gyro-phase. The total energy, E, the magnetic moment, μ, and drift surface, $\overline{X}^2 = X^2 + Y^2$, are constants of motion. The velocity gradient and total time derivative are

$$\frac{\partial}{\partial \mathbf{v}} = \frac{\mathbf{v}_\perp - \mathbf{V}_D}{B}\frac{\partial}{\partial \mu} + \mathbf{v}\frac{\partial}{\partial E} + \frac{\hat{\phi}}{v_\perp}\frac{\partial}{\partial \phi} + \frac{1}{\omega_c}\hat{\mathbf{b}} \times \frac{\partial}{\partial \overline{\mathbf{X}}} \tag{4}$$

$$\frac{D}{Dt} = \frac{\partial}{\partial t} + v_\|\frac{\partial}{\partial s} + \mathbf{V}_D \cdot \nabla + \omega_c\frac{\partial}{\partial \phi} \tag{5}$$

The gradient term in Equation 4 can be written as $(\hat{v_D}/\omega_c)\partial/\partial\overline{X}$ with $\hat{v}_D$ defined as $\hat{b} \times \hat{\overline{x}}$. Furthermore, if $\overline{\Theta}$ is defined as $\tan(Y/X)$, then $\mathbf{V}_D = \hat{v}_D\omega_D\overline{X}$ and $\mathbf{V}_D \cdot \nabla = \omega_D\, \partial/\partial\overline{\Theta}$ where $\omega_D = d\overline{\Theta}/dt$. The average particle distribution is assumed to be independent of ϕ, ψ, and $\overline{\Theta}$. This simple geometry is adequate for the kinetic theory presented here since the resonant particle effects ultimately depend only upon local gradients. See Horton, *et al.*[10] for a formal derivation of a particle's motion in a mirror.

A1.3. A Monochromatic Wave

The perturbations to this orbit due to an electromagnetic wave can be analyzed in a manner similar to Jaeger, *et al.*[11]. Consider an electric field, constrained to be

$$\mathbf{E} = \mathbf{E}_k \exp(-i\omega t + i\mathbf{k} \cdot \mathbf{x})$$

and

$$\frac{dE}{dt} \approx B\frac{d\mu}{dt} = \frac{q}{m}\mathbf{E}_\perp \cdot \mathbf{v}_\perp \tag{6}$$

where electron Landau damping, for cases when $E_\parallel \neq 0$, is ignored. To solve Equation 6, the right hand side is integrated along a particle's orbit, and the (assumed to be) dominant term linearly proportional to E_k is retained. This gives

$$\Delta\mu_{bounce} = -\frac{q}{m}E_k \sum_n \oint_{bounce} J_n(k_\perp \rho)\frac{\rho\omega_c}{B}e^{in\phi}\exp\left(-i\int_0^t dt\nu_n(t)\right)dt \tag{7}$$

where

$$\nu_n(t) = \omega - n\omega_c(t) - k_\parallel v_\parallel(t) - \mathbf{k}_\perp \cdot \mathbf{V}_D(t) \tag{8}$$

and where $\hat{y}$-axis has been aligned with the (assumed to be linearly-polarized) electric field. The primed bessel function means differentiation with respect to its argument, or $J_n = J_{n-1} - (n/k_\perp \rho)J_n$. For $k_\perp \rho \ll 1$ and $n = 1$, the primed bessel function is approximately $\sim 1/2$. When evaluating Equation 7, it is assumed that $|\Delta\mu| \ll \mu$ since only the first-order change to the unperturbed orbit is evaluated.

Since the integrand is highly phase dependent, the largest contributions to the integral arise when $\nu(t^*) \approx 0$. For parabolic, magnetic well and for $\mathbf{V}_D = 0$, this is when

$$\delta\omega_{n0} - n\omega_{c0}\frac{s^{*2}}{L_B^2} - k_\parallel v_\parallel^* \approx 0 \tag{9}$$

where $\delta\omega_{n0} = \omega - n\omega_{c0}$, $s^* = s(t^*)$, and $v_\parallel^* = v_\parallel(t^*)$. Figure 1 illustrates $(v_\parallel, s)$ phase space for $\mathbf{V}_D = 0$, fixed $V_{\perp,0}$ and for $k_\parallel$, $\delta\omega_{n0} \neq 0$. Particles with $V_{\parallel,0} < \delta\omega_{n0}/k_\parallel$ have four stationary points. Particles with larger $V_{\parallel,0}$ have only two resonance points, and those with $V_{\parallel,0} = \delta\omega_{n0}/k_\parallel$ have three. For each resonance crossing, the net change in the magnetic moment will be proportional to the product of an effective time in resonance and a phase dependent term. To calculate the interaction time several cases are considered. When the stationary points are well separated, then $\nu(t) \approx (t - t^*)\nu(t^*)$, and the integral can be approximated by the leading term

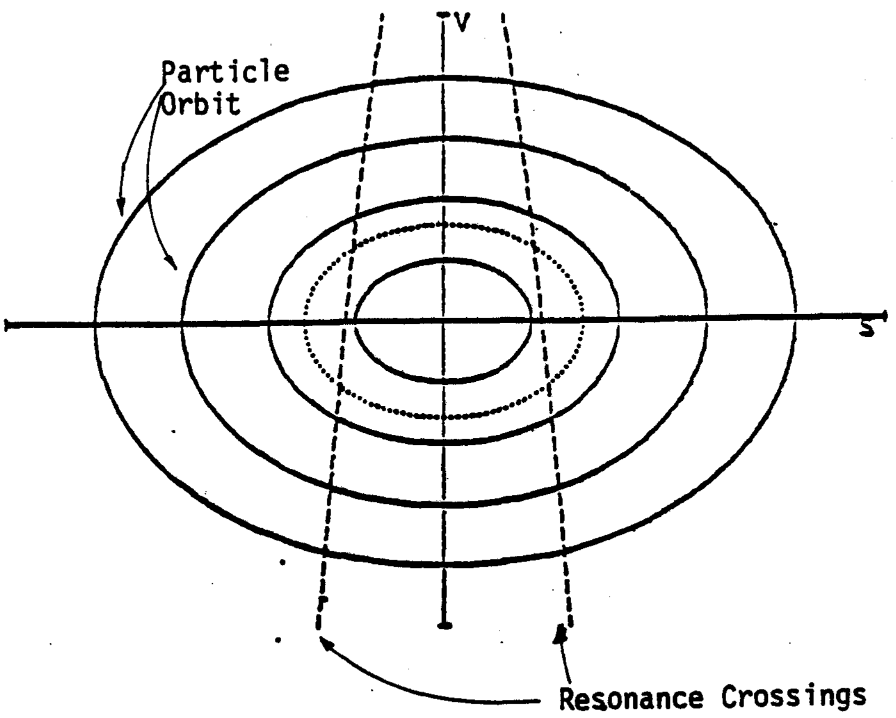

Figure 1. Illustration of resonance points along bounce orbits of the particles in a parabolic well. Verticle axis is $V_{\|,0}$, horizontal is s_m. For $V_D = 0$, fixed $\omega_B = 50 Mrad/s$, $N_\| = 0.4$, $\omega_c 0 = 32 Mrad/s$. and for $\delta\omega_{n0} \neq 0$. This corresponds to $4kev$ electrons in Constance II. The dashed lines are the resonance points, and the dotted line is the boundary between the $p < 0$ and $p > 0$ bounce-resonances.

$$Re\{\Delta\mu^*\} \approx -\frac{q}{m} E_k J_n(k_\perp \rho) \frac{\rho\omega_c}{B} \pi^{1/2} \tau_{eff} \sin(n\phi + \pi/4) \tag{10}$$

In this case, $\tau_{eff}^{-2} = \nu(t^*)/2$. All of the slowly varying quantities are evaluated at t^*. When $\nu(t^*) < 0$, then the phase of the argument of sine changes by $\pi/2$.

When two successive resonances are separated by a time of the order of τ_{eff}, then $\nu(t^*) \approx 0$, and the approximation leading to Equation 10 breaks down. In this case, $\nu(t) \approx \nu(t^*) + (t - t^*)^2 \nu(t^*)/2$ and

$$Re\{\Delta\mu_*\} \approx -\frac{q}{m} E_k J_n(k_\perp \rho) \frac{\rho\omega_c}{B} 2\pi\tau_{eff} \sin(n\phi + \pi/2) Ai(\nu^* \tau_{eff}) \tag{11}$$

where, now, $\tau_{eff}^{-3} = \nu(t^*)/2$ and Ai is the Airy function. When ν is negative, the real branch is used for τ_{eff}. For the parabolic well illustrated in Figure 1, $\nu = 0$ when $s^* = 0$ and $v_\|^* = k_\| \omega_B^2 L_B^2 / 2n\omega_{c0}$. Notice that Equations 10 and 11 are identical in form, the only difference being that the effective time spent in resonance is redefined from $(\nu^*/2\pi)^{-1/2}$ to $2\pi(\nu^*/2)^{-1/3} Ai[\nu^*(\nu^*/2)^{-1/3}]$. In fact, Berk[1] used the Airy function approximation at $s^* = 0$ for all particles, since he considered only $\delta\omega_{n0} \approx 0$ and $k_\| = 0$. A more general approximation is given by the rules:

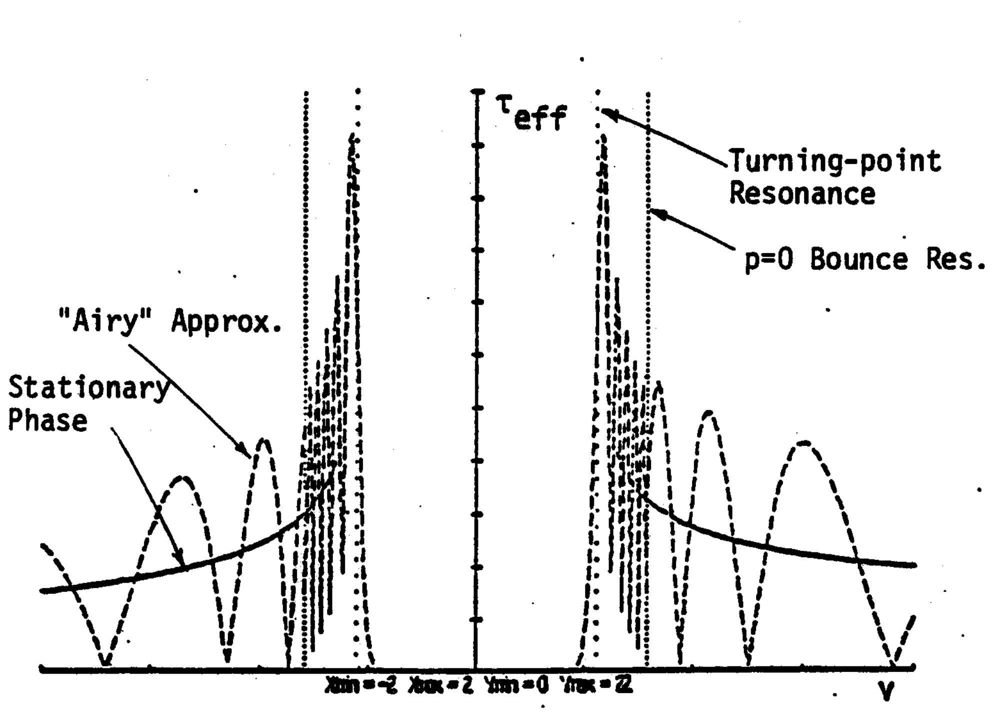

Figure 2. The magnitude of the the effective time in resonance per half-bounce as a function of $V_{\|,0}$ for the case shown in Figure 1. Verticle scale is 10^{-9}*sec*. The dashed line is the Airy approximation for the interaction time. The solid line is the uncorrelated sum of the stationary phase approximation. The dotted lines show the $p = 0$ bounce resonance and the turning-point resonance.

(1) when $v_{\|}^{*} < \delta\omega_0/k_{\|}\omega_B$, then expand about $s^{*} = 0$ for the particles with $|V_{\|,0}| > \min\{|\delta\omega_0/k_{\|}\omega_B|, V_{\perp,0}(2\delta\omega_0/n\omega_{c0})^{1/2}\}$ and expand about $v_{\|}^{*} = k_{\|}\omega_B^2 L_B^2/2n\omega_{c0}$ for the remaining particles, and (2) when $v_{\|}^{*} > \delta\omega_0/k_{\|}\omega_B$, then expand about $s^{*} = 0$ for all particles. Finally, it should be noted that both approximations breakdown when $\nu = \nu = \nu = 0$. This happens when $V_{\|,0} = \delta\omega_{n0}/k_{\|} = v^{*}$. In this case, the time integral is proportional to $\Gamma(1/4)\tau_{eff}\sin(n\phi + 3\pi/8)$. where $\tau_{eff}^{-4} = \nu(t^{*})/3$. Figure 2 summarizes these last two paragraphs. Here, the effective time in resonance is plotted for the particles shown in Figure 1. The oscillations shown in the figure result from retaining the phase information between two successive resonances for the Airy approximations. For some particles, the two interactions cancel. Both of the Airy approximations, at $s^{*} = 0$ and $v_{\|}^{*} = k_{\|}\omega_B^2 L_B^2/2n\omega_{c0}$ are included. The figure corresponds to $n\omega_{c0}/\omega_B \sim 600$ which corresponds to $4kev$ electrons in Constance II.

A1.4. Conditions for Stochasticity

As explained by Lieberman and Lichtenberg[8], when the phase, ϕ, at each resonance crossing is random and with $\Delta\mu \ll \mu$, then the magnetic moment under goes stochastic diffusion. $\langle\Delta\mu\rangle = 0$ and $D_\mu \sim \sum\langle\Delta\mu^*\rangle^2/\tau_B$. The diffusion equation is

$$\frac{\partial f_0}{\partial t} = \frac{1}{2}\frac{\partial^2}{\partial\mu^2} D_\mu f_0(\mu, t) \tag{12}$$

and

$$D_\mu = \sum_{res} \frac{q^2}{m^2}|E|^2 \tau_{eff}^2 \frac{\omega_c^2\rho^2}{B^2} J_n^2 \tag{13}$$

Note that, from Equation 6, the diffusion paths in (E, μ) phase space is given by $D_E \sim B^{*2} D_\mu$. When ϕ is not random, the electrons are superadiabatic[7], and no average energy is exchanged between the waves and the particles.

Three conditions may make ϕ random: (1) collisions, (2) the presence of many, uncorrelated waves, or (3) the overlap of the wave-particle bounce resonances. For electron temperatures greater than $\sim 200eV$, collisions will induce diffusion on a time scale $t > 10\tau_B$ which is usually the weakest of the three effects. Since the bandwidth of typical microwave sources is $\Delta\omega/\omega \sim 10^{-4}$, the statement "many uncorrelated waves" refers to a broad **k**-spectrum. However, since the RF is launched from a single horn, **k**(**r**) is fixed by geometry, and the k-spectrum is not broad if the power is absorbed on the first pass. Note, that even though the resulting resonances for each particle do not look like those in Figure 1 (since **k**(**r**) is a function of position) each particle still experiences a finite number of distinct resonances, and, in general, stochastic diffusion will not result. (Of course, density and temperature fluctuations change the ray geometry, but these effects are usually slow compared to a bounce time for moderately energetic electrons.) On the other hand, when the first pass absorption is poor, the microwaves will bounce several times within the over-moded vacuum chamber. Now, the **k**-spectrum would be very broad, and ϕ should be random. Figure 3 illustrates the many resonances for a weakly absorbant plasma.

The final condition for stochastic diffusion is the overlap of bounce resonances. For Constance II and other mirror ECRH experiments, this is the major justification for the use of the quasi-linear equation, since high, first-pass absorption is expected. To estimate the size of the electric field producing stochastic orbits, the particle motion in (μ, ϕ) space can be written by a set of coupled, difference equations, and KAM theory (Kolmogorov-Arnold-Moser), as summarized by Lichtenberg[12], can be applied. In general, the difference equation is fourth-order. However, when both $\delta\omega_{n0} \approx 0$ and $V_{\parallel,0} < \delta\omega_{n0}/k_\parallel$, then for most particles $\nu^* \sim \nu^* \sim 0$, and Equation 12 can be used for $\Delta\mu$ for each pass through the midplane. The effective interaction time is $\tau_{eff}^{-3} = n\omega_{c0}V_\parallel^2/L_B^2$, and $Ai(0) \approx 0.35$. A further simplification is to assume

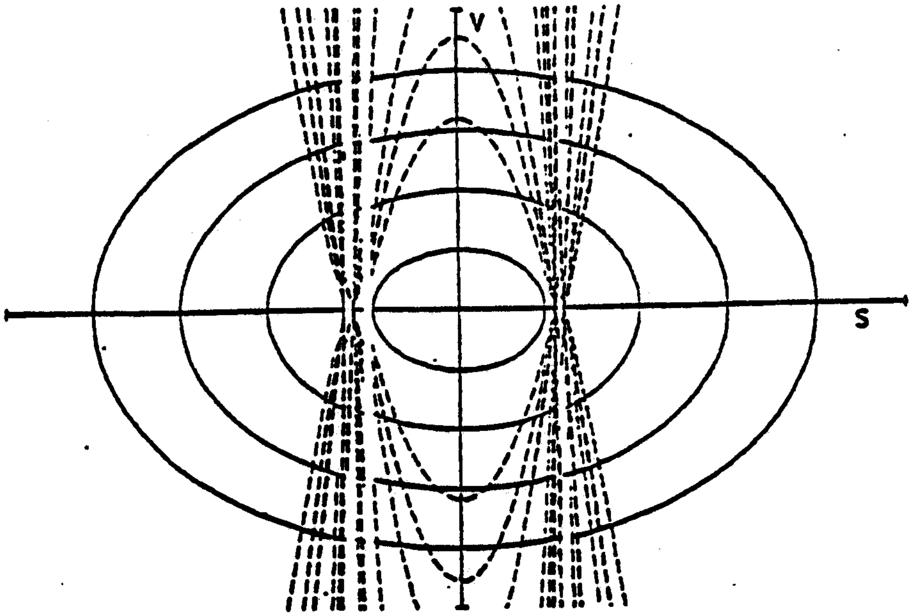

Figure 3. An example of a broad k-spectrum. Each dashed line represents one of many waves propagating through a very tenuous, weakly absorbant plasma. Axis same as Figure 1.

$\Delta\mu \ll \mu$, then the change in gyro-phase, ϕ, due to the resonant electric field can be ignored[7]. The approximate second order difference equation is

$$\begin{aligned} \mu_{n+1} &= \mu_n + \Delta\mu(\mu_n, \phi_n) \\ \phi_{n+1} &= \phi_n + \Delta\phi(\mu_{n+1}) \end{aligned} \tag{14}$$

where

$$\begin{aligned} \Delta\phi &\approx \oint_{\frac{1}{2}bounce} (\omega - \frac{d\phi}{dt})dt \\ &\approx -\frac{\pi}{2}\frac{n\omega_{c0}}{\omega_B}\frac{s_m^2}{L_B^2} \end{aligned}$$

In the last expression, the magnetic well was assumed to be parabolic. (μ_n, ϕ_n) are the magnetic moment and phase before the nth resonance crossing.

The first-order fixed points, (μ_0, ϕ_0), of Equation 14 are the bounce resonances. They are the solutions of $\Delta\phi(\mu_0) = 2\pi p$ and $\cos(n\phi_0) = 0$. Figure 4 illustrates the bounce resonances. Note, that for a real trap, $\omega_B \to 0$ at the loss-cone boundary. Linearizing about the fixed points give

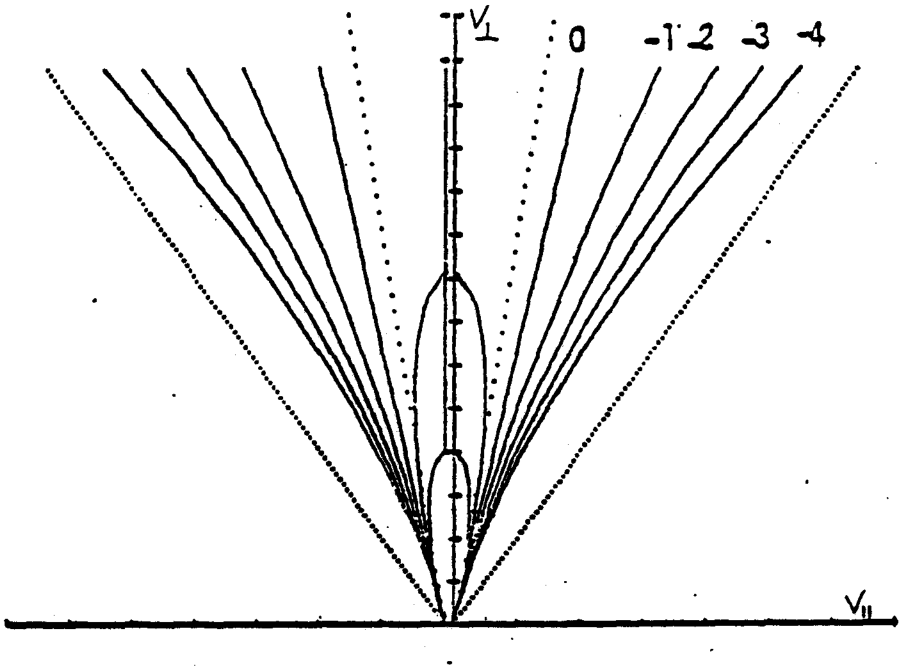

Figure 4. Primary bounce resonances for a parabolic, magnetic well. Shown are $p = 1, 2$ and $p = 0, -1, -2, -3, -4$. The verticle axis is $V_{\perp,0}$, and the horizontal is $V_{\parallel,0}$. The inner, dotted lines are the turning-point resonances. The outer are the loss-cone boundaries.

$$\tilde{\phi}_{n+1} = \tilde{\phi}_n + 3\pi \frac{n\omega_{c0}}{\omega_B}\left(\frac{V_{\parallel,0}}{V_{\perp,0}}\right)^2 \frac{\tilde{\mu}_n}{\mu_0} \qquad (15)$$

$$\tilde{\mu}_{n+1} = \tilde{\mu}_n + K \sin(n\tilde{\phi}_n)$$

where

$$\approx 1.1 \frac{qE_k}{m} \frac{\rho\omega_{c0}}{B} \tau_{eff}$$

and $\mu_n \approx \mu_0 + \tilde{\mu}_n$. From Lichtenberg[12], the condition for stochasticity is

$$\frac{3\pi K}{\mu_0} \frac{n^2\omega_{c0}}{\omega_B}\left(\frac{V_{\parallel,0}}{V_{\perp,0}}\right)^2 > 1 \qquad (16)$$

which was determined both numerically and analytically from solutions of the standard mapping of the Fermi accelerator. As explained by Lichtenberg, Equation 16 is actually a factor of two less severe than the condition of primary resonance overlap (given by $K_p + K_{p+1} > \mu_p - \mu_{p+1}$ for all $p \neq 0$) because of the overlap of higher-order bounce resonances. Equation 17 can be re-written as

$$\frac{q}{m}E_k\tau_{eff} > V_{\perp,0}\frac{\omega_B}{n^2\omega_c}\left(\frac{V_{\perp,0}}{V_{\parallel,0}}\right)^2 \tag{17}$$

which, for $V_{\perp,0}/V_{\parallel,0} \sim 4$ and $n = 1$, requires $E_k > 0.005V/cm$ for $T_\perp = 1keV$, and $E_k > 2.3V/cm$ for $T_\perp = 100keV$. Except for very small fields and very high temperatures, superadiabatic motion should not be expected in Constance II. The condition $\Delta\mu \ll \mu$ gives the upper bound on E_k as $50v/cm$ and $3kV/cm$, respectively. For ECRH in Constance II, the heating is initially highly non-linear ($T_e \lesssim 15ev$ before heating). In this case, the unperturbed orbits cannot be used to calculate $\Delta\mu$, and $\langle\Delta\mu\rangle$ no longer vanishes since the particles will change their phase and larmor radius as they accelerate. The non-linear heating rate is approximately given by $\langle\Delta\mu\rangle/\tau_B$ which scales roughly as $P_{rf}^{1/2}$ instead of the P_{rf} scaling for linear heating. In Constance II, the quasi-linear theory should become valid after a few microseconds for powers not greater than a few kilowatts.

A1.5. Bounce-Averaged Quasi-Linear Theory

The bounce-averaged quasi-linear equation is written symbolically as

$$\oint_{bounce}\frac{d\psi}{2\pi}\left\langle\frac{D}{Dt}f_0(E,\mu,\mathrm{R})\right\rangle_\phi = -\frac{q}{m}\oint_{bounce}\frac{d\psi}{2\pi}\left\langle\sum_{k,k}\delta_{-k,k}\delta_{-\omega,\omega}\,\mathrm{M}_k^{ij}\,E_k^j\,\frac{\partial f_k}{\partial v^i}\right\rangle_\phi \tag{18}$$

where

$$\mathrm{M}_k^{ij} = \delta^{ij}(1 - \frac{\mathbf{v}}{c}\cdot\mathrm{N}) + N^iN^j \tag{19}$$

$$E_k^j = \overline{E}_k^j(\mathbf{r},t)\exp\left[-j\omega t + i\lambda(\mathbf{r})\right] \tag{20}$$

and

$$f_k = -\frac{q}{m}\oint_{-\infty}^{t} dt\,\mathrm{M}_k^{ij}(t)\,E_k^j(t)\,\frac{\partial f_0}{\partial v^i(t)} \tag{21}$$

The first equation above is the bounce and gyro-average of the electron response to the RF fields. Strictly speaking, the diffusion due to untrapped, streaming plasma must be added to the right-hand side of Equation 18, but this is ignored. The delta-function, $\delta_{-k,k}$ implies the random-phase approximation which is not exactly true in an inhomogeneous plasma. The various field components will couple within bandwidths of the order of $\Delta\mathbf{k} \sim \nabla(\ln[f_0(\mathrm{r})])$, but this effect is ignored in this treatment. Note that the tensor M_k^{ij} commutes with the operator $\partial/\partial v^i$. The spatial phase, $\lambda(\mathrm{r})$, is the geometric optics approximation to the wave number of the waves, and $\mathrm{k}(\mathrm{r}) = \nabla\,\lambda(\mathrm{r})$. The index of refraction is $N^i = ck^i/\omega$. $\overline{E}_k^i$ is a slowly changing function of space and time, and ω is constant.

In Equation 21, the integral over t is along the unperturbed particle orbits as in Equation 7. However, in Equation 18, this orbit integral is multiplied by the complex conjugate of the electric field at $t = t$, and this phase-dependent product is then averaged over a full bounce. The resulting average is highly oscillatory unless the end-point corresponds to a stationary point, $\nu(t) \sim 0$. Said in another way, the orbit-integral is the sum of contributions from past stationary points ($t < t$) and from those near the end point ($t \sim t$). The phases of these terms are then added to the phase of the electric field which nearly cancels the phase of the end-point. Now, when the total phase of each term is bounce-averaged, then (1) the real part of the terms from past stationary points are zero, and (2) the real part of the end-point term is also zero except when the phase of the end-point and of the electric-field exactly cancel. The time during which this cancellation takes place is τ_{eff}. Therefore, the major contributions to the bounce-averaged quasi-linear equation are when $\psi(t)$ is near a stationary point. Note, that in this theory, the history of the particle has been truncated. The original global equation has been reduced to a sum of local wave-particle resonances. This is the same premise used to justify Equation 12. In a linear, bounce-averaged theory, if the phase information of the past resonance crossings were retained, superadiabaticity would result.

Keeping the remarks of the last paragraph in mind, the averages and integrals in Equations 18 to 21 can be performed by expanding the field about ($\overline{\mathbf{X}}$, s, t), the current guiding-center position and the current time. This gives

$$E_k^j(\mathbf{r},t) = \exp\left[-i\omega t + i\lambda(\mathbf{R})\right]\left\{\overline{E}_k^j(\mathbf{R},t) + (\mathbf{r}-\mathbf{R})\cdot\nabla\overline{E}_k^j(\mathbf{R},t) + (t-t)\frac{\partial}{\partial t}\overline{E}_k^j(\mathbf{R},t)\right\}$$
$$\times\left(1+\frac{i}{2}(\mathbf{r}-\mathbf{R})(\mathbf{r}-\mathbf{R}):\nabla\mathbf{k}\right)\exp\left[-i\omega(t-t) + i\int_{\mathbf{R}}^{\mathbf{r}} dt\mathbf{v}\cdot\mathbf{k}(\mathbf{R})\right] \tag{22}$$

Notice that the variation of **k** along the orbit is assumed to be slow enough such that $(\mathbf{r}-\mathbf{R})\cdot\nabla(\ln[k(\mathbf{R})]) \ll 1$, and the exponential containing $\nabla\mathbf{k}$ can be expanded. The double dot-product is $(r^i - R^i)(r^j - R^j)(\partial k^j/\partial R^i)$ where the repeated indices are assumed to be summed. Equation 22 can be re-written as

$$E_k^j(\mathbf{r},t) = \exp\left[-i\omega t + i\lambda(\mathbf{R})\right]\left\{\overline{E}_k^j - i\nabla\overline{E}_k^j\cdot\frac{\partial}{\partial\mathbf{k}} + i\frac{\partial\overline{E}_k^j}{\partial t}\frac{\partial}{\partial\omega}\right.$$
$$\left.-\frac{i}{2}\overline{E}_k^j\nabla\mathbf{k}:\frac{\partial}{\partial\mathbf{k}}\frac{\partial}{\partial\mathbf{k}}\right\}\exp\left[-i\omega(t-t) + i(\mathbf{r}-\mathbf{R})\cdot\mathbf{k}(\mathbf{R})\right] \tag{23}$$

The electric field, when $t = t$, can be expanded similarly as

$$E_k^j(\mathbf{r},t) = \exp\left[-i\omega t + i\lambda(\mathbf{R})\right]$$
$$\left\{\overline{E}_k^j - i\nabla\overline{E}_k^j\cdot\frac{\partial}{\partial\mathbf{k}} - \frac{i}{2}\overline{E}_k^j\nabla\mathbf{k}:\frac{\partial}{\partial\mathbf{k}}\frac{\partial}{\partial\mathbf{k}}\right\}\exp\left[i(\mathbf{r}-\mathbf{R})\cdot\mathbf{k}(\mathbf{R})\right] \tag{24}$$

Then, Equation 18 can now be written as

$$\begin{aligned}\oint \frac{d\psi}{2\pi}\left\langle \frac{\partial f_0}{\partial t} + v_{\parallel}\frac{\partial f_0}{\partial s}\right\rangle_{\phi} = \frac{q^2}{m^2}\oint \frac{d\psi}{2\pi}\Big\langle \sum_{k,k} \delta_{-k,k}\,\mathsf{M}_k^{ij} \\ \times \left\{\overline{E}_k^j - i\nabla \overline{E}_k^j \cdot \frac{\partial}{\partial \mathbf{k}} - \frac{i}{2}\overline{E}_k^j \nabla \mathbf{k} : \frac{\partial}{\partial \mathbf{k}}\frac{\partial}{\partial \mathbf{k}}\right\} \\ \cdot \frac{\partial}{\partial v^i}\int_{-\infty}^{t} dt\, \mathsf{M}_k^{lm}(t) \\ \times \left\{\overline{E}_k^m - i\nabla \overline{E}_k^m \cdot \frac{\partial}{\partial \mathbf{k}} + i\frac{\partial \overline{E}_k^m}{\partial t}\frac{\partial}{\partial \omega} - \frac{i}{2}\overline{E}_k^m \nabla \mathbf{k} : \frac{\partial}{\partial \mathbf{k}}\frac{\partial}{\partial \mathbf{k}}\right\} \\ \times \exp\left[-i\int_t^t (\omega - \mathbf{v}(t)\cdot \mathbf{k}(\mathbf{R}))dt\right] \cdot \frac{\partial f_0}{\partial v^l(t)}\Big\rangle_{\phi}\end{aligned} \tag{25}$$

where the argument of the electric field is $(\mathbf{R}, t)$, and where $k = -k$ and $\omega = -\omega$ were used to express the phase in the last exponential. Using Equations 2 and 3, the phase-dependent exponential can be simplified, since

$$(\mathbf{r} - \mathbf{R}) \cdot \mathbf{k}_{\perp} = \rho k_{\perp} \sin\left(\int_0^t \omega_c dt + \phi - \xi + \pi/2\right)$$

where the local wave-vector is $\mathbf{k} = k_{\parallel}\hat{s} + k_{\perp}(\cos\xi\hat{x} + \sin\xi\hat{y})$, then the standard bessel expansion allows

$$\begin{aligned}\exp\left[-i\int_t^t (\omega - \mathbf{v}\cdot\mathbf{k})dt\right] = \sum_{n,n} J_n J_n\, e^{i(\phi+\pi/2)(n-n)}\, e^{-i(\xi n - \xi n)} \\ \times \exp\left[-i\int_t^t \nu_n(t)dt\right]\end{aligned} \tag{26}$$

where $\nu_n(t)$ is given by Equation 8. The argument of the bessel function is $k_{\perp}\rho$.

Before making any further progress, Equation 25 can be greatly simplified by transforming to the complex basis defined by $(x, y, z) \rightarrow (r, l, z)$ where $r = (x - iy)/\sqrt{2}$, $l = r^*$, and $z = z$. The symbol, * or "star", denotes the complex conjugate. In this basis, if $E_k^l = E_k^z = 0$, then the electric field is right-hand circularly polarized in the direction of the magnetic field. A dot-product in the real, cartesian coordinate system is re-written in the new, complex basis as $\mathbf{A}\cdot\mathbf{B} \rightarrow \mathbf{A}\cdot\mathbf{B}^*$. Then, suppressing the gradient terms containing the dot and double-dot products, then right-hand side of Equation 25 can be written as

$$\begin{aligned}\sum_{k,k}\delta_{-k,k}\sum_{n,n}\frac{q^2}{m^2}\oint\frac{d\psi}{2\pi}\Big\langle \mathsf{M}_k^{i^*j} \cdot \frac{\partial}{\partial v^i}\left\{\overline{E}_k^{j*} - \ldots\right\}\left\{\overline{E}_k^m - \ldots\right\} \\ \times \int_{-\infty}^{0} dt\,\mathsf{M}_k^{lm^*}\, J_n J_n\, e^{i(\phi+\pi/2)(n-n)}\, e^{-i(\xi n - \xi n)} \exp\left[-i\int_0^t \nu_n dt\right] \cdot \frac{\partial f_0}{\partial v^{l^*}}\Big\rangle_{\phi}\end{aligned} \tag{27}$$

Note the location of the conjugated components. The only t dependence besides the phase integral is the product $\mathrm{M}_k^{ij^*}\ \partial/\partial v^{i^*}$, but with some algebra and Equations 4 and 19, this is

$$M^{m^*}_{op,n} \equiv \mathrm{M}_k^{lm^*} \frac{\partial}{\partial v^{l^*}} \tag{28}$$

whose componets are

$$\begin{aligned}
M^{r^*}_{op,n} = &\left\{\beta_{\overline{n}}\,\rho\,\omega_c\delta_{\overline{n},n-1} + \frac{cn\omega_c}{\omega}N_\perp\right\}\frac{1}{\sqrt{2}}e^{i\xi}\,\frac{1}{B}\frac{\partial}{\partial\mu} \\
&+\left\{(\beta_{\overline{n}}\,\rho\,\omega_c\delta_{\overline{n},n-1} + \frac{cn\omega_c}{\omega}N_\perp + N_\perp N_\| v_\|)e^{i\xi}\right. \\
&\qquad \left. +V_D(\beta_n + N_\perp^2 g^*(\overline{\Theta},\xi))e^{i(\overline{\Theta}+\pi/2)}\right\}\frac{1}{\sqrt{2}}\frac{\partial}{\partial E} \\
&+\left\{\beta_n + N_\perp^2 g^*(\overline{\Theta},\xi)\right\}e^{i(\overline{\Theta}+\pi/2)}\frac{1}{\sqrt{2}}\frac{1}{\omega_c}\frac{\partial}{\partial \overline{X}}
\end{aligned}$$

$$M^{l^*}_{op,n} = M^{r}_{op,n}$$

$$\begin{aligned}
M^{z^*}_{op,n} = &\, cN_\|\frac{n\omega_c}{\omega}\frac{1}{B}\frac{\partial}{\partial\mu} \\
&+\left\{\beta_n v_\| + N_\|^2 v_\| + cN_\|\frac{nw_c}{\omega} + V_D N_\perp N_\| \sin(\xi-\overline{\Theta})\right\}\frac{\partial}{\partial E} \\
&+V_D N_\perp N_\| \sin(\xi-\overline{\Theta})\frac{1}{\omega_c}\frac{\partial}{\partial\overline{X}}
\end{aligned}$$

and where

$$\begin{aligned}
g(\overline{\Theta},\xi) &= \sin(\xi-\overline{\Theta})e^{-i(\overline{\Theta}-\xi+\pi/2)} \\
\beta_n &= 1 - \frac{k_\| v_\|}{\omega} - \frac{\mathbf{k}_\perp\cdot\mathbf{V}_D}{\omega} - \frac{n\omega_c}{\omega}
\end{aligned}$$

The operator $\delta_{n,n\pm1}$ acts to raise or lower the order of the bessel function designated by n. This gives the identity $\delta_{n,n+1}+\delta_{n,n-1} = 2n/k_\perp\rho$ which was used to obtain these expressions. Note that the time dependence of $\mathbf{M}_{op,n}$ has been replaced by using these operators. This is because the operation of $\delta_{n,n-1}$ is equivalent to multiplication by $\exp\left[i(\int_0^t \omega_c dt + \phi - \xi + \pi/2)\right]$ and then re-defining the sum over n. Therefore, the complex conjugate of $\delta_{n,n+1}$ is $\delta_{n,n-1}$. The same operators can be used to express $M^{i}_{op,n} = \mathrm{M}_k^{ij^*}\ \partial/\partial v^i$ except, here, after complex conjugating the expression for $\mathrm{M}^{l^*}_{op}$ in Equation 28, the direction of the $\delta_{n,n\pm1}$ operators must be reversed due to the opposite sign of k. Physically, the operators, $\mathbf{M}_{op}$, give the diffusion paths of the electrons in $(E,\mu,\overline{X})$ phase-space.

Then, in the complex basis, and after replacing the time-dependances of the gradient operators by the delta-operators, Equation 25 is

$$\frac{\partial f_0}{\partial t} = \frac{q^2}{m^2} \oint \frac{d\psi}{2\pi} \sum_{n,n} \sum_{k,k} \delta_{-k,k} \times \left\langle M^j_{op,n} \left\{ \overline{E}^{j^*}_k - . \quad . \quad . \right\} \left\{ \overline{E}^m_k - . \quad . \quad . \right\} \Omega^{-1}_{n,n} M^{m^*}_{op,n} f_0 \right\rangle_\phi \tag{29}$$

where

$$\Omega^{-1}_{n,n} = \int_{-\infty}^{0} dt\, J_n J_n\, e^{i(\phi+\pi/2)(n-n)}\, e^{-i(\xi n - \xi n)} \exp\left[-i \int_0^t \nu_n\, dt\right] \tag{30}$$

Note, that the term containing $\partial/\partial\phi$ in $\partial/\partial v^i$ has been excluded since, when the averaged over ϕ, this term is highly phase dependent and therefore does not contribute to diffusion. Also, the bounce and gyro averages of Df_0/Dt leaves only the derivative of f_0 with respect to slow time changes since f_0 is independent of ψ and ϕ. Furthermore, since the only ϕ dependances in Equation 29 are contained in $\Omega_{n,n}$, the gyro-average sets n to n. (However, the conventions, explained in the last paragraph, between the raising and lowering operators, $\delta_{n,n\pm 1}$, designated by M^j_{op} and $M^{m^*}_{op}$ are still maintained.) Finally, the average over ψ is calculated as in Equation 8. The real-part of the integral will be dominated by the rapidly varying phase in the exponential which will give non-vanishing contributions only when ψ corresponds to a stationary point. Thus, resonant energy exchange is the sum of local interactions. The imaginary part of the average is global, since it represents the average "sloshing" wave energy along the particle's bounce path.

Following Berk[1], the gradient terms can now be inserted and the sum over k and k completed. Note that

$$\frac{\partial}{\partial \mathbf{k}} = \hat{s}\frac{\partial}{\partial v_\parallel} + \hat{x}\left(\frac{k_x}{k_\perp}\frac{\partial}{\partial k_\perp} - \frac{k_y}{k_\perp^2}\frac{\partial}{\partial \xi}\right) + \hat{y}\left(\frac{k_x}{k_\perp}\frac{\partial}{\partial k_\perp} + \frac{k_x}{k_\perp^2}\frac{\partial}{\partial \xi}\right) \tag{31}$$

since $k_\perp^2 = k_x^2 + k_y^2$ and $\xi = \tan^{-1}(k_y/k_x)$. Remember, also, that the derivatives with respect to ω and $\mathbf{k}$ act only upon Ω_n^{-1}. Then, since the terms proportional to $\overline{E}^{j^*}_{-k} \nabla \overline{E}^m_k - \overline{E}^m_k \nabla \overline{E}^{j^*}_{-k}$ sum to zero, the only first-order contributions come from the derivatives with respect to ξ and ξ. In other words, since

$$\frac{1}{k_\perp}\frac{\partial}{\partial \xi} = -\frac{1}{k_\perp}\frac{\partial}{\partial \xi} = -\frac{in}{k_\perp}$$

the final form of the quasi-linear equation is a sum of resonant interactions and a gradient term which acts on the electric field and the resonance function. The result is

$$\frac{\partial}{\partial t}F_0(E,\mu,\overline{X},t) = \frac{q^2}{m^2} \sum_{res} \sum_{k,n} M^j_{op}\{1 - \hat{b}\cdot(\frac{n\mathbf{k}}{k_\perp^2} \times \nabla)\} \times |\overline{E}^{j^*}\overline{E}^m|_k\, Re\{\overline{\Omega_n^{-1}}\} M^{m^*}_{op} F_0 \tag{32}$$

The gradient term can be considered as the correction to the field intensity and its interaction which results from expressing the field in guiding-center coordinates. As in Berk[1], F_0 is the average particle distribution after subtracting the "sloshing" energy due to the non-resonant wave-particle interactions, and $\overline{\Omega_n^{-1}}$ is the bounce-averaged resonance function. Finally, the sum over resonances does not necessarily refer to a sum over definite resonant layers in space. In general, $k_{\|} \neq 0$, and the resonances for each region of velocity-space will occur in different regions of coordinate-space.

F_0 is given by

$$F_0 = f_0 + \frac{1}{2}\frac{q^2}{m^2}\sum_{k,n}\oint\frac{d\psi}{2\pi}M^j_{op}|\overline{E}^{j^*}\overline{E}^m|_k\frac{\partial}{\partial\omega}Im\{\Omega_n^{-1}\}M^{m^*}_{op}F_0 \tag{33}$$

In Section 8, F_0 will be shown to represent the particle kinetic energy after the "sloshing" wave energy is subtracted.

It should also be noticed that Equation 32 is real when summed over all field components since the term containing $|\overline{E}^{r^*}\overline{E}^r|$ is the complex conjugate of that term containing $|\overline{E}^{l^*}\overline{E}^l|$, etc. The total of all of the terms is twice the sum of the real parts of the terms proportional to $|\overline{E}^{r^*}\overline{E}^r|$, $|\overline{E}^{r^*}\overline{E}^l|$, $|\overline{E}^{r^*}\overline{E}^z|$, $|\overline{E}^z\overline{E}^r|$ plus the term containing $|\overline{E}^z\overline{E}^z|$.

Finally, for the simple example discussed in Section 3, $V_D = 0$, $\overline{\mathbf{E}} = \hat{y}\overline{E}$, and $\partial/\partial\overline{X} = 0$. Then, if the field is cyclotron resonant, $n = 1$, and if the plasma is cool enough such that $k_{\perp}\rho \ll 1$ and $v/c \ll 1$, then the quasi-linear equation can be written as

$$\begin{aligned}\frac{\partial F_0}{\partial t} = \frac{1}{2}\frac{q^2}{m^2}\sum_{res}\rho\omega_c(\beta_0 + \frac{1}{2}N_{\perp}^2)(\frac{1}{B}\frac{\partial}{\partial\mu} + \frac{\partial}{\partial E})\\ \times|\overline{E}^2|_k Re\{\Omega_1^{-1}\}\rho\omega_c\beta_0(\frac{1}{B}\frac{\partial}{\partial\mu} + \frac{\partial}{\partial E})F_0\end{aligned} \tag{34}$$

where $\beta_0 = 1 - k_{\|}v_{\|}/\omega$, and the slowly varying quantities which define the diffusion paths are evaluated at the resonances.

A1.6. Bounce-Averaged Resonance Function

To calculate the bounce-averaged resonance function, $\overline{\Omega_n^{-1}}$, the techniques used in Section 3 are used again. First, $\nu_n(\psi, t)$ is expanded about $t = 0$ and $\psi = \psi^*$, such that $\nu(\psi^*, 0) = 0$. Then,

$$
\begin{aligned}
-i\int_0^t \nu_n\,dt &\approx -i\int_0^t [\nu_n(\psi^*)(\psi-\psi^*)/\omega_B + t\,\nu(\psi^*)] \\
&\approx -i\tau_{eff}^2[t+(\psi-\psi^*)/\omega_B]^2 + i\tau_{eff}^2(\psi-\psi^*)^2/\omega_B^2 \qquad (35)
\end{aligned}
$$

and, for cases when $\nu_n \approx 0$, then

$$
\approx -i[\nu_n(\psi^*)t + \frac{t}{\tau_{eff}^3\omega_B^2}(\psi-\psi^*+t\omega_B/2)^2 + \tau_{eff}^{-3}t^3/12] \qquad (36)
$$

In the above equation, the identity $\omega_B\,\partial/\partial\psi = \partial/\partial t$ was used. In the first case, integrating first over time and then over bounce angle gives

$$
Re\{\overline{\Omega_n}^{-1}\} = \sum_{res} J_n^2\,\frac{1}{4}\omega_B\tau_{eff}^2 \qquad (37)
$$

while, in the second case, the first integration is over ψ, and the second over t, which gives

$$
\begin{aligned}
Re\{\overline{\Omega_n}^{-1}\} &\approx \sum_{res} J_n^2\,\frac{\omega_B}{2\sqrt{2}}\tau_{eff}e^{-i\pi/4}\int_{-\infty}^{0}\frac{dt}{\sqrt{\tau_{eff}^{-1}t}}\exp -i[\nu_n^*t+\tau_{eff}^{-3}t^3/12] \\
&\approx \sum_{res}\pi\omega_B\tau_{eff}^2[Ai^2(\nu_n^*\tau_{eff}) - iAi(\nu_n^*\tau_{eff})Bi(\nu_n^*\tau_{eff})] \qquad (38)
\end{aligned}
$$

using the Pearlstein identity[1]. The value of the resonant interaction is the same as that calculated in Equations 10 and 11.

It is also informative to calculate the resonance function in a manner which illustrates the points of Section 4. If we take a simple example, with $k_\parallel = V_D = 0$, then the exact orbits for electrons deeply-trapped in a magnetic well give

$$
\overline{\Omega_n}^{-1} = \sum_p J_n^2\,J_p^2(\tau_{eff}^{-3}\omega_B^{-3}/4)\frac{i}{\delta\omega_{0n} - \tau_{eff}^{-3}\omega_B^{-2}/2 - 2p\omega_B} \qquad (39)
$$

where $\tau_{eff}^{-3} = n\omega_{c0}V_{\parallel,0}^2/L_B^2$. The bounce resonances are those shown in Figure 4. The resonance function can be considered to represent the wave-particle interaction in the limit that $\overline{E} \to 0$ and $t \to \infty$. Those particles which do not have exactly the same phase during each pass through resonance cannot gain energy as $t \to \infty$. Of course, this condition is also the condition which defined the fixed-points of Equation 14.

However, when the electric field is finite, then the resonances overlap, and Equation 39 should be equivalent to Equation 38. To show this, a broadening term is added to the resonant denominator, so that the real part of Equation 30 is

$$
Re\{\overline{\Omega_n}^{-1}\} = J_n^2\sum_p J_p^2(\tau_{eff}^{-3}\omega_B^{-3}/4)\frac{\eta_k}{(\delta\omega_{0n} - \tau_{eff}^{-3}\omega_B^{-2}/2 - 2p\omega_B)^2 + \eta_k^2} \qquad (40)
$$

where η_k can be considered to be defined from

$$\eta_k\, f_k(E,\mu) \approx \frac{1}{2}\left[\frac{\partial^2}{\partial\mu^2}B^2 + \frac{\partial^2}{\partial E^2}\right]\sum_{res}\frac{\langle\Delta\mu\rangle^2}{\tau_B}\, f_k(E,\mu)$$

as in Equation 12. Then, since $J_p[p(1+z\,p^{-2/3})] \sim (2/p)^{1/3}\,Ai(-2^{1/3}z)$ as $p \to \infty$, Equation 40 becomes

$$Re\{\overline{\Omega_n}^{-1}\} \approx \sum_{p\ll 0} J_n^2\, 4\tau_{eff}^2\omega_B^2\, Ai^2(-\delta\omega_{0n}\tau_{eff}) \times \frac{\eta_k}{\omega_B^2(p-\delta\omega_{0n}/2\omega_B + 1/4\tau_{eff}^3\omega_B^3)^2 + \eta_k^2} \tag{41}$$

for p less than zero, and

$$Re\{\overline{\Omega_n}^{-1}\} \approx \sum_{p\gg 0}{}' J_n^2\, \tau_{eff}^2\omega_B^2\, Ai^2[(\delta\omega_{0n} - \omega_B^{-2}\tau_{eff}^{-3})\tau_{eff}] \times \frac{\eta_k}{\omega_B^2(p-\delta\omega_{0n}/2\omega_B + 1/4\tau_{eff}^3\omega_B^3)^2 + \eta_k^2} \tag{42}$$

for p greater than zero. To obtain these equations, the argument of the bessel function was evaluated at resonance, or when

$$\frac{1}{4p\tau_{eff}^3\omega_B^2} = -1 + \frac{\delta\omega_{0n}}{2p\omega_B} \tag{43}$$

Then, as $p \to \pm\infty$, $4\tau_{eff}^3\omega_B^3 \sim -1/p$. Also needed is the cube root of p which, when evaluated, the real branch is used. For large $|p|$, the sum over p is converted into an integral, and assuming that $\eta_k^2 > (\delta\omega_{0n}/2\omega_B - 1/4\tau_{eff}^3\omega_B^3)^2$, then the bounce-averaged resonance function is approximately

$$Re\{\overline{\Omega_n}^{-1}\} \approx J_n^2\,\pi\tau_{eff}^2\omega_B\, Ai^2(-\delta\omega_{0n}\tau_{eff}) \tag{44}$$

for those particles with $V_{\|,0} \gg V_{\perp,0}(2\delta\omega_{0n}/n\omega_{c0})^{1/2}$, and

$$\approx J_n^2\,\pi\tau_{eff}^2\omega_B\, Ai^2[(\delta\omega_{0n} - \omega_B^{-2}\tau_{eff}^{-3})\tau_{eff}] \tag{45}$$

for those particles resonant near their turning points. Equations 44 and 45 are independent of η_k. Note, that these results are the same as those obtained from Equation 38. Finally, when $p \sim 0$, the particles are resonant far from the bounce phases when either $s^* \sim 0$ or $v^* \sim 0$. In this case, no simple expression for $\overline{\Omega_n}^{-1}$ can be found independent of η_k. For these particles, Equation 37 is the only simple way to calculate the resonance function.

A1.7. WKB Theory

In this section, the WKB theory for the wave propagation from the launching horn through the plasma is discussed. The fundamentals of the theory of electromagnetic waves in an inhomogeneous plasma are well known (see, for example, Budden, 1961). When combined with the quasi-linear equation of Section 4, the theory presented in this report is the simplest, self-consistent model of non-relativistic electron-cyclotron heating in a mirror that conserves energy.

Two types of equations are needed. First, the local equation of energy conservation is derived which determines the geometric and physical optics solutions for the propagation of electromagnetic waves. The second is the bounce average of this equation, which gives the energy conservation equation for the trapped particles. Regenerative effects due to the "phase-memory" of bouncing particles is ignored (see Berk and Book, 1969).

From Maxwell's equations, Poynting's theorem is

$$\nabla \cdot (\bar{\mathbf{E}}_{-k} \times \bar{\mathbf{B}}_k) + \frac{1}{2}\frac{\partial}{\partial t}(|\bar{E}|_k^2 + |\bar{B}|_k^2) + \frac{4\pi}{c} Re\{\mathbf{E}_{-k} \cdot \mathbf{J}_k\} = 0 \tag{46}$$

which can be written as

$$\left[\frac{\partial}{\partial t}\frac{\partial}{\partial \omega} - \nabla \cdot \frac{\partial}{\partial k}\right]\{\omega(1-N^2)\delta_{ij} - \omega N^i N^j\}\,\frac{1}{2}|\bar{E}^i \bar{E}^j|_k = 4\pi Re\{\bar{\mathbf{E}}_{-k} \cdot \bar{\mathbf{J}}_k\} \tag{47}$$

The last term is

$$\begin{aligned} 4\pi Re\{\bar{\mathbf{E}}_{-k} \cdot \bar{\mathbf{J}}_k\} = &-\frac{4\pi q^2}{m}\sum_{\pm}\left\langle \int \frac{dE\,d\mu\,B}{|v_{\parallel}|}\, v^i\, \bar{E}^i_{-k} \int_{-\infty}^{0} dt \right. \\ &\left. \times\; M_k^{lm}(t)\,\bar{E}_k^m(t)\frac{\partial}{\partial v^l(t)} f_0(E,\mu,\mathbf{R}) \exp\left[-i\int_0^t dt(\omega - \mathbf{k}\cdot\mathbf{v})\right]\right\rangle_{\phi} \end{aligned} \tag{48}$$

The sum over ± refers to the direction of motion along the field lines. The time dependence of $M_k^{lm}\,\partial/\partial v^l$ can be treated as those in Equation 27 by transforming to the complex basis. $\bar{E}_k^m$ can be expanded as in Equations 23 and 24, except in this case, the field is expanded about $(\mathbf{r}, t)$ instead of the guiding-center coordinates since the local currents are to be found. In addition, $f_0(\bar{X}, s)$ can be expressed in terms of $\mathbf{r}$ as in Equation 32, which gives

$$f_0(E,\mu,\bar{X},s) \approx \{1 + \hat{b}\cdot(\frac{n\mathbf{k}}{k_{\perp}^2} \times \nabla)\} f_0(E,\mu,\mathbf{r})$$

Then, with $v_i = (\delta_{n,n-1}\rho\omega_c e^{-i\xi}/\sqrt{2},\ \delta_{n,n+1}\rho\omega_c e^{i\xi}/\sqrt{2},\ v_{\parallel})$, Equation 48 becomes

$$\begin{aligned} 4\pi Re\{\bar{\mathbf{E}}_{-k} \cdot \bar{\mathbf{J}}_k\} = Re\Bigg\{&\left[1 - \frac{i}{2}\frac{\partial}{\partial \mathbf{k}} \cdot \nabla + \frac{i}{2}\frac{\partial}{\partial \omega}\frac{\partial}{\partial t}\right]|\bar{E}^{i^*} \bar{E}^m|_k \\ &\times \frac{4\pi q^2}{m}\sum_n \sum_{\pm} \int \frac{dE\,d\mu B}{|v_{\parallel}|} v^i\, \Omega_n^{-1}\, M_{op}^{m^*}\{1 + \hat{b}\cdot(\frac{n\mathbf{k}}{k_{\perp}^2} \times \nabla)\} f_0\Bigg\} \end{aligned} \tag{49}$$

Which, when combined with Equation 47, gives the local, energy conservation equation

$$\nabla \cdot \left(-\frac{\partial \mathsf{D}_R^{ij^*}}{\partial \mathbf{k}} \frac{1}{2} |E^{i^*} E^j|_k \right) + \frac{\partial}{\partial t} \left(\frac{\partial \mathsf{D}_R^{ij^*}}{\partial \omega} \frac{1}{2} |E^{i^*} E^j|_k \right) + \mathsf{D}_I^{ij^*} |E^{i^*} E^j|_k = 0 \tag{50}$$

where $\mathsf{D}^{ij^*} = \mathsf{D}_R^{ij^*} + i\mathsf{D}_I^{ij^*}$ is the local dispersion tensor

$$\begin{aligned} \mathsf{D}^{ij^*} &= \omega \, \epsilon^{ij^*} \\ \epsilon^{ij^*} &= (1 - N^2)\delta^{ij} + N^i N^{j^*} \\ &\quad - i \frac{4\pi q^2}{\omega m} \sum_n \sum_{\pm} \int \frac{dE d\mu B}{|v_{\|}|} v_i M_{op}^{j^*} \Omega_n^{-1} \{ 1 + \hat{b} \cdot (\frac{n\mathbf{k}}{k_\perp^2} \times \nabla) \} f_0 \end{aligned} \tag{51}$$

Equation 50 contains the first terms of a WKB theory for electromagnetic wave propagation in an inhomogeneous plasma. This is a generalization of the one-dimensional, electrostatic WKB theory derived by Berk and Book, 1969. For electromagnetic waves, the dispersion relation to all orders is

$$\int d^3 r \, \mathsf{D}^{ij}(\mathbf{r} - \mathbf{r}, (\mathbf{r} + \mathbf{r})/2) \, \overline{E}^j(\mathbf{r}) e^{-i\lambda(\mathbf{r} - \mathbf{r})} = 0$$

or

$$\sum_{q,r} \frac{(-1)^{q+r}}{2^r \, q! \, r!} \left(\frac{\partial}{\partial \mathbf{k}^1} \cdots \frac{\partial}{\partial \mathbf{k}^q} \right) \left(\frac{\partial}{\partial \mathbf{k}^1} \cdots \frac{\partial}{\partial \mathbf{k}^r} \right) \left(\underset{1}{\nabla} \cdots \underset{r}{\nabla} \, \mathsf{D}^{ij}(\mathbf{k}(\mathbf{r}), \mathbf{r}) \right) \left(\underset{1}{\nabla} \cdots \underset{r}{\nabla} \, \overline{E}^j(\mathbf{r}) \right) \tag{52}$$

The zeroth-order equation, $\mathsf{D}_R^{ij^*} |\overline{E}^{i^*} \overline{E}^j|_k = D^i_{R,mode}(\mathbf{k}_{mode}, \omega) |\overline{E}^i|_k^2 = 0$, is an eigenvalue equation. The solutions to this equation give geometric optics. This is used to determine the path of mode-energy flow. However, the first-order terms are needed to show energy conservation. The eigenvectors are the polarizations of the local modes, and the eigenvalues are the solutions to $D^i_{R,mode} = 0$, or $\mathbf{k}_{mode} = \nabla \lambda_{mode}(\mathbf{r})$.

Briefly, the procedure for computing the ray path is as follows. First, the ray path is considered to be sub-divided into many small segments $\Delta\mathbf{r}$. Within each segment, the dispersion tensor is diagonalized, and the dispersion relation and polarization for each of the eigenvectors, or modes, is found. The electric field at the back-side of $\Delta\mathbf{r}$ is then expressed in the basis formed by the mode polarizations. Finally, each mode then propagates at its group velocity to the front-side of $\Delta\mathbf{r}$, and the process is repeated. The group velocity is

$$\mathbf{v}_g^i = -\frac{\partial D_R^i}{\partial \mathbf{k}} \left(\frac{\partial D_R^i}{\partial \omega} \right)^{-1} \tag{53}$$

and, from its role in Equation 50, the group velocity is the velocity of energy flow. Furthermore, since $D_R^i = 0$ for each mode, the change in $\mathbf{k}$ after crossing $\Delta\mathbf{r}$ is given by

$$\frac{\partial \mathbf{k}}{\partial t} = \nabla D_R^i \left(\frac{\partial D_R^i}{\partial \omega} \right)^{-1} \tag{54}$$

Together, Equations 53 and 54 can be considered as the velocity of the mode-energy in $(\mathbf{r}, \mathbf{k})$ phase-space. Note that Equation 54 incorporates Snell's law, since $\mathbf{k}$ only changes in the direction of the gradient of D_R^i.

To obtain the physical optics solution to the problem of the wave propagation, the next-order terms of the WKB dispersion equation are used. These are equivalent to the energy conservation equation already derived (*ie.* Equation 50). This equation can be put into the familiar form if D_R^{ij} is diagonalized as before and if the total energy per mode is defined as

$$W_k^i = \frac{1}{8\pi} |E^i|^2 \frac{\partial D_R^i}{\partial \omega} \tag{55}$$

This gives

$$\nabla \cdot (\mathbf{v}_g^i W_k^i) + \frac{\partial W_k^i}{\partial t} + 2\mathbf{k}_I \cdot \mathbf{v}_g^i W_k^i = 0 \tag{56}$$

where $\mathbf{k}_I$ is the imaginary part of $\mathbf{k}$ given approximately by

$$\mathbf{k}_I = -D_I^i \left(\frac{\partial D_R^i}{\partial \mathbf{k}} \right)^{-1}$$

The solution to Equation 56 for each mode gives the physical optics solution to wave propagation. If the medium is loss-free, then the field intensity increases as $\sim 1/v_g^i$ along its ray path. When $v_g^i \to 0$, higher order derivatives of the field must be added to Equation 50. If the turning point is linear, then the D_R^i can be expanded about $\mathbf{r} \approx r_0$, giving

$$\frac{1}{2} \frac{\partial}{\partial \mathbf{k}} \frac{\partial}{\partial \mathbf{k}} D_R^i : \nabla \nabla \vec{E}^i - (\mathbf{r} - \mathbf{r}_0) \cdot (\nabla D_R^i) \vec{E}^i \approx 0 \tag{57}$$

Then, assuming that the spatial dependances are locally separable, then this equation is an Airy equation for that component of propagation along the gradient D_R^i. In this way, the standard WKB connection formulas and reflection coefficients can be calculated[13].

A1.8. The Local Resonance Function

The local resonance function used in the WKB theory function differs from the bounce averaged version used to determine the electron energy evolution. The local resonance function includes both the reactive, induced plasma currents and the local, resonant dissipation. The induced currents determine the real part of the dispersion relation which is used to calculate $\mathbf{k} = \nabla \lambda(\mathbf{r})$.

The local resonance function has three forms. For particles far from a stationary point, the resonance function is

$$\Omega_n^{-1} \approx J_n^2 \frac{i}{\nu(t)} \tag{58}$$

At this location, these particles are purely reactive.

When, a particle is near a stationary point, then

$$\Omega_n^{-1} \approx J_n^2 \frac{\sqrt{\pi}}{2} e^{-i\pi/4} \tau_{eff} \tag{59}$$

And, when $\nu \approx \nu \approx 0$, then $Re\{\Omega_n^{-1}\} \approx J_n^2 \pi\tau_{eff} Ai(\nu_n \tau_{eff})$, and $Im\{\Omega_n^{-1}\} \approx J_n^2 \pi\tau_{eff}\, Gi(\nu_n \tau_{eff})$ where $Gi(x) \sim 1/\pi x$ and $Gi(-x) \sim (1/4\sqrt{\pi}) x^{-1/3} \cos(2x^{2/3}/3 + \pi/4)$ for large x.

A1.9. Bounce-Averaged Energy Conservation

The local, energy conservation equation can be bounce-averaged to show the self-consistency of the approach used in the report. The total loss of wave energy averaged over the bounce motion of the trapped particles is equal to the bounce-averaged change in particle kinetic-energy.

The bounce-average of Equation 50 is

$$\oint \frac{ds\,\omega_B}{v_{\parallel}} \left\{ \nabla \cdot \mathbf{v}_g^i W_k^i + \frac{\partial}{\partial t} \frac{\partial W_k^i}{\partial \omega} \right\} = -\frac{1}{4\pi} \sum_{res} \overline{D}_I^{ij^*} |E^{i^*} E^j| \tag{60}$$

What is meant by the bounce average of the left-hand side is that the integral over velocity-space within each term is to be carried out after the bounce average. The equation states that the average of the divergence of the Poynting's flux and the time rate of change of the electric energy along the particle's orbit is equal to the loss of particle kinetic energy due to the local resonances. The integral on the left-hand side will not be evaluated. However, the right-hand side is consistent with the bounce-averaged quasi-linear equation, previously derived. To show this, the time rate of change of the electron kinetic energy (after the "sloshing" wave energy has been removed) is

$$\begin{aligned} \frac{\partial}{\partial t} \sum_{\pm} \int \frac{dE\, d\mu B}{|v_{\parallel}|} E\, f_0 &= \int d^3v \frac{1}{2} m\, \mathbf{v} \cdot \mathbf{v} \frac{\partial F_0}{\partial t} \\ &= \frac{q^2}{m} \sum_{res} \int d^3v\, \frac{1}{2} \mathbf{v} \cdot \mathbf{v}\, M^{ij} \frac{\partial}{\partial v^i} Re\{\overline{\Omega_n^{-1}}\} |E^i E^j|_k M_{op}^{j^*} F_0 \end{aligned} \tag{61}$$

Equation 61 is now integrated by parts which is performed most easily when the left-most diffusion operator has been re-expressed in terms of a real, cartesian coordinate system. This gives

$$\begin{aligned} \frac{\partial}{\partial t}\sum_{\pm}\int \frac{dEd\mu B}{|v_{\|}|}E\,F_0 &= -\sum_{res}\frac{q^2}{m}\int \frac{dEd\mu B}{|v_{\|}|}v^i\,Re\{\overline{\Omega_n}^{-1}\}|\overline{E}^{i^*}\overline{E}^{j}|_k M_{op}^{j^*}F_0 \\ &= \frac{1}{4\pi}\sum_{res}\overline{\mathsf{D}}_I^{ij^*}\,|\overline{E}^{i^*}\overline{E}|_k \end{aligned} \tag{62}$$

Therefore, the increase in trapped particle energy is equal to the loss of wave energy. For each region in velocity-space, the energy is exchanged at local, resonant interactions.

Appendix 2

Description of Fokker-Planck Code

[Most of this appendix originally appeared as a research report: "Description of the Fokker-Planck Code used to Model ECRH of the Constance 2 Experiment", PFC-RR-82/2, (1982).]

This report describes both the time-dependent, partial differential equation used to describe the development of the electron distribution during ECRH of the Constance 2 mirror-confined plasma and the method by which this equation was solved. The electrons are modeled in (v, θ) phase-space, where $\theta = sin^{-1}(v_{\|}/v)$. The ion distribution is considered to be a Maxwellian with known density and temperature. The ECRH is modeled with a bounce-averaged quasilinear equation which is strictly correct only for linear heating of confined particles. However, since the magnetic field is assumed to be parabolic, the heating can be "extended" into the loss cone when the potential is positive. Changes in the particle energy are assumed to occur randomly, over several passes through resonance. The potential of the plasma is also assumed to be parabolic and a known function of time. Those particles within the loss region of velocity-space are loss at a rate determined from their transit time. Each point in velocity space is advanced in time using a modified Alternating Direction Implicit (ADI) technique used by Killeen and Marx[2].

The report is organized into six sections. The first section describes the Fokker-Plank model for electron-electron and electron-ion collisions. The second section describes the loss-cone term from which the electron loss current is calculated. The third section describes the programming of the ECRH term. The fourth section describes the numerical method used to solve the partial-differential equation. The fifth section lists the diagnostics available to evaluate the code's performance. And, the final section gives some examples and checks of the operation of the program.

A2.10. Collisions

A2.10.1. Rosenbluth Potentials . The electron-electron and electron-ion collisions are given by the Rosenbluth formulas[4], or

$$\frac{\partial F_e(\mathbf{v})}{\partial t} = -\mathsf{D}_i(J^i_{ele} + J^i_{ion}) \tag{1}$$

where

$$J^i_\beta = \Gamma_\beta\left\{F_e(\mathbf{v})\mathsf{D}^i H_\beta(\mathbf{v}) - \frac{1}{2}\mathsf{D}_j(F_e(\mathbf{v})\mathsf{D}^j\mathsf{D}^i G_\beta(\mathbf{v}))\right\} \tag{2}$$

and where the potentials H_β and G_β satisfy Poisson's equation

$$\nabla^2 H_\beta(\mathbf{v}) = -4\pi \frac{m_e}{M_{cm}} F_\beta(\mathbf{v}) \qquad (3)$$

$$\nabla^2 G_\beta(\mathbf{v}) = 2\frac{M_{cm}}{m_e} H_\beta(\mathbf{v}) \qquad (4)$$

and $\Gamma_\beta = 4\pi e^2 e_\beta^2 \Lambda_{e\beta}/m_e^2$. M_{cm} is the reduced mass, or $m_e m_\beta/(m_e + m_\beta)$. Note that the derivatives, D_i, in Equations 1 and 2 are covariant derivatives. This insures the obvious result that the scaler formed from the divergence of the vector J_β^i is invariant to changes in the description of the coordinate system. The integral solutions to Equation 3 and 4 are

$$G_\beta(\mathbf{v}) = \int d^3v|\mathbf{v} - \mathbf{v}|F_\beta(\mathbf{v}) \qquad (5)$$

$$H_\beta(\mathbf{v}) = \left(\frac{m_e}{M_{cm}}\right) \int d^3v \frac{F_\beta(\mathbf{v})}{|\mathbf{v} - \mathbf{v}|} \qquad (6)$$

As will be shown in the next subsection, only $G_{ele}(v,\theta)$ need be numerically integrated. Since for each phase-space point, this integration involves a summation over all grid points and is very time consuming. Therefore, all of the coefficients for the integration is saved on disk^2. Equation 5 can be expressed in terms of the elliptic integral of the second kind, or

$$G_{ele}(v,\theta) = \int_0^\infty v^2 dv \int_0^\pi \sin\theta d\theta 4\sqrt{a+b}\, E\left(\frac{2b}{a+b}\right) F_{ele}(v,\theta) \qquad (7)$$

where

$$a = v^2 + v^2 - 2vvcos\theta cos\theta$$

$$b = 2vvsin\theta sin\theta$$

$$E(m) = \int_0^{\pi/2} d\phi \sqrt{1 - msin^2\phi}$$

A2.10.2. Reduction of the Fokker-Plank Equation. For this program, the electrons are placed in a (v, θ, ϕ, ψ) coordinate system, and Equation 1 must be expressed in terms of these coordinates. The electrons are assumed to be independent of gyrophase, ϕ, and the collision term is trivially bounced-averaged over the bounce-phase, ψ, by assuming a square-well. (The ECRH and endloss terms assume parabolic magnetic and potential profiles.)

Equation 1 becomes

$$\frac{1}{\Gamma_\beta}\frac{\partial F_e}{\partial t}\bigg|_\beta = -(\partial_i F_e)(\partial^i H_\beta) - F_e\nabla^2 H_\beta + \frac{1}{2}\Big\{(\mathsf{D}_i\mathsf{D}_j F_e)(\mathsf{D}^i\mathsf{D}^j G_\beta) + 2(\partial_j F_e)(\partial^j\nabla^2 G_\beta) + F_e\nabla^2\nabla^2 G_\beta\Big\} \tag{8}$$

or

$$= -4\pi F_e F_\beta\left(1-\frac{m_e}{M_{cm}}\right) + \frac{M_{cm}}{m_e}(\partial_i F_e)(\partial^i H_\beta)\left(1-\frac{m_e}{M_{cm}}\right) + \frac{1}{2}(\mathsf{D}_i\mathsf{D}_j F_e)(\mathsf{D}^i\mathsf{D}^j G_\beta) \tag{9}$$

The electron and ion terms are therefore

$$\frac{1}{\Gamma_{ee}}\frac{\partial F_e}{\partial t}\bigg|_{ele} = 4\pi F_e F_e + \frac{1}{2}(\mathsf{D}_i\mathsf{D}_j F_e)(\mathsf{D}^i\mathsf{D}^j G_{ele}) \tag{10}$$

$$\frac{1}{\Gamma_{ei}}\frac{\partial F_e}{\partial t}\bigg|_{ion} = \frac{4\pi m_e}{m_i}F_e F_i + \frac{M_{cm}}{m_e}(1-m_e/m_i)(\partial_i F_e)(\partial^i H_{ion}) + \frac{1}{2}(\mathsf{D}_i\mathsf{D}_j F_e)(\mathsf{D}^i\mathsf{D}^j G_{ion}) \tag{11}$$

The metric in the (v,θ) coordinate system can be found by transforming the metric of spherical coordinates to obtain

$$g_{ij} = \hat{v}\hat{v} + v^2\hat{\theta}\hat{\theta} + v^2 sin^2\theta\hat{\psi}\hat{\psi} \tag{12}$$

The most complicated term is the tensor formed from the covariant derivative of the velocity-space gradient, which, in terms of ordinary partial derivatives, is

$$\mathsf{D}_i\mathsf{D}_j F_e = \frac{\partial^2 F_e}{\partial v^i \partial v^j} - \Gamma^\lambda_{ij}\frac{\partial F_e}{\partial v^\lambda} \tag{13}$$

where Γ^λ_{ij} is the affine connection or *Christoffel symbol*[5] and is defined from the metric as

$$\Gamma^\lambda_{ij} = \frac{1}{2}g^{\lambda k}\Big\{\partial_i g_{kj} + \partial_j g_{ki} - \partial_k g_{ij}\Big\} \tag{14}$$

Since F_e is independent of the gyrophase, then only the matrices Γ^v_{ij} and Γ^ρ_{ij} need be calculated. They are

$$\Gamma^v_{ij} = -v\hat{\rho}\hat{\rho} - v sin^2\theta\hat{\phi}\hat{\phi} \tag{15}$$

$$\Gamma^\rho_{ij} = \frac{1}{v}\hat{v}\hat{\rho} + \frac{1}{v}\hat{\rho}\hat{v} - sin\theta cos\theta\hat{\phi}\hat{\phi} \tag{16}$$

This gives

$$\mathsf{D}_i\mathsf{D}_j F_e = \begin{pmatrix} \dfrac{\partial^2 F_e}{\partial v^2} & \dfrac{\partial^2 F_e}{\partial v\partial\theta} - \dfrac{1}{v}\dfrac{\partial F_e}{\partial\theta} & 0 \\ \dfrac{\partial^2 F_e}{\partial v\partial\theta} - \dfrac{1}{v}\dfrac{\partial F_e}{\partial\theta} & \dfrac{\partial^2 F_e}{\partial\theta^2} + v\dfrac{\partial F_e}{\partial v} & 0 \\ 0 & 0 & v sin^2\theta\dfrac{\partial F_e}{\partial v} + sin\theta cos\theta\dfrac{\partial F_e}{\partial\theta} \end{pmatrix} \tag{17}$$

and the tensor product of the two double gradients become

$$(1/2)g^{ik}g^{jl}(\mathrm{D}_i\mathrm{D}_jF_e)(\mathrm{D}_k\mathrm{D}_lG) = B\frac{\partial F^e}{\partial v}+C\frac{\partial F^e}{\partial \theta}+D\frac{\partial^2 F^e}{\partial v^2}+E\frac{\partial^2 F^e}{\partial \theta^2}+F\frac{\partial^2 F^e}{\partial v\partial \theta} \tag{18}$$

where

$$\begin{aligned}
2B &= \frac{1}{v^3}\left\{\frac{\partial^2 G}{\partial \theta^2}+2v\frac{\partial G}{\partial v}+ctn\theta\frac{\partial G}{\partial \theta}\right\}\\
2C &= \frac{1}{v^3 sin\theta}\left\{\frac{2-cos^2\theta}{vsin\theta}\frac{\partial^2 G}{\partial \theta^2}-2sin\theta\frac{\partial^2 G}{\partial v\partial \theta}+cos\theta\frac{\partial G}{\partial v}\right\}\\
2D &= \frac{\partial^2 G}{\partial v^2}\\
2E &= \frac{1}{v^4}\left\{\frac{\partial^2 G}{\partial \theta^2}+v\frac{\partial G}{\partial v}\right\}\\
2F &= \frac{2}{v^2}\left\{\frac{\partial^2 G}{\partial \theta\partial v}-\frac{1}{v}\frac{\partial G}{\partial \theta}\right\}
\end{aligned}$$

For the ions, H and G are independent of pitch-angle which allows an analytic expression for the electron-ion collision term and simplifies the tensor term above.

A2.10.3. The Electron-Ion Term . Although for electron-electron collisions, the potential, $G_{ele}(v,\theta)$, must be calculated from the evolving electron velocity distribution, the ions are assumed to be Maxwellian. Their potential can be calculated analytically.

Assuming,

$$F_{ion}(v,\theta,\phi) = \frac{n_{ion}}{\pi^{3/2}v_{thi}^3}e^{-(v/v_{thi})^2}$$

where $v_{thi}^2 = T_{ion}/m_i$. Only, the terms $\frac{\partial H_{ion}}{\partial v}$, $\frac{\partial G_{ion}}{\partial v}$, $\frac{\partial^2 G_{ion}}{\partial v^2}$ need be calculated. $\frac{\partial H_{ion}}{\partial v}$ can be found from Gauss's law and Equation 3,

$$\frac{\partial H_{ion}}{\partial v} = -2\frac{m_e}{M_{cm}}\frac{n_{ion}}{v_{thi}^2}G(v/v_{thi}) \tag{19}$$

where

$$G(x) = \frac{erf(x)-(2/\sqrt{\pi})xe^{-x^2}}{2x^2}$$

and, likewise, for G_{ion}

$$\begin{aligned}
\frac{\partial G_{ion}}{\partial v} &= \frac{2}{v^2}\frac{M_{cm}}{m_e}\int_0^v H_{ion}(v)v^2dv\\
&= \frac{2}{v^2}\frac{M_{cm}}{m_e}\left\{\frac{1}{3}v^3H_{ion}(v)-\frac{1}{3}\int_0^v v^3\frac{\partial H_{ion}}{\partial v}dv\right\}
\end{aligned} \tag{20}$$

But, $H_{ion}(v \to \infty) \to 0$, so

$$\begin{aligned} H_{ion}(v) &= -\int_v^\infty \frac{\partial H_{ion}}{\partial v} dv \\ &= \frac{m_e}{M_{cm}} \frac{n_{ion}}{v} erf(v/v_{thi}) \end{aligned} \tag{21}$$

Furthermore,

$$\begin{aligned} \int_0^v v^3 \frac{\partial H_{ion}}{\partial v} &= -2\frac{m_e}{M_{cm}} n_{ion} v_{thi}^2 \int_0^{v/v_{thi}} x^3 G(x) dx \\ &= -\frac{m_e}{2M_{cm}} n_{ion} v^2 \{erf(v/v_{thi}) - 3G(v/v_{thi})\} \end{aligned} \tag{22}$$

which gives

$$\frac{\partial G_{ion}}{\partial v} = n_{ion}\{erf(v/v_{thi}) - G(v/v_{thi})\} \tag{23}$$

and

$$\frac{\partial^2 G_{ion}}{\partial v^2} = \frac{2n_{ion}}{v} G(v/v_{thi}) \tag{24}$$

A2.10.4. Summary of Collision Terms . The Fokker-Plank collision terms can, thus, be summarized as

$$\begin{aligned} \Gamma_e^{-1} \frac{\partial F_e}{\partial t}\bigg|_{collisions} =& (A_{ee} + A_{ei})F_e + (B_{ee} + B_{ei})\frac{\partial F_e}{\partial v} + (C_{ee} + C_{ei})\frac{\partial F_e}{\partial \theta} \\ &+ (D_{ee} + D_{ei})\frac{\partial^2 F_e}{\partial v^2} + (E_{ee} + E_{ei})\frac{\partial^2 F_e}{\partial \theta^2} + F_{ee}\frac{\partial^2 F_e}{\partial v \partial \theta} \end{aligned} \tag{25}$$

where

$$\begin{aligned} A_{ee} &= 4\pi F_e \\ B_{ee} &= \frac{1}{2v^3}\left\{\frac{\partial^2 G}{\partial \theta^2} + 2v\frac{\partial G}{\partial v} + ctn\theta\frac{\partial G}{\partial \theta}\right\} \\ C_{ee} &= \frac{1}{2v^3 sin\theta}\left\{\frac{2 - cos^2\theta}{v sin\theta}\frac{\partial^2 G}{\partial \theta^2} - 2sin\theta\frac{\partial^2 G}{\partial v \partial \theta} + cos\theta\frac{\partial G}{\partial v}\right\} \\ D_{ee} &= \frac{1}{2}\frac{\partial^2 G}{\partial v^2} \\ E_{ee} &= \frac{1}{2v^4}\left\{\frac{\partial^2 G}{\partial \theta^2} + v\frac{\partial G}{\partial v}\right\} \\ F_{ee} &= \frac{1}{2v^2}\left\{\frac{\partial^2 G}{\partial \theta \partial v} - \frac{1}{v}\frac{\partial G}{\partial \theta}\right\} \end{aligned}$$

and

$$
\begin{aligned}
A_{ei} &= 4\pi\frac{m_e}{m_i}F_{ion}\\
B_{ei} &= \frac{n_{ion}}{v^2}\Big\{erf(v/v_{thi}) - G(v/v_{thi})\Big[1 + 2(1 - m_e/m_i)(v/v_{thi})^2\Big]\Big\}\\
C_{ei} &= \frac{n_{ion}cos\theta}{2v^3 sin\theta}\{erf(v/v_{thi}) - G(v/v_{thi})\}\\
D_{ei} &= \frac{n_{ion}}{v}G(v/v_{thi})\\
E_{ei} &= \frac{n_{ion}}{2v^3}\{erf(v/v_{thi}) - G(v/v_{thi})\}
\end{aligned}
$$

A2.10.5. A Simple Check . As a check of the formula, the function $F_e(v,\theta) \sim e^{-(v/v_{the})^2}$ must be a stationary solution to the Fokker-Plank collision operator. Ignoring the slower, electron-ion collisions,

$$\frac{\partial F_e}{\partial t} = 4\pi v_{the}^3 F_e^2 + \frac{n}{x^2}\{erf(x) - G(x)\}\frac{\partial F_e}{\partial x} + \frac{n}{x}G(x)\frac{\partial^2 F_e}{\partial x^2} \qquad (26)$$

But,

$$
\begin{aligned}
F_e &= \frac{n}{\pi^{3/2}v_{the}^3}e^{-x^2}\\
\frac{\partial F_e}{\partial x} &= -2xF_e\\
\frac{\partial^2 F_e}{\partial x^2} &= -2F_e + 4x^2F_e
\end{aligned}
\qquad (27)
$$

so that, when Equation 26 is substituted into Equation 25, $\frac{\partial F_e}{\partial t} = 0$. It is also easy to show that when $T_e = T_i$, the electron-ion term vanishes.

A2.11. End Losses and Sources

For particles in the loss-cone, the particle loss rate is given by

$$\left.\frac{\partial F_e}{\partial t}\right|_{losscone} = -\frac{F_e}{\tau_{transit}} \qquad (28)$$

where $\tau_{transit}$ is the time for a particle to go from the midplane to the mirror-peak.

The loss-boundary is given by $v_{\|}(s = s_{mp}) = 0$, or

$$\mu B_{mp} - \frac{q}{m}\Phi_{mp} = \mu B_0 + \frac{1}{2}V_{\|,0}^2 - \frac{q}{m}\Phi_0 \qquad (29)$$

or

$$V_{\perp,0}^2(1 - R_m) + V_{\|,0}^2 = \frac{2q}{m}\Delta\Phi \qquad (30)$$

where $\Delta\Phi = \Phi_0 - \Phi_{mp}$, and R_m is the mirror ratio. In (v,θ) phase-space,

$$v^2\Big\{1 - R_m sin^2\theta\Big\} = \frac{2q}{m}\Delta\Phi \qquad (31)$$

The condition of being within the loss-region is

$$v^2 > \frac{(2q/m)\Delta\Phi}{1 - R_m sin^2\theta} \tag{32}$$

for particles such that $|sin\theta| < \sqrt{1/R_m}$, and

$$v^2 < \frac{(2q/m)\Delta\Phi}{1 - R_m sin^2\theta} \tag{33}$$

for particles such that $|sin\theta| > \sqrt{1/R_m}$. As can be seen, for positive $\Delta\Phi$, only the first inequality is used, and for negative $\Delta\Phi$, only the second is used.

The transit time is obtained from the equations of motion. Since

$$B(s) = B_0(1 + \frac{s^2}{L^2}) \tag{34}$$

$$\Phi(s) = \Delta\Phi(1 - \frac{s^2}{L^2}) \tag{35}$$

then

$$s(t) = \frac{V_{\|,0}}{\omega_B} \sin(\omega_B t + \psi) \tag{36}$$

where

$$\begin{aligned} \omega_b^2 &= \frac{2}{L_2}(\mu B_0 + (q/m)\Delta\Phi) \\ &= \frac{v^2 sin^2\theta}{L^2} + \frac{2q\Delta\Phi}{mL^2} \end{aligned} \tag{37}$$

Therefore,

$$\tau_{transit} = \frac{1}{\omega_B} sin^{-1}\left(\frac{L\omega_B}{v cos\theta}\right) \tag{38}$$

When $\omega_B < 0$, then $\tau_{transit} \sim sinh^{-1}(L\omega_B / v\,cos\theta)$. Note that Yushmanov particles are not included in this analysis.

In addition, a Maxwellian distribution of electrons are assumed to be at the mirror peak and enter the mirror-region at the same transit rate calculated above. Note that energy is conserved for the incoming particles so that this Maxwellian distribution is mapped to the passing region of velocity space. Finally, ionization with a given pressure of hydrogen gas is included. The ionization cross-section is approximated by ???. For a region of velocity-space, (v, θ), $F(v, \theta)$ decreases according to the difference between the ionization rate at (v, θ) and that region which is more energetic by 13.6ev. This reduces the energy of the electrons while a $\sim (1/2)ev$ source of cold electrons is added to the distribution that is proportional to the total ionization rate.

A2.12. The ECRH Term

A2.12.1. The Diffusion Paths . The ECRH term used for this code was derived by Mauel[1]. In this model, only linear heating of trapped, electrons are heated. Since the effect of the heating is bounced-averaged, particles in the loss region of velocity-space are not heated.

The bounce-averaged diffusion equation is

$$\frac{\partial F_e}{\partial t} = \alpha_R^2 \sum_{res} \frac{\partial}{\partial \chi} D_{res} \frac{\partial}{\partial \chi} F_e \tag{39}$$

where $\alpha_R^2 = \frac{1}{2}\frac{q^2}{m^2}|E_R|^2$ is the square of the right-handed, electric acceleration, and

$$D_{res} = (\rho_B \omega_c)^2_{res} \, Re\{\overline{\Omega_n^{-1}}\} \, J_n^2(\rho k_\perp) \tag{40}$$

$$\frac{\partial}{\partial \chi} = \frac{1}{B_{res}} \frac{\partial}{\partial \mu} + \frac{\partial}{\partial E} \tag{41}$$

For the program, the diffusion equation is simplified by re-writting the Equation 41as

$$\frac{\partial F_e}{\partial t} = \alpha_R^2 \sum_{res} \left\{ D_{res} \frac{\partial^2 F_e}{\partial \chi^2} + \frac{2D_{res}}{v_{perp}^2} \frac{\partial F_e}{\partial \chi} \right\} \tag{42}$$

This uses the (very good) approximation that the dominant $v_{\perp,res}$-dependance in D_{res} is the velocity-factor $v^2_{\perp,res}$.

The gradient along the diffusion path, $\partial / \partial \chi$, can be written in (v, θ) coordinates by using the identities

$$f(E, \mu, v, \theta) = E - \frac{1}{2}v^2 - q\Phi/m = 0$$

$$g(E, \mu, v, \theta) = B_0 \mu - \frac{1}{2} v^2 sin^2\theta = 0 \tag{43}$$

and the appropriate Jacobians. For instance,

$$\frac{\partial \theta}{\partial E} = -\frac{\dfrac{\partial(f,g)}{\partial(E,v)}}{\dfrac{\partial(f,g)}{\partial(\theta,v)}} = -\frac{tan\theta}{v^2} \tag{44}$$

and, likewise,

$$\frac{\partial \theta}{\partial \mu} = \frac{B_0}{v^2 sin\theta cos\theta} \tag{45}$$

$$\frac{\partial v}{\partial E} = \frac{1}{v} \tag{46}$$

$$\frac{\partial v}{\partial \mu} = 0 \tag{47}$$

This gives the gradient along the diffusion paths as

$$\frac{\partial}{\partial\chi}=\frac{1}{v}\frac{\partial}{\partial v}+\xi\frac{\partial}{\partial\theta} \tag{48}$$

where $\xi=(1/R_{res}-sin^2 0)/v^2 cos\theta sin\theta$. Also, after some algebra,

$$\frac{\partial^2}{\partial\chi^2}=\frac{1}{v^2}\frac{\partial^2}{\partial v^2}-\frac{1}{v^3}\frac{\partial}{\partial v}+\frac{2\xi}{v}\frac{\partial^2}{\partial\theta\partial v}+\xi^2\frac{\partial^2}{\partial\theta^2}-\xi\left\{\xi\frac{2cos^2\theta-1}{sin\theta cos\theta}+\frac{4}{v^2}\right\}\frac{\partial}{\partial\theta} \tag{49}$$

The ECRH term can then be summarized as

$$\begin{aligned}\frac{1}{\alpha_R^2}\frac{\partial F_e}{\partial t}\bigg|_{ECRH} ={}& B_{ECRH}\frac{\partial F_e}{\partial v}+C_{ECRH}\frac{\partial F_e}{\partial\theta}+D_{ECRH}\frac{\partial^2 F_e}{\partial v^2}\\ &+E_{ECRH}\frac{\partial^2 F_e}{\partial\theta^2}+F_{ECRH}\frac{\partial^2 F_e}{\partial v\partial\theta}\end{aligned} \tag{50}$$

where

$$\begin{aligned}B_{ECRH}&=\frac{1}{v}D_2-\frac{1}{v^3}D_1\\ C_{ECRH}&=\xi\left\{D_2-D_1\left[\xi\frac{2cos^2\theta-1}{sin\theta cos\theta}+\frac{4}{v^2}\right]\right\}\\ D_{ECRH}&=\frac{1}{v^2}D_1\\ E_{ECRH}&=\xi^2 D_1\\ F_{ECRH}&=\frac{2\xi}{v}D_1\end{aligned}$$

A2.12.2. The Resonance Function. In this section, the rules used to evaluate D_{res} are explained. Since $\rho_B k_\perp \ll 1$,

$$D_{res}=(\rho_B\omega_c)^2_{res}Re\{\overline{\Omega}^{-1}_{n=1,2}\}\begin{cases}1, & \text{if } n=1.\\ (1/4)\,k_\perp^2\rho_B^2, & \text{if } n=2\end{cases} \tag{51}$$

where

$$Re\{\overline{\Omega_n}^{-1}\}=\frac{1}{4}\omega_B\tau^2_{eff} \qquad (\text{where } \tau^{-2}_{eff}=\nu_n/2) \tag{52}$$

$$Re\{\overline{\Omega_n}^{-1}\}=2\pi\omega_B\tau^2_{eff}Ai^2(\nu_n\tau_{eff}) \qquad (\text{where } \tau^{-3}_{eff}=\nu_n/2) \tag{53}$$

and where $\nu_n=\omega-n\omega_c-k_\parallel v_\parallel$. Here, all quantities are evaluated at the point of resonance. Equation 51 is used for "simple" resonance points (*ie.* when $\nu_n\rightarrow 0$ while ν remains finite); and Equation 52 is used for "Airy" resonance points, which occur when both ν_n and $\nu_n\rightarrow 0$.

The type and number of resonance points depend upon R_{res}, $k_\parallel$, and the actual bounce-orbit of the electron. For the program, these variations can be classified into four categories which were shown in Chapter 4 in Figure 38. The mirror is assumed to be symmetric for interchange of s with $-s$.

A2.13. Numerical Methods

The Fokker-Plank equation (Equations 24, 27 and 38) is solved by the modified Alternating Direction Implicit (AID) method used by Killeen and Marx[2]. A grid in the (v, θ) phase space is defined with variable spacing in the v-direction to provide a wide energy resolution and in the θ-direction to allow quadrature integration. Typically, the grid has 45 v-points and 16-theta points. Integration in the v-direction is performed with Simpson's rule modified to for variable grid spacing[2].

The ADI solution consists of "splitting" the 2-dimensional partial differential equation into two parts so that the v and θ differences can be taken separately. This gives two equations which can be solved implicitly.

$$\begin{aligned}\frac{F_e^{t+dt/2} - F_e^t}{\Delta t} &= \frac{1}{2}S + \frac{1}{2}AF_e^{t+dt/2} + B\frac{\partial F_e^{t+dt/2}}{\partial v} \\ &\quad + D\frac{\partial^2 F_e^{t+dt/2}}{\partial v^2} + \frac{1}{2}F\frac{\partial^2 F_e^{t+dt/2}}{\partial v \partial \theta} \qquad (54)\end{aligned}$$

$$\begin{aligned}\frac{F_e^{t+dt} - F_e^{t+dt/2}}{\Delta t} &= \frac{1}{2}S + \frac{1}{2}AF_e^{t+dt} + C\frac{\partial F_e^{t+dt}}{\partial \theta} \\ &\quad + E\frac{\partial^2 F_e^{t+dt}}{\partial \theta^2} + \frac{1}{2}F\frac{\partial^2 F_e^{t+dt}}{\partial v \partial \theta} \qquad (55)\end{aligned}$$

If, in each equation, central differences are taken for each derivative (except for a backward derivative for the mixed term), each equation can be written as

$$A^n F_e^{n-1} + B^n F_e^n + C^n F_e^{n+1} = W^n \qquad (56)$$

where, for the v-split

$$\begin{aligned}A_v^{n,l} &= \frac{\Delta t}{\Delta v}(B - \frac{2D}{\Delta v_-} + \frac{1}{4}\frac{F}{\Delta \theta_-}) \\ B_v^{n,l} &= 1 - \frac{1}{2}\Delta t A + \frac{2\Delta t D}{\Delta v}(\frac{1}{\Delta v_+} + \frac{1}{\Delta v_-}) \\ C_v^{n,l} &= -\frac{\Delta t}{\Delta v}(B + \frac{2D}{\Delta v_+} + \frac{1}{4}\frac{F}{\Delta \theta_-}) \\ W_v^{n,l} &= F_e^{n,l} + \frac{1}{2}\Delta t S + \frac{\Delta t F}{4\Delta v \Delta \theta_-}(F_e^{n-1,l-1} - F_e^{n+1,l-1}) \\ &\quad + \frac{\Delta t F}{4\Delta v \Delta \theta_+}(F_e^{n+1,l+1} + F_e^{n-1,l-1} - F_e^{n-1,l+1} - F_e^{n+1,l-1})\end{aligned}$$

and, for the θ-split,

$$A_\theta^{n,l} = \frac{\Delta t}{\Delta\theta}(C - \frac{2E}{\Delta\theta_-} + \frac{1}{4}\frac{F}{\Delta v_-})$$
$$B_\theta^{n,l} = 1 - \frac{1}{2}\Delta t A + \frac{2\Delta t E}{\Delta\theta}(\frac{1}{\Delta\theta_+} + \frac{1}{\Delta\theta_-})$$
$$C_\theta^{n,l} = -\frac{\Delta t}{\Delta\theta}(C + \frac{2E}{\Delta\theta_+} + \frac{F}{\Delta v_-})$$
$$W_\theta^{n,l} = F_e^{n,l} + \frac{1}{2}\Delta t S + \frac{\Delta t F}{4\Delta\theta\Delta v_-}(F_e^{n-1,l-1} - F_e^{n-1,l+1}) + \frac{\Delta t F}{4\Delta\theta\Delta v_+}(F_e^{n+1,l+1} + F_e^{n-1,l-1} - F_e^{n+1,l-1} - F_e^{n-1,l+1})$$

where

$$\Delta v^{n,l} = v^{n+1,l} - v^{n-1,l}$$
$$\Delta v_+^{n,l} = v^{n+1,l} - v^{n,l}$$
$$\Delta v_-^{n,l} = v^{n,l} - v^{n-1,l}$$

and similarly for $\Delta\theta, \Delta\theta_+, \Delta\theta_-$. In the above equations, the index n refers to the v-direction and the index l refers to the θ-axis.

Using boundary conditions, these difference equations define a tri-diagonal matrix which can be easily transformed into upper triangular form. For example, the matrix defined in Equation 56 becomes

$$\begin{pmatrix} B^1 & C^1 & & & & \\ A^2 & B^2 & C^2 & & & \\ & A^3 & B^3 & C^3 & & \\ & & & \vdots & & \\ & & & A^{N-1} & B^{N-1} & C^{N-1} \\ & & & & A^N & B^N \end{pmatrix} \cdot \begin{pmatrix} F_e^1 \\ F_e^2 \\ F_e^3 \\ \vdots \\ F_e^{N-1} \\ F_e^N \end{pmatrix} = \begin{pmatrix} W^1 \\ W^2 \\ W^3 \\ \vdots \\ W^{N-1} \\ W^N \end{pmatrix} \tag{57}$$

which is equivalent to

$$\begin{pmatrix} 1 & E^1 & & & & \\ & 1 & E^2 & & & \\ & & 1 & E^3 & & \\ & & & \vdots & & \\ & & & & 1 & E^{N-1} \\ & & & & & 1 \end{pmatrix} \cdot \begin{pmatrix} F_e^1 \\ F_e^2 \\ F_e^3 \\ \vdots \\ F_e^{N-1} \\ F_e^N \end{pmatrix} = \begin{pmatrix} Y^1 \\ Y^2 \\ Y^3 \\ \vdots \\ Y^{N-1} \\ Y^N \end{pmatrix} \tag{58}$$

where

$$E^1 = \frac{C^1}{B^1} \qquad Y^1 = \frac{W^1}{B^1} \tag{59}$$
$$E^n = \frac{C^n}{B^n - A^n E^{n-1}} \qquad Y^n = \frac{W^n - A^n Y^{n-1}}{B^n - A^n E^{n-1}} \tag{60}$$

After the coefficients E^n and Y^n have been found, the solution is trivial:

$$F_e^N = Y^N$$
$$F_e^{n-1} = Y^{n-1} - E^{n-1} F_e^n \tag{61}$$

The boundary conditions of the program are

1. $\left.\frac{\partial F_e}{\partial v}\right|_{v=0,\theta=\pi/2} = 0$ due to azimuthal symmetry. $F_e^{0,1} = F_e^{1,1}$.
2. $F_e(n = N) = 0$.
3. $F_e^{0,l}$ is independent of l (*ie.* θ).
4. $\left.\frac{\partial F_e}{\partial \theta}\right|_{\theta=0,\pi} = 0$ due to azimuthal symmetry. $F_e^{n,L-1} = F_e^{n,L}$.
5. $\left.\frac{\partial F_e}{\partial \theta}\right|_{\theta=\pi/2} = 0$ from bounce-direction symmetry.

These boundary conditions are used to combine or eliminate terms in the upper left and bottom right corners of the matrix. In this way, the initial conditions for the sweep out and back through the grid indices are determined.

Finally, note that all of the gradients of $G_{e/e}(v,\theta)$ needed for the electron-electron collision term can be found using central differences since all of the boundary points are obtained implicitly from the interior points and the boundary conditions.

Appendix 3

Comments on Hot Electron Stablization of DCLC

The original goal of the Constance 2 experiments was to investigate the "mechanism" of hot electron statbilization, reported in the experiments of Ioffe, *et al.*, 1975, Klinkowstein and Smullin, 1978, Kanaev, 1979, and Mauel, 1979. The hope was that by repeating the conditions under which E-beam and ECRH stabilization was observed, the superior diagnostics of Constance 2 would be able to measure the electron population present during stabilization. One of the key issues to be determined by the experiments was whether or not a μ-trapped electron population depressed the potential, confining cool ions and stabilizing loss-cone instabilities or whether "some other mechanism" (such as hot-electron driven turbulence) was responsible for the observed stabilization.

The first step of this investigation was the formation of a hot, mirror-confined plasma which was unstable to loss-cone instabilities. For over a year and a half, experiments were conducted to try and reproduce this plasma consistently. As explained in Chapter 2, this required operating at low densities and at low Ioffe currents. For "optimum" gun conditions, the ion-cyclotron fluctuations, characteristic of DCLC, were observed. An example of this is shown in Figure 5. The sharp $> 30db$ peak at the ion-cyclotron frequency was the primary evidence that the instability was indeed of the DCLC type. For this shot, the gun diamagnetism was a factor of 5 larger than the shots which were typical for ECRH experiments reported in the main body of the text. The fluctuations corresponded to a rise of the floating potential and occured about 100μsec after crowbar. The line density did not appear to be strongly effected by the instability. However, the total ion endloss did show a marked increase during the fluctuations.

For the short time when the gun operated as decribed above, ECRH was used to repeat some of the stabilization results reported in Mauel, 1979. Figures 2 and 3 summarize these results. In Figure 2, the results of increasing the ECRH power for fixed injection times are shown. As in the Constance 1 experiments, for low powers, the intensity of the fluctuation increases and, for high powers, stabilization is observed. Figure 3 shows the effect of the changing fluctation intensity on the total ion endloss. For plasma formed under similar conditions, the "range" of fluctuation intensity shown in the figure was obtained by either varying the ECRH power or by turning-off the divertor coil. Clearly, the fluctuations were increasing the ion-loss rate. In other words, the ion-cyclotron

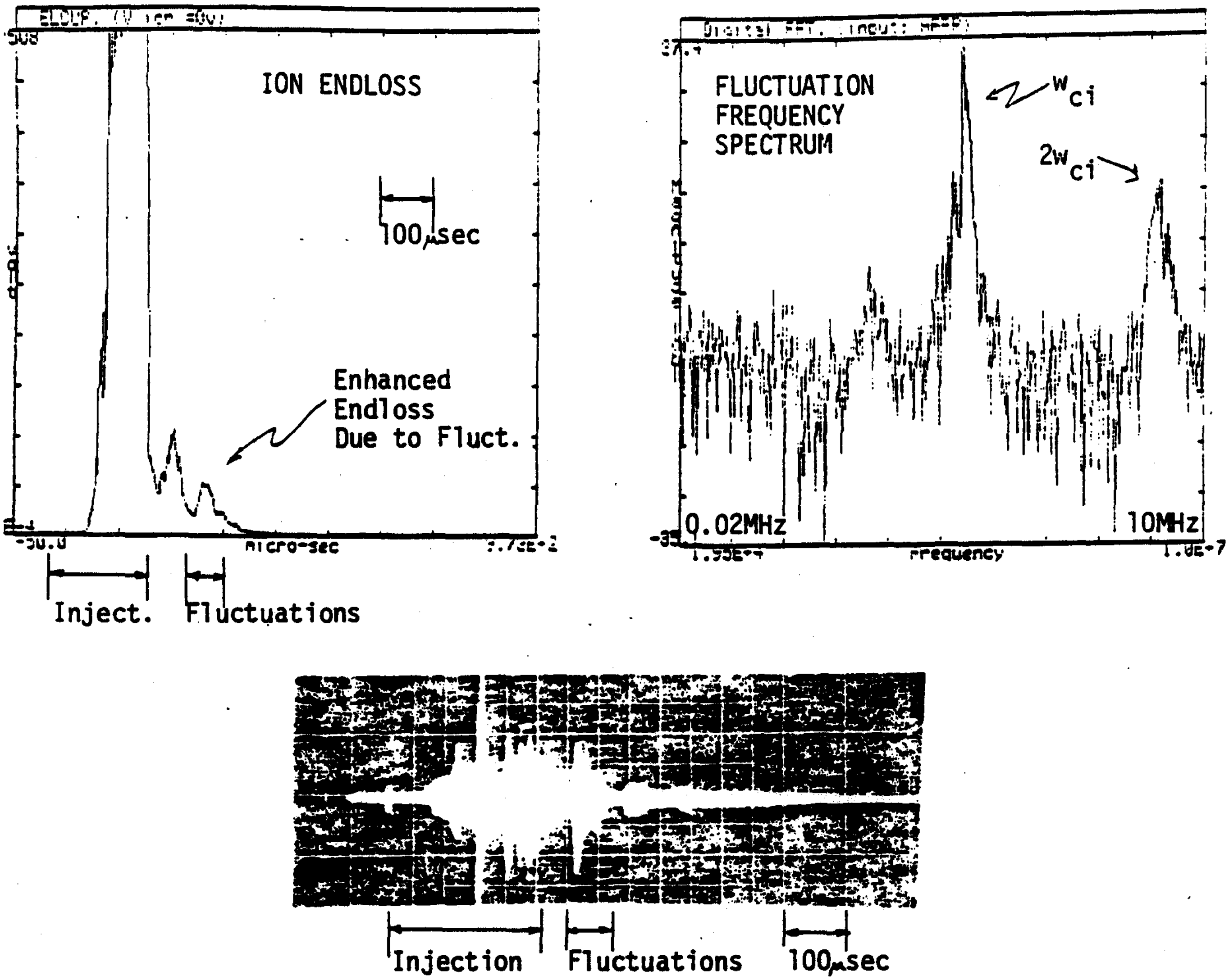

Figure 1. An example of the ion cyclotron fluctuations observed in the Constance 2 plasma under "optimum" gun operation, low density operation, and at low Ioffe currents.

heating of the instability was "pumping-out" the warm-trapped ions *in the same way as ECRH was observed to "pump-out" the warm, magnetically-trapped electrons in Chapter 5.* In the case of the DCLC instability, however, as the fluctuations pump ions into the loss region, the "drive" for the instability is reduced. A steady-state fluctuation level develops which balances the RF-driven losses into the loss-cone by the transit rate of these ions out of the mirror

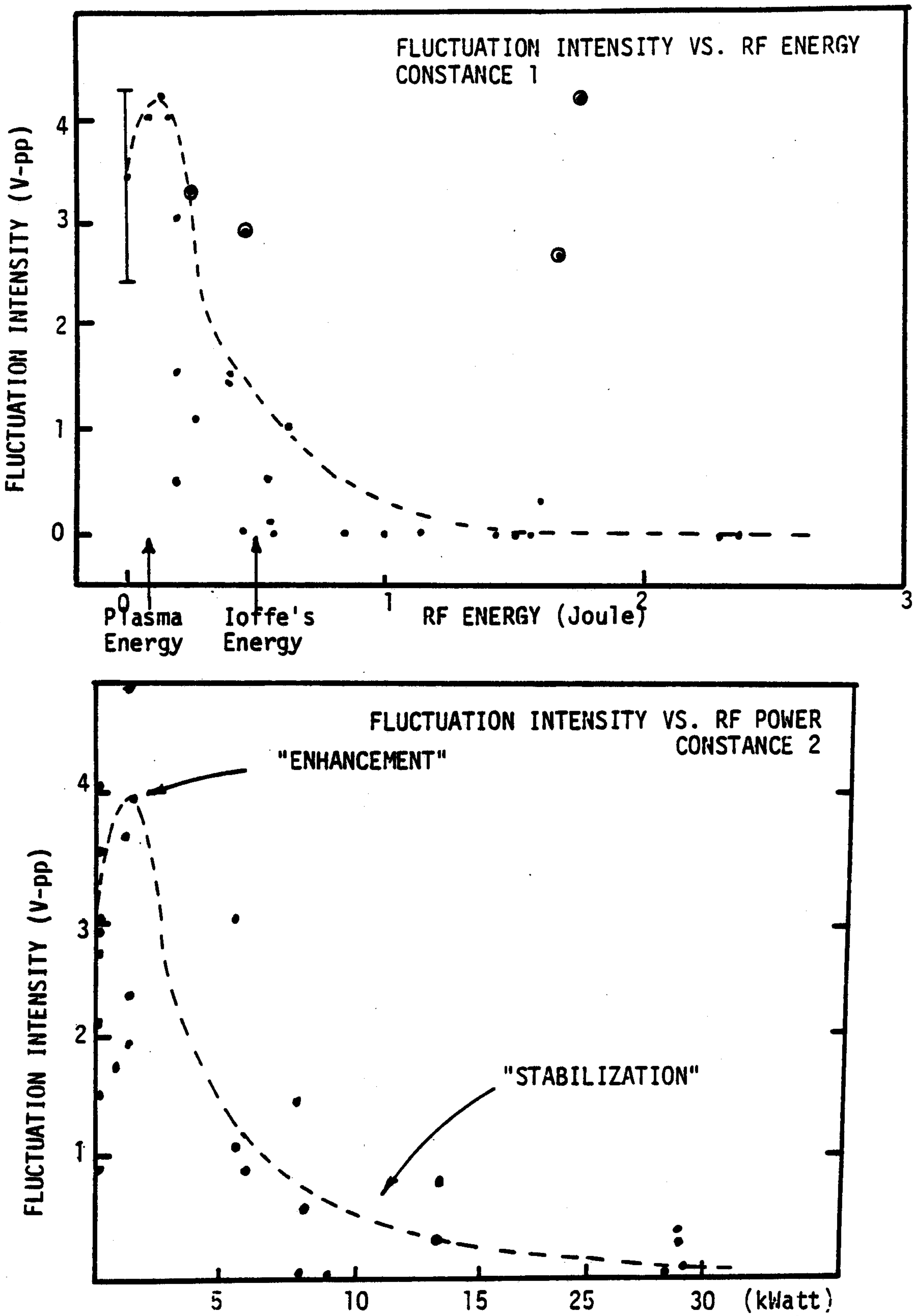

Figure 2. A summary of the ECRH stabilization observed in the Constance 1 (top) and Constance 2 (bottom) experiments. Notice that as the RF power was increased, the fluctuation intensity at first increases and then decreases.

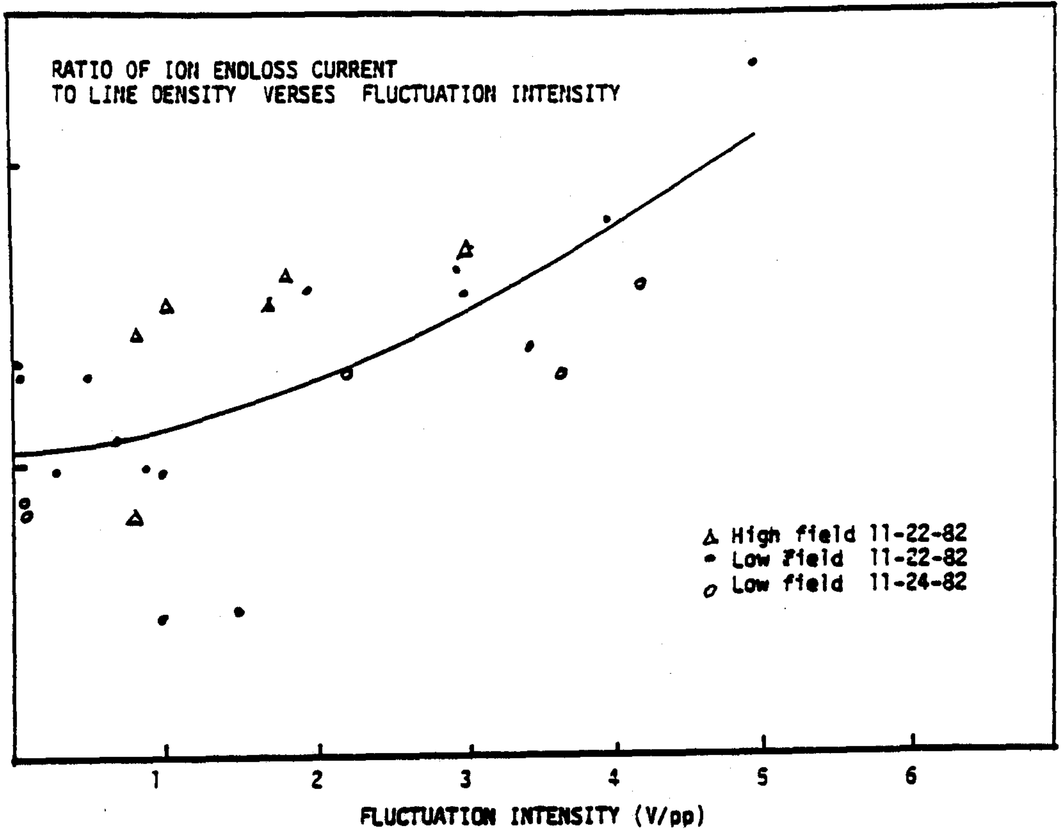

Figure 3. A graph of the total ion endloss as a function of the fluctuation intensity. The "range" of parameters was obtained for similar plasma while varying either the ECRH power (*i.e.* stabilization or enhancement) or turning off the divertor coil (which always produced a micro-stable plasma).

(Baldwin, *et al.* 1977).[1]

Although futher experiments were attempted, the strong instability could not be reproduced. Part of this is due to the inability to reproduce the "factor of 5" increase in diamagnetism observed during strong instability. However, if the density was reduced further, even 50ev ions should be unstable ***provided that good vacumn conditions are maintained in the experiment.*** It is likely that with proper use of Ti-gettering the fluctuations might be routinely reproduced in Constance 2.

Since the physics of ECRH has been thoroughly investigated, can any statement be made about the "mechanism" for DCLC stabilization? Two possiblities are suggested by the experiments summarized in this thesis. First, both the Fokker-Planck simulation and the diamagnetic and endloss measurements suggest that sizable fractions (> 10%) of 100-500ev

---

[1] This was one of the first *victories* of the quasilinear theory! Since the instability saturated at relatively low fluctuation levels, little non-linear wave-wave or wave-particle interactions occured, enabling a very accurate description of the 2XIIB experiment in the presence of the ion-cyclotron fluctuations.

"warm" electron populations are created for ECRH powers greater than 5-10kWatt. Under these conditions a $> 10\%$ reduction of the potential ($\delta\Phi \sim T_{e,bulk}\delta n_{warm}/n$) should result. This was the same conclusion reached in the Constance 1 ECRH experiments, and also the same reasoning used by Ioffe, *et al.*, 1976 and Kanaev, 1979. The implication of this observation is that significant depressions of the potential may occur. A difference between both the Constance 1 and 2 experiments and those of PR-6, however, is that, in the Constance experiments, the resonant zones were to either side of the midplane; whereas, in PR-6, the heating zone was at the midplane. Thus, the Constance 2 experiments suggest that either the depressions of the potential occured to either side of the midplane or that the potential throughout the entire trap was lowered. In either case, the results of this thesis suggest that sufficiently dense, μ-trapped electrons are created by the ECRH which appear to have stabilized the instability. However, the strong heating of the electrons at the edge of the plasma, which increases the plasma density (presumably) due to wall interactions, was also observed in this thesis. Density increases were observed in both the Constance 1 ECRH experiments and during the stabilization recorded with Constance 2. Since the DCLC instability is strongly affected by the plasma parameters at the steepest density gradient (*i.e.* the edge), the activity at the plasma's edge may also be responsible for the observed stabilization either because of the reduction of the outer plasma potential or perhaps because of "line-tying" to the walls.

The resolution of these hypotheses may be possible in future Constance experiments—especially if vacuum conditions are improved. In addition, if axial potential profiles could be estimated (from, for example, floating probe analysis), significant progress could be made toward realizing whether or not hot-electron potential modifications do in fact stabilize DCLC or whether the observations recorded in the Constance experiments were created by some "other", unknown mechanism.

References

Chapter 1.

1. Aamodt, R. E., "Particle Containment in Mirror Traps in the presence of Fluctuating Electric Fields," *Phys. Rev. Letters.* 27, (1971), 135.
2. Baldwin, D. E. and B. G. Logan, "Improved Tandem Mirror Fusion Reactor," *Physics Review Letters.* 43, (1980), 1318-1321.
3. Baldwin, D. E., *et al.*, eds., *Physics Basis for MFTF-B.* No. UCID-18496-Part1, Lawrence Livermore Laboratory, (1980).
4. Becker, M. C., R. A. Dandle, *et. al.*, "An Investigation of Electron Heating at the Cyclotron Frequency," *Nuclear Fusion: 1962 Supplement.* (1962), 345-352.
5. Berk, H. L., "Derivation of the Quasilinear equation in a magnetic field," *J. Plasma Physics.* 20, (1978), 205-219.
6. Bernstein, I. B., and D. C. Baxter, "Relativistic Theory of Electron Cyclotron Resonance Heating," *Physics of Fluids.* 24, (1981), 108-126.
7. Busnardo-Neto, J., *et al.*, "Ion-Cyclotron Resonance Heating of Plasmas and Associated Longitudinal Cooling," *Physical Review Letters.* 36, (1976), 28.
8. Cohen, *et al.*, "Particle and Energy Exchange between Untrapped and Electrostatically Confined Populations in Magnetic Mirrors," *Nuclear Fusion.* 20, (1980), 1421.
9. Damm, C. C., *et. al.*, *Preliminary Design of a Tandem-Mirror-Next-Step Facility,* UCRL-53060, LLL, (1980).
10. Dandle, R. A. *et. al.*, "Off-Resonance Effects on Electrons in Mirror-Contained Plasma," *Nuclear Fusion.* 11, (1971), 411-423.
11. Dandle, R. A, *et. al.*, *Electron Cyclotron Heating of Torodial Plasma with Emphasis on the results from the ELMO Bumpy Torus (EBT),* ORNL/TM-6703, Oak Ridge, (1979).
12. Fessenden, T. J., *Pulsed Electron-Cyclotron Resonance Discharge Experiment,* RLE Technical Report No. 442, (1966).
13. Grawe, H., "A Stochastic Model of Electron Cyclotron Heating," *Plasma Physics.* 11, (1969), 151.

14. Ikegami, H., *et. al.*, "Generation of Energetic Electrons by Electron Cyclotron Heating in a Mirror Field," *Nuclear Fusion.* 13, (1973), 351-361.

15. Ikegami, H. and R. A. Dandle, *Electron Cyclotron Heating for Bumpy Torus,* IPPJ-343, Nagoya, (1978).

16. Jaeger, F., *et al.*, "Theory of Electron Cyclotron Heating: Part 1. Short time and adiabatic effects," *Plasma Physics.* 18, (1972), 1073-1100.

17. Lichtenberg, A. L., "Determination of the Transition between Adiabatic and Stochastic Motion," *Intrinsic Stochasticity in Plasmas,* International workshop on stochasticity in plasmas, Corse, France, (1979), 13-40.

18. Lieberman, M. A., and A. J. Lichtenberg, "Theory of Electron Cyclotron Resonance Heating: Part 2, Long Time and Stochastic Effects," *Plasma Physics.* 15, (1973), 125-150.

19. Mauel, M. E., *Description of the Fokker-Plank Equation used to Model ECRH of the Constance 2 Expercimcnt,* PFC-RR-82/2, MIT, (1982a).

20. Mauel, M. E., *Heating Rates and Absorption Coefficients for Electron Cyclotron Heating in the Constance 2 Mirror Experiment,* M.I.T., (1982b).

21. Mauel, M. E., *Theory of Electron Cyclotron Heating in the Constance II Experiment,* PFC-RR-81/2, Massachusetts Institute of Technology, (1981).

22. Nexsen, W. E. and D. P. Grubb, "Operating Point for the TMX-U (Negative) Experiment," *Bull. Amer. Phys. Soc..* 26, (1981).

23. Porkolab, M., *Electron Cyclotron Resonance Heating of Tandem Mirrors,* UCRL-52634, LLL, (1978).

24. Porkolab, M, *et al.*, *Electron cyclotron resonance heating of plasmas in tandem mirrors,* UCRL-84345, Rev. 2, Lawrence Livermore Laboratory, (1980).

25. Porkolab and Chen, "Non-linear Wave Effects in Laboratory Plasmas: A comparison between theory and experiment," *Reviews of Modern Physics.* 50, (1978), 745.

26. Stallard, B. W., and E. B. Hooper, Jr., "Electron Heating by ECRH in TMX-Upgrade," *Bill. Amer. Phys. Soc..* 25, (1980).

27. Stallard, B. W., *et al.*, "Hot Electron thermal barrier startup in TMX-Upgrade," *Bull. of Amer. Physical Soc..* 26,New York, (1981), 926.

28. Sturrock, P. A., "Stochastic Acceraltion," *Physical Review.* 141, (1966), 186.

Chapter 2.

1. Begtson, *et al.*, "Observations of Plasma Heating in a Turbulent torus," *Physics of Fluids.* 18, (1974), 710.
2. Cohen, *et al.*, "Particle and Energy Exchange between Untrapped and Electrostatically Confined Populations in Magnetic Mirrors," *Nuclear Fusion.* 20, (1980), 1421.
3. Evans, R. D., *The atomic Nucleus,* New York, (1955).
4. Ferron, J. R., *et al., MHD Stability and Confinement in a Large Diameter Axisymmetric Mirror with High Mirror Ratio,* UCLA, (1981).
5. Griem, H. R., *Plasma Spectroscopy,* (1965).
6. Ioffe, M. S., *et. al.*, "Stabilization of Cone-Instability of a Collisional Plasma in a Mirror Trap," *Soviet Physics, JEPT.* 40, (1975).
7. Kanaev, B. I., and E. E. Yushmanov, "Investigation of Instability of a Collisional Plasma in a Mirror Trap," *Soviet Physics, JEPT.* 40, (1975).
8. Ioffe, M. S., *et. al.*, "Stabilization of Cone-Instability of a Collisional Plasma in a Mirror Trap," *Soviet Physics, JEPT.* 40, (1975).
9. Kanaev, B. I., "Stabilization of Drift Loss-Cone Instability (DCI) by addition of Cold Ions," *Nuclear Fusion.* 19, (1979), 347-359.
10. Klinkowstein, R. E., *et. al., Constance Mirror Program: Progress and Plans,* PFC-RR-81/3, M.I.T., (1981).
11. Klinkowstein, R. E., *Electron Beam Suppression of Loss Cone Instability in a Mirror Confined Plasma,* PhD thesis, Dept. of Electrical Engineering, MIT, (1978).
12. Mauel, M. E., *Hot Electron Stabilization of Electron Cyclotron Heating,* Plasma Research Report PRR-79/11, M.I.T., (1979).
13. Mauel, M. E., *et. al., The Collected Memorada of the Constance 2 Mirror Experiment,* Plasma Research Report PRR 80/13, MIT, (1980).
14. Molvik, A. W., *Large Acceptance Angle Gridded Analyzers in an Axial Magnetic Field,* LLL, (1981).

Chapter 3.

1. Akhiezer, A. I., *et. al.*, *Plasma Electrodynamics,* Vol. 1, Pergamon, (1975).
2. Batchelor, D. B., "Budden Tunneling in Parallel Stratified Plasma," *Plasma Physics.* 22, (1980), 41.
3. Bernstein, I. B., "Geometric Optics in Space- and Time-Varying Plasmas," *Physics of Fluids.* 18,, 320-324.
4. Budden, K. G., *Radio Waves in the Ionosphere,* Cambridge Press, (1961).

5. Fidone, I., *et. al.*, "Wave Absorption near the Electron Cyclotron Frequency," *Physics of Fluids.* 21, (1978), 645-652.
6. Friedland, L. and M Porkolab, *On the Electron-Cyclotron Resonance Heating in Plasmas with arbitrary Stratification of the Magnetic Field,* PFC-JA-80/21, Massachusetts Institute of Technology, (1980).
7. Garner, R., and M. E. Mauel, "Ray Tracing in the Constance 2 Mirror Experiment," *Bull. Amer. Phys. Soc..* 26, (1981), 893.
8. Mauel, M. E., *Heating Rates and Absorption Coefficients for Electron Cyclotron Heating in the Constance 2 Mirror Experiment,* M.I.T., (1982b).
9. Porkolab, M, *et al., Electron cyclotron resonance heating of plasmas in tandem mirrors,* UCRL-84345, Rev. 2, Lawrence Livermore Laboratory, (To be published).

Chapter 4.

1. Bernstein, I. B., and D. C. Baxter, "Relativistic Theory of Electron Cyclotron Heating," *Physics of Fluids.* 24, (1981), 108-126.
2. Berk, H. L., "Derivation of the Quasilinear Equation in a Magnetic Field," *J. Plasma Physics.* 20, (1978), 205-219.
3. Mauel, M. E., *Heating Rates and Absorption Coefficients for Electron Cyclotron Heating in the Constance 2 Mirror Experiment,* M.I.T., (1982b).
4. Stallard, B. W., *et al.*, "Hot Electron thermal barrier startup in TMX-Upgrade," *Bull. of Amer. Physical Soc..* 26,New York, (1981), 926.

Chapter 5.

1. Porkolab and Chen, "Non-linear Wave Effects in Laboratory Plasmas: A comparison between theory and experiment," *Reviews of Modern Physics.* 50, (1978), 745.

Appendix 1.

1. Berk, H. L., "Derivation of the quasi-linear equation in a magnetic field.," *J. Plasma Physics.* 20, (1978), 205-219.
2. Bernstein, I. B., and D. C. Baxter, "Relativistic theory of electron cyclotron resonance heating," *Physics of Fluids.* 24, (1981), 108-126.
3. Stallard, B. W., and E. B. Hogan, Jr., "Electron cyclotron resonance heating by ECRH in TMX-Upgrade," *Bull. of Amer. Physical Soc..* San Diego, (1980).
4. Baldwin, D. E., *et al.*, eds., *Physics Basis for MFTF-B,* No. UCID-18496-Part1, Lawrence Livermore Laboratory, (1980).

5. *Construction of TARA Tandem mirror facility,* PFC Project Proposal, Mass. Inst. of Tech., (1980).
6. Klinkowstein, R. E., *et al., Constance mirror program: progress and plans,* PFC-RR-81/3, Mass. Inst. of Tech., (1981).
7. Rosenbluth, M. N., "Superadiabaticity in mirror machines," *Physical Review Letters.* 29, (1972), 408-410.
8. Lieberman, M. A., and A. J. Lichtenberg, "Theory of electron cyclotron resonance heating: Part II. Long time and stochastic effects.," *Plasma Physics.* 15, (1973), 125-150.
9. Porkolab, M, *et al., Electron cyclotron resonance heating of plasmas in tandem mirrors,* UCRL-84345, Rev. 2, Lawrence Livermore Laboratory, (To be published).
10. Horton, C. W., *et al.*, "Microinstabilities in axisymmetric mirror machines," *Physics of Fluids.* 14, (1974).
11. Jaeger, F., *et al.*, "Theory of Electron Cyclotron Heating: Part 1. Short time and adiabatic effects," *Plasma Physics.* 18, (1972), 1073-1100.
12. Lichtenberg, A. J., "Determination of the transition between adiabatic and stochastic motion," *Intrinsic stochasticity in plasmas,* Intern. workshop on stochasticity in plasmas, Corse, France, (1979), 13-40.
13. Budden, K. G., *Radio Waves in the Ionosphere,* Cambridge Press, (1961).
14. Berk, H. L., and Book, D. L., "Plasma wave regeneration in inhomogeneous plasmas," *Physics of Fluids.* 12, (1969), 649-661.

Appendix 2.

1. Mauel, M. E., *Theory of Electron Cyclotron Heating in the Constance II Experiment,* PFC-RR-81/2, Massachusetts Institute of Technology, (1981).
2. Killeen, J. and K. D. Marx, "The solution of the Fokker-Plank Equation for a Mirror-Confined Plasma," *Advances in Plasma Physics,* Vol. ?, (19??), 421-489.
3. Cutler, T. A., L. D. Pearlstein and M. E. Rensink, *Computation of the Bounce-Average Code,* UCRL-52233, LLL, (1977).
4. Rosenbluth, M. N., W. M. MacDonald, and D. L. Judd, "Fokker-Plank Equation for an inverse-Square Force.," *Physical Review.* 107, (1957), 1-6.
5. Weinberg, S., *Gravitation and Cosmology,* Wiley, New York, (1972), 91-120.
6. Hornbeck, R. W., *Numerical Methods,* Quantum, New York, (1975).

Appendix 3.

1. Baldwin D. E., *et al*, "Turbulent Lifetimes in Mirror Machines," *Physical Review Letters*. 36, (1976).
2. Ioffe, M. S., *et. al.*, "Stabilization of Cone-Instability of a Collisional Plasma in a Mirror Trap," *Soviet Physics, JEPT,* 40, (1975).
3. Kanaev, B. I., "Stabilization of Drift Loss-Cone Instability (DCI) by addition of Cold Ions," *Nuclear Fusion*. 19, (1979), 347-359.
4. Klinkowstein and Smullin, "Suppresion of ω_{ci} Instabilities in a Mirror-Confined Plasma by Injection of an Electron Beam," *Physical Review Letters*. 40, (1978).
5. Mauel, M. E., *Hot Electron Stabilization of Electron Cyclotron Heating*, Plasma Research Report PRR-79/11, M.I.T., (1979).

Biographical Note

Michael E. Mauel was born in Madison, Wisconsin on August 3, 1956 and raised in Detroit, Michigan and South Bend, Indiana. He recieved a B.S.E.E. degree from the Massachusetts Institute of Technology in 1978 and was co-awarded the Guillemin Prize for his undergraduate thesis. He received the I.E.E.E. Fortesque Fellowship for his graduate training leading to his M.S.E.E. degree from the Massachusetts Institute of Technology in 1979. After completion of his doctorial work, Michael Mauel will begin work in the Magnetic Mirror division of M.I.T.'s Plasma Fusion Center.

PFC BASE MAILING LIST

Argonne National Laboratory, TIS, Reports Section
Associazione EURATOM - CNEN Fusione, Italy, The Librarian
Battelle-Pacific Northwest Laboratory, Technical Info Center
Brookhaven National Laboratory, Research Library
Central Research Institute for Physics, Hungary, Preprint Library
Chinese Academy of Sciences, China, The Library
The Flinders University of S.A., Australia, Jones, Prof. I.R.
General Atomic Co., Library
General Atomic Co., Overskei, Dr. D.
International Atomic Energy Agency, Austria,
Israel Atomic Energy Commission, Soreq Nucl. Res. Ctr., Israel
Kernforschungsanlage Julich, FRG, Zentralbibliothek
Kyushu University, Japan, Library
Lawrence Berkeley Laboratory, Library
Lawrence Livermore Laboratory, Technical Info Center
Max-Planck-Institut fur Plasma Physik, FRG, Main Library
Nagoya University, Institute of Plasma Physics, Japan
Oak Ridge National Laboratory, Fusion Energy Div. Library
Oak Ridge National Laboratory, Derby, Roger
Physical Research Laboratory, India, Sen, Dr. Abhijit
Princeton University, PPL Library
Rensselaer Polytechnic Institute, Plasma Dynamics Lab.
South African Atomic Energy Board, S. Africa, Hayzen, Dr. A.
UKAEA, Culham Laboratory, United Kingdom, Librarian
US Department of Energy, DOE Library
Universite de Montreal, Lab. de Physique des Plasmas, Canada
University of Innsbruck, Inst. of Theoretical Physics, Austria
University of Saskatchewan, Plasma Physics Lab., Canada
University of Sydney, Wills Plasma Physics Dept., Australia
University of Texas at Austin, Fusion Res. Ctr., Library
University of Wisconsin, Nucl. Eng. Dept., UW Fusion Library

INTERNAL MAILINGS

MIT Libraries
Industrial Liaison Office
G. Bekefi, A. Bers, D. Cohn, B. Coppi, R.C. Davidson,
T. Dupree, S. Foner, J. Freidberg, M.O. Hoenig, M. Kazimi,
L. Lidsky, E. Marmar, J. McCune, J. Meyer, D.B. Montgomery,
J. Moses, D. Pappas, R.R. Parker, N.T. Pierce, P. Politzer,
M. Porkolab, R. Post, H. Praddaude, D. Rose, J.C. Rose,
R.M. Rose, B.B. Schwartz, L.D. Smullin, R. Temkin, P. Wolff,
T-F. Yang